# Optical and Magnetization Studies on Europium Based Iron Pnictides

Von der Fakultät Mathematik und Physik der Universität Stuttgart
zur Erlangung der Würde eines Doktors der Naturwissenschaften
(Dr. rer. nat.) genehmigte Abhandlung

Vorgelegt von

**Sina Maria Ute Zapf**

aus Offenbach am Main

Hauptberichter: Prof. Dr. M. Dressel
Erster Mitberichter: Prof. Dr. B. Keimer
Zweiter Mitberichter: Prof. Dr. D. N. Basov

Tag der mündlichen Prüfung: 18.12.2014

1. Physikalisches Institut der Universität Stuttgart
2015

**Expect problems**
**and eat them for breakfast.**

***A. A. Montapert***

# ABSTRACT

Understanding the interplay of magnetism and superconductivity is one of the central topics in contemporary condensed matter research: while those are traditionally antagonistic phenomena, there is growing experimental evidence that unconventional superconductivity - for instance in cuprates, heavy fermion or organic materials - is closely linked to magnetism [1–3]. Among all these material classes, the cuprates garnered the most attention because for more than two decades, they were the only known "high-temperature superconductors". Only recently, they lost this monopoly position due to the discovery of relatively high critical temperatures in iron pnictides [4, 5].

One obvious common feature of cuprates and iron-based superconductors is an antiferromagnetic parent phase. While undoped cuprates are Mott insulators, the magnetism in iron pnictides is usually considered as rather itinerant with a metallic spin density wave ground state. Chemical substitution or external pressure continuously suppress the magnetic transition temperature, until superconductivity emerges. Thus, magnetic fluctuations are widely debated as a key ingredient for high-temperature superconductivity. Recently, however, another similarity has moved into the focus of interest: at the nematic phase transition, electronic interactions break the rotational symmetry of the crystal, accompanied by strong fluctuations [6]. Compared to the antiferromagnetic phase, this transition usually takes place at slightly higher temperatures. Unfortunately, the experimental access to this exotic phase is challenging, as crystals usually appear twinned, meaning that domains mask the intrinsic anisotropy.

The investigations carried out in the framework of this thesis mainly concentrate on europium based iron pnictides. These are a peculiar member of the 122 family as they develop at low temperatures ($\sim 20\,\mathrm{K}$) an additional magnetic order of the local rare earth moments (see Fig. 0.1). The $Eu^{2+}$ spin structure is a so-called "$A$-type" antiferromagnetism, meaning that spins of one layer are ferromagnetically aligned (along the $a$-axes), while neighbouring planes are coupled antiferromagnetically. Furthermore, neutron measurements revealed the possibility to detwin those compounds (*i.e.* to align the twinned domains along one direction) at low temperatures in laboratory-scale magnetic fields [7], a feat which is not possible in other iron pnictides and thus probably related to the rare

earth magnetism. Therefore, europium based iron pnictides provide a unique platform to study the interplay of structural, magnetic and electronic effects in high-temperature superconductors. For this challenging purpose, we have employed SQUID magnetometry and Fourier-transform infrared spectroscopy on $EuFe_2(As_{1-x}P_x)_2$ single crystals; the main results are summarized as followed.

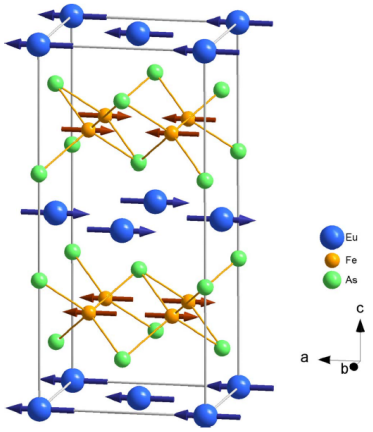


**Figure 0.1:** Magnetic structure of $EuFe_2As_2$ at 2.5 K [8]. $Fe^{2+}$ moments (brown arrows) align antiferromagnetically along the $a$- and the $c$-axis, but ferromagnetically along the $b$-axis. $Eu^{2+}$ moments (blue arrows) align within one europium layer ferromagnetically along the $a$-axis, and neighbouring $ab$-planes are coupled antiferromagnetically.

By systematic studies of the in- and out-of-plane magnetic properties of a series of $EuFe_2(As_{1-x}P_x)_2$ single crystals, we derived the complex magnetic phase diagram of europium based iron pnictides (see chapter 7, Ref. [9] and Ref. [10]). As depicted in Fig. 0.2, the $Eu^{2+}$ magnetic ordering involves two steps for all phosphorus substituted compounds. The transition at a higher temperature $T_N$ is characterized throughout the whole phase diagram by an antiferromagnetic interlayer coupling. One should note, however, that phosphorus substitution induces a ferromagnetic out-of-plane component, leading to canted $A$-type antiferromagnetism. This canting develops rather quickly at low substitution levels, similar to the suppression of $T_N$ and the spin density wave transition temperature. These observations imply that the $Eu^{2+}$ spin orientation is notably influenced by the spin density wave anisotropy. Thus, our measurements demonstrate significant interactions between the local $Eu^{2+}$ and the (quasi-) itinerant spin density wave magnetism, which is consistent with theoretical calculations [11].

The second magnetic transition in the europium subsystem displays glass-like dynamics, affecting the coupling between the planes. As its transition temperature $T_{glass}$ is lower than the onset of magnetic order, it is referred to as "re-entrant" spin glass phase. With increasing phosphorus substitution, $T_{glass}$ rises quickly until it approaches $T_N$, leading to successive transitions that are separated by $\sim 2\,K$. Thus, only measurements with rather small temperature steps are able to resolve both phases. Nevertheless, we find indications for similar dynamics when reviewing published data of other europium based

compounds (see chapter 6). Therefore, we suggest that the re-entrant spin glass phase is the key to understand how bulk superconductivity can coexist with the usually strong $Eu^{2+}$ magnetism.

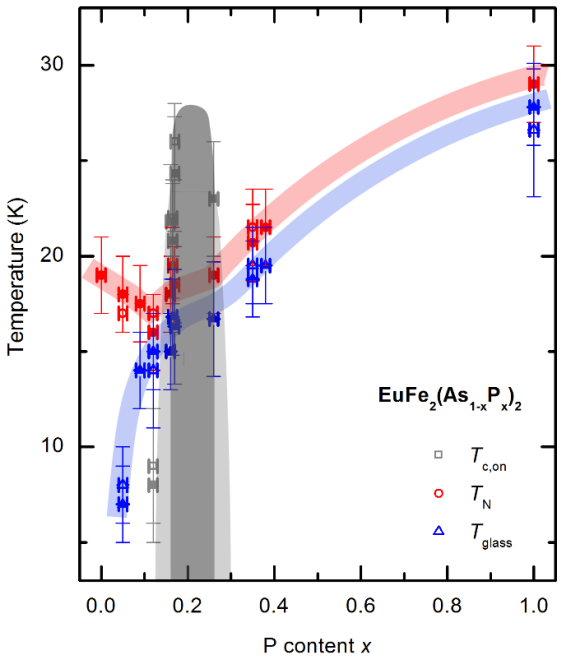


**Figure 0.2:** Phase Diagram of $EuFe_2(As_{1-x}P_x)_2$. $T_N$ (red dots) indicates a canted *A*-type antiferromagnetic transition, $T_{glass}$ (blue triangles) a spin glass transition, and $T_{c,on}$ the onset of superconductivity (grey squares). Closed symbols correspond to transition temperatures deduced from magnetization, open ones from resistivity measurements. Shadowed lines are guides to the eye. The light grey area indicates the onset of superconductivity, while bulk superconductivity is fully developed in the dark grey regime.

Despite the interactions of local and itinerant magnetism revealed by our magnetization studies, the electrodynamic response of $EuFe_2As_2$ is surprisingly unaffected by the $Eu^{2+}$ magnetic transition - the infrared spectra basically do not change when passing $T_N$ (see chapter 8). By comparing several fitting approaches, we find that the most realistic results are obtained with a model that contains two Drude components (probably representing electron and hole bands) and a Lorentzian around 1000 $cm^{-1}$, which can be attributed to interband transitions involving Fe hole pockets [12]. Importantly, we are able to extract trends that are independent from the fitting method. For instance, we conclude that the spin density wave transition affects not only both Drude components, but also the spectral weight transfer, which appears in iron pnictides usually up to very high energies. These observations provide interesting insights into the relation of this transfer to the localization of itinerant carriers driven by correlation effects.

Combining our expertise obtained from magnetization and optical studies on europium compounds, we have also performed magneto-optical measurements on $EuFe_2As_2$ (see chapter 9, [13]), which revealed a much more complex detwinning process than expected.

At temperatures below the local $Eu^{2+}$ ordering, the detwinning occurs in two steps, meaning that the crystal gets already partially detwinned with $b \parallel H$ at $\sim 0.1\,\mathrm{T}$, followed by a reverse reorientation of structural domains with $a \parallel H$ at $\sim 0.6\,\mathrm{T}$. Above $T_\mathrm{N}$, only the latter process takes place. We ascribe these observations to an indirect magneto-elastic coupling of the $Eu^{2+}$ ions via the $Fe^{2+}$ spins, which was - to our best knowledge - not proposed before. Moreover, we give a simple model for the two-step detwinning process based on the competition between magneto-crystalline anisotropy, antiferromagnetic exchange coupling and Zeeman energy (see Fig. 0.3).

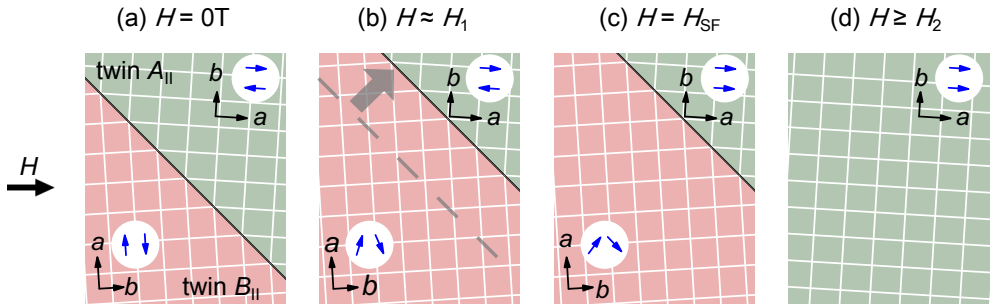


**Figure 0.3:** Sketch of the twin distribution of $EuFe_2As_2$ dependent on an (from left to right increasing) external magnetic field $H \parallel [110]_\mathrm{T}$ at $T < T_\mathrm{Eu}$. (a) For $H = 0\,\mathrm{T}$, the zero-field crystal is twinned and the domains are equally distributed. The $Eu^{2+}$ spins are ordered $A$-type antiferromagnetically with the spin direction along the $a$-axis. (b) With external field, twin variant $B_\parallel$ (red, bottom) with $b \parallel H$ gets energetically favoured and therefore grows on the expense of variant $A_\parallel$ (green, top), as soon as the energy difference exceeds the twin boundary pinning energy. (c) With further increasing field, $Eu^{2+}$ spins in the remaining type $A_\parallel$ twins flip along the field direction. Energetically, twin $B_\parallel$ is still more favourable. (d) At slightly higher fields, twin $A_\parallel$ is favoured and the crystal is detwinned with $a \parallel H$.

Most importantly, the induced detwinning is persistent, meaning that a significant imbalance of twin domains remains when the magnetic field is switched off and the temperature is raised up to the nematic and spin density wave transition. Such strongly hysteretic behaviour is surprising from a very fundamental point of view, as the detwinning that is induced at low temperatures with very small magnetic fields persists up to much higher temperatures, *i.e.* energy scales. Thus, our whole studies on europium based pnictides reveal a remarkable interdependence between magnetic, electronic and structural effects that might be very important to understand the unconventional superconductivity in these fascinating materials.

# ZUSAMMENFASSUNG

Eines der zentralen Themen der heutigen Festkörperforschung ist es, die Wechselwirkungen zwischen Supraleitung und Magnetismus besser zu verstehen. Obwohl diese Phänomene traditionell nicht miteinander vereinbar sind, mehren sich die Hinweise, dass unkonventionelle Supraleitung, die beispielsweise in Kupferoxiden, Schweren Fermionen oder organischen Materialien vorkommt, überraschenderweise sehr eng mit Magnetismus verbunden ist [1–3]. Dabei stellen die Kupferoxide vermutlich die am meisten untersuchte Materialklasse dar, da sie mehr als 20 Jahre die einzigen bekannten Vertreter der "Hochtemperatursupraleiter" waren. Tatsächlich ging diese Monopolstellung erst kürzlich verloren, als Supraleitung mit überraschend hohen Übergangstemperaturen in Eisenpniktiden entdeckt wurde [4, 5].

Vergleicht man verschiedene Hochtemperatursupraleiter, so ist eine offensichtliche Gemeinsamkeit, dass Antiferromagnetismus eine wichtige Rolle im Phasendiagramm spielt: während undotierte Kupferoxide Mott-Isolatoren sind, geht man bei Eisenpniktiden in den meisten Fällen von einem metallischen Spindichtewellen-Grundzustand aus. Durch chemische Substitution oder das Anlegen von externem Druck wird dessen Übergangstemperatur kontinuierlich verringert, bis schließlich Supraleitung einsetzt. Deshalb liegt es nahe, antiferromagnetische Fluktuationen mit dem Auftreten von Hochtemperatursupraleitung zu assoziieren. Aktuell rückt allerdings eine weitere Gemeinsamkeit immer mehr in den Fokus der Forschung: bei dem sogenannten "nematischen" Übergang wird die Rotationssymmetrie des Kristalls durch elektronische Wechselwirkungen gebrochen; dabei treten sehr starke Fluktuationen auf [6]. Verglichen mit der antiferromagnetischen Phase findet dieser Übergang im Normalfall bei einer leicht höheren Temperatur statt. Leider ist seine Erforschung relativ kompliziert, da die resultierende strukturelle und elektronische Anisotropie durch Domänenbildung maskiert wird.

Die im Rahmen dieser Arbeit durchgeführten Untersuchungen konzentrieren sich auf Europium-haltige Eisenpniktide. Diese entwickeln zusätzlich zur Spindichtewelle bei tiefen Temperaturen (ca. 20 K) eine lokale magnetische Ordnung. Hierbei sind die $Eu^{2+}$ Spins innerhalb einer Ebene ferromagnetisch, aber benachbarte Ebenen antiferromagnetisch gekoppelt - auch "*A*-typ" Antiferromagnetismus genannt (vgl. Abbildung 0.4). Desweiteren

ging aus Neutronenstreuungs-Experimenten hervor, dass in $EuFe_2As_2$ relativ niedrige Magnetfelder $\sim 1\,T$ ausreichen, um bei Temperaturen unterhalb der $Eu^{2+}$-Ordnung alle Domänen gleich auszurichten [7]; in anderen Eisenpniktiden ist dies nicht möglich. Aus diesem Grund bieten Europium-haltige Eisenpniktide die außergewöhnliche Möglichkeit, strukturelle, magnetische und elektronische Effekte, sowie deren Wechselwirkungen in Hochtemperatursupraleitern zu untersuchen. Dafür wurden im Rahmen dieser Arbeit Magnetisierungsmessungen und Fourier-Transform-Infrarotspektroskopie an $EuFe_2(As_{1-x}P_x)_2$ Einkristallen durchgeführt. Die wichtigsten Ergebnisse werden im Folgenden vorgestellt.

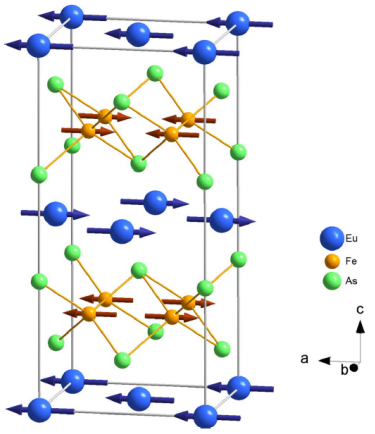


**Abbildung 0.4:** Magnetische Struktur von $EuFe_2As_2$ bei 2.5 K [8]. Die $Fe^{2+}$ Spins (braune Pfeile) sind antiferromagnetisch entlang der $a$- und $c$-Achse, aber ferromagnetisch entlang der $b$-Achse ausgerichtet. Die $Eu^{2+}$ Spins (blaue Pfeile) einer Ebene sind ferromagnetisch gekoppelt und zeigen in Richtung der $a$-Achse; benachbarte Ebenen sind antiferromagnetisch gekoppelt.

Auf der Basis von richtungsabhängigen Untersuchungen der magnetischen Eigenschaften von $EuFe_2(As_{1-x}P_x)_2$ Einkristallen konnte das komplexe magnetische Phasendiagramm von Europium-haltigen Eisenpniktiden bestimmt werden; dieses ist in Abb. 0.5 zu sehen (s. Kapitel 7, Ref.[9] und Ref. [10]). Man stellt fest, dass die lokale $Eu^{2+}$-Ordnung tatsächlich schrittweise abläuft. Betrachtet man zunächst den Übergang bei höherer Temperatur $T_N$, so bleibt die Kopplung zwischen den Ebenen durch das gesamte Phasendiagramm antiferromagnetisch. Allerdings entwickelt sich mit steigender Phosphor-Substitution rasch eine ferromagnetische Komponente entlang der $c$-Richtung; man spricht von "gekantetem" $A$-typ Antiferromagnetismus. Da die Zunahme dieser Komponente mit einer Unterdrückung der Ordnungstemperatur von Spindichtewelle und lokalem $Eu^{2+}$-Magnetismus verbunden ist, liegt es nahe, dass die beiden magnetischen Ordnungen sich gegenseitig beeinflussen; dies wird auch durch theoretische Berechnungen unterstützt [11].

Der zweite magnetische Übergang bei tieferen Temperaturen $T_{glass}$ ist glasartig und betrifft die Kopplung zwischen den Ebenen. Da er einer magnetischen Ordnung folgt, spricht man auch von einem "*re-entrant*" Spin-Glas. Betrachtet man den Verlauf der Übergangstemperatur $T_{glass}$, so steigt sie bei niedrigen Phosphor-Konzentrationen schnell an und

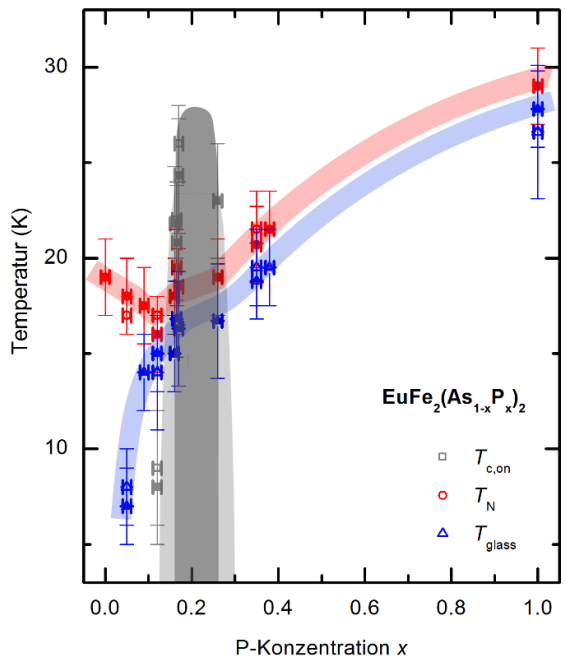


**Abbildung 0.5:** Phasendiagramm von $EuFe_2(As_{1-x}P_x)_2$. $T_N$ (rote Punkte) ist die Übergangstemperatur des gekanteten $A$-typ Antiferromagnetismus, $T_{glass}$ (blaue Dreiecke) die des Spin-Glas Übergangs, und $T_{c,on}$ die der Supraleitung (graue Quadrate). Geschlossene Symbole wurden aus Magnetisierungsmessungen, offene aus Widerstandskurven extrahiert. Transparente Linien zeigen die wichtigen Trends; während die hellgraue Fläche das Einsetzen von Supraleitung markiert, entspricht die dunkelgraue Region der voll entwickelten Supraleitung.

folgt dann $T_N$ im Abstand von etwa 2 K. Aus diesem Grund kann dieses ungewöhnliche Verhalten nur in Messungen mit sehr kleinen Temperaturschritten aufgelöst werden. Nichtsdestrotrotz wurden ähnliche Beobachtungen auch bei anderen Europium-haltigen Eisenpniktiden gemacht (s. Kapitel 6). Deshalb ist dieses glasartige Verhalten vermutlich der Schlüssel, um die Koexistenz von Europium-Magnetismus und Supraleitung zu erklären.

Trotz der Wechselwirkungen zwischen den magnetischen und elektronischen Subsystemen, die durch diese Magnetisierungsmessungen nachgewiesen werden konnten, ist das optische Spektrum von $EuFe_2As_2$ überraschend unbeeinflusst von der lokalen $Eu^{2+}$ Ordnung (s. Kapitel 8). Der Vergleich mehrerer Modellierungsansätze ergibt, dass die realistischsten Ergebnisse durch eine Analyse mit zwei Drude- und einer Lorentzkomponenten (bei 1000 $cm^{-1}$) erhalten werden. Dabei repräsentieren erstere vermutlich Elektronen- und Lochbänder, letztere Interbandübergänge in die Eisen-Lochtaschen [12]. Vor allem aber können durch diesen Vergleich Trends bestimmt werden, die unabhängig vom Modellierungsansatz sind: der Spindichtewellen-Übergang beeinflusst nicht nur beide Drude-Komponenten, sondern auch den Transfer von spektralem Gewicht, der in Eisenpniktiden üblicherweise bis zu sehr hohen Energien auftritt. Diese Beobachtungen liefern interessante Informationen, inwiefern dieser Transfer mit der Lokalisierung von freien Ladungsträgern aufgrund von Korrelationseffekten zusammenhängt.

Die Erfahrungen mit magnetischen und optischen Messungen wurden schließlich genutzt, um eine Reihe von magneto-optischen Untersuchungen an $EuFe_2As_2$ durchzuführen (s. Kapitel 9 und Ref. [13]). Dabei konnte aufgedeckt werden, dass dem Ausrichten der Domänen im Magnetfeld ein wesentlich komplexerer Prozess zu Grunde liegt, der jedoch durch ein relativ einfaches Modell erklärt werden kann (s. Abb. 0.6). Bei Temperaturen unterhalb von $T_N$ verläuft diese Ausrichtung in zwei Schritten: zunächst wird ein Großteil der Domänen schon bei sehr niedrigen Feldern von $\sim 0.1\,T$ mit der $b$-Achse parallel zum Magnetfeld $H$ ausgerichtet; dem folgt eine Ausrichtung mit der $a$-Achse parallel zu $H$ bei Feldern von etwa 0.6 T. Oberhalb von $T_N$ findet nur letzterer Prozess statt. Dieses Verhalten deutet auf eine bis dahin unbekannte indirekte magneto-elastische Kopplung hin, bei denen die $Eu^{2+}$-Spins über die $Fe^{2+}$-Momente mit dem Gitter wechselwirken können.

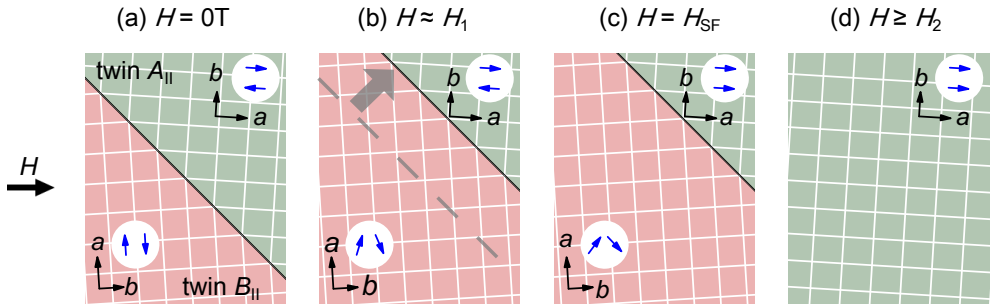


**Abbildung 0.6:** Schematische Darstellung der Domänenverteilung in $EuFe_2As_2$ in Abhängigkeit eines (von links nach rechts zunehmenden) externen magnetischen Feldes $H \parallel [110]_T$ bei Temperaturen $T < T_{Eu}$. (a) Bei $H = 0\,T$ sind die Domänen ("*twins*") gleichmäßig verteilt, wenn der Kristall im Nullfeld abgekühlt wurde. (b) In einem externen Feld werden zunächst die Domänen $B_\parallel$ (rot, unten) mit $b \parallel H$ energetisch begünstigt, weswegen ihr Anteil auf Kosten der Domänen $A_\parallel$ (grün, oben) steigt, sobald die Energie die der Haftung der Domänenwände übersteigt. (c) Wird das externe Feld weiter erhöht, kommt es zu einem $Eu^{2+}$ Spin-Flip in den verbleibenden $A_\parallel$-Domänen; energetisch sind jedoch noch die anderen bevorzugt. (d) Dies ändert sich erst bei leicht höheren Feldern und alle Domänen werden mit der $a$-Achse entlang von $H$ ausgerichtet.

Die vermutlich wichtigste Beobachtung bei diesen Studien ist, dass das magnetfeldinduzierte Ungleichgewicht der Domänen bestehen bleibt, auch wenn das Feld ausgeschaltet und die Temperatur bis zum Spindichtewellen- und nematischen Übergang erhöht wird. Berücksichtigt man die relevanten Energieskalen, so ist eine solch robuste Hysterese tatsächlich sehr überraschend. Somit konnten die im Rahmen dieser Arbeit durchgeführten Studien an Europium-haltigen Eisenpniktiden ein bemerkenswertes Zusammenspiel von magnetischen, elektronischen und strukturellen Effekten aufdecken, welches einen wichtigen Einblick in die faszinierenden Zusammenhänge unkonventioneller Supraleiter gibt.

# PUBLICATIONS

**Some results of this work have been already published:**

- **S. Zapf**, D. Wu, L. Bogani, H. S. Jeevan, P. Gegenwart, and M. Dressel
  *Varying $Eu^{2+}$ magnetic order by chemical pressure in $EuFe_2(As_{1-x}P_x)_2$*
  Phys. Rev. B **84**, 140503(R) (2011).

- **S. Zapf**, B. Gorshunov, D. Wu, E. Zhukova, V. S. Nozdrin, S. Haindl, K. Iida, and M. Dressel
  *Intra-gap absorption in superconducting $Ba(Fe_{1-x}Co_x)_2As_2$ thin films studied by a Fabry-Pérot resonant technique*
  J. Supercond. Nov. Magn. **21**, 1557 (2013).

- **S. Zapf**, H. S. Jeevan, T. Ivek, F. Pfister, F. Klingert, S. Jiang, D. Wu, P. Gegenwart, R. K. Kremer, and M. Dressel
  *$EuFe_2(As_{1-x}P_x)_2$: reentrant spin glass and superconductivity*
  Phys. Rev. Lett. **110**, 237002 (2013).

- A. S. Prokhorov, E. S. Zhukova, A. A. Boris, I. E. Spektor, B. P. Gorshunov, V. S. Nozdrin, E. A. Motovilova, L. S. Kadyrov, **S. Zapf**, S. Haindl, K. Iida, M. Dressel, K. V. Chizh, M. S. Storozhevykh, L. V. Arapkina, V. A. Chapnin, O. V. Uvarov, V. P. Kalinushkin, and V. A. Yuryev
  *Submillimeter quasioptical spectroscopy of multilayer conducting and superconducting systems*
  Radiophys. Quant. Electr. **56**, 620 (2014).

- A. E. Karakozov, **S. Zapf**, B. Gorshunov, Y. G. Ponomarev, M. V. Magnitskaya, E. Zhukova, A. S. Prokhorov, V. B. Anzin, and S. Haindl
  *Temperature dependence of the superfluid density as a probe for multiple gaps in $Ba(Fe_{0.9}Co_{0.1})_2As_2$: Manifestation of three weakly interacting condensates*
  Phys. Rev. B **90**, 014506 (2014).

- A. E. Karakozov, B. P. Gorshunov, Y. G. Ponomarev, A. S. Prokhorov, M. V. Magnitskaya, E. Zhukova, K. Iida, M. Dressel, **S. Zapf**, and S. Haindl

*Studying the structure of the superconducting state in Co doped multiband $BaFe_2As_2$ compounds*
JETP Letters **100**, 328 (2014).

- **S. Zapf**, C. Stingl, K. W. Post, J. Maiwald, N. Bach, I. Pietsch, D. Neubauer, A. Löhle, C. Clauss, S. Jiang, H. S. Jeevan, D. N. Basov, P. Gegenwart, and M. Dressel
*Persistent detwinning of iron pnictides by small magnetic fields*
Phys. Rev. Lett. **113**, 227001 (2014).

- **S. Zapf**, D. Neubauer, A. Kadau, K. Post, H. S. Jeevan, P. Gegenwart, D. N. Basov, and M. Dressel
*Electronic scattering effects in Europium based iron pnictides*
in preparation.

**Additional scientific publications which are not presented in this thesis:**

- B. Gorshunov, E. Zhukova, V. I. Torgashev, L. Motovilova, L. S. Kadyrov, F. Fischgrabe, V. Moshnyaga, T. Zhang, R. Kremer, U. Pracht, **S. Zapf**, and M. Dressel
*Boson peak in overdoped manganites $La_{1-x}Ca_xMnO_3$ ($0.5 \leq x \leq 1$)*
Phys. Rev. B **87**, 245124 (2013).

- B. P. Gorshunov, E. S. Zhukova, V. I. Torgashev, L. S. Kadyrov, E. A. Motovilova, F. Fischgrabe, V. Moshnyaga, T. Zhang, R. Kremer, U. Pracht, **S. Zapf**, and M. Dressel
*Boson peak in manganites*
J. Phys.: Conf. Ser. **486**, 012001 (2014).

- S. Haas, E. Heintze, **S. Zapf**, B. Gorshunov, M. Dressel, and L. Bogani
*Direct observation of the discrete energy spectrum of two lanthanide-based single-chain magnets by far-infrared spectroscopy*
Phys. Rev. B **89**, 174409 (2014).

- L. S. Kadyrov, B. P. Gorshunov, E. S. Zhukova, V. I. Torgashev, A. S. Prokhorov, E. A. Motovilova, F. Fischgrabe, V. T. Moshnyaga, T. Zhang, R. K. Kremer, U. Pracht, **S. Zapf**, J. Pokorný, G. Untereiner, S. Kamba, and M. Dressel
*Terahertz-infrared electrodynamics of overdoped manganites $La_{1-x}Ca_xMnO_3$*
Phase Transitions **87**, 1050 (2014).

# Contents

# 1 INTRODUCTION

The discovery of high temperature superconductivity in cuprates as well as iron-based pnictides and chalcogenides unified two conventionally antagonistic fields of solid state physics: magnetism and superconductivity. While magnetic interactions were fascinating already the ancient Greeks, superconductivity is a relatively "young" phenomenon, discovered only in 1911 [2, 14].

Conventional superconductors exhibit two characteristic properties below a critical temperature $T_c$: zero-resistivity and the expulsion of any external magnetic field. Both characteristics have a huge potential for applications, such as non-dissipative power lines, energy storages and levitating transport vehicles. Accordingly, enormous efforts were made to understand the microscopic origin of superconductivity. Nevertheless, it took almost 50 years until Bardeen, Cooper and Schrieffer solved this puzzle by introducing a coherent ground state formed out of electron pairs with opposite spin and momentum [15]. As internal or external magnetic fields directly act on those properties, it is evident that magnetism and superconductivity are traditionally competing phenomena.

One of the main drawbacks for applications is that the "glue" which holds those electron pairs together consists conventionally of electron-phonon interactions [16, 17], which require very low temperatures to manifest [18]. Therefore, the discovery of high temperature superconductivity (up to 164 K [19]) in cuprates [20] and iron-based superconductors [4] shook the scientific world and attracted tremendous interest even in the general public.

Interestingly, the phase diagram of both material classes contains a magnetically ordered phase that can be suppressed upon doping, chemical substitution or mechanical pressure, until superconductivity emerges [3]. While the parent compounds of cuprates are antiferromagnetic Mott insulators, those of iron pnictides are metals that exhibit a spin density wave phase. A similar situation can be found in a variety of other superconductors with unconventional properties, such as heavy fermion or organic materials [1]. Therefore, the idea developed that magnetic fluctuations might be the "pairing glue" of unconventional superconductors.

It turned out, however, that a uniform description of high-temperature superconductors is much more complicated than expected. One reason is that a close inspection of their phase diagrams reveals a number of exotic phases that appear in the vicinity of the superconducting dome; it is not clear whether these additional phases support or compete with superconductivity [21]. One example that attracted recently a lot of attention is the nematic phase, which is the breaking of the rotational $C_4$ symmetry driven by electronic interactions [6]. This means that additionally to a tetragonal-to-orthorhombic structural transition, an electronic in-plane anisotropy sets in, whose magnitude is much larger than one would expect from the lattice distortion. Unfortunately, the experimental investigation of this exotic phase is challenging, as the induced orthorhombic distortion is so small that crystals usually appear twinned, meaning that domains mask the intrinsic anisotropy. While in cuprates, mechanical clamps and magnetic fields were found to detwin single crystals [22, 23], in the case of iron pnictides, the effect of laboratory magnetic fields on the twin domain distribution is typically rather weak [24] and thus, only mechanical clamps are commonly used [6]. However, this introduces an explicit symmetry breaking by uniaxial pressure, meaning that one disturbs the anisotropy which one actually wants to measure [25].

$EuFe_2As_2$ is a peculiar parent compound of the iron pnictides, since, in addition to the spin density wave in the FeAs layers ($\sim 190\,\mathrm{K}$), it exhibits long-range magnetic order of the $Eu^{2+}$ local moments at low temperatures ($\sim 19\,\mathrm{K}$) [26–28]. Nevertheless, bulk superconductivity up to $\sim 30\,\mathrm{K}$ can be induced by mechanical pressure [29], isovalent substitution [30, 31] and doping [32–34]. Furthermore, neutron studies revealed that magnetic fields in the range of $1\,\mathrm{T}$ are able to detwin $EuFe_2As_2$ [7], allowing the study of the electronic in-plane anisotropy at typical laboratory-scale fields. Thus, Eu based iron pnictides offer the extraordinary possibility to investigate the interplay of unconventional electronic properties, superconductivity, itinerant and local magnetism. Therefore, systematic (magneto-)optical and magnetization studies of $EuFe_2(As_{1-x}P_x)_2$ single crystals were performed in the framework of this thesis.

The following text is organized as follows: first, the basic concepts of magnetic and superconducting materials are summarized (see chapters 2 and 3), focusing on high-temperature superconductivity and the interplay of magnetism and superconductivity. Subsequently, the electrodynamic properties of metals, broken symmetry phases, and in particular iron pnictides are reviewed (see chapter 4), which is followed by a brief summary of the investigated materials and chosen methods (see chapter 5). The experimental part of this thesis is introduced in chapter 6 with a review of Eu based iron pnictides. This paves the way for the magnetic phase diagram of $EuFe_2(As_{1-x}P_x)_2$ that is gained by our magnetization studies presented in chapter 7; from the comparison with literature, we discuss further implications for other Eu based materials.

Despite the peculiar local magnetic order, $EuFe_2As_2$ displays typical electrodynamic properties of correlated materials. Therefore, we use it in chapter 8 as a model system to compare various fitting approaches that are commonly applied to iron pnictides. Finally, magneto-optical measurements on $EuFe_2As_2$ are presented that reveal a much more complicated magnetic detwinning mechanism than expected (see chapter 9), uncovering a unique possibility to study the intrinsic in-plane anisotropy of iron pnictides without the application of any symmetry-breaking external force. All those findings are concluded in chapter 10, evidencing a remarkable interplay of magnetic, electronic and structural effects in Eu based iron pnictides.

# 2
# MAGNETISM

Magnetism in condensed matter contains a wide variety of phenomena: the response of a solid on an external magnetic field depends delicately on whether its magnetic moments are interacting or basically isolated from each other. In this chapter, a sound basis should be established to understand the complex magnetic order(s) in Eu based iron pnictides. Therefore, important magnetic quantities are introduced, followed by a brief introduction of magnetic interactions in solids. Finally, different types of magnetism are categorized and phenomenologically described. If not declared explicitly, explanations follow Ref. [14].

## 2.1 Basic definitions

In free space, a magnetic field with strength $\mathbf{H}$ leads to a magnetic flux density $\mathbf{B}$ of:

$$\mathbf{B} = \mu_0 \mathbf{H} \tag{2.1}$$

with the permeability of free space $\mu_0$.

However, if **H** acts on a magnetic solid, one has to account also for the magnetization **M** of this solid and equation 2.1 transfers into[1]:

$$\mathbf{B} = \mu_0(\mathbf{H} + \mathbf{M}). \tag{2.2}$$

The magnetic susceptibility $\chi$ describes, how much a material gets magnetized by a magnetic field and is generally defined (along a certain direction) as:

$$\chi = \frac{dM}{dH}. \tag{2.3}$$

For a so-called "linear material", equation 2.2 can be rewritten as:

$$\mathbf{B} = \mu_0(1 + \chi)\mathbf{H} = \mu_0\mu_\mathrm{r}\mathbf{H} \tag{2.4}$$

with the relative permeability of the material $\mu_\mathrm{r} = 1 + \chi$.

When analysing experimental data, one further has to take into account that in magnetic solids, the internal magnetic field strength $\mathbf{H}_\mathrm{int}$ is reduced with respect to the external one, $\mathbf{H}_\mathrm{ext}$:

$$\mathbf{H}_\mathrm{int} = \mathbf{H}_\mathrm{ext} - N\mathbf{M} \tag{2.5}$$

with the demagnetization factor $N$, which depends on the geometry of the sample and varies $0 \leq N \leq 1$.

An intuitive picture for this field reduction is the following [35]: in a magnetized sample, the magnetic moments are preferentially aligned along one direction. Imagining these magnetic moments as miniature magnets with north and south poles (see Fig. 2.1a), neighbouring poles will cancel each other out; only poles at the surface will be left (see Fig. 2.1b). The latter will cause an internal magnetic field, which is opposed to the magnetization and therefore called "demagnetization field". Its strength $\mathbf{H}_\mathrm{d}$ will be very sensitive to the shape of the material. For a very thin sample and an in-plane magnetic field, there is basically no place for the formation of these surface poles, causing negligible demagnetization effects ($N \to 0$). For the out-of-plane direction, however, the situation is vice versa and the demagnetization factor approaches unity.

Thus, the experimentally determined susceptibility of a linear material is actually:

$$\chi_\mathrm{exp} = \frac{M}{H_\mathrm{ext}} = \frac{M}{H_\mathrm{int} + NM} = \frac{\chi_\mathrm{intrinsic}}{1 + N\chi_\mathrm{intrinsic}} \tag{2.6}$$

1 With a relative permeability of $\mu_\mathrm{r} \approx 1$.

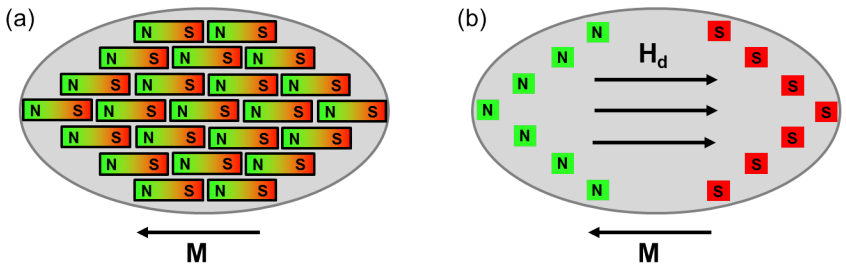


**Figure 2.1:** Schematic drawing to explain the demagnetization field (adapted from Ref. [35]). (a) In a magnetized sample, magnetic moments depicted as miniature magnets with north (N) and south (S) poles are preferentially aligned. (b) As neighbouring poles will cancel each other out, only poles at the surface will be left. These cause an internal magnetic field ("demagnetization field" with strength $\mathbf{H}_\mathrm{d}$) opposed to the magnetization $\mathbf{M}$.

with the intrinsic susceptibility:

$$\chi_\mathrm{intrinsic} = \frac{M}{H_\mathrm{int}} \tag{2.7}$$

As usually $\chi_\mathrm{intrinsic} \ll 1$, demagnetization effects are often negligible. However, sample shape effects might determine the measured susceptibility in ferromagnets (see section 2.3), causing $\chi_\mathrm{exp} \to 1/N$.

## 2.2 Magnetic interactions

In order to describe magnetic long range order, one has to understand the underlying interactions between the magnetic moments. Usually, magnetic dipolar interactions are negligible, and the dominant mechanism can be described by exchange interactions via the Heisenberg Hamiltonian:

$$\mathcal{H} = -2\sum_{i>j} J_{ij}\mathbf{S}_i\mathbf{S}_j \tag{2.8}$$

with the exchange constant $J_{ij}$ between the $i^\mathrm{th}$ and $j^\mathrm{th}$ spin, whose sign determines the magnetic ground state.

If the overlap between neighbouring magnetic atoms is high enough, direct exchange interaction is possible. However, this is often not the case, for instance for the $4f$-orbitals of rare earth elements, and indirect exchange has to be considered. In metals, conduction electrons can mediate the exchange between local moments via spin-polarization. This is known as "RKKY-exchange", named after the discoverers Ruderman, Kittel, Kasuya and Yosida [36]. Depending on the details of the Fermi surface and the distance between the magnetic moments, the RKKY-exchange constant oscillates between positive and negative sign.

## 2.3 Types of magnetism

In this section, different types of magnetism are phenomenologically described. Starting with the behaviour of non-interacting moments in a magnetic field, diamagnetism and paramagnetism are introduced. In contrary, ferro-, antiferro-, and helimagnetic materials show long-range magnetic order, where the involved magnetic moments act cooperatively. Finally, also glassy short-range dynamics are discussed.

### Diamagnetism

All materials exhibit diamagnetism: due to the orbital motion of the electrons, an external magnetic field induces a magnetic moment opposed to the direction of the applied field. This process is rather temperature-independent (see Fig. 2.2a). However, the induced negative susceptibility (see Fig. 2.2b) is usually much smaller than other magnetic contributions. One exception are superconductors which are "perfect diamagnets", as will be discussed in more detail in chapter 3.3.1.

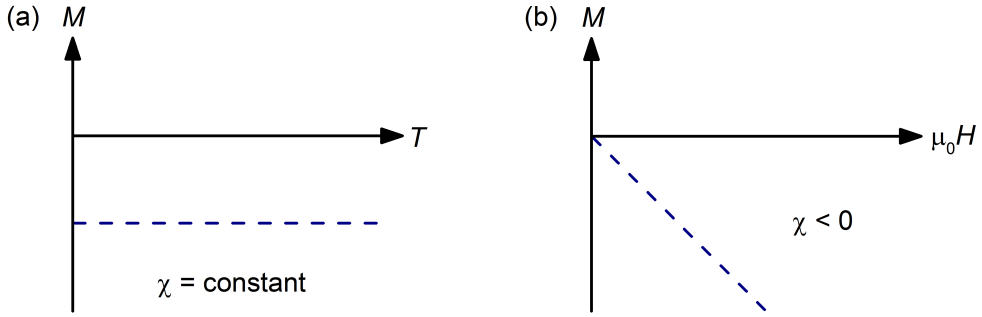


**Figure 2.2:** Typical (a) temperature- and (b) field-dependent magnetization of a diamagnetic material. The susceptibility is temperature-independent and negative.

### Paramagnetism

The key ingredient for paramagnetism are unpaired, non-interacting electrons: while their magnetic moments do not have any preferred orientation in zero field, they can be aligned by an external magnetic field. The degree of alignment depends on the strength of the external field as well as on the temperature, as thermal fluctuations counteract the field-enforced order.

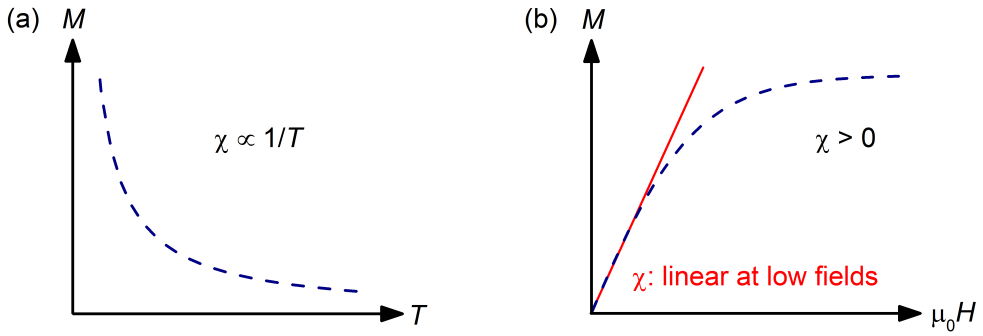


**Figure 2.3:** Typical (a) temperature- and (b) field-dependent magnetization of a paramagnetic material. (a) The temperature-dependent magnetization can be described by the Curie law $\chi \propto 1/T$. (b) The magnetization follows with increasing field a Brillouin function, which is almost linear at low fields (as can be seen by the red line, a guide to the eye).

From a quantum mechanical description of non-interacting electrons with total angular momentum $\mathbf{J} = \mathbf{L} + \mathbf{S}$ ($\mathbf{L}$: orbital momentum, $\mathbf{S}$: spin momentum), one can derive the magnetic field dependence of a paramagnet as (see Fig. 2.3b):

$$M = M_{\mathrm{s}} \mathrm{B}_J \left( \frac{g_J \mu_{\mathrm{B}} J B}{k_{\mathrm{B}} T} \right) \tag{2.9}$$

with the saturation magnetization:

$$M_{\mathrm{s}} = n g_J \mu_{\mathrm{B}} J, \tag{2.10}$$

the Brillouin function:

$$\mathrm{B}_J(x) = \frac{2J+1}{2J} \coth\left( \frac{2J+1}{2J} x \right) - \frac{1}{2J} \coth\left( \frac{x}{2J} \right), \tag{2.11}$$

the Landé $g$-factor:

$$g_J = \frac{3}{2} + \frac{S(S+1) - L(L+1)}{2J(J+1)}, \tag{2.12}$$

the number of spins per unit volume $n$, the Bohr magneton $\mu_{\mathrm{B}}$, the Boltzmann constant $k_{\mathrm{B}}$, and the temperature $T$.

In typical paramagnetic materials, except for very high fields and very low temperatures, the magnetization shows a linear field dependence and the temperature-dependent susceptibility follows the Curie law (see Fig. 2.3a):

$$\chi = \frac{n \mu_0 \mu_{\mathrm{eff}}^2}{3 k_{\mathrm{B}}} \frac{1}{T} \tag{2.13}$$

with the effective magnetic moment:

$$\mu_{\text{eff}} = g_J \mu_{\text{B}} \sqrt{J(J+1)}. \tag{2.14}$$

**Ferromagnetism**

Due to exchange interactions, a ferromagnet exhibits below the Curie temperature $T_{\text{C}}$ - even in the absence of any external field - a spontaneous magnetization, as all magnetic moments align along one direction. The corresponding Hamiltonian (including an applied magnetic field) can be written as:

$$\mathcal{H} = -2 \sum_{i>j} J_{ij} \mathbf{S}_i \mathbf{S}_j + g\mu_{\text{B}} \sum_j \mathbf{S}_j \mathbf{B} \tag{2.15}$$

with the first term expressing the Heisenberg exchange energy with $J_{ij} > 0$ (see equation 2.8) and the second term giving the Zeeman energy in an external field ($g$: the electron's $g$-factor). This Hamiltonian can be solved using a mean field approach.

It follows that at low temperatures, the magnetic order is even in the absence of any external field self-sustaining, meaning that the alignment of moments causes an internal (molecular) field, that in turn favours the parallel alignment of the spins. This results in a spontaneous magnetization. At elevated temperatures, thermal fluctuations counteract this process until any order is destroyed at the Curie temperature. The transition itself is a second-order phase transition, as the derivative of the spontaneous magnetization (and thus the second derivative of the system's free energy) shows a discontinuous jump at $T_{\text{C}}$. However, the transition smears out for a finite external magnetic field and thus, no more "true" phase transition takes place.

In magnetization measurements, three characteristic observations are commonly used to identify ferromagnetic order (see Fig. 2.4):

- For temperatures $T > T_{\text{C}}$, the susceptibility follows at small external fields the Curie-Weiss law:
$$\chi \propto \frac{1}{T - T_{\text{C}}}. \tag{2.16}$$
- At $T < T_{\text{C}}$, the field-dependent magnetization resembles that of a paramagnet, however, the saturation fields are much lower.
- Most remarkably, irreversibility effects appear in the temperature- and field-dependent magnetization at temperatures $T < T_{\text{C}}$. One has to distinguish whether the crystal was cooled down through $T_{\text{C}}$ with or without external magnetic field.

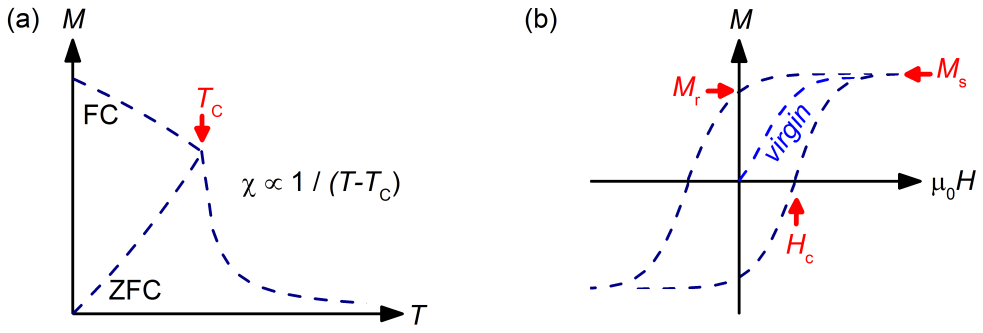


**Figure 2.4:** Typical (a) temperature- and (b) field-dependent magnetization of a ferromagnetic material. (a) For $T > T_C$, the temperature-dependent magnetization follows the Curie-Weiss law $\chi \propto 1/(T - T_C)$. For $T < T_C$, the magnetization increases with increasing temperature if the crystal was cooled down in zero field (ZFC), and decreases if the crystal was cooled down in an external field (FC). (b) The field-dependent magnetization shows at temperatures $T < T_C$ a hysteresis, defined by the virgin curve, saturation magnetization $M_s$, remanent magnetization $M_r$, and coercive field $H_c$.

These irreversibility effects are also known as "magnetic hysteresis". They result, as ferromagnets typically consist of many domains, which are energetically favourable as they reduce the demagnetization fields introduced in section 2.1. Whereas in each domain, the magnetic moments are uniformly aligned, different domains (separated by domain walls) are randomly oriented with respect to each other. Thus, the total net magnetization in the absence of any external field is zero.

An external magnetic field is in principle able to move domain walls. However, they can be pinned due to strains or impurities. Thus, only if the magnetic field overcomes the associated pinning energy, the domain wall can move further. At higher fields, it is also possible that all spins of one domain rotate at once. In any case, one has to consider also the magneto-crystalline anisotropy, meaning that crystals posses crystallographic directions that are preferred ("easy axis") or unpreferred ("hard axis") in a magnetization process. Thus, with increasing field, one single domain will be created where the magnetic moments point along the easy axis closest to the direction of the external field. Only when the magnetic field energy gets high enough, the moments will rotate away from the easy axis to the direction of the external field. As in all those dynamics certain energy thresholds need to be overcome, a magnetic hysteresis results.

The hysteresis in field-dependent magnetization measurements is defined by (see Fig. 2.4b):

- the initial magnetization curve after the crystal was cooled down in zero magnetic field to temperatures $T < T_C$, called "virgin curve"
- the saturation magnetization $M_s$

- the remanent magnetization $M_\mathrm{r}$ which stays after the sample was once fully magnetized and the field was switched off
- the coercive field $H_\mathrm{c}$ which needs to be applied to reduce the magnetization from the remanent value to zero.

For temperature-dependent magnetization measurements (in a small magnetic field), one has to distinguish below $T_\mathrm{C}$ (see Fig. 2.4b):

- zero-field cooled (ZFC) curve: the magnetization increases (from zero) with increasing temperature, as thermal fluctuations allow more and more domains to be oriented along the field
- field-cooled (FC) curve: as the symmetry of the system was broken externally while cooling through $T_\mathrm{C}$, a preferred spin direction was initialized; thermal fluctuations are weakening the order and lead to a decrease of the magnetization with increasing temperature.

**Antiferromagnetism**

For an exchange constant $J_{ij} < 0$, neighbouring spins tend to align antiparallel. This leads below the Néel temperature $T_\mathrm{N}$ to antiferromagnetic order. For a theoretical description following equation 2.15, an antiferromagnet can be considered to consist of two opposite, interpenetrating ferromagnetic sublattices.

Antiferromagnetic behaviour can be usually identified by (see Fig. 2.5):

- For temperatures $T > T_\mathrm{N}$, the susceptibility follows at small external fields the Curie-Weiss law
$$\chi \propto \frac{1}{T + T_\mathrm{N}}. \tag{2.17}$$
- At $T < T_\mathrm{N}$ and relatively small fields, the temperature-dependent magnetization is strongly direction-dependent.
- At $T < T_\mathrm{N}$, the field-dependent magnetization along the spin direction shows a step before achieving saturation.
- The temperature- and field-dependent magnetization does not display hysteretic behaviour.

In order to understand the direction-dependence of the magnetization below the Néel temperature, one should first consider the magnetization at small fields applied at 0 K

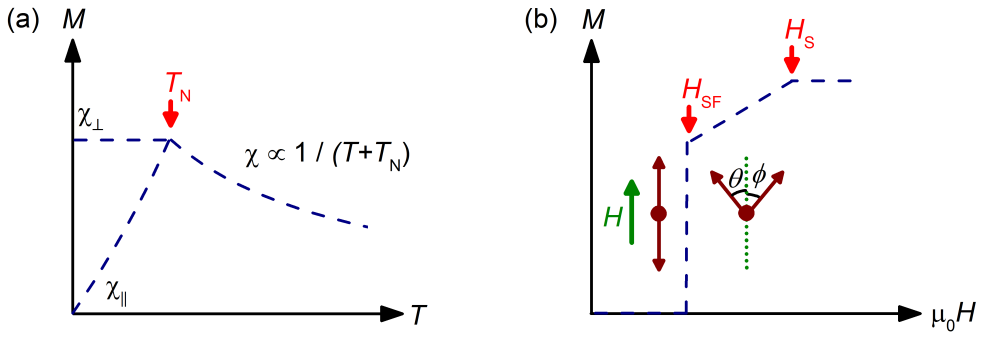


**Figure 2.5:** Typical (a) temperature- and (b) field-dependent magnetization of an antiferromagnetic material. (a) For $T > T_\mathrm{N}$, the temperature-dependent magnetization follows the Curie-Weiss law $\chi \propto 1/(T + T_\mathrm{N})$. For $T < T_\mathrm{N}$, the magnetization increases for the direction parallel to the external field, and stays constant for the perpendicular direction. (b) The field-dependent magnetization along the spin direction rises (at 0 K) abruptly at the spin-flop field $H_\mathrm{SF}$ and increases further until saturation is reached at $H_\mathrm{S}$. For finite temperatures below $T_\mathrm{N}$, this curve smears out due to thermal fluctuations. Brown arrows display schematically the field-dependent spin alignment.

parallel ($M_\parallel$) and perpendicular ($M_\perp$) to the spin direction (see Fig. 2.5a): while for the former case, small magnetic fields will not affect the antiparallel aligned spins and therefore the net magnetization is zero, in the latter case, the spins will be tilted slightly out of the balance position, leading to non-zero magnetization. With increasing temperature, the thermal fluctuations counteract the exchange interactions. This does not notably influence the effect perpendicular to the spin direction. Therefore, $M_\perp$ is almost flat for temperatures $T < T_\mathrm{N}$. However, for the field parallel to the spin direction, the field can act on the thermally excited spins and thus $M_\parallel$ increases with increasing temperature up to $T_\mathrm{N}$.

In the case of high magnetic fields [37], it is clear that at one point the external field must dominate over the internal exchange interaction, leading to a parallel alignment of spins along the field direction. If the field acts perpendicular to the spin direction, this will be a smooth process. However, the situation gets more complicated if the external field is aligned parallel to the spin direction (see Fig. 2.5b). In this case, Zeeman energy, exchange energy and magneto-crystalline anisotropy compete with each other, leading (at $T = 0\,\mathrm{K}$) to the total energy:

$$E = -MB(\cos\theta + \cos\phi) + JM^2\cos(\theta + \phi) - \frac{1}{2}\Delta(\cos^2\theta + cos^2\phi) \tag{2.18}$$

with the exchange coupling constant $J$ and the magneto-crystalline anisotropy $\Delta$. Thus, the ground state energy of the antiferromagnetic configuration is independent of the external field:

$$E_0 = -JM^2 - \Delta. \tag{2.19}$$

For higher fields, a "spin-flop" transition takes place: the spins rotate abruptly to a configuration where the angle between spins and external field is $< 90°$ and the same (counted clockwise and counter-clockwise) for both sublattices (see Fig. 2.5b). The energy of the spin-flop phase is therefore:

$$E = -2MB\cos\theta + JM^2\cos 2\theta - \Delta\cos^2\theta. \tag{2.20}$$

Minimizing this energy with respect to $\theta$ and re-inserting the result in equation 2.20, yields the minimum energy of the spin-flop phase:

$$E_{0,\mathrm{SF}} = -JM^2 - \frac{M^2B^2}{2JM^2 - \Delta}. \tag{2.21}$$

Comparing equations 2.19 and 2.21, the spin-flop takes place at:

$$B_{\mathrm{SF}} = \sqrt{2J\Delta - (\Delta/M)^2}. \tag{2.22}$$

The corresponding field-dependent magnetization is depicted in Fig. 2.5b. The magnetization rises abruptly at the spin-flop field and increases afterwards steadily, as the spins align gradually along the external field, until they are fully aligned.

One should also note that if the magneto-crystalline anisotropy is very strong, the spins can directly rotate from the antiparallel to the parallel alignment (with respect to the external field). This process is called "spin-flip".

### Helimagnetism

There exists a wide variety of other magnetic phases despite anti- und ferromagnetism, often related to one of them or even both. One possible ground state of particular interest for layered materials (such as several rare earth systems) is helimagnetism. In this case, the spins are ordered ferromagnetically within one layer, however the magnetic moments of neighbouring layers differ by a finite angle that is neither equal to zero (which would correspond to ferromagnetism) nor equal to $\pi$ (which would correspond to antiferromagnetic interlayer coupling). Thus, the spins will rotate along a spiral, which is not necessarily commensurate with the lattice.

### Spin glass

In materials where frustration and disorder play an important role, magnetic long-range order is prohibited [38]. In particular the RKKY-interaction, which oscillates between antiferromagnetic and ferromagnetic coupling, often leads to competing interactions. In these materials, one can distinguish in principle four temperature ranges: at very high temperatures, the spins are independent due to strong thermal fluctuations. When lowering the temperature, first local and then also long-range interactions will occur: the system starts seeking its ground state. However, due to the competing interactions, it gets stuck at the so-called "freezing temperature" $T_\mathrm{f}$ in a metastable state. As this "spin glass" phase is only metastable, hysteretic and time-dependent behaviour can be observed.

There exist several types of spin glasses. Systems with dominant short range interactions are sometimes called "mictomagnetic" or "cluster glass", as the short range interactions lead to magnetic clusters that freeze in at $T_\mathrm{f}$. It is also possible that a magnetically ordered state transforms at lower temperatures to a spin glass - although this is counterintuitive as one would expect a more ordered state at lower temperatures. The low-temperature phase resembles then a cluster glass, however, in order to make clear that this phase originates from another state than paramagnetism, it is referred to as "re-entrant spin glass". One theoretical explanation for this behaviour is that only the transverse spin components freeze at the glass transition [39].

# 3

# SUPERCONDUCTIVITY

In the beginning of the $20^{\text{th}}$ century, cryogenics was still in its early infancy. It was not before 1908 that H. K. Onnes managed to liquify $^4$He, pushing the experimentally accessible temperature range down to a few Kelvin. This opened a completely new world in condensed matter research. Only three years later, he observed during his studies on Hg at a critical temperature $T_c \sim 4.2\,\text{K}$ an abrupt resistivity drop to zero - superconductivity, until then an unknown state of matter, was discovered.

More than twenty years later, W. Meissner and R. Ochsenfeld found out that a superconductor is not just an ideal conductor: it is also a perfect diamagnet, meaning that magnetic fields can not penetrate into its bulk. Dubbed after its discoverers, this second characteristic of a superconductor is known today as "Meissner Ochsenfeld effect".

Although great progress was achieved in experiments and more and more superconducting compounds were found, a microscopic theoretical description was only developed in 1957 by J. Bardeen, L. N. Cooper and J. R. Schrieffer.

In the following chapter, a brief introduction in their "BCS theory" will pave the way to distinguish between conventional and unconventional superconductivity. Particular focus will be put on the discussion of high-temperature superconductors. Although magnetism and superconductivity are usually antagonistic phenomena, magnetic fluctuations might be the key to understand their extraordinary properties. This motivates some further insights into the interplay of magnetism and superconductivity. If not given explicitly, explanations follow Ref. [2] and [40] or references given at the beginning of a section.

## 3.1 BCS theory

Early theoretical descriptions of superconductivity were based on macroscopic, phenomenological models. The success of those approaches can be still seen today, as hereby defined characteristic quantities of the superconducting state such as the London penetration depth and the Ginzburg-Landau coherence length are still widely used[1].

In 1950, the observation of the so-called "isotope effect" introduced a relationship between the onset of superconductivity and the atomic mass of a superconducting compound [41, 42], indicating that superconductivity arises from interactions between electrons and lattice vibrations. A theoretical description of those interactions [16, 17] paved the way for the microscopic BCS theory [15].

The fundamental idea behind BCS theory is that electrons of opposite spin and momentum form pairs (so-called "Cooper pairs"), assuming an attractive potential due to weak electron-phonon-coupling that exceeds the repulsive Coulomb interactions. Those Cooper pairs condense in a coherent ground state, leading to a gap in the density of states. This energy gap is the order parameter of the superconducting state; its squared absolute value proportional to the Cooper pair density.

Originally, the effective attractive potential between electrons was assumed to be independent of momentum, leading to an isotropic $s$-wave gap:

$$2\Delta_0(T=0) = 3.5 k_\mathrm{B} T_\mathrm{c} \tag{3.1}$$

with a temperature-dependence that can be well approximated by:

$$\frac{\Delta(T)}{\Delta(0)} = \tanh\left[\frac{T_\mathrm{c}}{T}\frac{\Delta(T)}{\Delta(0)}\right]. \tag{3.2}$$

The experimental verification of this energy gap, demonstrated by optical spectroscopy [43], was one of the big successes of BCS theory.

## 3.2 Unconventional high-temperature superconductivity

Although BCS theory describes successfully a huge variety of superconductors, there exist also some materials where it fails. Even in some elemental superconductors such as Pb and

1 The London penetration depth gives the distance where an (electro-) magnetic field inside a superconductor is screened to $1/e$ of its initial value; the Ginzburg-Landau coherence length describes the length scale over which the superconducting order parameter varies due to a local distortion, such as a vortex.

Hg, the observed behaviour slightly differs from BCS predictions. It turns out that the latter compounds are still "conventional superconductors" with a strong electron-phonon coupling and Eliashberg theory can achieve a proper description [44]. However, if the coupling between electrons is not mediated via phonons, total spin or orbital momentum are non-zero, superconductivity is inhomogeneous or magnetic interactions are observed, the term "unconventional superconductivity" is used. Famous examples are heavy fermion superconductors, ruthenates, cuprates, organic and iron-based superconductors [1].

One subclass of unconventional superconductors are high-temperature superconductors, which have in common that (as their name already suggests) their critical temperature exceeds any limit accessible by electron-phonon interactions [18, 45]. Up to now, only two classes of high-temperature superconductors are known: the cuprates and the iron-based superconductors, whose high critical temperatures were discovered in 1986 by G. Bednorz and K. A. Müller [20] and in 2008 by the group of H. Hosono [4], respectively.

### 3.2.1 Cuprates

Cuprates are layered materials, where superconducting $CuO_2$ planes alternate along the crystallographic $c$-axis with spacer layers, resembling in total perovskite materials. Probably the most studied compounds are doped $YBa_2Cu_3O_7$ ("YBCO", [46]) and $Bi_2Sr_2CaCu_2O_8$ ("BSCCO", [47]) which show maximum critical temperatures around $\sim 90\,\mathrm{K}$. At present, the highest observed $T_c$ is 164 K for $HgBa_2Ca_2Cu_3O_8$ under pressure [19].

In the following, the generic phase diagram of cuprates is described (see Fig. 3.1), giving a basis to elaborate similarities and differences to iron pnictides. Tuning through the phase diagram results from electron or hole doping[1]; the spacer layers serve as charge reservoir.

#### Antiferromagnetic Mott insulator

The parent phase of cuprates is an antiferromagnetic Mott insulator that can be well described by the Hubbard model: although the conduction band is half filled and thus metallic behaviour would be expected, correlations (*i.e.* the Coulomb repulsion) between electrons are strong enough to localize the electrons. With electron or hole doping, the Mott phase gets suppressed.

#### $d$-wave superconductivity

While the Cooper pairs are conventional singlets, the superconducting order parameter has unconventional $d_{x^2-y^2}$-wave symmetry. This means that the gap changes sign along

1 The phase diagrams for electron and hole doping are slightly asymmetric: for electron doping, the Mott phase is usually more robust and the superconducting dome narrower.

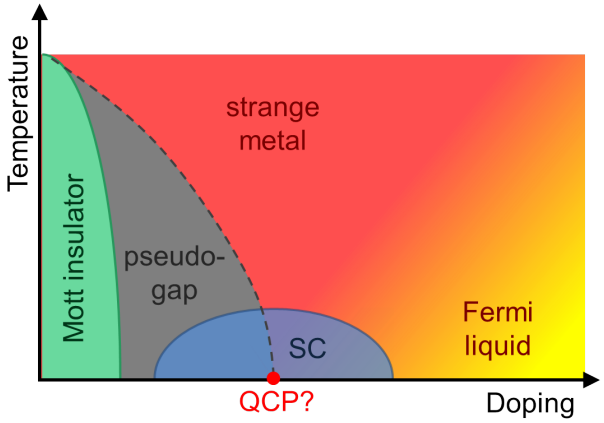


**Figure 3.1:** Generic phase diagram of cuprates. The parent compounds are antiferromagnetic Mott insulators (green). With doping, the magnetic long range order is suppressed and a pseudogap phase (grey) appears, separating the Mott phase and the superconducting dome (SC: blue). Above the superconducting dome, strange metal behaviour (red) is observed, with a crossover to a Fermi liquid (yellow) in the overdoped range. This might indicate a quantum critical point (QCP: red) buried by the superconducting dome.

the Fermi surface, leading to nodes in the order parameter at the diagonals of the Brillouin zone, where the superconducting gap vanishes (see Fig. 3.2a,b). The maximum gap value does not follow the BCS relation given in equation 3.1 and is typically much higher.

There is now broad consensus that the main pairing interactions take place between carriers within the $CuO_2$ layers. As the coherence length is rather small, a three-dimensional superconducting state appears due to Cooper pair tunneling along the $c$-axis. Thus, cuprates display natural Josephson junctions.

### Unconventional normal state properties

One of the main problems about a theoretical description of superconductivity in cuprates is that the normal state from which superconductivity arises is still not understood: when passing at high temperatures through the phase diagram, the Mott insulator gets replaced by a "pseudogap" phase, which is followed by "strange metal" behaviour; conventional Fermi liquid[1] behaviour sets in only in the overdoped region.

In the pseudogap phase, a momentum-dependent gap appears [48]. While its absolute value does not vary strongly with temperature, the gap opens for different momenta at

1 Landau's Fermi liquid theory describes a system of interacting fermions by introducing long living excitations. Those quasiparticles possess renormalized dynamical properties (such as an effective mass), but can be described like a free electron gas. This results at sufficiently low temperature in a $T^2$- and $\omega^2$-dependence of the scattering rate.

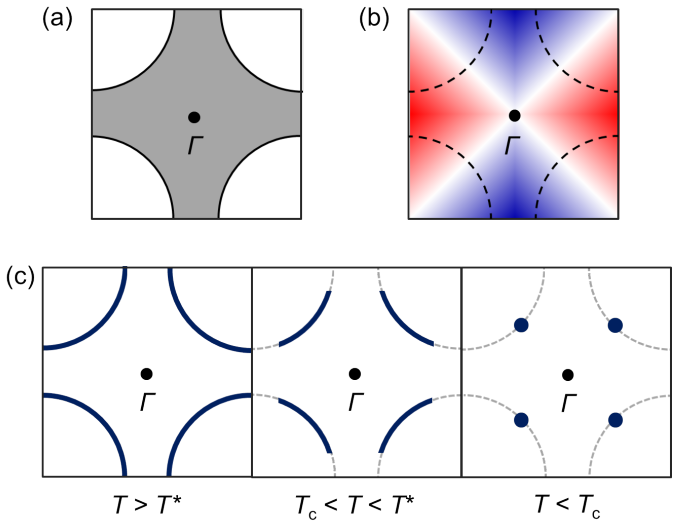


**Figure 3.2:** (a) Schematic Fermi surface of the cuprates. The grey shaded area marks the occupied electron states. (b) Fermi surface superimposed with the $d_{x^2-y^2}$-wave symmetry of the superconducting order parameter. Red and blue correspond to different signs of the order parameter, which has nodes (white) along the diagonals of the Fermi surface. (c) Development of the Fermi surface: the normal state Fermi surface ($T > T^*$) is first reduced to Fermi arcs in the pseudogap phase ($T_c < T < T^*$), which develop until superconductivity sets in ($T < T_c$) to nodes.

different temperatures. This leads to a reduction of the Fermi surface to arcs[1], which shrink further with decreasing temperature (see Fig. 3.2c). When superconductivity sets in, almost the entire Fermi surface is already gapped: only the region at the nodes is still occupied. Those nodes remain in the superconducting phase, consistent with the $d_{x^2-y^2}$-wave symmetry of the superconducting order parameter. Due to those (and many more) similarities of the two gaps, the idea was developed whether the pseudogap phase is a precursor of superconductivity, where non-coherent Cooper pairs form.

In contrast, recent results point more towards another explanation: the pseudogap seems to be a separate phase. Indeed, ARPES and high-resolution STM measurements found a small feature which they identified as a superconducting gap, with a smaller absolute value than the pseudogap [52–54]. However, there is not yet consensus about the nature of the pseudogap. To complicate this issue further, there are more and more additional phases found by careful studies on cuprates such as (fluctuating) charge density waves [55–58] and nematicity [59, 60]. Whether all those orders are competing with superconductivity,

1 Recent quantum oscillation measurements indicate that those arcs could be indeed small electron pockets; charge order wave vectors that reconnect the remaining arcs might play a crucial role [49–51].

a necessary key ingredient, or just appear due to an unknown "mother phase" needs to be seen [21].

Another mystery in cuprates is the strange metal behaviour right above the superconducting dome. In this regime, the Mott-Ioffe-Regel limit is violated, meaning that the mean free path of carriers is less than the interatomic distance [62, 63]. Thus, coherent transport should not be possible and incoherent dynamics set in, as will be further discussed on the basis of optical measurements in chapter 4. Furthermore, the resistivity displays over a wide temperature range linear behaviour, which might stem from spin fluctuations or a quantum critical point[1] [64].

### 3.2.2 Iron-based superconductors

Similar to cuprates, iron-based superconductors are layered materials [3, 5, 65]. Their common ingredient are layers where $Fe^{2+}$ is tetrahedrally surrounded by pnictogen or chalcogen atoms. Thus, one differs between iron pnictides and iron chalcogenides. Further classification results from the stoichiometric composition of the parent compounds.

According to this classification scheme, $LaFeAsO_{1-x}F_x$ (which originally caused the "iron age of superconductivity" [69]) belongs to the "1111"-family. Replacing La by other rare earth elements increases $T_c$ up to 56 K in bulk materials; recent work on FeSe ("11"-chalcogenide) monolayers indicated even higher accessible critical temperatures [67]. However, most research was done up to now on "122" iron pnictides due to the availability of high quality single crystals, focusing on materials with $BaFe_2As_2$ as parent compound (see Fig. 3.3a). Eu based iron pnictides also belong to this family; more detailed discussions concerning their magnetic and electronic properties can be found in chapter 6. Here, the focus is on the generic phase diagram of 122 iron pnictides (see Fig. 3.3b); tuning through the phase diagram can be reached by electron or hole doping[2], mechanical pressure, as well as isovalent substitution.

#### Antiferromagnetism

Iron pnictides are multiband systems, where up to five Fe 3*d*-bands cross the Fermi energy. This leads to a Fermi surface that consists usually of multiple quasi-two-dimensional hole and electron pockets centered around the (0,0)-"$\Gamma$"- and ($\pi$,0)/(0,$\pi$)-"$X$"-points of the

1 A quantum critical point is a second order phase transition that takes place at absolute zero temperature. It leads to a divergence of several physical quantities.

2 In literature there is an ongoing debate, whether superconductivity is induced in iron pnictides and chalcogenides due to doping or disorder [68]. However, this should not be in the focus of this thesis and for simplicity, the expression "doping" is used.

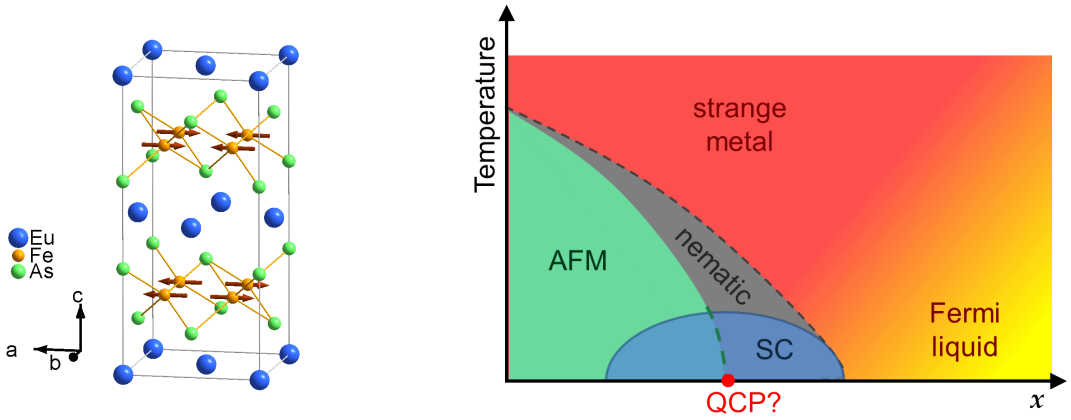


**Figure 3.3:** Crystal structure (adapted from Ref. [8]) and generic phase diagram of 122 iron pnictides. (a) Conducting Fe (beige) - pnictogen (green) planes are separated by spacer layers, consisting of another element such as Eu, Ba, Sr or Ca (blue). In the antiferromagnetic phase, the itinerant electrons of Fe order in a stripe-like configuration (brown arrows). (b) The antiferromagnetic (AFM) phase (green) is found in the parent compounds. At slightly higher temperatures, a nematic phase transition (grey) takes place, accompanied by a tetragonal-to-orthorhombic structural transition. With doping, mechanical pressure or isovalent substitution ("$x$"), those orders are suppressed and superconductivity sets in (SC: blue). Above the superconducting dome, strange metal behaviour (red) is observed, with a crossover to a Fermi liquid (yellow) in the overdoped range. This might indicate a quantum critical point (QCP: red) buried by the superconducting dome.

unfolded[1] Brillouin zone (see Fig. 3.4a). In general, the electronic system is more three-dimensional than in the case of cuprates, visible in Fermi sheets that slightly warp along the $k_z$-direction and a less pronounced electronic anisotropy.

The ground state of the parent phase is an antiferromagnetic metal with a magnetic moment per Fe atom of typically $< 1\,\mu_B$. This value is much smaller than the possible $6\,\mu_B$ for $Fe^{2+}$. Indeed, it was found that the antiferromagnetic ordering vector is usually $(\pi,0)$ or $(0,\pi)$, matching the nesting vector between electron and hole pockets (see Fig. 3.4a); the corresponding stripe-like spin order which is ferromagnetic in one direction and antiferromagnetic in the others is depicted in Fig 3.3a. This points (at least for the 122 iron pnictides) towards a rather itinerant magnetism with a spin density wave ground state. However, one should note that in some compounds, there are also indications for a more local character of magnetism; one example are 11 chalcogenides, where the magnetic order vector differs from the nesting vector. Therefore, magnetism in iron-based super-

1 The folded Brillouin zone is that of the actual lattice, considering Fe and pnictogen atoms; the unfolded Brillouin zone arises when only the Fe atoms are considered. While the $\Gamma$-point is the same in both, the $X$-point in the unfolded scheme corresponds to the $M$-point in the folded one.

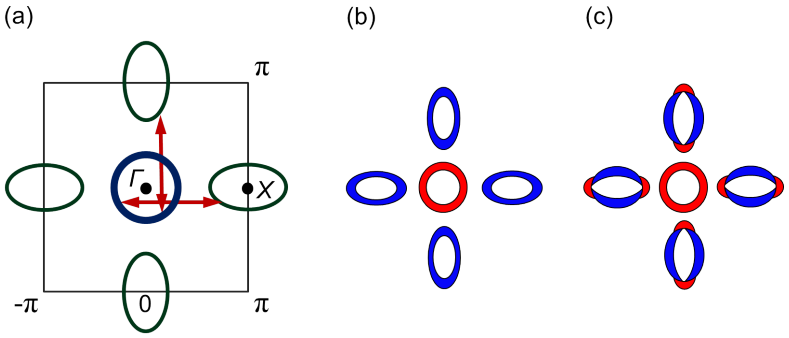


**Figure 3.4:** Schematic Fermi surface as well as superconducting gap symmetry and structure of iron pnictides (adapted from Ref. [65, 71]). (a) The Fermi surface usually consists of multiple hole (dark blue) and electron pockets (dark green) centered around the (0,0)-"$\Gamma$"- and $(\pi,0)/(0,\pi)$-"$X$"-points of the unfolded Brillouin zone. Those pockets are nested by the antiferromagnetic ordering vectors (dark red). (b) A superconducting order parameter with $s_{\pm}$-symmetry is isotropic and changes sign between electron and hole pockets. (c) For the extended $s_{\pm}$-symmetry, the order parameter might contain accidental nodes which can be lifted by scattering [72].

conductors has probably a dual character with signatures of both, local and itinerant magnetism.

### Superconductivity

While it is consensus that the Cooper pairs are singlets, the symmetry of the superconducting order parameter of iron pnictides is still under debate. Mostly favoured is the so-called "$s_{\pm}$-symmetry", where $s$-wave gaps at the different Fermi surface sheets have opposite sign (see Fig. 3.4b, [70, 71]). In the "extended $s_{\pm}$-wave" scenario, those gaps may have accidental nodes (see Fig. 3.4c) which are not given by symmetry and can be therefore lifted by scattering [72]. This possibly explains the variety of contradictory measurements concerning nodes in the order parameter, as their occurrence would be strongly affected by scattering and thus the sample quality. Any analysis about gap sizes and symmetries are further hampered by the multiband character of the iron pnictides, which causes the opening of several superconducting gaps. Further details on this topic and a possible smoking gun experiment to prove the $s_{\pm}$-symmetry with the help of optical spectroscopy are given in the attachment.

Despite the gap symmetry, another interesting difference between cuprates and iron-based superconductors concerns the separation of superconductivity and long-range magnetic order in the phase diagram. In iron pnictides, the maximum $T_c$ appears usually close to the (extrapolated) end point of the antiferromagnetic phase transition. In some compounds, even a coexistence region of spin density wave and superconducting order emerges

(in contrast to cuprates, where the Mott insulating phase and the superconducting dome are separated by the pseudogap phase). The observation of competing order parameters suggests that this coexistence appears on the microscopic scale [73, 74].

### Unconventional normal state properties

Although the pseudogap phase governs the phase diagram of cuprates, it is either absent or at least much less pronounced in the case of iron pnictides (see chapter 4.4.5). Nevertheless, the normal state above the superconducting dome is anything but conventional. There is growing experimental and theoretical evidence for a "nematic phase" transition that precedes or accompanies the antiferromagnetic ordering [6, 25, 75–80, 240]. The term "nematic" is borrowed from liquid crystal theory and describes the breaking of the $C_4$ rotational symmetry. Interestingly, this does not only mean that a tetragonal-to-orthorhombic phase transition takes place: an electronic in-plane anisotropy sets in, whose magnitude is much larger than the orthorhombic lattice distortion. Furthermore, the $b$-axis resistivity is higher than that along the $a$-direction, although one would expect the opposite[1]. In other words, the itinerant electrons do not just follow the lattice anisotropy. Therefore, the transition is generally believed to be driven electronically either by spin or orbital fluctuations. Unfortunately, no matter which of those interactions is responsible, at the transition one will always observe an anisotropy of all - structural, orbital and spin degrees of freedom - as they are strongly entangled. Thus, it is extremely difficult to decide what is actually driving the nematic order. However, exactly this question is of particular interest: the nematic phase in the iron pnictides phase diagram extends far above the superconducting dome and appears also in cuprates. Therefore, it might be the essential key ingredient for high-temperature superconductivity.

The experimental investigation of nematicity is challenging. In order to probe the fluctuations above the transition, piezo elements can be used that induce some small amount of strain on the sample [25, 81]. Those experiments uncovered a huge nematic susceptibility that diverges at the transition temperature, independent of crystal type or quality [81].

Below the nematic transition, as the orthorhombic distortion is only small, the formation of twin domains usually obscures the intrinsic anisotropy. In cuprates, mechanical clamps and magnetic fields were found to detwin single crystals [22, 23]. In the case of iron pnictides, the effect of typical laboratory magnetic fields on the Fe spins is rather weak: 14 T detwin $BaFe_2As_2$ only by $\sim 10\,\%$ [24]. Thus, mechanical clamps are commonly

1 A stronger orbital overlap along the shorter $b$-axis as well as the ferromagnetic spin alignment should both lead to a higher conductivity with respect to the $a$-axis.

used [6]. However, this introduces an explicit symmetry breaking by uniaxial pressure, which must be considered carefully [25]: similar to ferromagnets, where the magnetization depends on the external magnetic field, the intrinsic nematic response can only be measured in the limit of zero external symmetry-breaking force. Indeed, mechanical clamps were found to significantly enhance the transition temperatures in iron pnictides and even induce additional anisotropy above [78].

In the framework of this thesis, it was uncovered that small magnetic fields are enough to persistently detwin $EuFe_2As_2$. This provides the unique possibility to study the low temperature electronic in-plane anisotropy of iron pnictides without applying any symmetry-breaking external force. The corresponding results are discussed in chapter 9 and Ref. [13].

Despite the nematic phase, another similarity can be found between cuprates and iron pnictides when looking at their normal state behaviour: a strange metal phase extends far above the superconducting dome, accompanied by linear resistivity. In $BaFe_2(As_{1-x}P_x)_2$ - which is usually considered as a very clean material as P substitution does not induce appreciable scattering - a diverging effective mass around the optimum substitution level was verified [83, 84]. Therefore, similar to cuprates the existence of a quantum critical point and its relation to unconventional superconductivity is discussed.

### 3.2.3 Magnetic fluctuations

Due to the proximity of high-temperature superconductivity to a magnetic phase in both, cuprates and iron-based superconductors, it is intriguing to consider magnetic spin fluctuations as a possible pairing glue for Cooper pairs. However, those interactions lead to a repulsive pairing potential, opposite to the basic assumptions of BCS theory (see section 3.1). Further insight how such a potential can still support superconductivity can be found when looking at the BCS self-consistency gap equation for singlet pairing [85]:

$$\Delta(\mathbf{k}) = -\sum_{\mathbf{k}'} \frac{V^{\text{eff}}(\mathbf{k}-\mathbf{k}')}{2\sqrt{\Delta^2(\mathbf{k})+\epsilon^2(\mathbf{k})}}\Delta(\mathbf{k}') \tag{3.3}$$

with the momenta $\mathbf{k}$ and $\mathbf{k}'$, the energy gap $\Delta$, the effective two-particle pairing interaction $V^{\text{eff}}$, as well as the dispersion of the electrons in the normal state $\epsilon(\mathbf{k})$. Obviously, an attractive pairing potential $V^{\text{eff}} < 0$ (as assumed by Bardeen, Cooper and Schrieffer) might support superconductivity, as left and right sides of equation 3.3 can obtain the same sign. For $V^{\text{eff}} > 0$, equation 3.3 can be only fulfilled for a strong momentum-dependent potential that leads to gaps with opposite sign for the momenta $\mathbf{k}$ and $\mathbf{k}'$. The simplest solution for this problem is a $d$-wave gap, as indeed observed in cuprates. However, also the $s_{\pm}$-symmetry favoured in iron-based superconductors fulfils those conditions.

In order to get experimental information about the importance of spin fluctuations, inelastic neutron scattering has turned out to be a very powerful tool. It was found that a resonance peak in the superconducting spin excitation spectrum is a unique feature of unconventional superconductors [5, 65, 88]. This magnetic resonance appears at the same wave vector as the static magnetism in the parent compounds: at temperatures $T < T_c$, the antiferromagnetic neutron scattering signal gets depleted at lowest energies and a peak appears at energies smaller than $2\Delta$. Theory predicts such a peak if the superconducting energy gap takes opposite values on different parts of the Fermi surface. Thus, it indicates unusual repulsive electron pairing. In iron pnictides, such a resonance was demonstrated for the first time for $Ba_{0.6}K_{0.4}Fe_2As_2$ [89].

One can further compare the spectrum of spin excitations with the Eliashberg spectral function $\alpha^2F(\omega)$, where $\alpha$ denotes the electron-boson coupling strength and $F(\omega)$ the frequency-dependent bosonic density of states [86, 87]. While the former can be measured with inelastic neutron scattering, the latter can be extracted from tunneling or infrared spectroscopy data. If spin fluctuations are responsible for Cooper pair formation, $\alpha^2F(\omega)$ should be proportional to the imaginary part of the spin susceptibility. Indeed, both - iron pnictides and cuprates superconductors - show that the resonance mode coincides with features in $\alpha^2F(\omega)$ [5], further supporting the idea of magnetic fluctuations as pairing glue.

## 3.3 Superconductivity and Magnetism

As the electrons forming a Cooper pair contain within the BCS theory opposite spin and momentum, it is very clear that magnetism and superconductivity are conventionally antagonistic phenomena. Their interplay is in the focus of the following sections.

### 3.3.1 Type I and II superconductors

A “type I” superconductor is a perfect diamagnet, meaning that an external magnetic field gets shielded completely by supercurrents in a thin surface layer. Importantly, this holds no matter whether the magnetic field is switched on below or above $T_c$, if the field does not exceed a critical value $B_{c2}$ where superconductivity breaks down.

However, the detailed shielding mechanism depends on the cooling procedure. In the case of zero-field cooling, shielding currents are induced that counteract the application of the magnetic field; those currents do not decay, because the resistance is zero. As this is nothing else than Lenz’s law, the same behaviour would also occur in an ideal conductor.

The difference between a superconductor and an ideal conductor lies in the field-cooled behaviour: at temperatures $T > T_c$, magnetic flux can penetrate inside both specimen; for

$T < T_c$, however, this flux is expelled only in the case of a superconductor. This additional effect that can not be explained by Lenz's law was discovered by Meissner and Ochsenfeld. Therefore, the corresponding phase is called the "Meissner phase".

High-temperature superconductors belong to another class of superconductors, the "type II" superconductors, where an intermediate "Shubnikov phase" appears: above the critical field $B_{c1}$, the external field can penetrate inside the material within "Abrikosov vortices". The Cooper pair density is zero at the core of such a vortex; it increases away from the core within the Ginzburg-Landau coherence length. Correspondingly, the magnetic field has a maximum at the core of the vortex; it decreases away from the core within the London penetration depth. The ground state of the system is a triangular vortex lattice, where each vortex contains a single flux quantum; higher magnetic fields lead to a higher density of vortices, until superconductivity breaks down at $B_{c2}$.

### 3.3.2 Magnetization of a superconductor

Magnetization measurements are often used to characterize a superconductor, as a diamagnetic signal indicates bulk superconductivity. However, the interpretation of those magnetization measurements can be very complex, as will be shown below.

#### Temperature-dependent magnetization

The first case that should be discussed are temperature-dependent magnetization measurements [90, 91]. In the strictest sense, only a susceptibility of -1 that was gained in a field-cooled measurement proves 100% bulk superconductivity. This can be understood intuitively when considering a type I superconducting cylinder which has an axial hole, where a magnetic field is applied parallel to the cylinder axis. For zero-field cooling, surface currents will shield everything "inside", also the hole - the whole specimen acts as a perfect diamagnet. For field-cooling, however, the result is different: the magnetix flux that could penetrate inside the specimen in the normal conducting phase needs to be expelled. This takes place only in the superconducting volume; the flux in the hole remains. Therefore, only the superconducting volume acts as a perfect diamagnet. In summary, the field-cooled susceptibility will be less negative than the zero-field cooled curve; only the field-cooled response will give the true superconducting volume fraction.

Unfortunately, a less negative field-cooled signal does not mean necessarily a bad sample quality or a smaller superconducting volume fraction. For instance, granular superconductors have intergranular spaces that can trap flux. Another example are type II superconductors, where vortex dynamics can lead to very complex hysteretic behaviour, which will be discussed in more detail in the next section.

### Field-dependent magnetization

Real type II superconductors contain imperfections. Indeed, the system can win energy when the vortices run through normal-conducting defects, as this effectively reduces the vortex length. Thus, the vortices are "pinned" to those defects. If this pinning is strong, the superconductor is characterized as "hard", leading to interesting hysteresis effects due to flux trapping.

The magnetization curves of such hard superconductors can be well described by Bean's critical state model [92]. While at $B < B_{c1}$, the penetration of the magnetic field is given by the London penetration depth, at $B > B_{c1}$, vortices will start penetrating into the material. Bean assumed that those vortices get pinned when entering through the surface, leading below the surface to a broadened shielding volume with a homogeneous critical current density $j_c$. For external fields much smaller than the upper critical field, $j_c$ is assumed as constant.

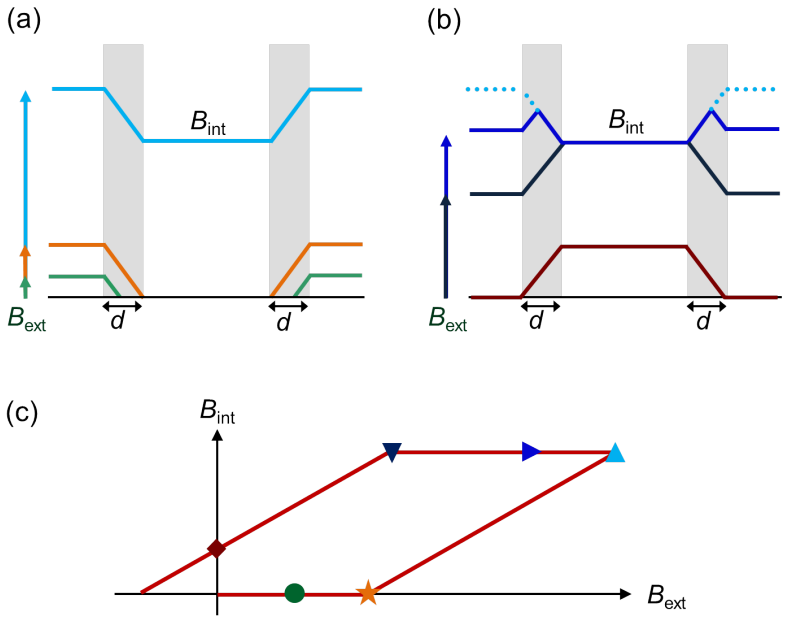


**Figure 3.5:** Development of an internal magnetic field $B_{int}$ inside a hollow superconducting cylinder (wall thickness $d$) when an external magnetic field $B_{ext}$ is applied ($B_{ext} > B_{c1}$), following Bean's critical state model. The field distribution is schematically depicted in (a) for increasing $B_{ext}$ and in (b) for decreasing $B_{ext}$. (c) $B_{int}$ dependent on $B_{ext}$; fields displayed in (a) and (b) are marked by symbols with the same colour. A distinct hysteresis results, as vortices get directly pinned when entering the superconductor: with increasing field, the cylinder gets gradually "filled" with vortices from the outside to the inside; with decreasing field, opposite supercurrents cancel the vortices - again from the outside to the inside. Thus, vortices are trapped inside the walls for a certain range of $B_{ext}$.

In order to understand the implications of those assumptions, a hollow superconducting cylinder with thin walls of thickness $d$ and neglectable small $B_{c1}$ can be considered, where a magnetic field $B_{ext}$ is applied along the cylinder axis (see Fig. 3.5a). For small fields, $B_{ext}$ gets completely shielded within the cylinder walls and the magnetic field at the center of the cylinder $B_{int}$ stays zero (see Fig. 3.5c). With increasing $B_{ext}$, the volume where vortices penetrate the superconductor increases until the cylinder walls are completely filled. From this point, an increasing external field also leads to an increase of $B_{int}$. The hysteretic effects get obvious when the external field is decreased (see Fig. 3.5c): due to the decrease, an opposed critical current is induced at the surface, meaning that the density of vortices decreases where this current flows. When decreasing $B_{ext}$ further, $B_{int}$ does not change until a homogeneous state is reached in the whole cylinder. At zero external field, a finite internal field is trapped inside the hollow cylinder.

Indeed, the processes in a bulk sample are very similar [93], leading to characteristic strongly hysteretic magnetization curves that appear also in iron pnictides [94]. Considering that $j_c$ should decrease when approaching the upper critical field, magnetization curves of hard superconductors can be well described by Bean's critical state model [95].

### 3.3.3 Upper critical field(s)

As already mentioned, superconductivity gets destroyed at the upper critical field $B_{c2}$. In principle, there are two processes responsible for breaking up the Cooper pairs: spin and orbital pair-breaking [96]. The first case only happens in spin singulett superconductors, where the Cooper pairs consist of electrons with opposite spin: As the magnetic field induces an energy splitting between those (Zeeman effect), superconductivity gets destroyed in the so-called "Pauli" or "Chandrasekhar-Clogston limit" [97, 98] as soon as this difference exceeds the condensation energy of the Cooper pairs. In the case of orbital or diamagnetic pair-breaking, the Cooper pairs are literally torn apart, as they possess opposite momentum and thus the Lorentz force in a magnetic field will act in opposite directions. While the upper critical field of most of the conventional superconductors is determined by the orbital pair-breaking (described by the Werthamer-Helfand-Hohenberg theory [99]), the Pauli limit plays a more important role in unconventional superconductors.

### 3.3.4 Exotic phases

Intuitively, one would not expect superconductivity in magnetic materials, as the magnetic exchange field between spins creates usually very high internal fields. Nonetheless, in some cases superconductivity is still energetically favourable, leading to exotic behaviour.

Here, some of the effects that were discussed for Eu based 122 iron pnictides are shortly introduced.

The first phenomenon that is observed in many of the Eu based iron pnictides is the "re-entrant superconductivity": for temperatures $T < T_c$, superconductivity is first destroyed ($T_{n,re}$) and then re-enters at lower temperatures ($T_{c,re}$). This behaviour results from temperature-dependent magnetic interactions and was initially predicted in 1971 for materials that exhibit the Kondo effect [100]; in this case the pair-breaking first increases with decreasing temperature due to the Kondo effect, until it decreases again at the coherence temperature. Such a full cascade of transitions was experimentally verified in 1977 on La-Y-Ce alloys [101] with $T_c = 0.55\,\mathrm{K}$, $T_{n,re} = 0.27\,\mathrm{K}$ and $T_{c,re} = 0.05\,\mathrm{K}$.

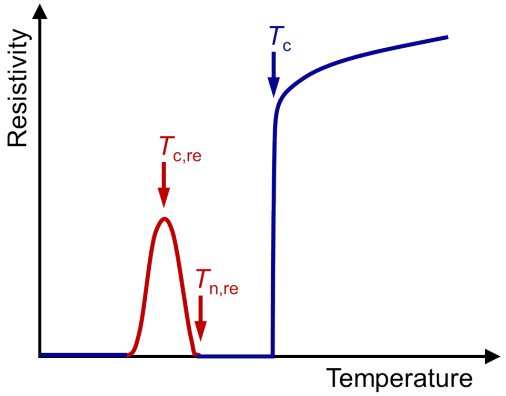


**Figure 3.6:** Typical temperature-dependent resistivity of a re-entrant superconductor. Superconductivity that sets in at $T_c$ gets suppressed at slightly lower temperatures $T_{n,re}$ due to competing magnetism. If the pair-breaking effects get weaker with decreasing temperature, superconductivity can eventually re-enter at $T_{c,re}$.

Nowadays, several rare earth materials are known to show re-entrant superconductivity. One example are borocarbides [102], which have a similar crystal and magnetic structure as $EuFe_2As_2$. In $Ho(Ni_2Co_2)B_2C$, three different magnetic phases exist below $T_c$. In the low temperature phase, spins within one layer are ferromagnetically coupled (with a small out-of-plane component) and neighbouring planes are coupled antiferromagnetically. The higher temperature phases are similar, but show slightly incommensurate spirals. It turns out that the incommensurable magnetism is harmful to superconductivity, in contrast to the commensurable phase. Theoretically, this behaviour is yet not well understood, but leads to the characteristic temperature-dependence of a re-entrant superconductor, where superconductivity is recovered when the commensurable magnetism sets in. The situation is more clear in superconducting cluster glasses such as $(Gd,La)Ru_2$ and $(Nd,Th)Ru_2$ [102], where the short-range ferromagnetic interactions compete with superconductivity, leading to re-entrant superconductivity. In this case, the superconducting state is probably recovered, when larger ferromagnetic clusters become unstable at low temperatures.

While the phenomenon of re-entrant superconductivity directly shows that superconductivity and magnetism compete, the question of how ferromagnetism and superconductivity can coexist microscopically is more challenging to reply and several theoretical predictions have been made.

In 1964, Fulde and Ferrell as well as Larkin and Ovchinnikov considered independently from each other the effect of ferromagnetic moments on conventional singlet superconductors [103–105]. They found a stable phase, where the Cooper pairs contain non-zero momentum, corresponding to the momentum difference of the Fermi surfaces of spin-up and down electrons. This leads to a spatial modulation of the superconducting order parameter, meaning that the Cooper pair density varies periodically in space. Although it was yet not possible to verify this "FFLO-state" in ferromagnetic superconductors, there are strong indications that such a spatially modulated state exists at high fields in unconventional superconductors [106].

Another approach to this topic is that conventional ferromagnetism could be even hampered to occur in a superconducting phase. In this spirit, it was suggested already in 1959, that in the superconducting phase only very small ferromagnetic domains will appear, which cancel each other out on the scale of the superconducting coherence length in a "cryptoferromagnetic" alignment [107].

Furthermore, it was also predicted that in a ferromagnetic superconductor, spontaneous vortices can occur, lowering the system's energy similar to the Shubnikov phase in conventional type II superconductors [108, 109]. At the moment, this effect is favoured to occur in Eu based iron pnictides [31], although a direct experimental proof is still missing.

Finally, one should note that an external magnetic field can in principle also enhance superconductivity if it acts against the internal magnetism. In rare earth materials such as the Chevral-phase compound $Eu_xSn_{1-x}Mo_6S_8$ [111, 112], the appearance of a second superconducting dome at high magnetic fields was observed, while the original superconducting dome was already suppressed at lower fields. This effect was theoretically explained in 1962 [110]: in those superconductors, the exchange field between conduction electrons and local magnetic moments can be positive or negative, *i.e.* parallel or antiparallel to the local moment direction. In the latter case, the exchange field is opposed to an external magnetic field. Thus, for a certain field range, the external and internal magnetic fields almost cancel each other out, significantly reducing the conduction electron polarization. This leads to a re-appearance of superconductivity.

# 4

# ELECTRODYNAMIC PROPERTIES

Optical spectroscopy is a powerful method to gather information about the electrodynamic properties of materials, as it is able to resolve the energy scales of electronic interactions. In this chapter, basic definitions and concepts to describe metals and broken symmetry states are introduced, following Ref. [113] and [114]. Those concepts are then employed to review the electrodynamic properties of 122 iron pnictides [115].

## 4.1 Basic definitions

In analogy to the relation of magnetic flux density and field strength discussed in chapter 2.1, an electric displacement field $\mathbf{D}$ can be defined in free space as:

$$\mathbf{D} = \epsilon_0 \mathbf{E} \tag{4.1}$$

with the permeability of free space $\epsilon_0$ and the electric field $\mathbf{E}$.

In a linear and isotropic dielectric material, an external electric field creates a polarization $\mathbf{P}$ and equation 4.1 needs to be extended:

$$\mathbf{D} = \epsilon_0 \mathbf{E} + \mathbf{P} = \epsilon_0 \epsilon_\mathrm{r} \mathbf{E} \tag{4.2}$$

with the relative dielectric constant (*i.e.* permittivity) $\epsilon_\mathrm{r}$, which can be related to the refractive index $\tilde{n}$ of the medium via:

$$\tilde{n} = \sqrt{\epsilon_\mathrm{r}}. \tag{4.3}$$

In a dispersive medium, $\tilde{n}$ and $\epsilon_\mathrm{r}$ are both complex frequency-dependent quantities:

$$\tilde{n}(\omega) = n(\omega) + ik(\omega) \tag{4.4}$$

$$\epsilon_\mathrm{r}(\omega) = \epsilon_1(\omega) + i\epsilon_2(\omega). \tag{4.5}$$

Despite $\{n(\omega),\ k(\omega)\}$ and $\{\epsilon_1(\omega),\ \epsilon_2(\omega)\}$, there exist also two other pairs of optical constants that are commonly used for describing the electrodynamic properties of solids. The first is the frequency-dependent conductivity:

$$\sigma(\omega)\ = \sigma_1(\omega) + i\sigma_2(\omega) \tag{4.6}$$

that relates to the relative dielectric constant as:

$$\epsilon_r(\omega) = \epsilon_\infty + i\frac{\sigma(\omega)}{\epsilon_0\omega} \tag{4.7}$$

with $\epsilon_\infty$ being the relative permittivity at $\omega \to \infty$.

A common way to excess those optical constants are reflection measurements, where the reflected wave displays a phase shift $\theta(\omega)$ and an amplitude change $r(\omega)$ with respect to the incident wave. In an experiment, the measured quantity is usually the reflectivity:

$$R(\omega) = |r(\omega)|^2 = \frac{(n-1)^2 + k^2}{(n+1)^2 + k^2}. \tag{4.8}$$

Unfortunately, the phase shift

$$\theta = \arctan^{-1}\left[\frac{2k}{n^2 + k^2 - 1}\right] \tag{4.9}$$

is accessible only by some measurement techniques such as ellipsometry or time domain spectroscopy. However, as for all optical constants the causality condition holds, the Kramers-Kronig transformation can be used to calculate the phase shift:

$$\theta(\omega) = -\frac{\omega}{\pi}\mathcal{P}\int_0^\infty \frac{\ln R(x)}{x^2 - \omega^2}\mathrm{d}x \tag{4.10}$$

where $\mathcal{P}$ denotes the Cauchy principle value. As usually the reflectivity is measured only over a limited frequency range, $R(\omega)$ needs to be extrapolated properly to low and high frequencies. Once this is done, one has obtained the last pair of optical constants from which all the others: $\{n(\omega),\, k(\omega)\}$, $\{\epsilon_1(\omega),\, \epsilon_2(\omega)\}$ or $\{\sigma_1(\omega),\, \sigma_2(\omega)\}$ can be calculated. Indeed, Kramers-Kronig transformations connect all real and imaginary parts of optical constants, and can be utilized to derive "sum rules", which are powerful tools in the analysis of spectroscopic measurements.

It should be noted that within this thesis, uniformly the SI system is used. However, in optical spectroscopy often the CGS notation or even a mixture of unit systems can be found. Most importantly, frequency and scattering rate are commonly given in $[\mathrm{cm}^{-1}]$. By using the conversion:

$$[\mathrm{cm}^{-1}]_{\mathrm{CGS}} \quad \xrightarrow{*2\pi c} \quad [1/s]_{\mathrm{SI}} \tag{4.11}$$

the corresponding SI unit $[1/s]$ can be obtained.

## 4.2 Metals

The electrodynamic properties of metals can be well understood considering the phenomenological Drude and Lorentz model. While the former describes intraband interactions, the latter accounts for interband transitions. In order to model the electrodynamics in a real material, contributions from both models are included. While the reflectivity is not additive, the conductivity is (according to Matthiessen's rule).

### Drude model

In the Drude model, a metal is described as a classical gas of electrons. Such an electron interacts with its environment only in the form of collisions; the average time between subsequent collisions is given by the relaxation time $\tau$ or the scattering rate $\Gamma = 1/\tau$. This leads in the presence of a time-dependent external field $E(t)$ to the equation of motion:

$$m\frac{\mathrm{d}r^2}{\mathrm{d}t^2} + \frac{m}{\tau}\frac{\mathrm{d}r}{\mathrm{d}t} = qE(t) \tag{4.12}$$

with mass $m$ and charge $q$ of the free carriers. By solving this equation, one obtains for the real and imaginary part of the frequency-dependent conductivity:

$$\sigma_1(\omega) = \sigma_{\mathrm{dc}}\,\frac{1}{1+\omega^2\tau^2} = \epsilon_0\omega_{\mathrm{p}}^2\tau\,\frac{1}{1+\omega^2\tau^2} \tag{4.13}$$

$$\sigma_2(\omega) = \sigma_{\mathrm{dc}}\,\frac{\omega\tau}{1+\omega^2\tau^2} = \epsilon_0\omega_{\mathrm{p}}^2\tau\,\frac{\omega\tau}{1+\omega^2\tau^2} \tag{4.14}$$

with the frequency-independent prefactor given either by the dc conductivity

$$\sigma_{\mathrm{dc}} = \frac{Nq^2\tau}{m} \tag{4.15}$$

or the plasma frequency

$$\omega_{\mathrm{p}} = \sqrt{\frac{Nq^2}{\epsilon_0 m}} \tag{4.16}$$

that depend on the density $N$ of the free carriers.

The Sommerfeld extension of the Drude model accounts for the existence of a Fermi surface, leading to a more realistic description with an effective mass $m^*$ in equations 4.12 - 4.15 and a mean free path $l$ given by the Fermi velocity $v_{\mathrm{F}}$:

$$l = v_{\mathrm{F}}\tau. \tag{4.17}$$

In Fig. 4.1a, the reflectivity $R(\omega)$ of a typical Drude response is displayed. For $\omega \ll 1/\tau$, the electrodynamic properties of a metal depend mainly on the dc conductivity and the reflectivity can be well described by the Hagen-Rubens relation:

$$R(\omega) \approx 1 - 2\sqrt{\frac{2\epsilon_0\omega}{\sigma_{\mathrm{dc}}}}, \tag{4.18}$$

as can be seen in the inset of Fig. 4.1a. With increasing frequencies, the reflectivity stays close to unity, until it drops rapidly at $\omega_{\mathrm{p}}$ and the metal gets transparent.

Fig. 4.1b displays the corresponding complex conductivity. $\sigma_1(\omega)$ is almost flat at low frequencies with $\sigma_1 \approx \sigma_{\mathrm{dc}}$ and decreases at higher frequencies rather rapidly to zero, with the inflection point of the curve at the scattering rate. In contrast, $\sigma_2(\omega)$ vanishes at low frequencies and has a maximum at $1/\tau$. One should note that the area below the real part of the conductivity is a measure of the carrier density and effective mass. This can be directly seen when integrating:

$$\int_0^\infty \sigma_1(\omega)\mathrm{d}\omega = \frac{\epsilon_0\pi}{2}\ \omega_p^2 = \frac{Nq^2\pi}{2m} \tag{4.19}$$

Indeed, this so-called "$f$-sum rule" is valid independent from the Drude model.

### Extended Drude model

In the Drude model, the scattering rate is assumed to be frequency-independent. However, this assumption is invalid for many correlated materials, where the carriers couple to a

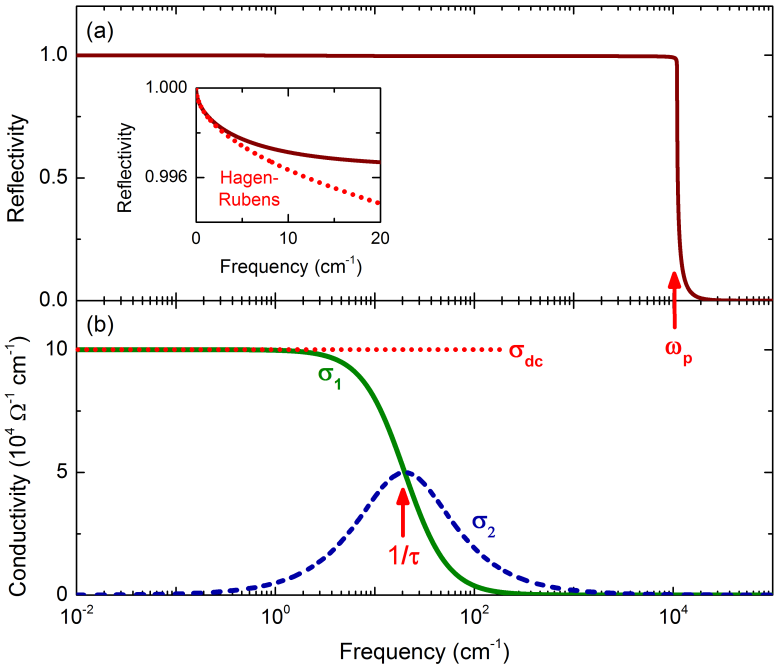


**Figure 4.1:** Typical (a) reflectivity and (b) conductivity of a metal according to the Drude model. (a) $R(\omega)$ (brown line) is close to unity until it drops rapidly at $\omega_\mathrm{p}$. The inset shows that at low frequencies, the reflectivity can be well described by the Hagen-Rubens equation (red dotted line). (b) $\sigma_1(\omega)$ (green line) is close to $\sigma_\mathrm{dc}$ (red dotted horizontal line) and decreases at higher frequencies with the inflection point of the curve at $1/\tau$, where $\sigma_2(\omega)$ (blue dashed line) displays a maximum.

bosonic mode. Therefore, an extended Drude model was introduced [116], where $1/\tau$ got replaced by a complex damping function:

$$M(\omega) = \frac{1}{\tau(\omega)} - i\omega\lambda(\omega) \tag{4.20}$$

with the frequency-dependent scattering rate $1/\tau(\omega)$ and the optical mass enhancement factor $\lambda(\omega)$. Those parameters can be derived from the optical conductivity:

$$\frac{1}{\tau(\omega)} = \epsilon_0\omega_\mathrm{p}^2\,\frac{1}{\sigma_1(\omega)} \tag{4.21}$$

$$1+\lambda(\omega) = \frac{m^*}{m_\mathrm{b}} = -\epsilon_0\omega_\mathrm{p}^2\,\frac{1}{\omega}\,\frac{1}{\sigma_2(\omega)} \tag{4.22}$$

with the band mass $m_\mathrm{b}$. This is of particular interest for unconventional superconductors, as from $1/\tau(\omega)$ the Eliashberg spectral function $\alpha^2F(\omega)$ (introduced in chapter 3.2.3) and the coupling strength to the bosonic mode $\lambda$ (also called "mass renormalization factor") can be calculated.

### Lorentz model

In many cases, resonant interaction of light with matter can be phenomenologically described by the Lorentz model of damped harmonic oscillators. Typical examples are ionic or phononic vibrations, as well as interband transitions. It follows for the real and imaginary part of the frequency-dependent conductivity:

$$\sigma_1(\omega) = \epsilon_0 \omega_\mathrm{p}^2 \frac{\omega^2/\tau}{(\omega_0^2 - \omega^2)^2 + \omega^2/\tau^2} \tag{4.23}$$

$$\sigma_2(\omega) = -\epsilon_0 \omega_\mathrm{p}^2 \frac{\omega(\omega_0^2 - \omega^2)}{(\omega_0^2 - \omega^2)^2 + \omega^2/\tau^2} \tag{4.24}$$

with the same definition of the plasma frequency $\omega_\mathrm{p}$ as in the Drude model; the damping $1/\tau$ accounts for the energy loss of the oscillating dipoles due to collisions.

In Fig. 4.2a, the reflectivity $R(\omega)$ of a Lorentz oscillator is displayed. While the reflectivity is rather flat at low frequencies, it increases strongly around $\omega_0$ due to the onset of interband transitions. For higher frequencies, the reflectivity stays again rather constant, until it drops similar to the Drude model at $\omega_\mathrm{p}$.

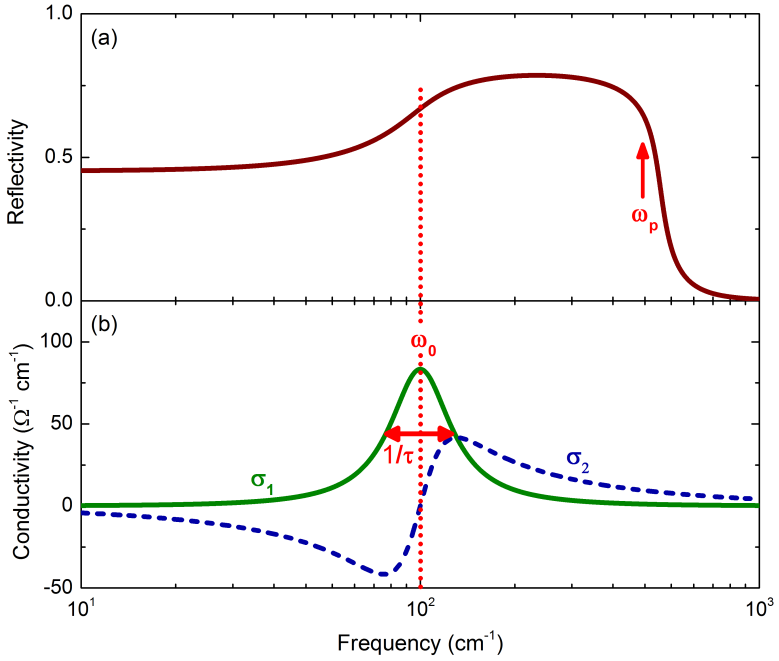


**Figure 4.2:** Typical (a) reflectivity and (b) conductivity of a Lorentz oscillator. While $R(\omega)$ (brown line) is rather flat at low frequencies, it increases around $\omega_0$, flattens again, and drops finally similar to the Drude model at $\omega_\mathrm{p}$. While $\sigma_1(\omega)$ (green line) displays a maximum at $\omega_0$ with the FWHM $= 1/\tau$, $\sigma_2(\omega)$ (blue dashed line) has an inflection point at $\omega_0$ and extrema at $\omega_0 \pm 1/2\tau$.

The corresponding conductivity can be seen in Fig. 4.2b. As the interband transitions lead to strong absorption, $\sigma_1(\omega)$ displays a maximum at $\omega_0$ with the full width at half maximum (FWHM) given by $1/\tau$; $\sigma_2(\omega)$ is negative below $\omega_0$ and positive at higher frequencies, with extrema at $\omega_0 \pm 1/2\tau$.

## 4.3 Broken symmetry states in metals

Electron-electron and electron-boson interactions might trigger in a metal a phase transition to an ordered, coherent ground state with broken symmetry. Examples are superconductivity and density wave states. While in the former case, gauge symmetry is broken via the Higg's mechanism, in the latter case, translational symmetry is broken due to a periodic variation of spin or charge. Further differences can be found when considering the pairing conditions: while for conventional superconductors[1], electrons with opposite momentum pair, in density waves electrons and holes pair with a total momentum of $Q = 2k_\mathrm{F}$. Therefore, the latter process requires a substantial nesting of the Fermi surface, meaning that parts of the Fermi surface can be mapped on top of each other by translation with $Q$.

### 4.3.1 General quantum mechanical description

In the metallic phase, the interaction of light with matter can be described sufficiently in the framework of the classical Drude and Lorentz model, as discussed in section 4.2. For superconductors and density waves, however, a quantum mechanical description is necessary.

According to Fermi's golden rule, the net transition rate from an initial (occupied) to a final (unoccupied) state (with energies $E$ and $E + \hbar\omega$, respectively) depends on:

- the energy of the external probe $\hbar\omega$
- the number of occupied quasiparticle states, given by $f(E)\mathcal{D}(E)$ (with the energy-dependent Fermi distribution $f(E)$ and the density of states $\mathcal{D}(E)$)
- the number of unoccupied states, given by $[1 - f(E + \hbar\omega)]\mathcal{D}(E + \hbar\omega)$
- the transition matrix element $\mathcal{M}$

1 This section will focus on conventional superconductors with an isotropic energy gap.

and can be calculated in general as:

$$W \propto \int |\mathcal{M}|^2 \mathcal{D}(E)\mathcal{D}(E+\hbar\omega)\,[f(E)-f(E+\hbar\omega)]\,\mathrm{d}E. \tag{4.25}$$

For broken symmetry states, one needs to consider some peculiarities about the density of states and the transition matrix element that will be discussed below.

### Single particle density of states

In the broken symmetry phase, a temperature-dependent energy gap appears in the single particle excitation spectrum, as already discussed for a (conventional) superconductor in chapter 3.1; the gap equation is the same for a density wave. The corresponding single particle density of states is depicted in Fig. 4.3. Above the critical temperature where the symmetry is broken ($T > T_\mathrm{c}$), the density of states is basically flat and the occupation of states follows the Fermi distribution. In the broken symmetry phase, states within the energy gap can not be occupied. As the total number of states needs to be conserved, the gapped states are reshuffled, leading to a divergent density of states at $E_\mathrm{F} \pm \Delta$.

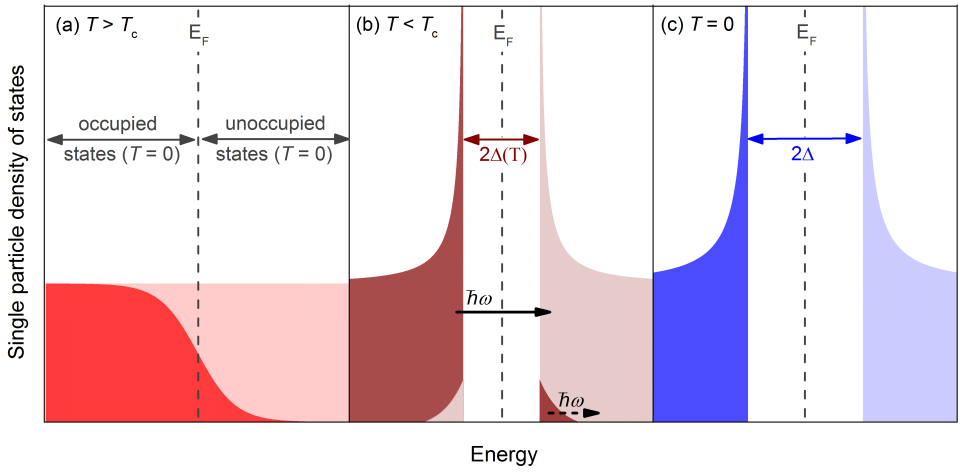


**Figure 4.3:** Single particle density of states for a metal that exhibits at $T_\mathrm{c}$ a transition to a broken symmetry phase for (a) $T > T_\mathrm{c}$, (b) $0 < T < T_\mathrm{c}$, and (c) $T = 0$; dark areas mark occupied states, light colours unoccupied ones. (a) For $T > T_\mathrm{c}$, the density of states follows the Fermi distribution. (b,c) Below $T_\mathrm{c}$, a temperature-dependent gap develops around $E_\mathrm{F}$, leading to a divergence of the density of states at $E_\mathrm{F} \pm \Delta$. The absorption of photons with $\hbar\omega \geq 2\Delta(T)$ can break Cooper pairs (black solid arrow). (b) Only for $T > 0$, thermally activated electrons are available to absorb photons (dashed black arrow).

The formation of an energy gap has important implications for the absorption of photons: while Cooper pairs can be broken only for energies $\hbar\omega \geq 2\Delta(T)$, thermally excited

electrons can also absorb photons with lower energies. This leads to two independent absorption channels, whose properties will be discussed in the next sections.

### Coherence effects

While transitions between different states are independent for a metal, the situation is more complicated in the case of a broken symmetry phase where carriers are condensed into a coherent ground state [40, 61]. As a quasiparticle of such a ground state consists of two carriers with well-defined momentum- and spin-relation, it can be shown that one will always find pairs of transitions that involve the same excitation states, although the scattering process is different (for a typical example, see table 4.1).

| Process | State | $(\mathbf{k}_1, \uparrow)$ | $(-\mathbf{k}_1, \downarrow)$ | $(\mathbf{k}_2, \uparrow)$ | $(-\mathbf{k}_2, \downarrow)$ |
|---|---|---|---|---|---|
| 1 | initial | **1** | 0 | 0 | 0 |
| 1 | final | 0 | 0 | **1** | 0 |
| 2 | initial | 1 | 0 | 1 | **1** |
| 2 | final | 1 | **1** | 1 | 0 |

**Table 4.1:** Two processes in a superconductor that lead to a scattering of an electronic excitation from the initial state $(\mathbf{k}_1, \uparrow)$ to the final state $(\mathbf{k}_2, \uparrow)$. States that are occupied by an electron are noted as "1", unoccupied ones by "0". Pairs of opposite spin and momentum that form a Cooper pair are marked in blue; if in such a pair only one electronic state is occupied, this is called electronic excitation (red). While the first process involves a scattering of an electron from $(\mathbf{k}_1, \uparrow)$ to $(\mathbf{k}_2, \uparrow)$ (marked in bold signs), the second process involves a scattering from $(-\mathbf{k}_2, \downarrow)$ to $(-\mathbf{k}_1, \downarrow)$. However, the initial and final states concerning the electronic excitation are the same.

This needs to be considered when calculating the transition matrix elements, as equivalent matrix elements have to be added coherently before taking the squared absolute value in equation 4.25. It turns out that a proper mathematical description can be achieved via so-called "coherence factors" $\mathcal{F}$, transforming the transition matrix element as:

$$|\mathcal{M}|^2 \rightarrow \mathcal{F}|\mathcal{M}|^2 \tag{4.26}$$

in the broken symmetry state. The absolute value of $\mathcal{F}$ depends on the type of perturbation and varies between zero and one.

Fig. 4.4a displays the frequency-dependence (at $T = 0\,\mathrm{K}$) of the electromagnetic absorption for a superconductor and a spin density wave system, calculated from equation 4.25 with considering the appropriate coherence factors. While for the latter case, the singularity in the density of states is directly visible in the absorption spectrum, for a superconductor, the coherence factor approaches zero at the gap energy and cancels the singularity

in the density of states. This leads to a smooth increase of the absorption rate for energies above $2\Delta$. In Fig. 4.4b, also the temperature-dependence of the absorption rate is depicted for electromagnetic irradiation with small energies $\hbar\omega \ll 2\Delta$. In the case of a superconductor, one can observe just below $T_c$ a surprising enhancement of the absorption rate. As this enhancement rises again from the coherence factor, this feature is usually referred to as "coherence peak".

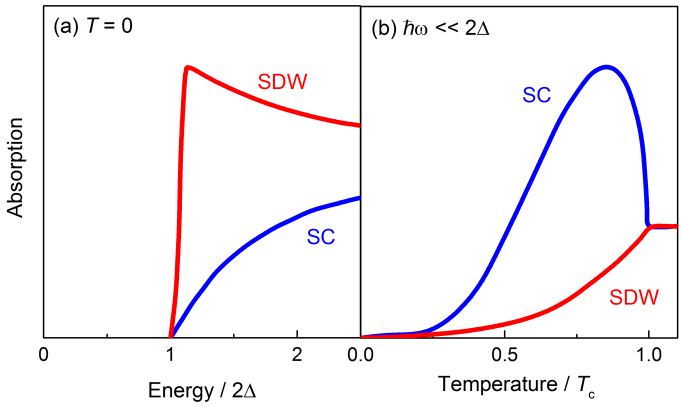


**Figure 4.4:** (a) Frequency- and (b) temperature-dependent absorption of photons for a superconductor (blue) and a spin density wave material (red) at $T = 0$ and $\hbar\omega \ll 2\Delta$, respectively, as resulting from Fermi's golden rule (adapted from Ref. [113]). (a) In both cases, an energy gap appears below $2\Delta$. While for the spin density wave, the singularity in the density of states is directly visible in the absorption spectrum, for a superconductor, coherence effects lead to a smooth increase of the absorption. (b) A coherence peak slightly below $T_c$ is only visible for a superconductor.

### 4.3.2 Superconductors

In the so-called "two-fluid" model, the electrodynamic properties of a superconductor are approximated as a superposition of the response of superconducting and normal-conducting electrons, neglecting any superconducting gap and coherence effects. For the condensed electrons, such a classical descriptions transforms the Drude conductivity (see equation 4.13) in the limit $\tau \to \infty$ to:

$$\sigma_1(\omega) = \frac{\pi}{2}\frac{Nq^2}{m}\delta(\omega = 0) = \frac{\pi}{2}\frac{\epsilon_0}{\lambda_L^2}\delta(\omega = 0) \tag{4.27}$$

$$\sigma_2(\omega) = \frac{Nq^2}{m}\frac{1}{\omega} = \frac{\epsilon_0}{\lambda_L^2}\frac{1}{\omega} \tag{4.28}$$

with a delta-function in $\sigma_1(\omega)$ at zero frequency $\delta(\omega = 0)$, the London penetration depth:

$$\lambda_{\mathrm{L}} = \sqrt{\frac{m}{\mu_0 N q^2}} = \frac{c}{\omega_{\mathrm{p,c}}} \tag{4.29}$$

and charge and mass of a single electron, if $N$ is defined as the density of superconducting electrons. When all electrons are condensed in the superconducting ground state, the plasma frequency in the normal state $\omega_{\mathrm{p}}$ corresponds to that of the superconducting condensate $\omega_{\mathrm{p,c}}$. One should note that despite $\lambda_{\mathrm{L}}$, sometimes also a more general, frequency-dependent penetration depth is defined:

$$\lambda = \sqrt{\frac{\epsilon_0}{\sigma_2(\omega)\omega}}. \tag{4.30}$$

The $1/\omega$-divergence in $\sigma_2(\omega)$ leads to a rapid, characteristic increase of the reflectivity towards unity.

### FGT sum rule

As the $f$-sum rule must hold also when passing from the normal to the superconducting state, it follows that the missing spectral weight that appears in the superconducting phase due to the opening of the gap is transferred to the delta-function at zero frequency. This directly leads to the "FGT sum rule" (named after Ferrell, Glover and Tinkham [117–119]), relating the conductivity in the normal state $\sigma_1^n(\omega)$, the conductivity in the superconducting state $\sigma_1^s(\omega)$, and the London penetration depth by:

$$\int_0^\infty [\sigma_1^n - \sigma_1^s] \mathrm{d}\omega = \frac{\epsilon_0 \pi}{2} \frac{c^2}{\lambda_{\mathrm{L}}^2}. \tag{4.31}$$

### Dirty vs. clean limit

For a more detailed description of the electrodynamics, one has to consider the different characteristic length scales; their relative magnitude determines the nature of the superconducting state. In particular, one has to distinguish between the dirty (local) and the clean limit, $1/\tau > \Delta$ and $1/\tau < \Delta$, respectively. Thus, in the clean limit most of the spectral weight of the Drude component lies below $2\Delta$ and for $T < T_{\mathrm{c}}$, almost all free carriers collapse into the condensate. In contrast, in the dirty limit a significant amount of Drude weight lies above $2\Delta$. Therefore, only a fraction of the Drude spectral weight collapses into the condensate, leading to a more pronounced gap feature in the optical spectrum.

### Mattis-Bardeen description

Based on the BCS theory, the electrodynamic properties of a superconductor were first analytically calculated by Mattis and Bardeen [120], assuming $\tau \to \infty$, and extended for finite scattering rates by Zimmermann *et al.* [121]. Fig. 4.5 displays the real and the imaginary part of the conductivity for a superconductor in the dirty limit at $T = 0.8\ T_c$, decomposed into contributions from Cooper pairs (broken by absorbed phonons) and thermally activated electrons; Fig. 4.6 adds the temperature-dependence of $\sigma_1$. The general features that were discussed up to now, *i.e.* the non-diverging behaviour of $\sigma_1(\omega \leq 2\Delta)$, the coherence peak in $\sigma_1(T)$ (for $\omega \ll 2\Delta$) and the $1/\omega$-dependence of $\sigma_2(\omega)$ are all nicely visible.

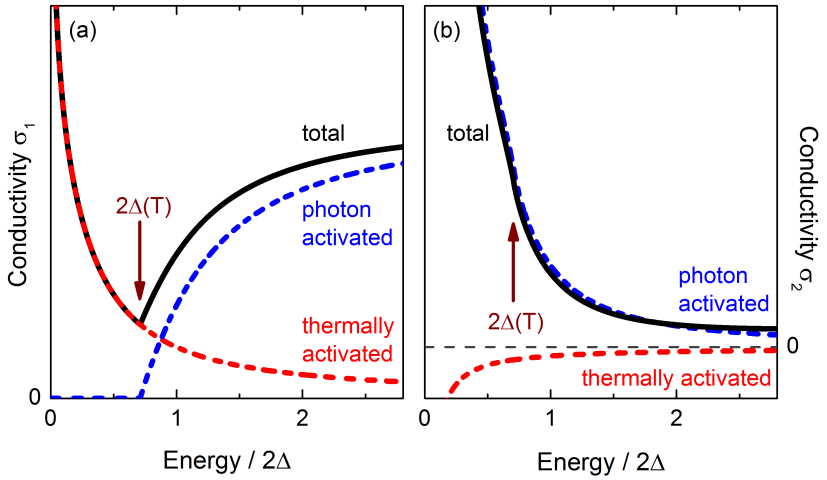


**Figure 4.5:** Frequency-dependence of the (a) real and (b) imaginary part of $\sigma(\omega)$ (black line) for a superconductor in the dirty limit at $T/T_c = 0.8$, decomposed into contributions from Cooper pairs (blue dashed line) and thermally activated electrons (red dashed line) (adapted from Ref. [122]). (a) The photon activated electrons contribute only for energies $\hbar\omega > 2\Delta(T)$ to $\sigma_1(\omega)$; coherence effects cancel the singularity in the density of states, leading to a continuous increase of their response. The contribution of thermal electrons decreases with increasing frequency, following the behaviour of the density of states. The sum of both contributions displays a characteristic minimum at $2\Delta(T)$. (b) The $1/\omega$-behaviour of the phonon activated electrons dominates the response of $\sigma_2(\omega)$; the contribution of the thermally activated electrons is opposite, but negligible. At $2\Delta(T)$, only a very weak kink is visible.

## 4.4 Iron-based superconductors

Optical spectroscopy revealed valuable information about correlations [123] and broken symmetry states [124–127, 266] already within the first year after the discovery of iron-based superconductors. Most of the relevant charge dynamics take place in the infrared

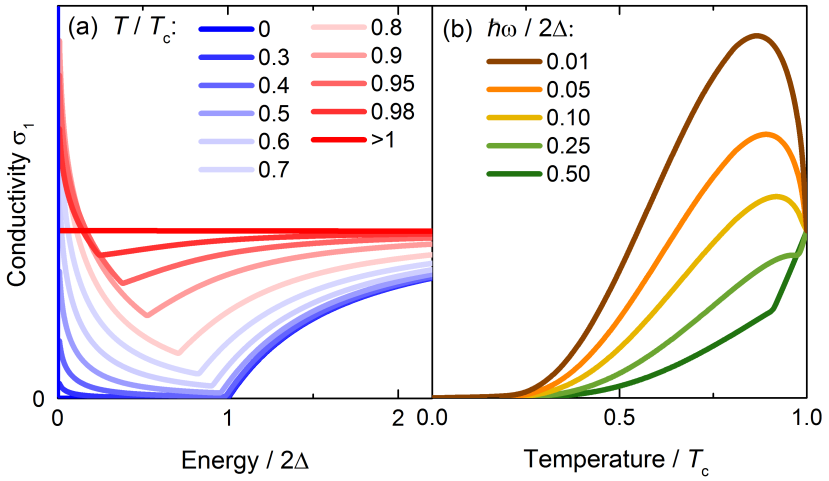


**Figure 4.6:** (a) Frequency- and (b) temperature-dependence of $\sigma_1(\omega)$ for a superconductor in the dirty limit for several temperatures and photon energies, respectively. (a) The pronounced gap feature vanishes with increasing temperature. However, the response of thermally activated electrons at very low energies gets strongly enhanced close to $T_c$. (b) The latter is consistent with a pronounced coherence peak at energies $\hbar\omega \ll 2\Delta$.

frequency range, as summarized in Fig. 4.7. This section provides an overview of great achievements and open questions provoked by optical investigations on 122 iron pnictides.

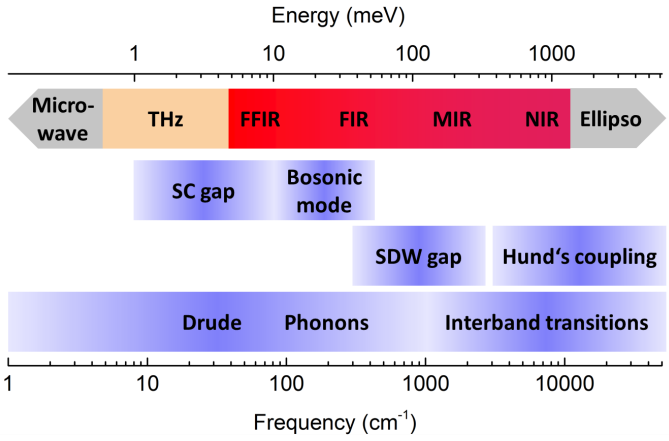


**Figure 4.7:** Characteristic energy scales in iron-based superconductors. In order to study the superconducting gap, terahertz (THz) and far-far-infrared (FFIR) frequencies have to be covered. While itinerant dynamics are relevant in the far-infrared (FIR) energy range, incoherent transport and interband transitions govern the mid- and near-infrared (MIR and NIR, respectively). Ellipsometry measurements can be extended to very high energies.

### 4.4.1 Spectral features of the normal state

Similar to cuprates, the normal state in-plane reflectivity and optical conductivity of 122 iron pnictides do not show well-separated components, leading despite a zero-energy Drude peak to a broad mid-infrared plateau that is rather untypical for a metal and often referred to as "incoherent" region; no clear plasma edge is visible (see Fig. 4.8b, [128, 129, 266]). At higher frequencies, humps characteristic for interband transitions appear.

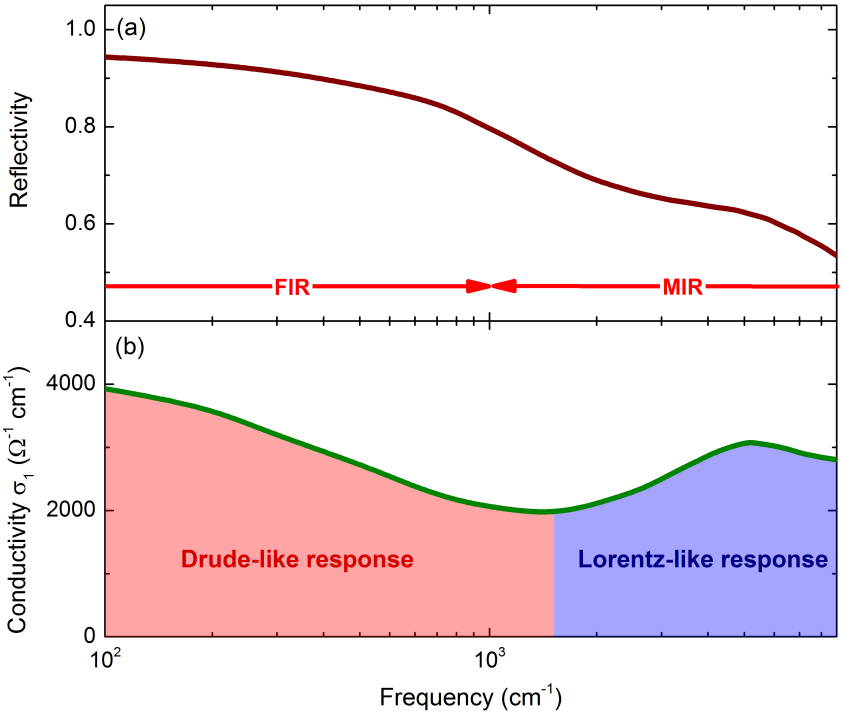


**Figure 4.8:** Characteristic (a) reflectivity and (b) conductivity of 122 iron pnictides in the normal state (adapted from Ref. [266]). (a) $R(\omega)$ (brown line) typically displays in the FIR an overdamped metallic frequency-dependence; at higher frequencies, no clear plasma edge is visible - only humps typical for interband transitions. (b) Correspondingly, $\sigma_1(\omega)$ is slowly decreasing at low frequencies with a long tail extending in the MIR region; it is followed by a pronounced peak structure around 5000 $\mathrm{cm}^{-1}$. A cut-off separating itinerant Drude-like behaviour (red area) from local and interband (Lorentz-like) dynamics (blue area) is often set around 1500 $\mathrm{cm}^{-1}$. However, in reality a significant overlap exists.

With decreasing temperature, the response gets more metallic, meaning that spectral weight is shifted within the mid- and far-infrared region to lower frequencies. However, spectral weight shifts occur also at higher frequencies up to the visible spectral range, indicating that correlation effects are of importance [130], as discussed further in section 4.4.5.

Along the *c*-direction, the flat MIR background dominates, which decreases with decreasing temperature[1] [131]. However, lowering the temperature also uncovers a weak Drude component, indicating interlayer coherence. Thus, iron pnictides display much less electronic anisotropy than cuprates. Nevertheless, both families of high-temperature superconductors share the broad plateau-like background in the mid-infrared, that is not a simple Drude response.

### 4.4.2 Analysis methods

In the case of cuprates, two principal approaches exist that are commonly used to describe the mid-infrared charge dynamics: one-component and multi-component models [116]. In the former case, it is assumed that the low-frequency response originates from itinerant carriers with a frequency-dependent scattering rate and mass. The formalism of this extended Drude model was already introduced in section 4.2. In the multi-component approach, the conductivity spectrum is described by a free-carrier Drude term and a set of Lorentzian oscillators, accounting for example for interband transitions or impurity states.

The debate which model describes better the charge dynamics in cuprates is yet not solved. On the one hand, well-separated absorptions in lightly doped cuprates favour the multi-component approach. On the other hand, the extended Drude formalism could uncover a frequency-dependent scattering rate over a broad energy range and many interesting aspects like the violation of Fermi liquid theory or the coupling to a temperature-dependent bosonic mode, both consistent with other measurement techniques.

In the case of iron pnictides, the multiband character further complicates both, single- and multi-component analysis. In principle, hole and electron bands with different scattering rates should be considered. Furthermore, as five Fe *d*-bands are situated close to the Fermi energy, low-lying interband transitions are plausible. Indeed, recent infrared studies uncovered for Ba, Sr and Ca compounds two well-defined features around 1000 and 2300 $\mathrm{cm}^{-1}$ [12]. Due to its temperature- and doping-dependence, the former one can be attributed (via a comparison to ARPES measurements) to interband transitions involving Fe hole pockets. The origin of the second feature is yet not clear; the same holds for another hump in the optical conductivity, that was observed in several compounds at even lower energies (around 150 $\mathrm{cm}^{-1}$) [132–137]. Despite that, Dirac physics might also play a certain role [139, 140].

1 Moon *et al.* demonstrate that a true *c*-direction response can be only obtained for cleaved samples, not for polished specimen [131].

Disentangling all those processes in a multi-component analysis is almost impossible. Therefore, a "broad Drude" approach was suggested by Wu *et al.*: they modelled the mostly temperature-independent background of eight different 122 compounds by a very broad Drude and two high-frequency Lorentzians that account for interband transitions [128, 130]. The remaining temperature-dependent part of the spectrum can be described by one narrow Drude. There is no spectral weight transfer between the different subsystems. This model has the advantage that the coherent dynamics are described by only a few parameters.

Nakajima *et al.* extended this approach, allowing the broad Drude component to vary with temperature [129]. However, fitting the spectra was still possible without spectral weight transfer between the different subsystems. In further publications, the broad background narrowed and was more and more attributed to the hole bands [141].

There exist also advocates of the conventional multi-component approach known from cuprates, where one or a series of Lorentzians is used to model the mid-infrared plateau. They argue that the mean free path of a very broad Drude would violate the Mott-Ioffe-Regel limit, indicating that the conductivity in such a band is no longer metallic and therefore better described by a bound excitation [142]. It turns out that in this case, enough free parameters exist in order to fit the spectrum with only one Drude. In order to account for electron and hole bands, one needs additional information, such as the relative spectral weights of the Drude components which can be extracted from photoemission experiments [143, 144].

The ambiguity of different modelling approaches is a serious drawback of optical spectroscopy on iron pnictides. Maybe one of the biggest problems is that usually one group only publishes results using a single modelling approach. Thus, it gets not clear whether (on the first view) contradictory studies result from different fitting approaches, sample quality or have a physical meaning. As a direct comparison of different modelling approaches is still lacking, such a study was performed in the framework of this thesis and is presented in chapter 9.

### 4.4.3 Antiferromagnetism

The early observation of energy gaps opening at the high-temperature phase transition in iron pnictide parent compounds is one of the great achievements of optical spectroscopy: already in 2008, Dong *et al.* proposed on the basis of optical measurements on polycrystalline LaOFeAs a spin density wave, driven by a nesting instability between electron and hole Fermi surfaces [124]. Only six months later, Hu *et al.* reported more detailed studies on single crystals of Ba- and $SrFe_2As_2$ [266].

At the spin density wave transition, the reflectivity develops a rather sharp edge in the far-infrared, above which $R(\omega)$ gets substantially suppressed (see Fig. 4.9a). This is a typical signature of the formation of an energy gap. However, with decreasing temperature the low-frequency reflectivity still increases, indicating that the Fermi surface is only partially gapped. The remaining Drude response is dramatically narrowed, with the scattering rate being decreased by $\sim 90\,\%$.

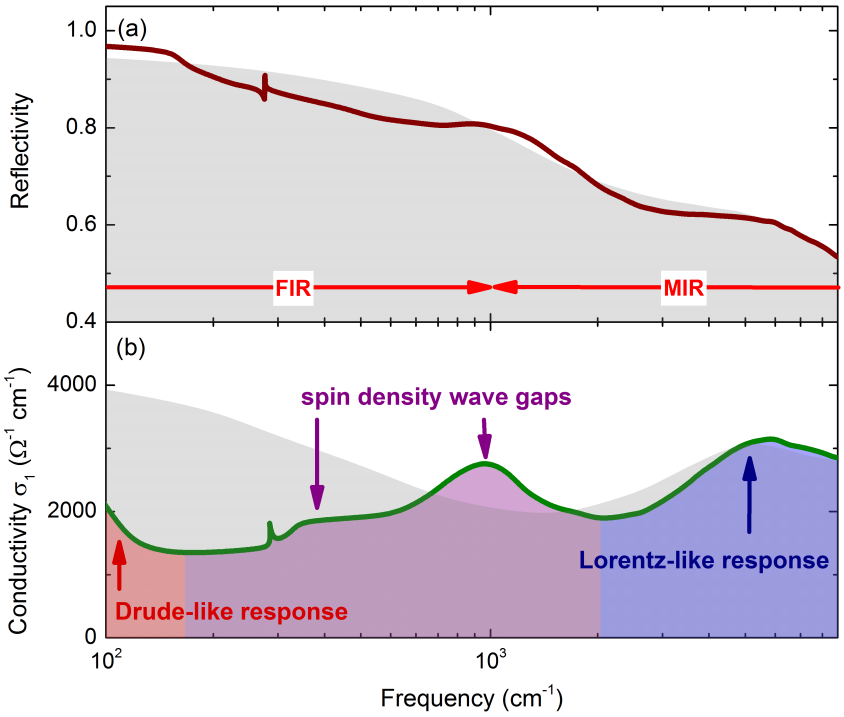


**Figure 4.9:** Characteristic (a) reflectivity $R(\omega)$ and (b) conductivity $\sigma_1(\omega)$ of 122 iron pnictides in the spin density wave state (solid curves) compared to the normal state (grey light area) (adapted from Ref. [266]). The Fermi surface gets only partially gapped, visible in an increase of $R(\omega)$ and $\sigma_1(\omega)$ at low frequencies (red area). Spectral weight is shifted to higher frequencies; $\sigma_1(\omega)$ displays two bump-like features corresponding to two different gaps (purple area). An additional spectral weight shift appears even in the range of interband transitions (blue area), indicating correlations. The sharp peak around $260\,\mathrm{cm}^{-1}$ is the signature of an FeAs phonon [145].

In the real part of the optical conductivity, the spin density wave becomes noticeable as spectral weight is reshuffled from the far-infrared to higher frequencies, where it piles up usually in the form of two well-separated peaks, corresponding to two different energy gaps (see Fig. 4.9b). The peak position marks the gap energy; it is around $2\Delta/k_\mathrm{B}T_\mathrm{SDW} \sim 3.5$ for the smaller and $\sim 10$ for the bigger gap. As only spectral weight and peak position of the lower gap follow the mean field temperature-dependence, it was suggested in accordance with band structure calculations that this one has itinerant character, while the higher gap

appears due to local exchange splitting [146]. A different interpretation results from $c$-axis measurements, where exclusively the smaller gap is visible [147]. From this, the authors proposed that the larger gap is due to the nesting of 2D Fermi surfaces and the smaller gap results from the backfolding of the magnetic Brillouin zone that cuts the 3D Fermi sheet. Finally, also a magnon-assisted indirect spin density wave excitation was discussed that could lead to the high energy gap [139].

### 4.4.4 Superconductivity

Optical signatures of a clear superconducting gap were first seen in 1111 $LaFeAsO_{0.9}F_{0.1-\delta}$ and $NdFeAsO_{0.82}F_{0.18}$ polycrystalline samples [125, 126]. A more quantitative analysis could be only achieved after 122 single crystals were available [127]. Since then, most optical studies were carried out on (nearly) optimally Co doped Ba 122 compounds due to the availability of high quality single crystals [128–130, 133, 134, 142, 154, 155] and thin films [148–153].

#### Dirty vs. clean limit

It turned out that the in-plane optical response of $Ba_{1-x}K_xFe_2As_2$ and $Ba(Fe_{1-x}Co_x)_2As_2$ is quite different in the superconducting regime: while the former displays over a broad frequency range a quasilinear dependence of $\sigma_1(\omega)$, the latter shows a steep onset of absorption at energies corresponding to (one of) the smaller superconducting gap(s) [135]. Charnukha *et al.* demonstrated that both behaviours can be explained by using an effective two-band Eliashberg theory with a strong coupling to spin fluctuations, if K substitution leads to effective bands in the clean limit, while Co doped compounds are in the dirty limit.

#### Superconducting gaps

The same calculations yield for $Ba_{0.68}K_{0.32}Fe_2As_2$ isotropic superconducting gaps with $2\Delta/k_BT_c \sim 2.2$ and $\sim 6$, in quantitative agreement with other measurement techniques such as ARPES, STM and specific heat. The situation is much more complicated in the case of $Ba(Fe_{1-x}Co_x)_2As_2$, where several reports exist which show neither consensus about the gap sizes, nor about the number of gaps (see Fig. 4.10a). While most reports agree on one directly visible gap at around the BCS mean field value, fitting approaches usually need at least one more gap at significantly higher or lower energies for a satisfactory description.

Similar to cuprates [116], an unexpected high intra-gap absorption was evidenced in the superconducting state of $Ba(Fe_{1-x}Co_x)_2As_2$, which cannot be accounted for by thermally

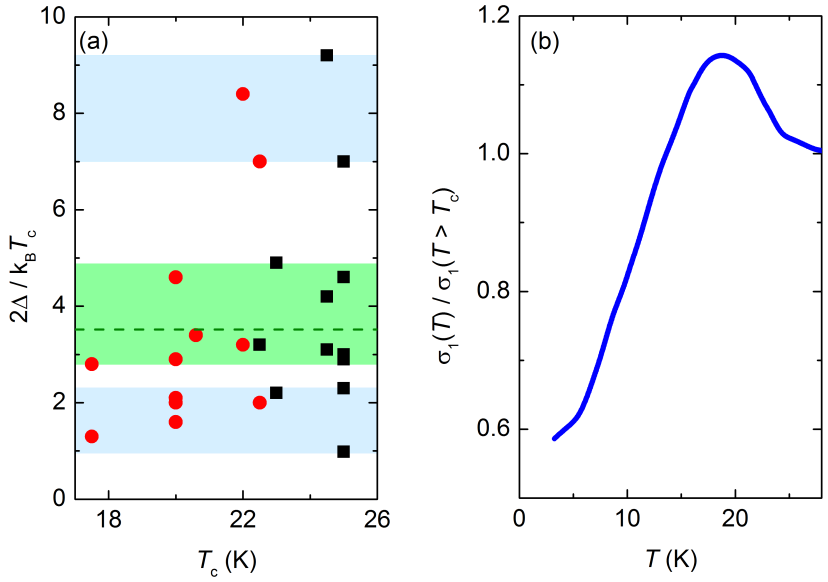


**Figure 4.10:** (a) Extracted superconducting gap sizes [128–130, 133, 134, 142–144, 148–155] and (b) typical temperature-dependent conductivity in the THz frequency range for nearly optimally doped $Ba(Fe_{1-x}Co_x)_2As_2$ (adapted from Ref. [151]). (a) While most reports agree on one directly visible gap at around the BCS mean field value (green dashed line / green area), fitting approaches usually need at least one more gap at significantly higher or lower energies for a satisfactory description (light blue areas). Black squares denote measurements on single crystals, red points on thin films. (b) A coherence peak is commonly observed below $T_c$ at very low frequencies. However, the conductivity does not approach zero at lowest temperatures, indicating an anisotropic gap or pair-breaking interband scattering.

broken pairs [134, 148, 150, 151]. It appears in films as well as single crystals. As it can be fitted with a Drude peak (with an overall conserved spectral weight), a low-lying impurity band is unlikely the reason [134]. Other explanations are an anisotropic gap [151] or pair-breaking interband scattering[1] [150, 156].

An important difference between K and Co doping is that in the former case, atoms out of the FeAs planes are substituted, while in the latter case, the FeAs planes are directly affected [156]. Therefore, stronger impurity scattering is expected for Co doping, consistent with smaller residual resistivity ratios and superconductivity in the dirty limit. It needs to be seen, whether this enhanced scattering is also responsible for the strong intra-gap absorption. Proving this would be another very strong indication for the $s_\pm$-symmetry of the superconducting order parameter. Measurements on $Ba(Fe_{1-x}Co_x)_2As_2$

1 In an $s_\pm$ superconductor, interband scattering by non-magnetic impurities is pair-breaking, as it mixes hole and electron states that have superconducting order parameters of opposite phase [156].

thin films, where the impurity scattering gets step-wise enhanced by proton irradiation, were performed and supervised within this thesis and are presented in the attachment.

### Coherence peak

Optical spectroscopy on $Ba(Fe_{1-x}Co_x)_2As_2$ thin films was able to resolve a well-pronounced coherence peak in the THz frequency range (see Fig. 4.10, [148, 150, 151]). In general, a coherence peak can arise when the portions of Fermi surface that are coupled by an experimental probe have gaps of the same sign and magnitude [150]. As the momentum transfer of light at THz frequencies is negligible compared to the reciprocal lattice momentum, only parts of the same Fermi sheets are coupled. Therefore, the observed coherence peak is consistent with an $s_{\pm}$-symmetry of the superconducting order parameter. Furthermore, the position of the coherence peak can be used in multiband superconductors as a quantitative measure of the lower superconducting gap, demonstrated by Dahm *et al.* for $MgB_2$ [157].

### FGT sum rule

All infrared studies agree on a rapid recovery of the missing spectral weight in the FIR frequency range, yielding in-plane London penetration depths (in accordance with the extraction from $\sigma_2(\omega)$) between 200-400 nm. However, one very careful ellipsometry study performed by Charnukha *et al.* on $Ba_{0.68}K_{0.32}Fe_2As_2$ uncovered a superconductivity-induced suppression of an interband transition at energies well above the plasma edge [158]. Although the transferred spectral weight is only $\sim 0.5\,\%$ and therefore too small to be detected in infrared studies, it could have a big effect on reducing the kinetic energy of the system, pointing towards an unconventional pairing mechanism. Such an effect was already proposed for cuprates, however, is there still under debate [116].

### Bosonic spectrum

As the extended Drude analysis accounts only for itinerant carriers, the contribution of all interband transitions needs to be eliminated before any further data processing. Moreover, one has to keep in mind that due to the multiband nature of iron pnictides, only an average spectrum for bosonic excitations can be extracted.

Up to now, an extended Drude analysis was carried out mainly on K and Co doped iron pnictides [130, 135, 142, 159–161]. In all cases, a frequency-dependent scattering rate is observed at low frequencies, which increases linearly with frequency (at least) up to $\sim 50\,\mathrm{meV}$. A further Eliashberg analysis reveals a strongly temperature-dependent bosonic spectrum, which is inconsistent with phonon coupling. The mass renormalization

factor increases with decreasing temperature, reaching values between 3-4[1], much above the electron-phonon coupling constant $\lambda = 0.21$. Both, the temperature-dependence of the bosonic spectrum as well as the high coupling constant would be consistent with spin fluctuations playing a key role for bosonic excitations in pnictides. This situation is very similar to that in cuprates [116].

#### *c*-axis coherence

Measurements on cleaved $Ba(Fe_{0.926}Co_{0.074})_2As_2$ crystals reveal not only interlayer coherence in the normal state, but also a robust interlayer superconducting condensate with a penetration depth of $\sim 1000\,\text{nm}$ [131]. This is in stark contrast to underdoped cuprates, where normal state transport is incoherent along the *c*-axis, leading to Josephson coupling of $CuO_2$ layers in the superconducting phase [116].

### 4.4.5 Unconventional normal state properties

Optical spectroscopy is able to reveal important information on the unconventional normal state charge dynamics of high-temperature superconductors, as already demonstrated impressively for cuprates [116]. Therefore, similar approaches were applied to iron-based superconductors in order to identify (via a comparison to cuprates) key ingredients for high-temperature superconductivity. It turned out that iron pnictides are moderately correlated materials, where (instead of Mott physics) Hund's coupling plays an important role. While the appearance of a pseudogap or a quantum critical point is yet not well established, the nematic phase drew enormous attention - even giving a feedback effect for research on cuprates. Important insights gained from infrared spectroscopy on iron pnictides are summarized below.

#### Correlations

A comparison between the kinetic energy of electrons obtained by band structure calculations and optical measurements revealed that iron pnictides are moderately correlated materials[2] [123]. This indicates that coherent and incoherent processes play both a certain role in transport properties, in good agreement with the broad mid-infrared plateau discussed above.

1 One has to keep in mind that the absolute value of the mass renormalization factor strongly depends on the plasma frequency and thus on the model chosen for the analysis. This is probably the reason why Tu *et al.* report smaller values than those given here [142].

2 A similar result can be obtained experimentally by comparing the spectral weight of coherent and incoherent processes [162]. However, this method is very sensitive to the fitting approach.

In particular, LaFeAsO was found to be more correlated than LaFePO [165]. This observation fits well with systematic room temperature studies performed by Nakajima *et al.* on electron doped $Ba(Fe_{1-x}Co_x)_2As_2$, hole doped $Ba_{1-x}K_xFe_2As_2$, and isovalently substituted $BaFe_2(As_{1-x}P_x)_2$ [129, 141, 166]. They conclude that coherent transport is enhanced by Co and P substitution, and slightly suppressed by K doping; incoherent transport is basically not affected by Co doping, reduced by P substitution and enhanced by K doping. Therefore, it seems that chemical substitution controls the Drude spectral weight in quite different ways depending on dopant sites or type. The commonality found in those studies is that superconductivity seems to be suppressed when the charge dynamics become too coherent.

### Hund's coupling

The renormalization of electronic bands due to correlations does not only reduce the Drude response (compared to band theory predictions), it also implies that additional spectral weight is present at higher energies [163]. This can lead to unusual temperature-dependent effects at high energies, which can not be attributed to interband transitions. Such temperature-dependent spectral weight transfer around $5000\,\mathrm{cm}^{-1}$ was already reported in 2008 for the *ab*-plane of Ba- and $SrFe_2As_2$ [266], and later also confirmed along the *c*-axis of $Ba(Fe_{0.926}Co_{0.074})_2As_2$ [131]. The direction of spectral weight transfer, its independence of Co doping and its energy scale are not compatible with a Mott-like correlation mechanism, but can be explained with Hund's rule coupling effects [163, 164].

Due to Hund's coupling, electron spins tend to align parallel. This can lead on the one hand to the localization of electrons, if their kinetic energy is smaller than the coupling energy; on the other hand, the thus induced local and itinerant electrons are not isolated from each other, but still coupled via Hund's coupling [164]. As at low temperatures, thermal excitations become weak, more and more itinerant electrons get localized by this interaction, explaining an increasing spectral weight transfer to high energies.

### Pseudogap

In cuprates, the pseudogap in the density of states is directly visible in the out-of-plane conductivity: while $\sigma_c(\omega)$ is rather flat at $T > T^*$ (indicating incoherent transport), the low-frequency conductivity gets suppressed below $T^*$. Surprisingly, the gap value is basically temperature-independent. An extended Drude analysis indicates that this process is intimately related to a gap in the excitation spectrum, visible as the onset of in-plane coherence and a gap in the frequency-dependent in-plane scattering rate (due to the coupling to a bosonic resonance mode).

In iron pnictides, the appearance of a pseudogap is yet not well established. Up to now, two different "types" of pseudogaps were proposed from optical measurements. In underdoped $Ba_{1-x}K_xFe_2As_2$, spin density wave and superconducting order coexist. Additionally, a gap-like hump structure appears well above $T_c$ for frequencies around $150\,cm^{-1}$, corresponding to the energy range of the superconducting gap [136, 137]. Dai *et al.* argued via a spectral weight analysis that while the spin density wave is a competitive order to superconductivity, this pseudogap acts as a precursor ($T_c < T_{PG} < T_{SDW}$) [137].

One should note, however, that a similar feature was already observed in $BaFe_2As_2$ [132], as well as optimally electron and hole doped compounds [133–135]. In those cases, alternative interpretations were given, involving a low-lying interband transition [133, 134] or an impurity band [134].

Moon *et al.* investigated single crystals of the Ba 122 family [138]. For optimally substituted Co and P compounds, they observed a shallow dip in the conductivity around $650\,cm^{-1}$ that is accompanied by a threshold in $1/\tau(\omega)$, typically for the pseudogap in cuprates. This feature does not appear in the parent compound and the overdoped region, coinciding with the development of antiferromagnetic correlations. Therefore, they suggested that in iron pnictides, antiferromagnetic fluctuations related to the spin density wave instability of the parent compound cause a pseudogap.

### Nematic phase and in-plane anisotropy

Optical studies on mechanically detwinned $Ba(Fe_{1-x}Co_x)_2As_2$ as-grown and annealed samples were performed by Dusza [167, 170, 172] and Nakajima *et al.* [169, 171], respectively. In both cases, a pronounced anisotropy at finite frequencies appears that can be attributed to an anisotropic spin density wave gap formation (see Fig. 4.11). This anisotropy extends up to very high frequencies, well exceeding the energy scale of $k_B T_{s,SDW}$. Moreover, the FeAs phonon around $260\,cm^{-1}$ gets highly anisotropic; in $BaFe_2As_2$, it basically disappears along the $a$-axis. Detailed measurements on twinned $BaFe_2As_2$ evidenced a phonon splitting below $T_{s,SDW}$, with the minority contribution (along the $a$-axis) having a higher center frequency [174].

Using local density approximation combined with dynamical mean field theory, Yin *et al.* [168] calculated the anisotropic optical conductivity for $BaFe_2As_2$ resulting from orbital polarization. They found three extra excitations appearing in the spin density wave phase around $1000\,cm^{-1}$. While two lower energy excitations are much more pronounced along the $a$-direction, the third peak is more pronounced along the $b$-direction. All this is in good agreement with the results shown in Fig. 4.11. However, one should note that the

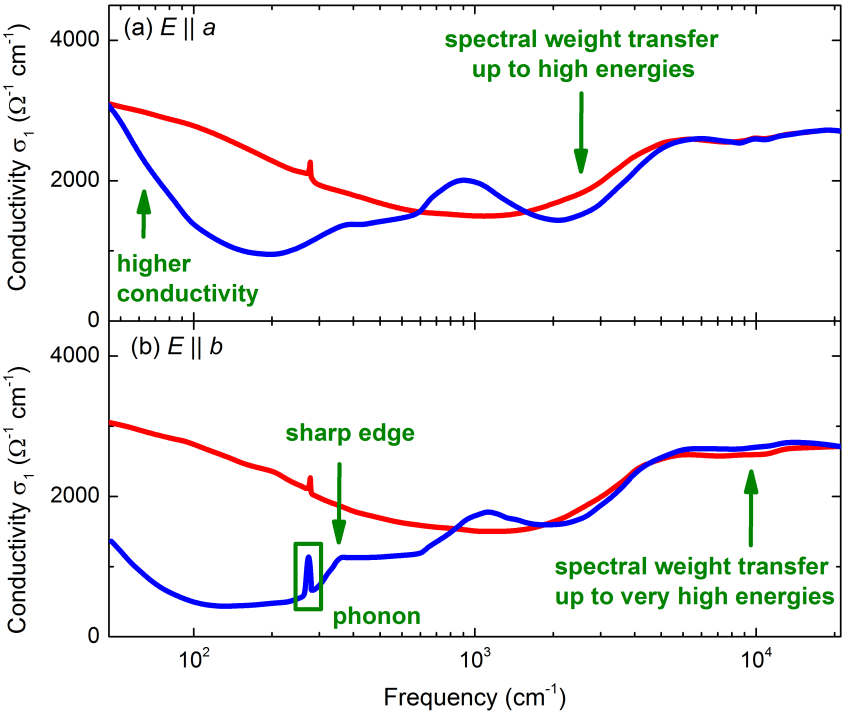


**Figure 4.11:** In-plane conductivity of mechanically detwinned $BaFe_2As_2$ (adapted from Ref. [169]) for (a) $E \parallel a$ and (b) $E \parallel b$-axis and temperatures below (blue line) and above (red line) $T_{\mathrm{s,SDW}}$. At low energies and temperatures, $\sigma_a > \sigma_b$ is observed, consistent with resistivity measurements. A pronounced anisotropy appears in particular at finite frequencies that can be attributed to an anisotropic spin density wave gap formation. Furthermore, the FeAs phonon around $260\,\mathrm{cm}^{-1}$ disappears in $\sigma_a(\omega)$. A cusp-like shape for the lowest energy spin density wave feature in $\sigma_b$ is only observed by Nakajima *et al.*. Along the $b$-direction, spectral weight is transferred up to very high energies.

experiments reveal spectral weight transfer to even higher energies than predicted, in particular along the $b$-direction ($\sim 17000\,\mathrm{cm}^{-1}$).

From a multi-component analysis one should be able to distinguish whether the unconventional behaviour $\rho_b > \rho_a$ results from the anisotropy in the scattering rate or the Fermi surface parameters $n/m^*$ (determined by the Drude spectral weight), as $1/\rho = \sigma_{\mathrm{dc}} = nq^2\tau/m^*$. Unfortunately, there is no consensus concerning this topic: Dusza *et al.* claim that the anisotropy results from the Fermi surface parameters, outweighing the conventionally expected $1/\tau_a > 1/\tau_b$ [167, 170]. In contrast, Nakajima *et al.* conclude $1/\tau_b > 1/\tau_a$, while the Drude weight stays rather isotropic [171]. In chapter 9, we will discuss our results for magnetically detwinned $EuFe_2As_2$.

While those measurements were obtained under constant external stress due to a mechanical clamp, Mirri *et al.* investigated the optical anisotropy that is induced in $BaFe_2As_2$

by a tunable Helium gas pressure cell [173]. While optical anisotropy can be induced by pressure below and above $T_{\mathrm{s,SDW}}$ (consistent with resistivity measurements), a hysteretic behaviour and a persistent detwinning (after the pressure is reduced to zero) can be only detected below $T_{\mathrm{s,SDW}}$. Furthermore, they observe at $T_{\mathrm{s,SDW}}$ a divergence of the reflectivity anisotropy normalized to the applied pressure. This behaviour is strikingly similar to resistivity measurements under tunable strain, indicating a nematic transition [25].

### Quantum criticality

In the proximity of an antiferromagnetic quantum critical point, spin fluctuations should be strong enough to modify the scattering process of quasiparticles and induce non-Fermi liquid behaviour. Optical measurements are in principle an ideal tool to get further insight into this topic: different conduction channels can be disentangled, uncovering the dc conductivity and scattering rate of coherent carriers.

In $Ba(Fe_{0.92}Co_{0.08})_2As_2$ and $Ba(Fe_{0.95}Ni_{0.05})_2As_2$, the normal state resistivity can be well fitted up to high temperatures with $R(T) \propto T^n$, using the exponents $n = 1.25$ and $n = 1.5$, respectively [128, 130]. However, a multi-component analysis by Wu *et al.* uncovered in both cases a "hidden" Fermi liquid behaviour $1/\sigma_{\mathrm{dc}}(T) \propto 1/\tau(T) \propto T^2$ of the narrow Drude, being masked by a temperature-independent incoherent background.

In contrast to those compounds, the resistivity in $Ba_{0.6}K_{0.4}Fe_2As_2$ is rather linear at low temperatures, but shows a tendency towards saturation above 175 K [161]. Here, Dai *et al.* concluded from a multi-component analysis that the incoherent background masks non-Fermi liquid behaviour of the narrow Drude ($1/\sigma_{\mathrm{dc}}(T) \propto 1/\tau(T) \propto T$), extending up to room temperature. This holds also for $BaFe_2(As_{0.7}P_{0.3})_2$. Most importantly, the authors demonstrated that the spectral weight at a certain cut-off frequency follows the same temperature-dependence as the inverse scattering rate, giving a model-independent proof of their findings.

As already mentioned in chapter 3.2.2, a diverging effective mass around the optimum substitution level was up to now only uncovered for $BaFe_2(As_{1-x}P_x)_2$, but not for Co doped compounds [83, 84]. Therefore, those on the first view contradictory results of Wu and Dai *et al.* could be another indication how sensitively the electronic properties of iron pnictides dependent on the substitution position. A model-independent spectral weight analysis on electron doped compounds could shed further light on this topic.

# 5

# MATERIALS AND METHODS

In this chapter, the basic concepts of Fourier-ransform Intfrared (FTIR) spectroscopy and Superconducting Quantum Interference Device (SQUID) magnetometry are introduced. As the corresponding setups used for the measurements in this thesis are either commercial machines or cryostats constructed in the framework of another thesis, the description concentrates on the main principles. The chapter concludes with an overview about the investigated samples.

## 5.1 FTIR spectroscopy

Fourier-transform spectroscopy is a powerful tool to study the electrodynamic properties of solids [113]. Instead of time-consuming frequency sweeps needed for example in conventional grating spectrometers, the energy resolution is gained via a Fourier transformation of interfered light. Today, this method is widely used in the infrared, as here light sources, beamsplitters, mirrors, filters, windows and detectors are available that cover a broad frequency range; the commercially available setups contain usually modifications of a Michelson interferometer (see Fig. 5.1).

In a conventional Michelson interferometer, monochromatic light is split into two approximately equal parts, which follow different beam paths, before they interfere again at the beamsplitter and pass (or get reflected by) a sample. The interference pattern depends on the optical path difference. By modulating the length of one of the light paths with

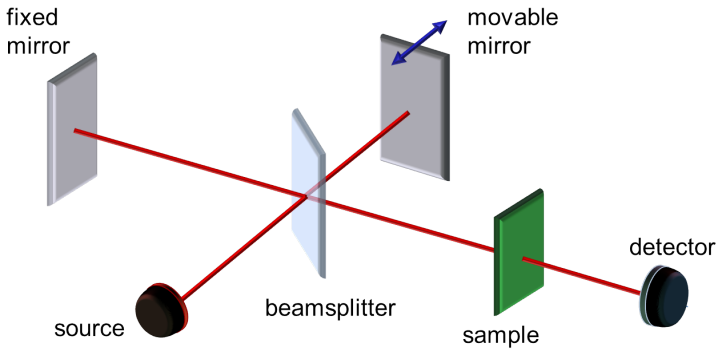


**Figure 5.1:** Schematic drawing of the beampath in a Michelson interferometer. Light from a source passes a semi-transparent beamsplitter; half of the light gets reflected by a fixed mirror, the other half by a movable one. After the reflection on these mirrors, the two beams meet again at the beamsplitter and interfere. The interfered light passes the sample (or gets reflected on it) and finally is collected by the detector that records the intensity dependent on the position of the movable mirror (*i.e.* on the optical path difference).

a movable mirror, one obtains the intensity as a function of mirror position; this spatial dependence can be translated to a frequency-dependence via Fourier transformation, no matter whether the light is mono- or polychromatic. This allows rapid recording of spectra over a broad energy range.

As an obtained spectrum contains both, information about the sample and the light source, one has to normalize it properly. For a transmission spectrum, this normalization is done by a comparison measurement without the sample; for a reflection spectrum, the response of a metallic mirror (usually gold, silver or aluminium) that possesses a reflection close to unity is taken.

In order to obtain reliable absolute values, one has to make sure that sample and reference have the same size and surface consistence. There are basically three widely used technical implementations in order to satisfy those requirements:

- The same size of sample and reference can be guaranteed by taking the same aperture in both measurements. This is commonly done for transmission measurements, as well as for reflection measurements on films or other homogeneous, rather flat and big samples.

- A microscope can be used to focus infrared light on very small, flat and homogeneous areas of both, sample and mirrors. The spot size is much smaller than the dimensions of sample and reference, guaranteeing the same amount of light hitting both specimens.

- Alternatively, after measuring the reflection of a sample, one can coat its surface in-situ with a thin gold layer, creating the corresponding "perfect" mirror with the same size and surface consistence; all measurements are then repeated on the gold coated samples (under the same experimental conditions). In order to account for any time-dependent influences (for example caused by source or detector), one can take additionally the spectrum of a standard reference mirror.

Table 5.1 summarizes which approaches were taken for the infrared reflection measurements performed in the framework of this thesis, as well as important technical parameters. Microscope measurements were carried out on a Bruker Vertex spectrometer with attached Hyperion microscope at the 1$^{st}$ Physical Institute, Stuttgart; gold evaporation measurements on a Bruker IFS 66v/s in the group of D. N. Basov at the UC San Diego. In gold evaporation measurements, the sample gets mounted point-like on a copper cone. This does not only avoid back-reflections from the sample holder, but also minimizes the glued area and thus induced strain on the sample, being important for the magnetic detwinnnig experiments described in chapter 9. The interesting temperature range between 15 K and 290 K was accessible by Helium flow cryostats; all cryostats were designed to contain a mechanically movable holder that allows precise positioning of sample and reference in the focus of the light (see Ref. [175] and [176] for the detailed designs).

| Range | Magnet | Technique | Detector | Beamsplitter | Source | Window |
|---|---|---|---|---|---|---|
| FFIR | no | gold | 1.6 K Bolometer | Mylar 23$\mu$m | Xenon | PP |
| FIR | no | gold | 4.2 K Bolometer | Mylar 6$\mu$m | Globar | PP |
| MIR | no | microscope | 77 K Photovoltaic | KBr | Globar | KBr |
| NIR | no | microscope | 77 K InSb | $CaF_2$ | Tungsten | KBr |
| FFIR | yes | gold | 1.6 K Bolometer | Mylar 23$\mu$m | Xenon | PP |
| FIR | yes | gold | 4.2 K Bolometer | Mylar 6$\mu$m | Globar | PP |
| MIR | yes | gold | 4.2 K Photovoltaic | KBr | Globar | PP |

**Table 5.1:** Technical parameters of the FTIR-measurements performed in the framework of this thesis for the different frequency ranges. One can distinguish between measurements with and without magnetic field, as well as measurements, where absolute values were obtained via in-situ gold evaporation or the availability of small spot sizes in a microscope setup. Furthermore, the used detectors, beamsplitters, sources and windows (PP: polypropylene) are given. One should note that the mid-infrared spectral range was not recorded by a conventional MCT-detector, as it displays strong non-linearity effects non-negligible in the case of high reflecting iron pnictides.

Fig. 5.2 displays the advanced design of the magneto-optical setup [177]. A helium flow cryostat is directly connected to a 9 T Oxford Spectromag, meaning that only one polypropylene window has to be transmitted in reflection measurements. This reduces

intensity losses caused by the window; however, this window can not be changed, meaning that most of the light in the mid-infrared frequency range gets absorbed. A linear translator allows the positioning of sample and reference mirror in the focus of the light, as well as the movement of the sample to the gold evaporation unit.

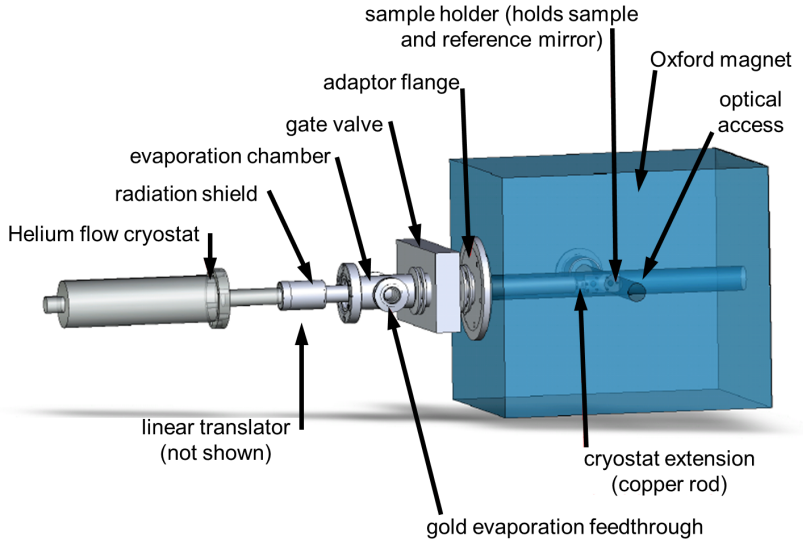


**Figure 5.2:** Magneto-optical setup as designed and constructed in the group of D. N. Basov, UC San Diego (adapted from Ref. [177]). A helium flow cryostat is directly connected to the vacuum chamber of a 9 T Oxford Spectromag magnet. A linear translator allows the positioning of sample and reference in the focus of the light, as well as the movement of the sample to the gold evaporation unit.

## 5.2 SQUID magnetometry

A Superconducting Quantum Interference Device is able to convert magnetic flux to a voltage with an extremely high sensitivity that reaches the quantum limit [2, 178]. It consists of a superconducting loop that is interrupted by one (rf or ac SQUID) or two (dc SQUID) Josephson junctions. In an external magnetic field, the combination of Josephson effect and flux quantization causes a voltage drop across the loop that varies periodically with the external field (if the bias current through the loop is fixed); the periodicity is one elemental flux quantum $\Phi_0$.

In order to enhance the sensitivity, the SQUID sensor is usually not directly exposed to the magnetic field that should be measured, but shielded from the environment. The magnetic field of interest is then inductively coupled to the SQUID via a flux transformer

that consists in the easiest case of a pickup coil (exposed to the environment) and an input coil (close to the SQUID). In order to avoid background signals, one can also use a gradiometer; it consists of coils wound in opposite directions. As a magnetic field rapidly decreases spatially, one can thus distinguish between local and distant magnetic field sources: while the latter induces equally, but opposite currents within the two coils, local fields of interest will cause a net signal.

### Magnetic Property Measurement System

Magnetization measurements performed in the framework of this thesis were obtained on a 7 T MPMS XL (Magnetic Property Measurement System) built by Quantum Design [91]. It consists of an rf SQUID sensor, protected by a superconducting shield that guarantees a stable environment. The detection coil is a second-order gradiometer, consisting of three sets of coils, where the outer coils are wound opposite to the inner ones. In the dc mode, the sample is moved through those detection coils, changing the flux. This flux change is then detected by the SQUID sensor; the overall output signal is the absolute magnetization in "emu" (electromagnetic unit), which is usually normalized to the mass of the sample.

Furthermore, one can also perform ac measurements, where a small ac drive magnetic field is applied. This causes a time-dependent moment in the sample that allows the measurement of the "dynamic susceptibility" without motion [179]. At very low frequencies, this quantity corresponds to the static susceptibility $\chi$ that can be extracted from the slope of field-dependent dc magnetization measurements. At higher frequencies, however, the signal might gain a phase shift $\varphi$. In this case, the susceptibility is conventionally described by the real and imaginary parts:

$$\chi' = \chi \cos\varphi \tag{5.1}$$

$$\chi'' = \chi \sin\varphi \tag{5.2}$$

where the imaginary component $\chi''$ indicates dissipative processes in the sample; those appear for example in ferromagnets, spin glasses or type II superconductors.

The MPMS includes computer controlled temperature and magnetic field stabilization; temperatures between 1.6 K and 400 K, as well as magnetic fields between -7 T and 7 T are accessible. In order to reveal hysteretic behaviour, special care has to be taken concerning the temperature and field setting mode [10]. When measuring at stabilized temperatures $T$, the stabilization process usually also includes oscillating around the target temperature and its duration depends on the setpoint temperature. For a material with time-dependent magnetization $M$, both lead to non-reproducibile $M(T)$ curves. Therefore, we typically

chose to sweep the temperature in $M(T)$ measurements[1]. For the field setting, the "oscillating mode" is the most accurate, as the magnetic field over- and undershoots the target value in cycles with decreasing relative amplitude in order to acquire an optimal result. However, for hysteretic samples one should take the "no overshoot" mode, meaning that the magnetic field is changed monotonously to the desired value.

Furthermore, one has to consider the effect of the remanent magnetization captured in the superconducting coils. Usually, we therefore determine the zero field by searching at temperatures above any hysteretic phase the magnetic field (in the range of a few G), which leads to zero signal at the SQUID. However, as the cooling process in a homogeneous zero field can be crucial (especially for superconductors), some measurements were also done using the Quantum Design "ultra low field" option which guarantees field nulling better than 0.05 G remanent field[2]. We did not find any qualitative difference of the magnetization compared to measurements with our standard procedure to determine the zero field.

Samples are typically mounted with the help of a plastic straw. In the case of low-signal measurements, the mounting should be as symmetric as possible around the sample in order to avoid that the background signal has a different center than the sample position; in this case, an asymmetric signal would be generated that can not be analysed by the MPMS software. For measurements with the magnetic field applied along the cleaved surface of a plate-like sample, the sample can be fixed between two stripes of plastic foil by wrapping Teflon tape around them. For the perpendicular direction, both halfs of a gelatine capsule are padded by Teflon tape or cotton to form a plateau where in between the sample can be placed. Both, plastic foil and gelatine capsule, can be sewed in the straw.

## 5.3 Investigated samples

In the framework of this thesis, several $EuFe_2(As_{1-x}P_x)_2$ high quality single crystals synthesized in the group of P. Gegenwart (University of Göttingen / Augsburg) by the Bridge-

1 Typical measurements take less than 10 s with the settings: 4 cm scan length, 2 scans per measurements and 24 points, *i.e.* for a temperature sweep with 0.2 K/min, the temperature error is less than 0.05 K and thus negligible (visible also in the absent thermal hysteresis in the paramagnetic regime). For ac measurements covering a big temperature range, we typically chose the sweep velocity 0.1 K/min, as here measurements usually are slower. With the parameters: 1 G drive amplitude, 7 Hz wave frequency, amplifier gain 1, 1 block to average, 1 scan per measurement and 1 s settling time, measurements are faster than 1 min, *i.e.* in this case the temperature error is less than 0.1 K.

2 Those measurements were performed in the group of R. Kremer, MPI FKF, Stuttgart

man method [230] were investigated by magnetization measurements (see chapter 7); Table 5.2 summarizes their compositions $x$ and masses $m$.

| $\boldsymbol{x}$ | 0 | 0.055 | 0.09 | 0.12 | 0.16 | 0.165 |
|---|---|---|---|---|---|---|
| $\boldsymbol{m}$(mg) | 6.1 | 9.7 | 0.45 | 1.1 | 2.3 | 7.0 |
| $\boldsymbol{x}$ | 0.17 | 0.26 | 0.35 | 0.39 | 1 | |
| $\boldsymbol{m}$(mg) | 1.2 | 0.44 | 0.59 | 4.0 | 0.16 | |

**Table 5.2:** Compositions $x$ and masses $m$ of $EuFe_2(As_{1-x}P_x)_2$ single crystals investigated in magnetization measurements (see chapter 7).

For optical measurements in the infrared frequency range (see chapter 8), further freshly cleaved $EuFe_2As_2$ and $BaFe_2As_2$ single crystals with shiny surfaces $> 1\,\mathrm{mm}^2$ were available; for terahertz measurements (see attachment A), thin $Ba(Fe_{1-x}Co_x)_2As_2$ films grown by pulsed laser deposition [180] were supplied by S. Haindl and K. Iida (IFW Dresden).

# 6

# EU BASED IRON PNICTIDES

$EuFe_2As_2$ is exceptional among the parent compounds of the iron pnictides, as it exhibits - additional to the Fe spin density wave - long-range magnetic order of the $Eu^{2+}$ local moments at low temperatures. Nevertheless, bulk superconductivity can be induced by mechanical pressure, isovalent substitution and by electron or hole doping. Thus, Eu based iron pnictides offer the extraordinary possibility to study the interplay of unconventional superconductivity, itinerant and local magnetism.

In this chapter, first the magnetic properties of $EuFe_2As_2$ are introduced. Their development under pressure, doping and Eu substitution are in the focus of the following discussion, providing a basis for a unified phase diagram which will be presented in chapter 7. Afterwards, the electronic properties of Eu based iron pnictides are reviewed, focusing on the influence of the $Eu^{2+}$ magnetic moments. Additionally, measurements on Eu 122 compounds that revealed important general properties for iron pnictides are shortly presented.

## 6.1 $EuFe_2As_2$

Measurements using a commercial SQUID magnetometer are ideal to get first insight into the magnetic properties of a material. The standard procedures commonly employed to Eu 122 iron pnictides are summarized in Table 6.1. One should note that further investigations

such as (resonant) x-ray scattering, Mössbauer studies and neutron diffraction[1] are usually needed to completely understand the magnetic ordering of such layered materials, in which often inter- and intralayer interactions compete, causing "exotic" types of magnetism.

| Measurement | Information |
|---|---|
| $M(T)$ at $T = T_{\mathrm{s,SDW}}$ | Feature at spin density wave transition. |
| $M(T)$ at $T > T_{\mathrm{Eu}}$ | Curie-Weiss fit provides information about the predominant magnetic interactions between $Eu^{2+}$ spins and the valency of Eu. |
| $M(T)$ and $M(H)$ at $T \leq T_{\mathrm{Eu}}$ | Shape of curves provides information about the ordering. |
| $M(T)$ at $T = T_{\mathrm{Eu}}$ | $T_{\mathrm{Eu}}$ shifts with increasing field to lower temperatures for antiferromagnetic order, to higher temperatures for ferromagnetism. |
| $M(T)$ at $T < T_{\mathrm{Eu}}$ | Hysteresis often results from ferromagnetism, spin glass behaviour or superconductivity. |
| $M(H)$ at $T < T_{\mathrm{Eu}}$ | Saturated moment gives evidence about the Eu valency. |

**Table 6.1:** Summary of standard procedures to get information about the magnetism in Eu 122 iron pnictides from temperature- ($T$) and field- ($H$) dependent magnetization ($M$) measurements.

Combined magnetization and Mössbauer studies revealed already in 1993 that $EuFe_2As_2$ exhibits two magnetic transitions: an itinerant ordering in the Fe subsystem at $\sim 190\,\mathrm{K}$ is followed at lower temperatures ($\sim 19\,\mathrm{K}$) by the local ordering of magnetic $Eu^{2+}$ moments [216]. The itinerant order can be identified as a spin density wave that is accompanied by a tetragonal-to-orthorhombic structural phase transition [26]. Resistivity and specific heat show only one sharp feature at $T_{\mathrm{s,SDW}}$, indicating a first-order transition similar to $SrFe_2As_2$ (see Fig. 6.1a-b, [27, 28, 181]). The spin density wave is also visible as a jump in the magnetization (see Fig. 6.1c, [182]). However, as divalent $Eu^{2+}$ magnetic moments ($S = 7/2, L = 0$) dominate the magnetization, usually a paramagnetic background has to be subtracted before identifying the tiny feature.

Below $T_{\mathrm{Eu}} \sim 19\,\mathrm{K}$, the temperature-dependent magnetization is basically constant along the $c$-axis, while a clear cusp appears for magnetic fields applied in the $ab$-plane (see Fig. 6.1d-e). Both evidences antiferromagnetic behaviour. However, the Curie-Weiss fit indicates predominant ferromagnetic interactions among the $Eu^{2+}$ spins [28, 182, 216]. Therefore, in analogy to other layered systems, $A$-type antiferromagnetism was proposed, meaning that spins order ferromagnetically within the $ab$-plane plane, but neighbouring layers are coupled antiferromagnetically. This suggestion was confirmed by neutron and

1 Unfortunately, Eu is a strong neutron absorber, complicating those investigations [8].

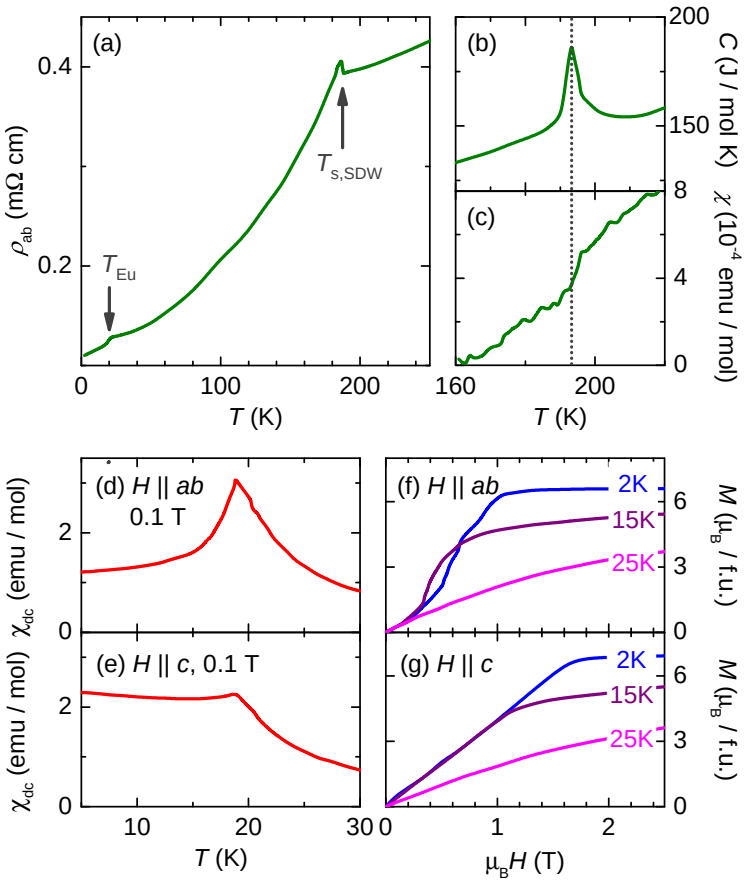


**Figure 6.1:** Standard characterization measurements on $EuFe_2As_2$. (a) The resistivity $\rho_{ab}(T)$ shows kinks at $T_{s,SDW}$ and $T_{Eu}$ [224]. (b) While the specific heat $C(T)$ exhibits a pronounced peak at $T_{s,SDW}$, (c) for magnetization measurements the paramagnetic background first has to be extracted to identify a tiny feature caused by the spin density wave transition [28]. (d) The temperature-dependent dc susceptibility $\chi_{dc}(T) = M(T)/\mu_0 H$ shows for an in-plane magnetic field ($H \parallel ab$) a cusp at $T_{Eu}$ and (e) flattens at $T < T_{Eu}$ for $H \parallel c$. Both is typical for an antiferromagnet with the easy axis in the $ab$-plane. (f) At 2 K (blue line), $M(H)$ saturates for $H \parallel ab$ at $\sim 1.0$ T, (g) for $H \parallel c$ at $\sim 1.6$ T. The saturation fields increase for 15 K (purple line) and 25 K (magenta line). A step-like increase for $H \parallel ab$ indicates a spin-flip or flop (also called "metamagnetic transition"), which is typical for an antiferromagnet [182].

resonant x-ray diffraction measurements [8, 183, 189]; the detailed magnetic structure of $EuFe_2As_2$ is shown in Fig. 6.2. Both, itinerant Fe and local $Eu^{2+}$ order are commensurate, with the spins pointing parallel or antiparallel along the $a$-axis, consistent with theoretical predictions [181]. One should note that Mössbauer and magnetic torque measurements indicate a slight canting ($\sim 10°$) of the $Eu^{2+}$ moments out of the $ab$-plane [234, 253], which was not observed by neutron and resonant x-ray measurements [8, 183, 189, 195]. While the $Eu^{2+}$ magnetic order is already suppressed at fields of only $\sim 1$ T [7], the spin density wave is still robust in pulsed magnetic fields of 55 T [190].

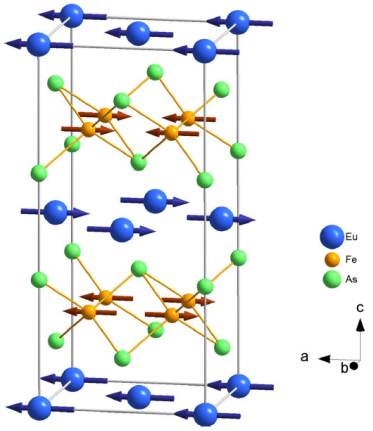


**Figure 6.2:** Magnetic structure of $EuFe_2As_2$ at 2.5 K [8]. $Fe^{2+}$ moments (brown arrows) align antiferromagnetically along the *a*- and the *c*-axis, but ferromagnetically along the *b*-axis. $Eu^{2+}$ moments (blue arrows) align within one Eu layer ferromagnetically along the *a*-axis, and neighbouring *ab*-planes are coupled antiferromagnetically.

Table 6.2 summarizes the magnetic properties of related compounds that are located at the "end" of Eu 122 phase diagrams. Only $EuFe_2As_2$ exhibits a spin density wave transition. Furthermore, the $Eu^{2+}$ magnetic order varies tremendously among the different compounds, although Eu is in all cases divalent[1]. The origin of the huge diversity of different phases is quite simple: as different layers are too far separated for a direct overlap of the Eu $4f$-orbitals, the magnetic interactions are probably mediated via conduction electrons by the indirect RKKY-exchange [36]. However, this indirect coupling oscillates between ferro- and antiferromagnetic regimes depending on the details of the Fermi surface. Theoretical calculations by Akbari *et al.* revealed even an influence of the spin density wave on the RKKY-exchange (see also chapter 7.1, [11, 219]). Thus, when passing through the Eu 122 phase diagrams, strong changes in the $Eu^{2+}$ magnetic order can be expected.

| Compound | $T_{Eu}$ | Weiss | Proposed order | Direction | Ref. |
|---|---|---|---|---|---|
| $EuFe_2As_2$ | 19 K | FM | *A*-type AFM | *a*-axis | [8, 216] |
| $EuFe_2P_2$ | 29 K | FM | FM | *c*-axis | [210, 211] |
| $EuRu_2As_2$ | 17 K | FM | FM | *c*-axis | [215] |
| $EuCo_2As_2$ | 39 K | FM | *A*-type AFM vs. helical | *ab*-plane vs. almost along *c*-axis | [214, 251] |
| $EuNi_2As_2$ | 14 K | AFM | | | [216] |

**Table 6.2:** Characteristic information about the $Eu^{2+}$ magnetism in Eu 122 parent compounds: magnetic ordering temperature $T_{Eu}$, predominant spin exchange given by the sign of the Curie or Néel temperature, proposed order and spin direction.

1 In the case of $EuCo_2P_2$ and $EuRh_2As_2$, mixed Eu valencies between 2 and 3 appear [217, 218]. For both, incommensurate helimagnetism was observed. Bandstructure calculations indicate a strong sensitivity of the magnetic configuration on the Eu valency [218].

## 6.2 Phase diagrams

In order to compare several compounds, the transition temperatures are consistently determined as followed: superconductivity is defined by its onset and the zero resistivity temperature, $T_{c,on}$ and $T_{c,0}$, respectively. The $Eu^{2+}$ magnetic ordering temperature $T_{Eu}$ corresponds to a kink in resistivity and a peak in magnetization measurements. Standard measurements on Eu 122 pnictides often do not show clearly distinguishable features that would allow a distinct separation of structural and spin density wave transition temperatures. Thus, for the sake of simplicity, those transitions will be treated as one and referred to as $T_{s,SDW}$.

### 6.2.1 Pressurized systems

In the case of isovalent substitution, a certain element is replaced by a smaller (larger) one to shrink (expand) the unit cell similar to applied mechanical pressure. However, one should keep in mind that even isovalent substitution induces additional chemical disorder. It is still under debate, whether such disorder could be the actual tuning parameter through the iron pnictide phase diagrams [68].

#### Mechanical pressure

In 2009, Miclea *et al.* reported that pressures around 2 GPa induce in $EuFe_2As_2$ superconductivity up to $\sim 30$ K [29]. However, zero resistivity was prohibited by a re-entrance of resistivity at the $Eu^{2+}$ magnetic ordering temperature (see Fig. 6.3a). Detailed investigations by Matsubayashi and Kurita *et al.* revealed that bulk superconductivity is achieved only if hydrostatic pressure is transmitted ([222, 224], see Fig. 6.3b), reconciling several pressure studies [188, 220, 221, 223, 225–229, 232].

Fig. 6.4 displays the phase diagram of $EuFe_2As_2$ under hydrostatic pressure [222, 224]. At low pressures, the spin density wave gets continuously suppressed and the $Eu^{2+}$ magnetic ordering temperature increases slightly (see also Fig. 6.3c). Around $\sim$2 GPa, $T_{Eu}$ starts to rise strongly. Surprisingly, this change in $Eu^{2+}$ magnetism coincides with the pressure, where the onset of superconductivity - without reaching zero resistance - can be observed. Thus, in a narrow pressure range, $Eu^{2+}$ magnetism, spin density wave order and traces of superconductivity coexist. Zero resistance and bulk superconductivity occurs only between $\sim 2.5 - 3$ GPa. It disappears as soon as the $Eu^{2+}$ magnetic ordering temperature is as high as $T_{c,on}$.

Magnetization measurements indicate that *A*-type antiferromagnetic $Eu^{2+}$ order coexists with superconductivity. Above $\sim 6$ GPa, a ferromagnetic signal is observed, visible in a clear out-of-phase signal of the ac susceptibility (see Fig. 6.3d, [222]). $T_{Eu}$ increases fur-

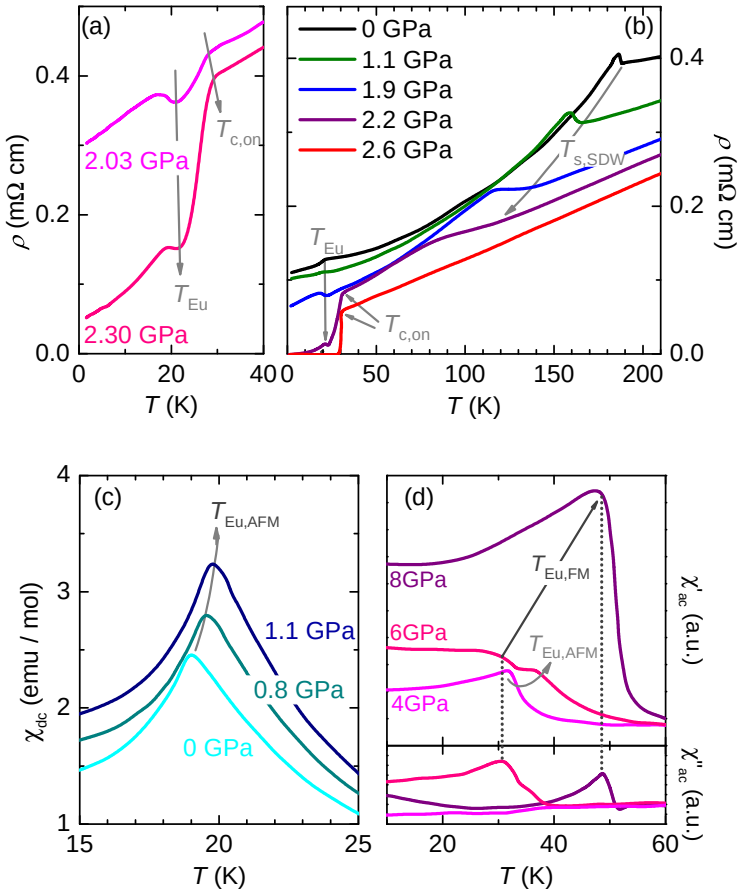


**Figure 6.3:** Characteristic temperature-dependent in-plane resistivity and magnetization of $EuFe_2As_2$ under pressure. Grey arrows highlight the development of the transition temperatures with pressure. (a) Using silicone oil as pressure transmitter, superconductivity sets in at $T_{c,on} \sim 30\,K$, but due to a resistivity re-entrance at $T_{Eu}$, zero resistivity is not achieved [29]. (b) Using Daphne 7474 as transmitting medium, $T_{s,SDW}$ is continuously suppressed with pressure. Around 2.6 GPa, zero resistance without re-entrance and non-Fermi liquid behavior ($R(T) \sim T$ for $T > T_c$) is observed [224]. (c) DC susceptibility: at low pressures, $T_{Eu}$ increases slightly. The cusp is typical for antiferromagnetic order [222]. (d) AC susceptibility: antiferromagnetism does not induce an out-of-phase signal ($\chi'' \approx 0$ at 4 GPa). However, at $\sim 6\,GPa$ a second feature appears with $\chi'' > 0$ that strongly shifts to higher temperature and gets dominant with increasing pressure. The strong out-of-phase signal is typical for ferromagnetism [222].

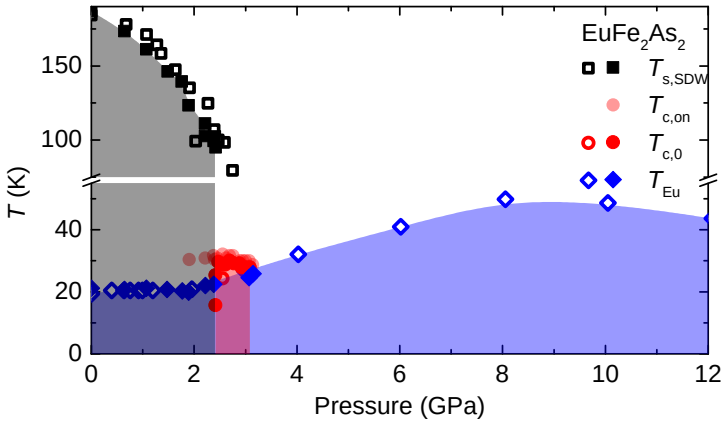


**Figure 6.4:** Phase diagram of $EuFe_2As_2$ under pressure (open symbols: Ref. [222], closed symbols: Ref. [224]). $T_{Eu}$ (blue diamonds) slightly increases at low pressures and starts to rise stronger just before $T_{s,SDW}$ (black squares) gets suppressed and the superconducting dome is positioned ($T_{c,on}$: light red circles, $T_{c,0}$: red circles).

ther up to pressures around 10 GPa, where a collapsed tetragonal phase transition takes place [221, 223]. As the ionic radius of $Eu^{2+}$ is larger than that of $Eu^{3+}$, this structural phase transition coincides with an increase of the Eu valency. As trivalent Eu is nonmagnetic, $T_{Eu}$ decreases for higher pressures [222].

### Isovalent substitution: $EuFe_2(As_{1-x}P_x)_2$

In 2009, Ren *et al.* discovered in $EuFe_2(As_{0.7}P_{0.3})_2$ superconductivity that sets in at $\sim$ 26 K and coexists with $Eu^{2+}$ ferromagnetism below $\sim$ 20 K [30]. Both transitions are visible in the specific heat, proving their bulk character. This observation attracted tremendous interest in the condensed matter community, as superconductivity and ferromagnetism are usually antagonistic phenomena (see chapter 3.3) and "chemical" pressure was discovered as a tuning parameter through the iron pnictide phase diagram.

It turned out that the electronic properties of $EuFe_2(As_{1-x}P_x)_2$ are extremely sensitive to the synthesis, possibly due to procedure-dependent internal strain: for single crystals grown by the Bridgeman method, the superconducting dome appears around $x \sim 0.2$ [9, 10, 230, 233, 235, 238, 240, 241, 272, 280], while for polycrystals as well as single crystals grown by solid state reaction the dome is shifted to $x \sim 0.3$ [30, 231, 232, 234, 236, 237, 243]. However, the $Eu^{2+}$ magnetic order is not affected by the growth process. Fig. 6.5 compares the resulting phase diagrams, which resemble a lot $EuFe_2As_2$ under pressure. Most remarkably, $T_{Eu}$ starts to increase above $x \sim 0.12$, which again coincides with the onset of superconductivity. This reveals a significant interplay between electronic and magnetic properties in those compounds.

However, in contrast to $EuFe_2As_2$ under pressure, $T_{Eu}$ decreases at lower substitution levels. It is intriguing to assign the minimum around $x \sim 0.12$ to the change from anti- to ferromagnetic $Eu^{2+}$ ordering, as signatures of ferromagnetism are observed at high substitution levels, consistent also with theoretical calculations [207, 239]. However, several measurements indicated antiferromagnetic $Eu^{2+}$ order up to significantly higher P concentrations [230, 243]. Furthermore, even results for the pure P compound are contradictory: while Mössbauer and magnetization measurements indicate a successive helical ordering around 26 K with the spins tilted 15 ° from the $c$-axis, neutron measurements state pure ferromagnetism. It should be noted that indications for successive magnetic orderings were also reported for mixed compounds [232, 234, 236, 237, 243]; in Ref. [242], the lower transition was attributed to a minority phase. One contribution of this thesis was to reconcile those - on the first view contradictory - reports (see Table 6.3), which is presented in more detail in chapter 7, as well as in Ref. [9] and [10].

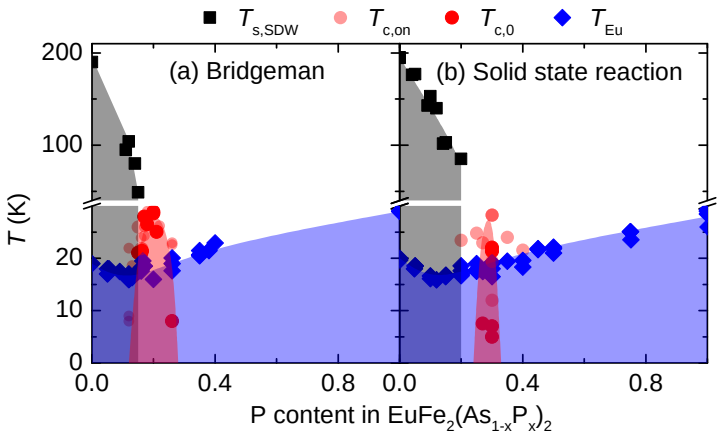


**Figure 6.5:** Phase Diagram of $EuFe_2(As_{1-x}P_x)_2$ for samples grown by (a) the Bridgeman method [9, 10, 230, 233, 235, 238, 240, 241, 272, 280] and (b) solid state reaction [30, 231, 234, 236, 237]. In both cases, $T_{Eu}$ (blue diamonds) shows a minimum around $x \sim 0.12$. This minimum is close to the composition, where $T_{s,SDW}$ gets suppressed (black squares) and superconductivity sets in ($T_{c,on}$: light red circles, $T_{c,0}$: red circles).

### Isovalent substitution: $Eu(Fe_{1-x}Ru_x)_2As_2$

An alternative way of isovalent substitution is the replacement of Fe by Ru. It should be noted that Ru influences the volume of the unit cell much less than P substitution [246]. Nevertheless, $Eu(Fe_{1-x}Ru_x)_2As_2$ also shows bulk superconductivity in a narrow range around $x \sim 0.2$ (see Fig. 6.6, [31, 245]). However, the onset of superconductivity can be observed at least up to $x = 0.55$, which is in stark contrast to the mechanically pressurized or P substituted case. One obvious difference to those systems is that the

| Technique | Sample | Observation | $Eu^{2+}$ | Ref. |
|---|---|---|---|---|
| Specific heat | Poly | Increasing magnetic field broadens and shifts anomaly to higher temperatures. | FM | [30] |
| Magnetic compton scattering | Poly | Enhanced spin polarization of the Fe-3$d$ orbital. | FM | [231] |
| Mössbauer | Poly | Increased Eu hyperfine field, $Eu^{2+}$ spins almost aligned along $c$-axis (20° tilted). | FM | [234] |
| Neutron | Single | No antiferromagnetic reflections, $Eu^{2+}$ spins aligned along $c$-axis. | FM | [241] |
| Neutron | Single | $Eu^{2+}$ spins aligned along $c$-axis, minority phase with lower ordering temperature. | FM | [242] |
| Magnetization | Single | Shape and field-dependence of magnetization. | AFM | [230, 243] |
| Muon, Mössbauer | Single | $Eu^{2+}$ spins almost aligned along $c$-axis (12° tilted). | AFM | [243] |

**Table 6.3:** Arguments for $Eu^{2+}$ ferromagnetism (FM) vs. antiferromagnetism (AFM) in superconducting $EuFe_2(As_{1-x}P_x)_2$ polycrystalline samples (poly) or single crystals (single).

$Eu^{2+}$ magnetic ordering temperatures of $EuFe_2As_2$ and $EuRu_2As_2$ are quite similar and therefore, $T_{Eu}$ basically stays constant in the whole phase diagram. Thus, it is intriguing to conclude that superconductivity gets suppressed, if the $Eu^{2+}$ magnetic ordering exceeds $T_c$. However, this conclusion does not explain why $Eu(Fe_{1-x}Ru_x)_2As_2$ exhibits bulk superconductivity only in a very narrow range.

Despite the lower ordering temperatures than in the case of $EuFe_2P_2$, $EuRu_2As_2$ is also suggested to order ferromagnetically along the $c$-axis (see Table 6.2). Therefore, it is not surprising that for $Eu(Fe_{1-x}Ru_x)_2As_2$, successive anti- and ferromagnetic transitions were observed [31, 245], too, and Mössbauer studies on a superconducting sample indicate a reorientation of the $Eu^{2+}$ spins towards the $c$-axis [31].

### Mechanical vs. chemical pressure

In order to compare the influence of mechanical and chemical pressure, Sun and Tokiwa *et al.* investigated $EuFe_2As_2$ and $EuFe_2(As_{1-x}P_x)_2$ under pressure, concluding that the

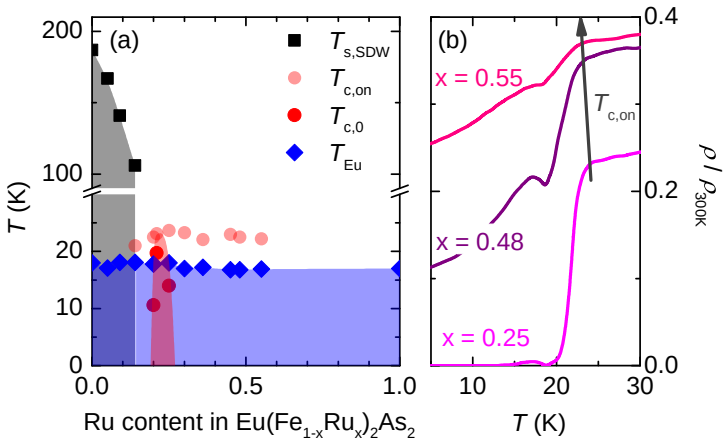


**Figure 6.6:** (a) Phase diagram of $Eu(Fe_{1-x}Ru_x)_2As_2$ [245]. $T_{Eu}$ (blue diamonds) stays almost constant. Superconductivity sets in (light red circles), as soon as $T_{s,SDW}$ (black squares) is suppressed. While zero resistivity (red circles) is achieved only around $x \sim 0.2$, traces of superconductivity exist up to $x = 0.55$, (b) visible in resistivity measurements for $x = 0.25$ (magenta line), 0.48 (purple line) and 0.55 (pink line), which also exhibit a resistivity re-entrance at $T_{Eu}$.

overall behaviour is very similar [232, 238][1]. However, when incorporating also the $Eu^{2+}$ magnetic order in the phase diagram, as it is done in Fig. 6.7, it gets obvious that the actual processes are more complex: choosing the equivalent pressure for complete P substitution $x \mathrel{\hat{=}} 15.4\,\mathrm{GPa}$, one can map reasonable well the electronic properties on top of each other, however, not the $Eu^{2+}$ magnetic ordering temperature. Moreover, when comparing the influence on the crystallographic $c$- and $a$-axes (see Fig. 6.8), mechanical pressure compresses the $c$-axis significantly stronger than P substitution if one uses the above chosen equivalent. Thus, assuming that isovalent substitution just acts as chemical pressure is clearly oversimplified: actually superconductivity is induced much faster compared to mechanical pressure. The most plausible scenario is that the disorder induced by isovalent substitution causes the differences in the phase diagram. Disorder could also weaken the RKKY-exchange, explaining why $T_{Eu}$ first decreases in $EuFe_2(As_{1-x}P_x)_2$.

1 Sun *et al.* proposed that a pressure-induced valence change of Eu sets in already at the left side of the superconducting dome for both, $EuFe_2As_2$ under mechanical pressure and $EuFe_2(As_{1-x}P_x)_2$ [232]. This could lead to additional electron doping, possibly even favouring superconductivity. However, previous Mössbauer studies on superconducting $EuFe_2(As_{0.7}P_{0.3})_2$ did not reveal any $Eu^{3+}$ foreign phase [243] and Matsubayashi *et al.* [222] revealed valency changes in $EuFe_2As_2$ only at much higher pressures. Intriguingly, changes in the valency are reported in both cases close to the solidification of the pressure transmitting medium. It is not clear how this should induce a measurement error, nevertheless further investigations are necessary to clarify this issue.

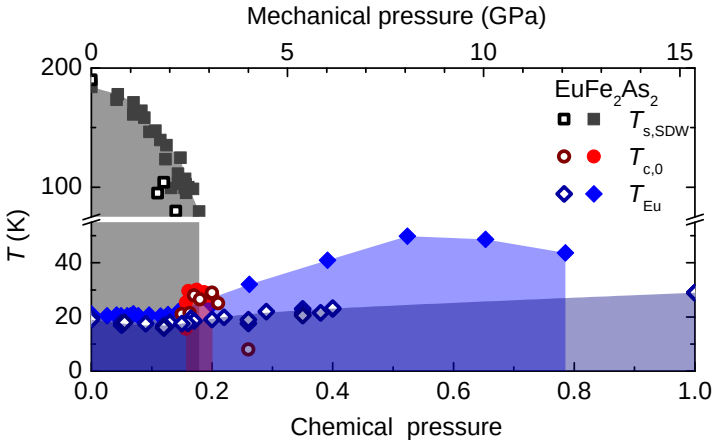


**Figure 6.7:** Phase diagrams of $EuFe_2As_2$ single crystals under chemical (P substitution, open dark symbols, [9, 10, 230, 233, 235, 238, 240, 241, 272, 280]) and mechanical pressure (closed bright symbols, [222, 224]) mapped on top of each other, using the relation: P substitution $x \hat{=} 15.4\,\mathrm{GPa}$. While the electronic properties are quite similar, $T_{\mathrm{Eu}}$ (blue diamonds) develops differently. However, in both cases $T_{\mathrm{Eu}}$ starts to increase stronger close to the pressure, where $T_{\mathrm{s,SDW}}$ (black squares) gets suppressed and superconductivity appears ($T_{\mathrm{c,0}}$: red circles).

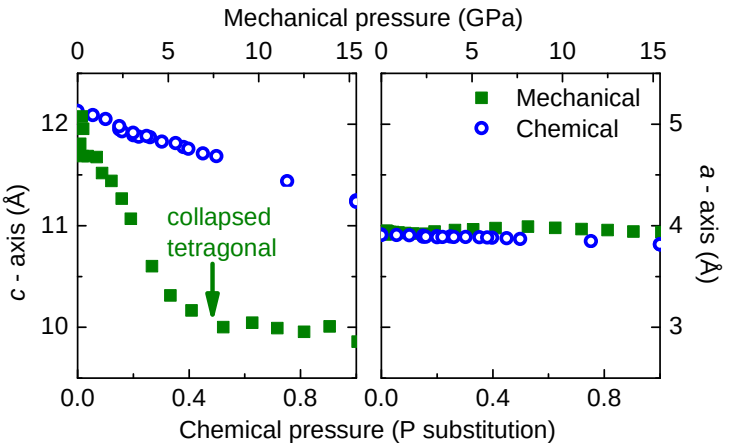


**Figure 6.8:** Crystallographic $c$-axis (left) and $a$-axis (right) of $EuFe_2As_2$ under chemical (P substitution, blue open points, [230, 236]) and mechanical pressure (green squares, [221]). Using the equivalent: P substitution $x \hat{=} 15.4\,\mathrm{GPa}$ that maps the electronic properties on top of each other, reveals that mechanical pressure contracts the $c$-axis much stronger than P substitution.

**Summary**

In summary, when comparing the phase diagram of mechanically pressurized $EuFe_2As_2$ with those of $EuFe_2(As_{1-x}P_x)_2$ and $Eu(Fe_{1-x}Ru_x)_2As_2$, we can conclude for the interplay of superconductivity and magnetism:

- Microscopic coexistence of spin density wave ordering and superconductivity was yet not evidenced.
- $T_{Eu}$ does not behave universal. However, for mechanically pressurized $EuFe_2As_2$ and $EuFe_2(As_{1-x}P_x)_2$, it increases strongly as soon as the spin density wave is suppressed and superconductivity sets in.
- Considering only bulk superconductivity, the superconducting dome is rather narrow in all cases. For mechanical pressure and P substitution, superconductivity is suppressed as soon as $T_{Eu} \approx T_{c,on}$.
- In all phase diagrams, the $Eu^{2+}$ magnetic order changes with substitution. However, contradictory reports exist which kind of magnetism coexists with superconductivity.

### 6.2.2 Electron doping

In the case of 122 iron pnictides, electron doping can be realized by the substitution of Fe by an atom that prefers a lower valence state. Indeed, superconductivity up to $\sim 25\,K$ was found in Co doped $BaFe_2As_2$ [247]. However, similar approaches were much less successful for Eu based 122 iron pnictides.

#### $Eu(Fe_{1-x}Co_x)_2As_2$

In 2009, Jiang *et al.* presented results on $Eu(Fe_{0.89}Co_{0.11})_2As_2$ single crystals grown by using (Fe,Co)As as self-flux, which showed the onset of superconductivity at $\sim 21\,K$ [32]. However, with this synthesis technique only polycrystals where produced that exhibit zero resistivity at low temperatures [249], but no single crystals [248–251, 258, 260].[1] The synthesis of single crystals with zero resistance could be achieved only by using Sn-flux, however, with very low transition temperatures (significantly below 10 K) [252–257, 259]. Fig. 6.9 compares the resulting phase diagrams[2]. One should note that here, the growth

1 Chen *et al.* argued that in their polycrystals, the coupling between conduction electrons and local $Eu^{2+}$ moments is reduced, visible in resistivity measurements with less obvious features at $T_{Eu}$ and the absence of re-entrant superconductivity [249].

2 Only the study by Ying *et al.* [248] does not fit to the others. The reason is probably that only nominal sample compositions are given. Due to this uncertainty, it is excluded from the further discussions.

technique influences all properties, also the $Eu^{2+}$ magnetic transition. In both cases, the $Eu^{2+}$ magnetic ordering temperature shows a minimum, where structural as well as spin density wave gets suppressed and the rather narrow superconducting dome is positioned around this composition. Mössbauer experiments on superconducting compounds indicate that the spin density wave does not take place in the whole sample volume [254]. Thus, again rather phase separation than microscopic coexistence of superconductivity and itinerant Fe magnetism is observed.

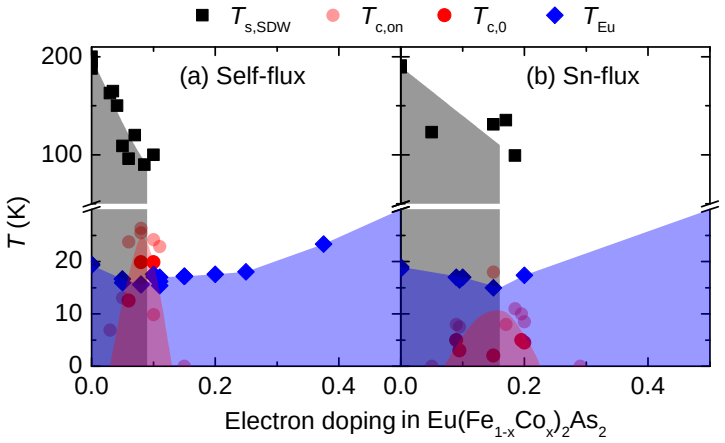


**Figure 6.9:** Phase diagram of $Eu(Fe_{1-x}Co_x)_2As_2$ samples grown using (a) self-flux [249–251, 258, 260] and (b) Sn-flux [252–257, 259]. In both cases, the $Eu^{2+}$ magnetic ordering temperature (blue diamonds) shows a minimum around the composition, where $T_{s,SDW}$ (black squares) gets suppressed and the superconducting dome is positioned ($T_{c,on}$: light red circles, $T_{c,0}$: light red circles). Zero resistivity for self-flux grown samples was only observed in polycrystalline samples [249].

More similarities to mechanically pressurized and isovalently substituted $EuFe_2As_2$ can be found when comparing the evolution of $Eu^{2+}$ magnetic order throughout the phase diagram: as soon as the spin density wave gets suppressed, the $Eu^{2+}$ spins cant more and more out of the *ab*-plane. Although magnetization measurements show up to high Co contents indications for antiferromagnetic interlayer coupling (often interpreted in terms of canted antiferromagnetism [253, 254, 257] or helimagnetism [32, 251]) and multiple magnetic transitions [250, 251, 256, 257], neutron diffraction measurements on a superconducting sample concluded ferromagnetic ordering along the *c*-direction with a moment size of $6.2\,\mu_B$, slightly lower than the theoretical expected value of $\sim 7\,\mu_B$. Those contradictory reports get even more mysterious, when considering that $EuCo_2As_2$ shows very similar magnetic behaviour to $EuFe_2As_2$: even signatures of a metamagnetic transition were observed in $M(H)$-curves around $\sim 3\,T$ [214].

### $Eu(Fe_{1-x}Ni_x)_2As_2$

Surprisingly, Ni substitution on the Fe site does not induce superconductivity at all [251, 261, 262]. Mössbauer measurements on doped compounds reveal a canting of the $Eu^{2+}$ spins out of the *ab*-plane and multiple magnetic transitions appear that were interpreted in terms of a crossover from anti- to ferromagnetism. Ren *et al.* concluded that this ferromagnetism suppresses superconductivity [261]. However, this argumentation has two weak points: first of all, the end member $EuNi_2As_2$ is antiferromagnetic, and not ferromagnetic [216]. Secondly, when comparing the development of $T_{Eu}$ and $T_{s,SDW}$ for Co and Ni, both can be mapped perfectly on top of each other at low doping level[1] (see Fig. 6.10).

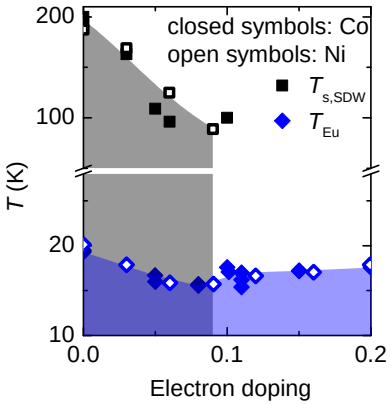


**Figure 6.10:** Phase diagram of $Eu(Fe_{1-x}Y_x)_2As_2$ with Y = Co [249, 258] (closed symbols) or Ni [261] (open symbols). The *x*-axis of the Ni phase diagram was expanded by a factor of two, as Ni can provide twice as much electrons as Co. $T_{Eu}$ (blue diamonds) and $T_{s,SDW}$ (black squares) perfectly match.

### $Eu(Fe_{1-x}Ir_x)_2As_2$

Up to now, the most "successful" approach to induce superconductivity by electron doping has turned out to be Ir substitution [33, 263, 264]. In 2013, Paramanik *et al.* reported for $Eu(Fe_{0.86}Ir_{0.14})_2As_2$ polycrystals an onset of superconductivity at 22.6 K and zero-resistivity as well as diamagnetic shielding at 19 K, which is disturbed by a resistivity re-entrance due to $Eu^{2+}$ magnetic ordering around 14 K [33]. Only two months later, Jiao *et al.* published results on $Eu(Fe_{0.88}Ir_{0.12})_2As_2$ single crystals with a sharp superconducting transition between 22 K and 21 K (without any resistivity re-entrance) [263]. Both groups proposed a canting of the $Eu^{2+}$ spins out of the *ab*-plane. However, whereas the first group suggested canted *A*-type antiferromagnetic ordering of $Eu^{2+}$, the latter favoured a ferromagnetic ordering.

1 In order to compare them correctly, one has to consider that Ni substitution provides two electrons per substituent, whereas Co provides only one. Thus, the *x*-scale of the Ni phase diagram should be expanded by a factor of two. Indeed, it is quite surprising that the mapping works out so well, as the end members of the phase diagrams, $EuNi_2As_2$ and $EuCo_2As_2$, have quite different $Eu^{2+}$ magnetic ordering temperatures (see Table 6.2).

#### Summary

Summing up, electron doping induces superconductivity in $EuFe_2As_2$ when substituting Fe by Co or Ir. While in the latter case, zero resistivity and a clear diamagnetic shielding was observed around 20 K, the results for Co doping are less convincing: the diamagnetic shielding is significantly lower and the phase diagram strongly depends on the growth technique. Ni substitution does not induce superconductivity at all, although $T_{s,SDW}$ and $T_{Eu}$ show exactly the same behaviour as for Co doping.

When comparing electron doping to isovalent substitution and mechanical pressure, the overall behaviour is very similar: superconductivity probably does not coexist with the spin density wave order on a microscopic scale and $T_{Eu}$ shows an almost identical behaviour as in the case of P substitution. The reports about the type of $Eu^{2+}$ magnetic order are as contradictory as for isovalent substitution. Despite those similarities, one new aspect concerning the interplay of superconductivity and magnetism should be emphasized: the results for Co doping clearly show that superconductivity with zero resistivity can appear, even when the onset temperature is much lower than $T_{Eu}$. Thus, one could speculate that superconductivity is only suppressed by the $Eu^{2+}$ magnetic order, if the two antagonistic phenomena would like to set in at similar temperatures. This might happen for Ni substitution, as Ni doping usually leads to slightly lower critical temperatures than Co [247, 265].

### 6.2.3 Eu dilution

Chemical substitution at the Eu site does not only act as doping or isovalent pressure, it also weakens the $Eu^{2+}$ magnetism. Up to now, poly- and single crystals were successfully grown for Ca, Sr, Ba, K, Na and La substitution: Ca, Sr and Ba are isovalent substitutions; K and Na substitution leads to hole doping, La to electron doping. In some cases, those approaches were further combined with physical pressure or additional substitutions at another element site ("codoping"). Unfortunately, although the magnetic and superconducting properties are directly linked to each other, detailed studies on the evolution of the $Eu^{2+}$ magnetism dependent on dilution level are still rare.

#### Isovalent substitution

Isovalent substitution on the Eu site is not expected to induce superconductivity, as corresponding 122 parent compounds exhibit "only" structural as well as spin density wave transitions. Those appear for Ca, Eu, Sr and Ba approximately at 170 K, 190 K, 205 K and 140 K, respectively [5]. One should note that the transition temperatures do not just

follow the ionic radii, which are increasing from Ca to Ba [66].[1] Thus, only Ca substitution will induce positive chemical pressure and shrink the unit cell volume, while Ba and Sr will have the opposite effect.

The dilution effect on the local $Eu^{2+}$ magnetic order can be summarized as followed:

- As expected, Ba substitution continuously suppresses $T_{s,SDW}$ [269]. While the lowest detectable $T_{Eu} = 0.5\,K$ was found for $x = 0.45$, all samples with higher Ba content (except $BaFe_2As_2$) still show at low temperatures an enhanced response of the specific heat. This indicates that $Eu^{2+}$ magnetic moments significantly influence the material's properties even at very high dilution levels.

- In the case of Ca substitution, the $Eu^{2+}$ magnetic transition is completely suppressed at $x = 0.75$, but for 50 % dilution still as high as 9 K [267, 268]. Additional physical pressure on $Eu_{0.5}Ca_{0.5}Fe_2As_2$ induces superconductivity with a maximum $T_c$ of 24 K and possibly a coexistence region of spin density wave ordering, local $Eu^{2+}$ magnetism and superconductivity (around $\sim 1.4\,GPa$).

- Several studies investigated the superconductivity in Sr diluted samples with additional 11-14 % Co-doping [270–274]. While $Eu(Fe_{1-x}Co_x)_2As_2$ often only shows traces of superconductivity, in Eu diluted specimen bulk superconductivity was observed up to 15 K. It was suggested that superconductivity disappears as soon as $T_c < T_{Eu}$ (see Fig. 6.11, [271]). Specific heat measurements under external magnetic fields showed that an antiferromagnetic $Eu^{2+}$ order at 2 K persists up to a Eu dilution of as high as 80 % [273].

Thus, the $Eu^{2+}$ magnetism in $EuFe_2As_2$ iron pnictides is surprisingly robust against isovalent dilution.

### Hole doping

In 2008, Jeevan *et al.* reported for hole doped $Eu_{0.5}K_{0.5}Fe_2As_2$ polycrystals a superconducting transition at 32 K [34]. The high quality of the samples was indicated by a rather sharp resistivity transition with a width of less than 2 K. Bulk superconductivity was evidenced by a well-defined anomaly in the specific heat and a full diamagnetic shielding. However, those measurements revealed only very weak features below 10 K

1 The reason why $BaFe_2As_2$ shows significantly lower structural and spin density wave transition temperatures as the others is yet not clear. Previous quantum oscillation measurements indicated effective masses systematically smaller than in the case of $EuFe_2As_2$, meaning that the latter is much more correlated [209].

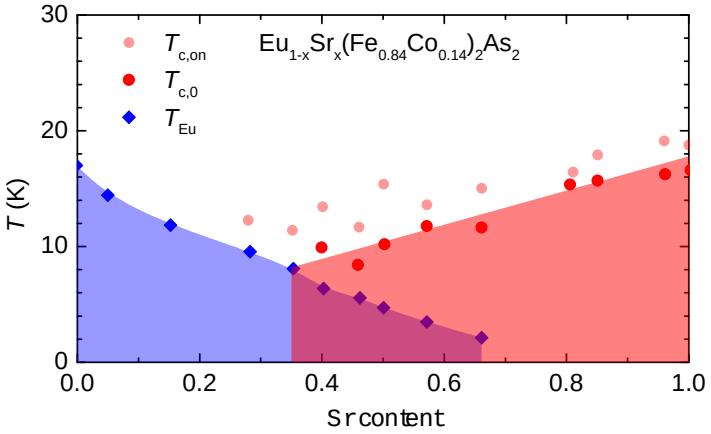


**Figure 6.11:** Phase diagram of $Eu_{1-x}Sr_x(Fe_{0.86}Co_{0.14})_2As_2$ [271]. The $Eu^{2+}$ magnetic order (blue diamonds) is continuously suppressed with Sr substitution. Superconductivity and magnetism coexist, as long as the onset of superconductivity ($T_{c,on}$: light red circle) and zero resistance temperature ($T_{c,0}$: light red circle) are well above $T_{Eu}$.

that could be ascribed to $Eu^{2+}$ magnetism. As dilution typically leads to the suppression of magnetic order, it is very tentative to assign weak signatures of $Eu^{2+}$ ordering to short-range interactions. However, one has to keep in mind that even in non-diluted compounds, the superconducting signal can be strong enough to mask $Eu^{2+}$ magnetism. Indeed, systematic magnetization studies on $x = 0.38$ polycrystals revealed that a small peak buried by the diamagnetic signal shifts with increasing magnetic field towards lower temperatures, indicating a long-range antiferromagnetic ordering [279]. Measurements on codoped $Eu_{0.5}K_{0.5}(Fe_{1-y}Ni_y)_2As_2$ give further evidence for such a long range magnetic order at 50 % dilution level: as soon as Ni doping has suppressed superconductivity, a strong antiferromagnetic $Eu^{2+}$ signal can be detected around 8 K [286].

Fig. 6.12 shows the phase diagram of $Eu_{1-x}K_xFe_2As_2$. Further experimental studies [275–282] showed that $x = 0.5$ actually represents the optimal doping level for poly- and single crystals. It should be noted that the synthesis of single crystals was successfully performed only in 2012, as K is highly reactive and hard to be controlled. Therefore, the single crystal phase diagram is still incomplete, especially concerning higher substitution levels. However, those doping levels are of special interest, as $KFe_2As_2$ is a particular end member of the iron pnictides: it is superconducting with a $T_c$ of 3.8 K [283]. In Fig. 6.12, also studies on the effect of Na doping are included [284, 285]. First measurements indicate a rather broad superconducting dome similar to K doping (see Fig. 6.12). Additional P substitution on a 30 % diluted sample was able to increase $T_c$ by 5 K [287].

In summary, hole doping combined with Eu dilution leads to a rather broad superconducting dome with high $T_c$, which is consistent with other 122 iron pnictides [80].

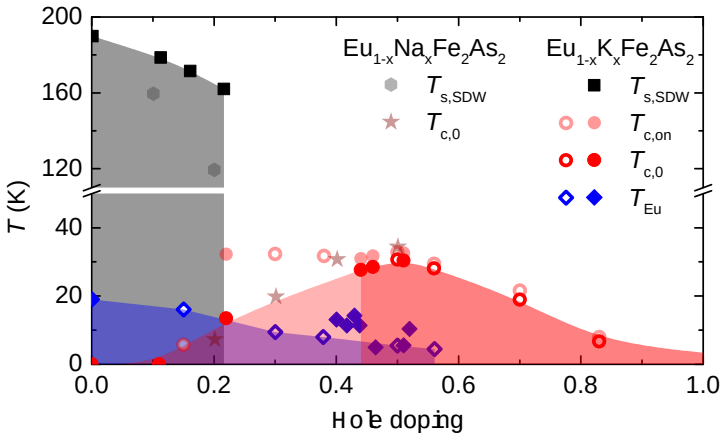


**Figure 6.12:** Phase diagram of hole doped $Eu_{1-x}Y_xFe_2As_2$ (Y = Na [286], K [279, 280]). The superconducting dome and the corresponding transition temperatures are marked in red (Na: dark red stars for $T_{c,0}$; K: light red circles for $T_{c,on}$ and red circles for $T_{c,0}$; closed symbols: single crystals [280], open symbols: polycrystalline samples [279]). The underdoped part of the dome is depicted more transparent, as here evidence for bulk superconductivity is not yet provided. $T_{s,SDW}$ is faster suppressed for Na (grey hexagons) than for K substitution (black squares). $T_{Eu}$ (blue diamonds) is continuously suppressed and disappears around 60 % substitution level.

Although Na substitution leads to the faster suppression of the structual and spin density wave transition, the superconducting domes are very similar. Experimental studies on the $Eu^{2+}$ magnetism are complicated, as the diamagnetic shielding typical for a bulk superconductor masks the $Eu^{2+}$ signal. However, there is growing experimental evidence indicating a coexistence of $Eu^{2+}$ long-range magnetic order and superconductivity, consistent with the results from isovalent Eu dilution.

### Electron doping

Substituting Eu by the rare earth ion La leads to the suppression of the structural and spin density wave transition, probably due to electron doping [288–291]. However, only traces of superconductivity were found for the maximum possible solid-solution of $x = 0.27$.

Zhang *et al.* applied additional pressure on $x = 0.22$ and 0.27 samples, successfully inducing superconductivity with sharp transitions and zero resistivity (see Fig. 6.13, [291]). Interestingly, neither La doping nor additional pressure up to 2.2 GPa do notably influence the $Eu^{2+}$ magnetic transition temperature. Indeed, $T_{Eu}$ slightly increases under pressure. Surprisingly, one can observe the coexistence of spin density wave magnetism, superconductivity and local $Eu^{2+}$ magnetism, while $T_c$ is always smaller than $T_{Eu}$.

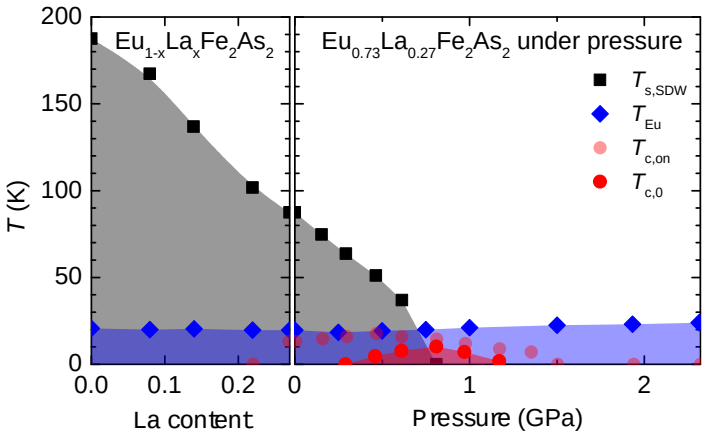


**Figure 6.13:** Phase diagram of $Eu_{1-x}La_xFe_2As_2$ (left) and $Eu_{0.73}La_{0.27}Fe_2As_2$ under pressure (right). Black squares correspond to $T_{s,SDW}$ and blue diamonds to $T_{Eu}$. While zero resistivity $T_{c,0}$ (red circles) appears only in a narrow dome for $Eu_{0.73}La_{0.27}Fe_2As_2$ under pressure, the onset of superconductivity $T_{c,on}$ (light red circles) appears in a much broader range. A coexistence region of spin density wave magnetism, superconductivity and local $Eu^{2+}$ magnetism shows up.

### Summary: Eu dilution

When summarizing all those studies on Eu diluted compounds, the most important findings concerning the interplay of magnetism and superconductivity are:

- There is growing experimental evidence that the $Eu^{2+}$ antiferromagnetic interlayer coupling is quite robust against dilution [273, 279, 286], as can be seen in Fig. 6.14. Overall, a rather smooth decrease of $T_{Eu}$ with dilution level takes place. This is typical for an intermetallic compound with local antiferromagnetism that is diluted with nonmagnetic ions [271]. Ba substitution seems to suppress the $Eu^{2+}$ magnetic ordering the fastest. Interestingly, ionic radii as well as $T_{s,SDW}$ changes the most in the case of Eu substitution by Ba. This indicates a complex interplay between structural, electronic and magnetic properties.

- It is quite surprising that when comparing $EuFe_2As_2$ and $Eu_{0.73}La_{0.27}Fe_2As_2$ under pressure, the latter diluted compound exhibits significantly lower critical temperatures [291]. This implies that in some cases, disorder might be even more harmful to superconductivity than $Eu^{2+}$ magnetism. In contrast, $T_c$ increases in $Eu_{0.7}Na_{0.3}Fe_2As_2$ by additional P substitution on the As site [287] and in $Eu_{1-x}Sr_x(Fe_{0.86}Co_{0.14})_2As_2$ by increasing Eu dilution [271].

- Indications for phase coexistence of (zero-resistance) superconductivity with spin density wave as well as diluted $Eu^{2+}$ magnetism was reported in several compounds

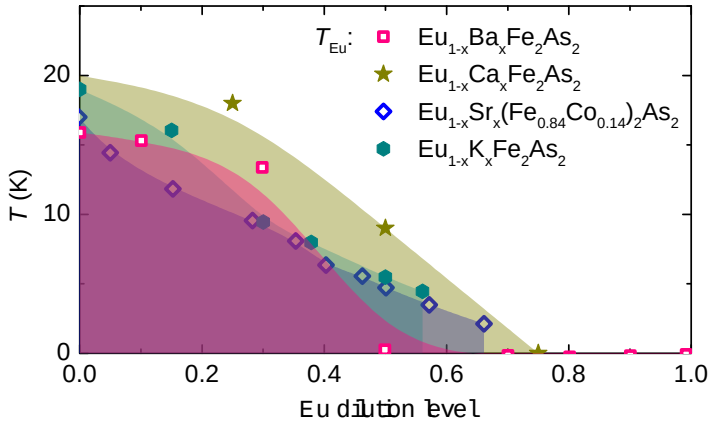


**Figure 6.14:** Suppression of the $Eu^{2+}$ magnetic ordering temperature $T_{Eu}$ with increasing Eu dilution for $Eu_{1-x}Y_xFe_2As_2$. Y = Ba (pink open squares, [269]), Ca (beige stars, [268]), Sr (codoped with 14 % Co) (blue open diamonds, [271]) and K (dark cyan closed hexagons, [279].

[267, 268, 285, 291], which is in stark contrast to non-diluted systems. Further systematic studies on these compounds is highly desirable in order to shed new light on the complex interplay between superconductivity and magnetism.

## 6.3 Electronic properties

### 6.3.1 Normal state properties

#### Band structure

Early angle resolved photoemission studies (ARPES) on $EuFe_2As_2$ [191, 192] revealed a band structure typical for 122 iron pnictides: in the paramagnetic phase, electron pockets around the $X$-point ($(\pi,\pi)$-point) and hole pockets around the $\Gamma$-point ((0,0)-point) could be resolved. Below the spin density wave transition, the electron-like bands (at the $X$-point) are folded back to the $\Gamma$-point, where they hybridize with the hole-like bands, leading to the opening of a spin density wave gap and a droplet-like Fermi surface. Such rather three-dimensional Fermi surface sections are also consistent with quantum oscillation measurements [209].

Those ARPES studies did not resolve any change when crossing the $Eu^{2+}$ magnetic ordering temperature, indicating a weak coupling between the Eu and FeAs subsystems. Therefore, Eu based compounds were examined in further studies in order to get characteristic information about 122 iron pnictides, and the $Eu^{2+}$ magnetic ordering was completely neglected [199, 205, 235, 290, 293]. For example, $EuFe_2(As_{1-x}P_x)_2$ was the first chemically pressurized superconductor investigated by ARPES [235]. It was found that P substitution

mainly influences the hole pockets in the center of the Brillouin zone, leading to a strongly three-dimensional Fermi surface with reduced nesting and (at least at low P substitution) to a charge-neutral development, which can not be described by a simple rigid-band shift[1].

In contrast to the early investigations on $EuFe_2As_2$, recent results show that the coupling between Eu and FeAs layers can not be neglected [204]. While former studies were carried out with energies, where the photoemission cross section of the *d*-orbitals is dominant, Adhikary *et al.* also used photon energies, which are sensitive to *p*-orbitals. This revealed that the electronic states near the Fermi energy level possess large *p*-orbital contributions due to Eu-As and Fe-As hybridizations, and are sensitive to the $Eu^{2+}$ ordering.

### Electronic transport

The electronic transport properties of $EuFe_2As_2$ are similar to other iron pnictides (see chapter 3.2.2, [188]): although a spin density wave takes place at elevated temperatures $T_{s,SDW} \sim 190\,K$, the resistivity (of twinned samples) stays metallic down to lowest temperatures (see also Fig. 6.1). At $T_{Eu}$, the resistivity exhibits only a slight kink; the influence on the scattering rate and thus also on the optical properties is negligible [184]. While Hall and thermopower measurements indicate that the carriers dominating the electronic transport above $T_{s,SDW}$ are holes [28, 280], also the influence of Dirac fermions was suggested [255].

In order to study the spin density wave, besides ARPES also optical spectroscopy [146, 184, 186] and scanning tunneling microscope (STM) measurements [203] were performed on $EuFe_2As_2$. While ARPES studies reported a spin density wave gap $2\Delta \approx 50 - 70\,meV$ [191], STM results indicate a gap value of $2\Delta \approx 90\,meV$, with a small suppression of the density of states at the Fermi energy that persists even up to higher temperatures than $T_{s,SDW}$. Further contradictory results were obtained from optical measurements in the infrared frequency range: while Wu *et al.* found only one spin density wave gap below 161 meV [184], Moon *et al.* resolved two energy gaps below 56 and 178 meV, consistent with $BaFe_2As_2$ and $SrFe_2As_2$ [146, 266].

1 It was found that an electron pocket with *yz*-orbital character and a hole pocket with *xy*-character do not change with P substitution. Both stay basically two-dimensional. However, a strongly dispersive hole pocket with $z^2$-orbital character increases with increasing P content, and the almost degenerate hole pockets with *xz*- and *yz*-orbital character are strongly suppressed at the $\Gamma$-point (and even disappear close to optimal doping), while they remain almost unchanged at the *Z*-point. A reduction from three to only one hole pocket at the $\Gamma$-point is consistent with DFT calculations [207].

### Coupling between magnetic and electronic subsystems

Probably the most interesting question about Eu 122 pnictides is, how strong the local $Eu^{2+}$ magnetic moments are coupled to the itinerant electrons in the FeAs layers. In the case of superconducting compounds, the influence of the $Eu^{2+}$ magnetism on the electronic properties is clearly visible in transferred hyperfine fields from the $Eu^{2+}$ moments on Fe of about 1 T [234, 251], causing phenomena such as the re-entrance of resistivity in the superconducting phase and field-enhanced superconductivity (see chapter 6.3.2). For $EuFe_2As_2$, however, the situation is more complicated: it was concluded that electron scattering on the local $Eu^{2+}$ moments plays only a minor role for the transport properties [188] and the reflectivity basically does not change at the $Eu^{2+}$ magnetic ordering temperature [184]. Only recently, ARPES [204], Mössbauer [200] and resonant x-ray measurements [195] could resolve signatures of coupled FeAs and Eu subsystems. In order to get more information about the coupling strength, electron and nuclear magnetic spin resonance studies are discussed in the following.

Electron spin resonance (ESR) is in principle a powerful tool to investigate the spin dynamics in Eu based iron pnictides, as one probes the relaxation of the local $Eu^{2+}$ spins which is dominated by the interaction with conduction electrons [187, 202, 248, 258, 269, 272, 277, 289]. Therefore, the resonance field and linewidth of the ESR signal both depend on the exchange coupling between $Eu^{2+}$ spins and itinerant electrons, as well as on the electronic density of states at the Fermi energy. In a common metal, the ESR linewidth increases linearly with temperature ("Korringa relaxation"); the $g$-factor, which is determined from the resonance field, is temperature-independent and shifted compared to its vacuum value ("Pauli susceptibility"). However, if the conduction electrons couple stronger to the $Eu^{2+}$ spins than to the lattice, the microwave energy absorbed by the $Eu^{2+}$ moments is not emitted fast enough to the lattice ("bottleneck scenario") [258, 272]. Instead, it is kept in the magnetic system of $Eu^{2+}$ spins and conduction electrons. As a consequence, the ESR response depends on experimental parameters such as microwave frequency and Eu concentration. Unfortunately, there is up to now no consensus whether such a bottleneck scenario is observed in Eu based iron pnictides or not [258, 269, 272].[1]

1 Garcia *et al.* argued that an almost unchanged $g$-factor through the phase diagram (which does thus not reflect the evolution of the Fermi surface), the measured magnetic field-dependence of the linewidth and opposing evolutions of the calculated density of states at the Fermi energy and the actual linewidth slope, all suggest a bottleneck scenario for $Eu(Fe_{1-x}Co_x)_2As_2$ [258]. However, Krug von Nidda *et al.* did neither observe any field dependence of the linewidth, nor that Eu dilution changes its slope [272]. Furthermore, Rosa *et al.* reported that when replacing Eu by Ba, the spin density wave is suppressed and the Korringa slope decreases simultaneously; opposite to what one would expect in the bottleneck scenario [269].

A much clearer picture can be drawn by nuclear magnetic resonance (NMR) spectroscopy, which probes the spin polarization of $^{75}$As nuclei that takes place via the Fermi contact interaction with delocalized carriers. If the $Eu^{2+}$ local moments are interacting with the conduction electrons, this should be visible in the signal. Thus, NMR spectroscopy is ideal to investigate the coupling between $Eu^{2+}$ magnetic moments and the FeAs layers. Up to now, $^{75}$As NMR investigations were performed on $Eu(Fe_{0.995}Co_{0.005})_2As_2$ [252] and Eu diluted compounds [273, 281]. It was found that the typical measurement parameters - spin-lattice relaxation rate, spin-spin relaxation rate and the shift of the central line - all follow a Curie-Weiss law. Furthermore, even in diluted compounds, the spin-lattice relaxation is more than two times larger than those of Ba 122 pnictides, and it increases with the Eu content; the latter is also true for the Curie-Weiss constant. All this proves that the $^{75}$As nuclei interact with the localized $Eu^{2+}$ moments. In order to get an estimate about the coupling between the FeAs layers and Eu subsystems, one can calculate the hyperfine coupling by relating the central line shift to the dc magnetic susceptibility. For $Eu(Fe_{0.995}Co_{0.005})_2As_2$, the hyperfine coupling is 60 times larger than for $NdFeAsO_{0.85}F_{0.15}$, providing direct experimental evidence for a strong coupling between the $Eu^{2+}$ localized moments and the conduction electrons in the FeAs layers [252].

### Electronic in-plane anisotropy

Up to now, most of the investigations on the in-plane anisotropy of iron pnictides concentrated on $Ba(Fe_{1-x}Co_x)_2As_2$. Recently, magnetic torque measurements on very small samples [295], as well as resistivity and thermopower measurements on mechanically detwinned crystals were also performed on Eu compounds [197, 240]. In those studies, the focus was on investigating the general in-plane anisotropy and possible nematic behaviour of iron pnictides, and the $Eu^{2+}$ magnetic order was neglected.

In order to examine whether the $Eu^{2+}$ magnetism leads to an additional anisotropic response, Fig. 6.15 depicts resistivity data for $Eu(Fe_{1-x}Co_x)_2As_2$ [197]. The overall behaviour is similar to Ba 122-compounds (see chapter 3.2.2); the $Eu^{2+}$ magnetic order does not notably induce additional anisotropy.

### Magnetic detwinning

Although magnetic fields are usually very ineffective to detwin iron pnictides [24], $EuFe_2As_2$ can be completely detwinned below $T_{Eu}$ by small magnetic fields ($\sim 1\,T$) applied along one of the orthorhombic axes [7]. In the corresponding experiment, Xiao *et al.* observed already at 0 T a strong imbalance of twin domains, possibly due to strain induced by

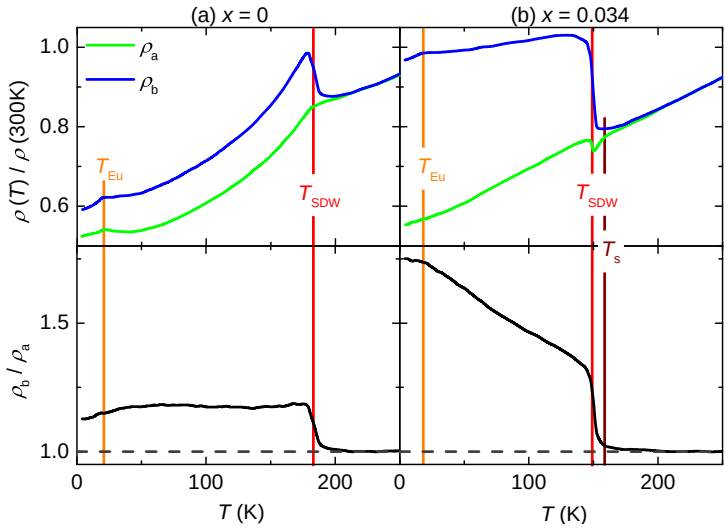


**Figure 6.15:** Temperature-dependent resistivity $\rho(T)$ [197] and its anisotropy for mechanically detwinned $Eu(Fe_{1-x}Co_x)_2As_2$ with (a) $x = 0$ and (b) $x = 0.034$. Vertical lines mark the transition temperatures $T_{Eu}$ (orange; kink in resistivity), $T_{SDW}$ (red; maximum in specific heat, minimum in $d\rho/dT$) and $T_s$ (brown; onset of hump in specific heat). The anisotropy with $\rho_b > \rho_a$ arises already slightly above $T_s$ and increases with doping. The $Eu^{2+}$ magnetic order does not notably induce additional anisotropy.

the mounting of the crystal[1], and a magnetic field was applied along the orthorhombic $a$-axis of the minority domain type (defined as $(100)_o$-direction). Fig. 6.16 summarizes the main results. At low fields, the intensity of the $(400)_o$-reflection (representing the minority twins) first decreases, before it abruptly increases around 0.7 T and the $(040)_o$-reflection completely disappears. Only a slight hysteresis was revealed. The authors attributed their observations to a giant spin-lattice coupling that leads at high fields to a detwinning of the crystal with its longer orthorhombic $a$-axis aligned parallel to the external magnetic field; the changes at low fields were interpreted in terms of a tilting of the minority domains out of their balance position due to internal strain induced by the detwinning process.

Xiao *et al.* also performed magneto-resistance measurements on $EuFe_2As_2$, concluding that the main observations can be well explained by $Eu^{2+}$ spin scattering [198]. For currents and magnetic fields applied parallel to one of the orthorhombic in-plane axes, a giant, unconventional magneto-resistance effect takes place: at temperatures $T < T_{Eu}$, the resistance first increases with increasing magnetic field, until it abruptly decreases at the $Eu^{2+}$ spin-flip field ($\sim 0.7$ T). The low field behaviour resembles the positive magneto-resistance that appears when an external magnetic field is applied parallel to the sublattice magnetization of an antiferromagnet; the abrupt decrease can be understood in terms of

1 Proposed in private communications by the main author Y. Xiao.

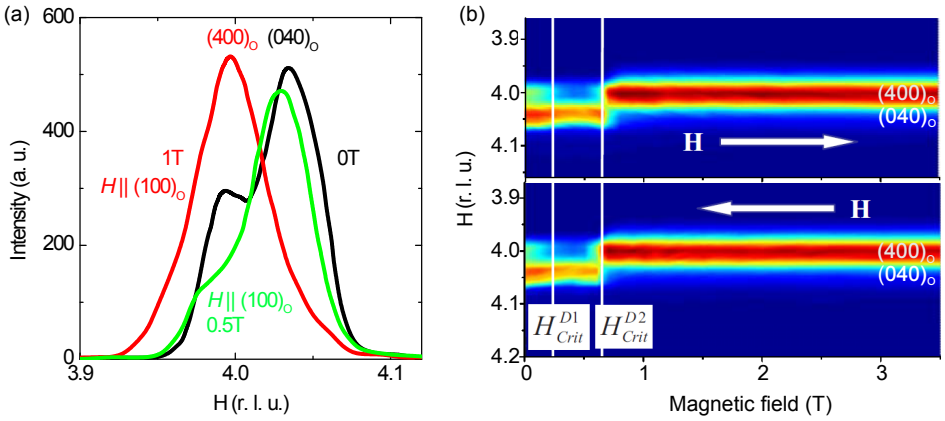


**Figure 6.16:** Selected Bragg reflections of $EuFe_2As_2$ at 2 K with the magnetic field applied along one of the orthorhombic axes [7]. Momentum transfer $Q$-scans around the $(400)_o$ and $(040)_o$ reflections (a) under three typical magnetic fields 0 T (black), 0.5 T (green) and 1 T (red line) as well as (b) for decreasing and increasing magnetic fields displayed in a contour plot. $H^{D1}_{Crit}$ marks the field, where twins tilt out of their balance position, caused by internal strain due to the detwinning at $H^{D2}_{Crit}$.

superzone boundary theory, which predicts an energy gap in the antiferromagnetic state; as soon as the $Eu^{2+}$ spins flip along the external magnetic field, the antiferromagnetic state and thus the energy gap gets destroyed and the resistivity decreases. In contrast, at temperatures slightly above the $Eu^{2+}$ magnetic ordering, the resistance directly decreases with increasing field. This can be explained in terms of suppressed spin fluctuations in a magnetic field.

Chapter 9 will show measurements done in the framework of this thesis, demonstrating that the magnetic detwinning is actually more complex than presented by Xiao *et al.*. Furthermore, those studies prove that the magneto-resistance is mainly governed by twin domain dynamics (and not $Eu^{2+}$ spin scattering), causing distinct hysteretic behaviour which can be observed when well-defined cooling procedures are obeyed.

### 6.3.2 Superconducting properties

#### Quantum criticality

Non-Fermi liquid behaviour, indicated for example by a linear temperature-dependence of the resistivity, was discovered in several unconventional superconductors around optimal doping [292]. Its appearance is widely discussed as due to an underlying quantum critical point or strong spin fluctuations in the vicinity of a suppressed magnetic order. While non-Fermi liquid behaviour above the superconducting dome is also commonly observed in iron pnictides, a divergent quasiparticle mass evidencing a quantum critical point was

(up to now) only confirmed for $BaFe_2(As_{1-x}P_x)_2$, possibly because this is a very clean system [83, 84].

In order to elucidate the origin of non-Fermi liquid behaviour in iron pnictides in more detail, Kurita *et al.* investigated pressurized $EuFe_2As_2$, which shows above the superconducting dome a linear temperature-dependence of the resistivity [229]. For optimum pressure, while resistivity and Hall measurements at 0 T ruled out any divergent quasiparticle mass, Fermi liquid behaviour could be restored in magnetic fields around 10 T. From those studies, the following conclusions were proposed: on the one hand, as $EuFe_2As_2$ under pressure can be considered as an even cleaner system as $BaFe_2(As_{1-x}P_x)_2$, the non-divergent quasiparticles mass demonstrates that quantum criticality is not the key ingredient for high temperature superconductivity in iron pnictides. On the other hand, the latter results under high magnetic fields indicate that spin fluctuations drive the unconventional scattering above the superconducting dome: probably, the external fields which are further enhanced by the $Eu^{2+}$ moments lead to a high enough internal field to suppress the spin fluctuations. This is an impressive example of how important information about unconventional superconductivity can be revealed by Eu based iron pnictides.

**Influence of Eu magnetism**

Understanding the interplay between superconductivity and magnetism is one of the great challenges of today's solid state physics. Indeed, the coexistence of $Eu^{2+}$ magnetic order and superconductivity is surprising from a very fundamental point of view: how can the Fe electrons contribute on the one hand to superconductivity and mediate on the other hand the $Eu^{2+}$ magnetic RKKY-exchange? In order to understand this interplay in more detail, here the main observations are summarized.

- The competition of the two orders gets very obvious in the case of the resistivity re-entrance which appears in several superconducting samples at $T_{Eu}$. Magnetic Compton scattering experiments on P and Co substituted Eu compounds indicated that the Fe 3*d*-contribution is strongly enhanced around $T_{Eu}$ [231, 260]. This enhancement can be quickly suppressed with relatively small magnetic fields in the *ab*-plane, consistent with the suppression of the re-entrance or even an enhancement of $T_c$ found in magneto-resistance measurements [32, 220, 256, 270]. Early work suggested that those observations are due to the suppression of magnon excitations [32, 270]. However, as previous experiments demonstrated below $T_{Eu}$ a spin canting of the $Eu^{2+}$ moments and thus a ferromagnetic component along the *c*-direction, it was proposed that the suppression of the canting by in-plane magnetic fields likely causes the field enhanced superconductivity [9, 256]. Interestingly, the re-entrance only appears when $T_{Eu}$ and $T_c$ are very close to each other [238]. This

is consistent with observations made in chapter 6.2: superconductivity can appear much below $T_{Eu}$ (for example in the case of Co doping), however, if $T_{Eu}$ and $T_c$ directly compete with each other, superconductivity disappears (for example for P substitution).

- Strikingly, the $Eu^{2+}$ magnetic order was also found to influence the superconducting gap: while in $BaFe_2(As_{1-x}P_x)_2$ nodal superconductivity was observed, for P substituted Eu compounds infrared and ESR measurements indicated an isotropic *s*-wave gap [233, 272]. One possible explanation for the different behaviour is that the nodes in iron-based superconductors are not given by symmetry and thus can be lifted by $Eu^{2+}$ spin scattering [72, 233]. However, a differing band structure due to the shortened *c*-axis (compared to Ba 122 compounds) might be also the reason [294].

- Microscopic coexistence of superconductivity and $Eu^{2+}$ magnetism was demonstrated recently by muon spin relaxation and Mössbauer spectroscopy on $EuFe_2(As_{1-x}P_x)_2$ [243].

### Upper critical fields

Compared to other iron pnictides, the Eu 122 family shows significantly reduced critical fields $B_{c1}$ and $B_{c2}$. In Eu diluted compounds, lower critical fields of only 10 -100 mT are reported [272, 276, 277, 279]; for non-diluted compounds, the Meissner state can be even completely absent [263]. While on the one hand, determining those very small lower critical fields is experimentally challenging, on the other hand, the reduction of $B_{c2}$ to an experimentally accessible scale opens new perspectives: in the case of $EuFe_2As_2$ under pressure, it was found that the upper critical fields ($\sim$ 20 T at 0 K) are slightly anisotropic, and their temperature-dependence revealed a concave curvature around 1 T, similar to the Jaccarino-Peter compensation effect (see chapter 3.3.3, [220, 225]). The results could be nicely described by an internal exchange field of $\sim$ 75 T due to the magnetic $Eu^{2+}$ moments, explaining the reduced upper critical fields compared to other iron pnictides. For diluted $Eu_{0.5}K_{0.5}Fe_2As_2$ [282] and $Eu_xSr_{1-x}(Fe_{0.89}Co_0.11)_2As_2$ ($x$ = 0.20 and 0.46) [274], the upper critical fields ($\sim$ 60 T for K and 20-30 T for Sr substitution) are consistent with a dominant Pauli paramagnetic effect that is proportional to the critical temperature $T_c$. Interestingly, a concave curvature similar to $EuFe_2As_2$ under pressure was also observed for Sr substitution. Although the authors ascribed the unconventional slope to multiband effects, the analysis in terms of internal compensation fields would be interesting; especially as the effect was observed to weaken with Eu dilution.

# 7

# MAGNETIZATION STUDIES ON $EuFe_2(As_{1-x}P_x)_2$

Although high quality single- and polycrystalline $EuFe_2(As_{1-x}P_x)_2$ samples were soon available after the discovery of superconductivity in $EuFe_2(As_{0.7}P_{0.3})_2$ [30], investigations on a series of samples are still rare (see chapter 6). In our opinion, however, it needs exactly such systematic studies in order to understand the complex dynamics in Eu based iron pnictides. Therefore, we have performed in- and out-of-plane magnetization measurements on a complete set of high quality $EuFe_2(As_{1-x}P_x)_2$ ($x$ = 0, 0.055, 0.09, 0.12, 0.16, 0.165, 0.17, 0.26, 0.35, 0.39, 1) single crystals (see chapter 5.3), which elucidated the complex magnetic ordering in those compounds and contributed important insights into the interplay of superconductivity and magnetism. The main results can be found in Ref. [9] and Ref. [10], as well as are described in the following in more detail.

## 7.1 Canted *A*-type antiferromagnetism

In 2011, the first phase diagrams were published for $EuFe_2(As_{1-x}P_x)_2$ [230, 234]. Despite the availability of single- and polycrystalline samples over the whole phase diagram, they could not deliver a clear picture of how the $Eu^{2+}$ order changes with chemical pressure and a serious debate was launched which kind of magnetism coexists with superconductivity. We approached this question by low-field in- and out-of-plane magnetization measurements

on a series of $EuFe_2(As_{1-x}P_x)_2$ single crystals ($x$ = 0, 0.055, 0.12 and 0.35) that should be non-superconducting according to the phase diagram of Ref. [230]; the results which are published partially in Ref. [9] are presented in this section.

### $EuFe_2(As_{0.88}P_{0.12})_2$

Fig. 7.1 shows the temperature-dependent dc susceptibility $\chi_{dc}(T) = M(T)/\mu_0 H$ for $x$ = 0.12, measured parallel and perpendicular to the $ab$-plane. The shape of the field-cooled curves (see Fig. 7.1a,b) is characteristic for the $A$-type antiferromagnetism identified in the parent compound: while at $T_N \sim 16\,K$, a cusp appears for $H \parallel ab$, the out-of-plane magnetization flattens. With increasing field, the transition temperature $T_N$ is suppressed and a broad shoulder appears that is typical for field-induced ferromagnetism; the suppression is faster for $H \parallel ab$, consistent with the anisotropy of $EuFe_2As_2$.

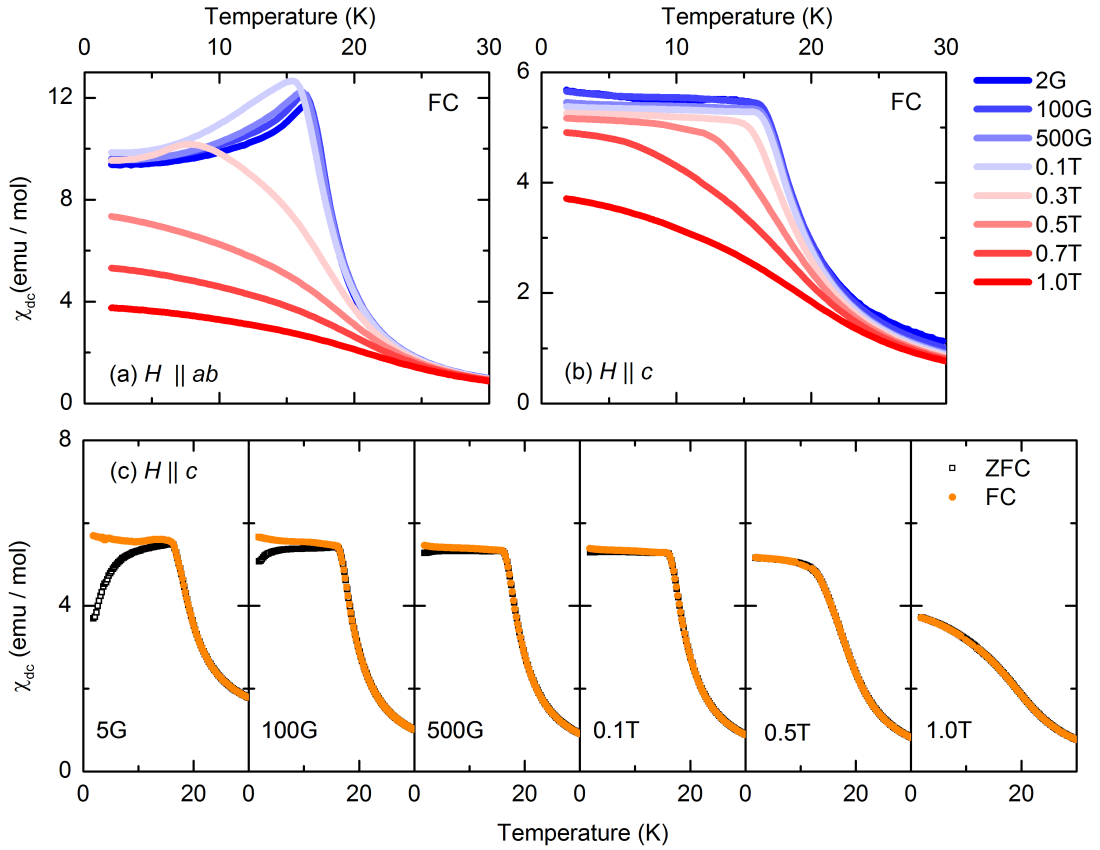


**Figure 7.1:** Temperature-dependent dc susceptibility $\chi_{dc}(T) = M(T)/\mu_0 H$ of $EuFe_2(As_{0.88}P_{0.12})_2$: (a) FC curves with $H \parallel ab$, (b) FC curves with $H \parallel c$ and (c) ZFC (black open squares) as well as FC (orange closed circles) curves with $H \parallel c$ for various applied fields. The shape of the FC curves is characteristic for antiferromagnetic interlayer coupling. However, a distinct hysteresis appears for $H \parallel c$ at small magnetic fields.

Nevertheless, we find at low magnetic fields a distinct difference between the field-cooled and zero-field cooled curves for $H \parallel c$ that is quickly suppressed with increasing field (see Fig. 7.1c). In order to study this hysteresis, we have also measured the field-dependence of the magnetization, concentrating on low fields (see Fig. 7.2a). We observe a clear hysteresis for $H \parallel c$; for $H \parallel ab$, only a much smaller hysteresis appears, which is likely caused by our limited precision in crystal alignment. To follow the opening of the hysteresis for $H \parallel c$, we plot in Fig. 7.2b the difference $\Delta M_c$ between the magnetization curves acquired by sweeping the field down and up (*i.e.* the hysteresis height). $\Delta M_c$ decreases on raising the temperature, until the hysteresis vanishes at $T_N$ and it is instructive to compare this trend with the difference between the ZFC and FC curves at the same field. The two trends coincide, demonstrating for $T < T_N$ the development of a ferromagnetic component along the crystallographic $c$-direction.

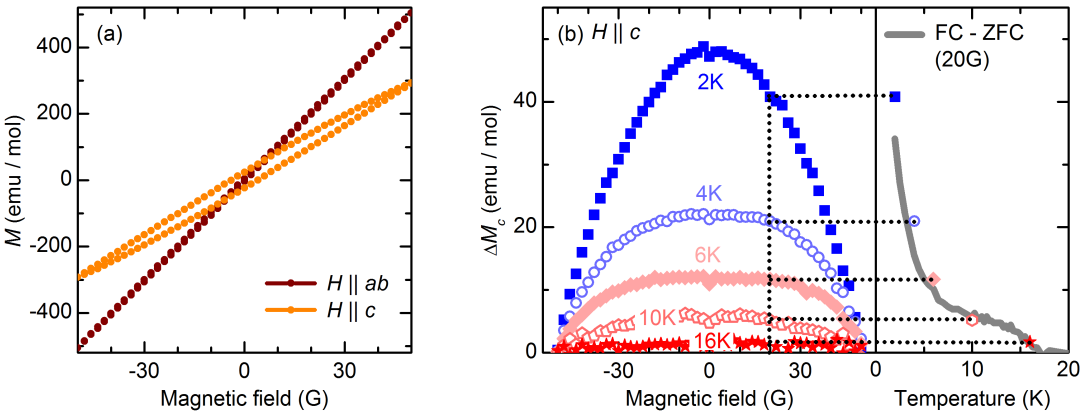


**Figure 7.2:** (a) Field-dependent isothermal magnetization $M(H)$ of $EuFe_2(As_{0.88}P_{0.12})_2$ for $H \parallel ab$ (brown) and $H \parallel c$ (orange) at $T = 2\,K$. (b) Height of the $H \parallel c$ hysteresis $\Delta M_c$ (difference between the magnetization curves acquired by sweeping the field down and up, left panel), compared to the temperature-dependence of the difference between the ZFC and FC curves at 20 G (right panel); the dotted lines are a guide to the eye to stress the correlation between the two trends.

### Other compositions

Further temperature-dependent out-of-plane measurements on a $x = 0.35$ single crystal reveal a similar behaviour as for $EuFe_2(As_{0.88}P_{0.12})_2$, while signatures of hysteretic behaviour in the $M(T)$ curves of $EuFe_2As_2$ and $EuFe_2(As_{0.945}P_{0.055})_2$ are much less clear; corresponding low-field hysteresis measurements at 2 K with $H \parallel c$ can not resolve a hysteresis for $x = 0$, while for $x = 0.055$ the hysteresis height is slightly and for $x = 0.35$ significantly positive (see Fig. 7.3). Therefore, we conclude that the ferromagnetic

component develops already at P concentrations much smaller than those where superconductivity sets in, and persists further in the overdoped range.

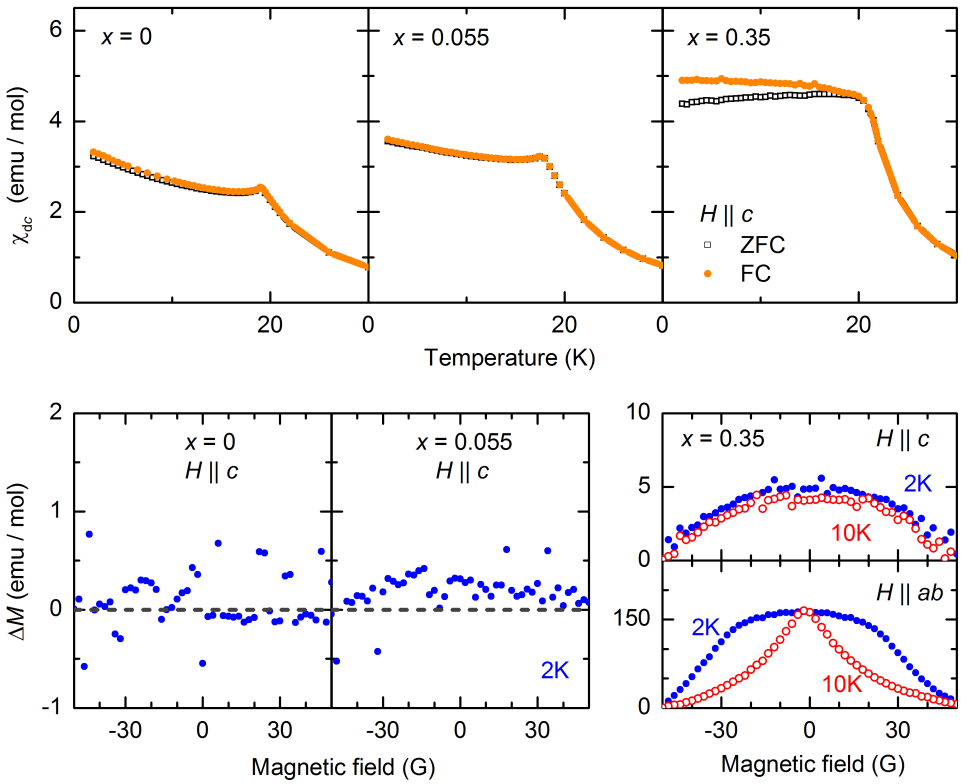


**Figure 7.3:** Magnetization curves of $EuFe_2As_2$, $EuFe_2(As_{0.945}P_{0.055})_2$, and $EuFe_2(As_{0.65}P_{0.35})_2$: temperature-dependent dc susceptibility $\chi_{dc}(T) = M(T)/\mu_0 H$ (upper panels) measured with $H = 20\,G$ ($H \parallel c$, ZFC: black open squares, FC: orange closed circles) and hysteresis height $\Delta M_c$ (lower panels, 2 K: blue closed circles, 10 K: red open circles); for $x = 0.35$, also $\Delta M_{ab}$ is given. The hysteresis height for $H \parallel c$ reveals already a small hysteresis for $x = 0.055$, which is much more evident for $x = 0.35$. In the latter case, a distinct hysteresis opening is also visible for in-plane measurements, which has a different temperature-dependence.

Fig. 7.3d also displays a comparison between isothermal in- and out-of-plane magnetization loops of $EuFe_2(As_{0.65}P_{0.35})_2$. One observes a distinct hysteresis opening for $H \parallel ab$ as well as a small opening for $H \parallel c$. The different temperature-dependence of $\Delta M_{ab}$ and $\Delta M_c$ indicates two unequal hysteretic mechanisms.

### Interpretation

By analysing measurements of the magnetic properties of various non-superconducting Eu 122 compounds, we identify a ferromagnetic contribution along the $c$-direction that

becomes stronger with increasing P substitution. Strikingly, we are able to verify a small out-of-plane ferromagnetic contribution already for $x = 0.055$, a concentration that is much smaller than those where superconductivity sets in. We have also investigated a single crystal of the overdoped substitution range ($x = 0.35$), where we find hysteretic behaviour for $H \parallel c$ and $H \parallel ab$. As in- and out-of-plane hysteresis show a different temperature-dependence, we conclude unequal hysteretic mechanisms for the two crystallographic directions. In the following discussion, we want to concentrate on the out-of-plane ferromagnetic component.

As already discussed in chapter 6, Mössbauer measurements indicate even for $EuFe_2As_2$ a small canting of the $Eu^{2+}$ moments out of the *ab*-plane; it increases strongly with increasing P substitution until the $Eu^{2+}$ spins are aligned almost along the *c*-direction when superconductivity sets in [234]. We show that this canting leads in magnetic susceptibility measurements to a ferromagnetic signal along the *c*-axis, *i.e.* hysteretic behaviour. The fact that one cannot resolve any hysteresis in the parent compound is consistent with an extremely small spin canting, which becomes already more pronounced for $EuFe_2(As_{0.945}P_{0.055})_2$.

We believe that the hysteresis loops observed in our single crystal measurements for $H \parallel c$ constitute the key to reconcile the various phase diagrams of Eu 122 pnictides proposed in literature [230, 234]. Since contributions from the *c*-direction are unavoidable in measurements on polycrystalline samples, a hysteresis is always seen as soon as the spin canting is sufficiently pronounced. In the following we compare the phase diagram of Ref. [230] (based on single crystal measurements with $H \parallel ab$) with that of Ref. [234] (where polycrystalline samples were investigated). While the former group observes signatures of antiferromagnetic $Eu^{2+}$ order in the superconducting phase, the latter claims the coexistence of ferromagnetism and superconductivity. Indeed, those statements do not contradict each other, if one considers that Ref. [230] is only sensitive to the ordering of the $Eu^{2+}$ moments in the *ab*-plane, while Ref. [234] detects a superposition of in- and out-of-plane coupling: both measurements are consistent with superconductivity that coexists with canted antiferromagnetism, meaning that the interlayer coupling is antiferromagnetically, but the spins are canted with a ferromagnetic net component along the *c*-direction.

It is intriguing that the canting develops with the suppression of the spin density wave, implying that the $Eu^{2+}$ spin orientation is defined by the spin density wave anisotropy. Calculations by Akbari *et al.* on multiband iron pnictides confirm an influence of the itinerant spin density wave phase on the RKKY-interaction between localized moments [11]. They show that the spin rotational symmetry is broken by the two-dimensional spin den-

sity wave which results in an anisotropic RKKY-interaction described by an anisotropic XXZ-type Heisenberg exchange. This anisotropy is only present in the spin density wave state and vanishes in the normal state. As this exchange is a general feature of rare earth based systems, such a ferromagnetic out-of-plane component that develops with the suppression of the spin density wave can be also expected for other Eu 122 pnictides.

## 7.2 Re-entrant spin glass

Although the in-plane magnetization measurements on $EuFe_2(As_{0.65}P_{0.35})_2$ presented in Fig. 7.3 imply for high P concentrations - in accordance with many other publications (see chapter 6) - ferromagnetic interlayer coupling, our detailed investigations reveal a more complex, time-dependent behaviour. Therefore, we have performed a systematic study of the superconducting and magnetic properties of a complete set of $EuFe_2(As_{1-x}P_x)_2$ ($x$ = 0, 0.055, 0.09, 0.12, 0.16, 0.165, 0.17, 0.26, 0.35, 0.39, 1) single crystals (see chapter 5.3) using dc and ac magnetization (see chapter 5.2), dc resistivity and heat capacity measurements[1]. In order to account for the time-dependencies, the temperature is usually swept continuously in $M(T)$ cycles (see chapter 5.2); furthermore we distinguish between field-cooled curves that were obtained while decreasing ("field-cooled cooled": FCC) and increasing ("field-cooled heat": FCH) the temperature. Results are published in Ref. [10][2].

**$EuFe_2P_2$**

Fig. 7.4 and Fig. 7.5 show the in-plane ($H \parallel ab$) magnetic behaviour of a $EuFe_2P_2$ single crystal. In a very small probing field of 2 G two consecutive magnetic transitions can be clearly resolved in the zero-field cooled and field-cooled dc magnetic susceptibility. A sharp peak at $T_1 \sim 29.0$ K is followed by an upturn starting at $T_2 \approx 27.7$ K, leading to a second peak at $\sim 27$ K in the ZFC magnetization. Whereas the transition at $T_1$ exhibits no thermal hysteresis, the second transition at $T_2$ is characterized by a pronounced ZFC-FCC hysteresis which vanishes if a larger dc magnetic field ($H \parallel ab$) is applied (see Fig. 7.5). It can be finally suppressed for fields around 500 G. Increasing the field even higher shifts the peak at $T_1$ down (see Fig. 7.4c) and at around 1 T, the peak has completely disappeared. Note that a broad shoulder develops at $\sim 0.3$ T, which was interpreted for $EuFe_2As_2$ as due to a metamagnetic transition [182]. Furthermore, specific heat measurements on the single

1 Magnetization data are complemented with four point dc resistivity measurements with a current of the typical value 1 mA. In the case of small resistances (especially for the $c$-direction measurements), lock-in technique with low frequencies (77 Hz) was used. Transition temperatures derived from resistivity measurements are indicated with "*". Heat capacities were measured with a relaxation-type calorimeter.

2 Preliminary studies can be also found in Ref. [296].

crystal show a sharp peak at $T_1$ with a broad shoulder at lower temperatures, consistent with the width of the anomaly for polycrystalline samples reported in Ref. [211] and prove that both transitions are bulk properties (see Fig. 7.4b).

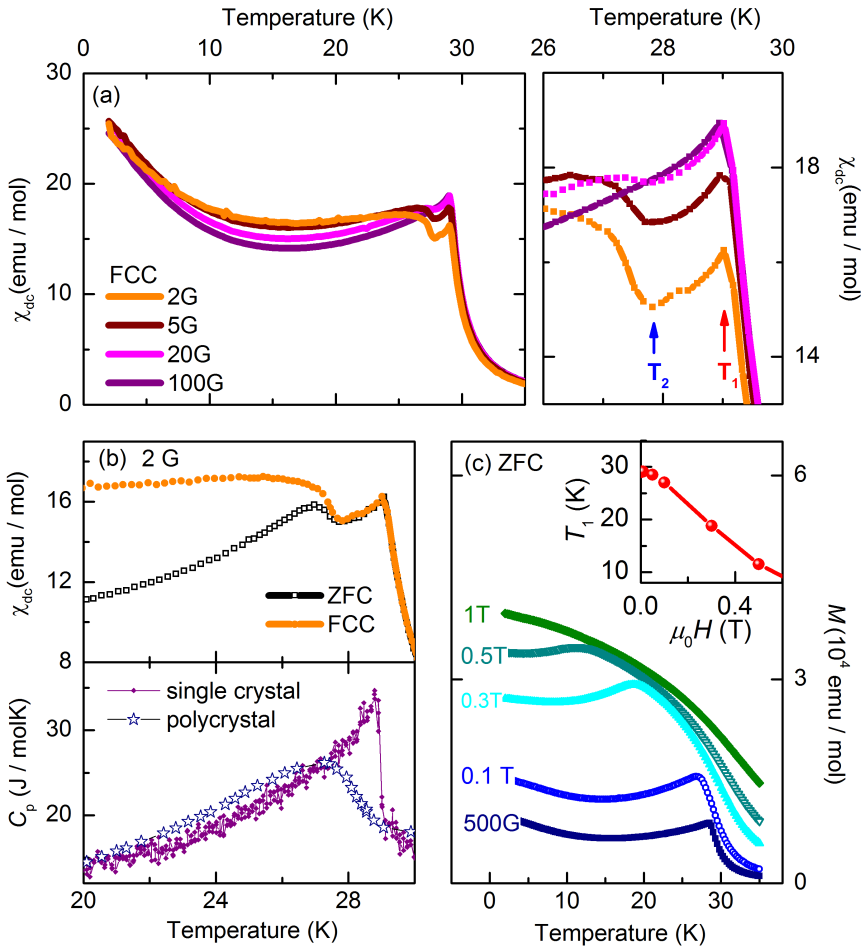


**Figure 7.4:** Magnetization curves of $EuFe_2P_2$ ($H \parallel ab$), together with specific heat data. (a) Temperature-dependent FCC curves $\chi_{dc}(T) = M(T)/\mu_0 H$ at small fields between 2 G (orange) and 100 G (purple) show two consecutive magnetic transitions at $T_1 = 29.0$ K and $T_2 = 27.7$ K; the transition at lower temperature $T_2$ is quickly suppressed in the external field. (b) Temperature-dependent ZFC (black open squares) and FCC (orange filled circles) dc susceptibility $\chi_{dc}(T)$ (upper panels) measured with $H = 2$ G, revealing that a strong hysteresis sets in at $T < T_2$. The lower panel adds the temperature-dependent heat capacity $C_p$ for our single crystal (purple filled diamonds) and for polycrystalline $EuFe_2P_2$ (open dark blue stars, [234]). The single crystal heat capacity shows a sharp feature at $T_1$ that is followed by a broad shoulder (visible also in the data of polycrystalline $EuFe_2P_2$). (c) ZFC magnetization for 500 G (dark blue), 0.1 T (blue), 0.3 T (cyan), 0.5 T (dark cyan) and 1 T (green). $T_1$ decreases with increasing external field, also depicted in the inset.

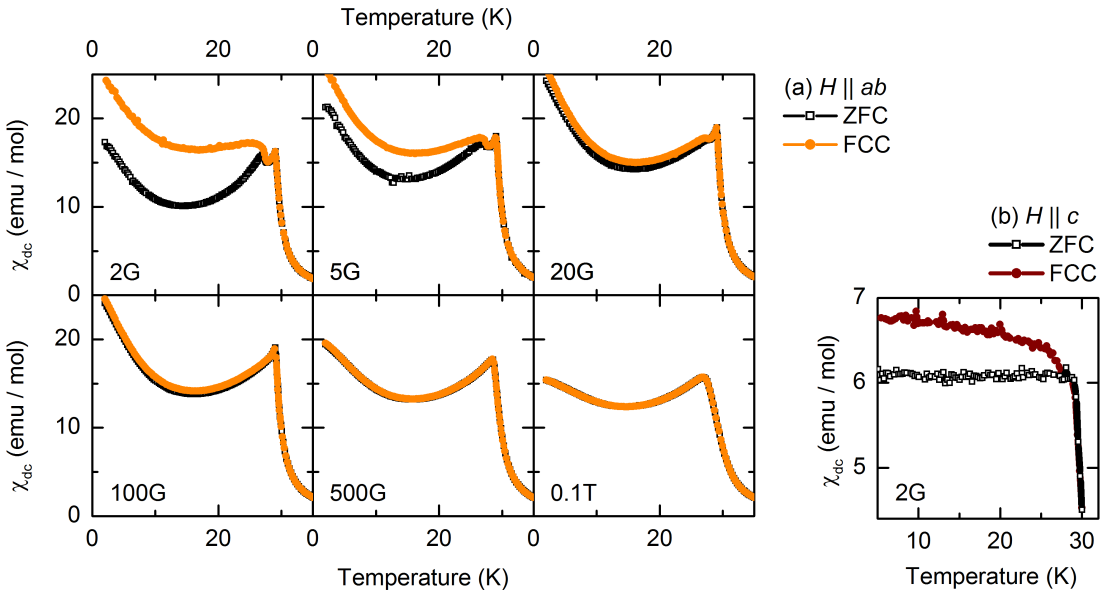


**Figure 7.5:** (a) ZFC (black open squares) and FCC (orange filled circles) in-plane magnetization curves of $EuFe_2P_2$ at $H = 2\,G$, $5\,G$, $20\,G$, $100\,G$, $500\,G$ and $0.1\,T$ ($H \parallel ab$), as well as (b) ZFC (black open squares) and FCC (brown filled circles) out-of-plane magnetization at $H = 2\,G$. The in-plane low-temperature transition and any irreversibility has disappeared at $500\,G$; out-of-plane, a small hysteresis due to spin canting can be identified at low fields.

In order to get more insight into the character of the second transition at $T_2$ we studied in detail its thermal hysteresis and frequency-dependence by ac magnetization measurements. Fig. 7.6a displays the differences between the ZFC, FCC and FCH susceptibilities for an in-plane field of 2 G. The thermal hysteresis is visible in the ZFC-FCC splitting at $T < T_2$. Repeated FCC and FCH cycles (heating / cooling rates 0.2 K/min) revealed a very slow time-dependence of the magnetization below $T_2$, leading to a growth of the magnetization and consequently a negative difference of FCH - FCC.

A time-dependence of the magnetization below $T_2$ is also visible in a time-dependence of the ZFC magnetization which after some rapid initial increase grows almost linearly in time with a rate of ∼1%/h (see Fig. 7.6b). The time-dependence of the magnetization becomes also apparent in a frequency-dependence of the real and imaginary component of the ac susceptibility, $\chi'_{ac}(T)$ and $\chi''_{ac}(T)$, as depicted in Fig. 7.6c. Below $T_2$ a peak appears in both components ($\chi'_{ac} \approx 50 \times \chi''_{ac}$) which shifts to higher temperature with increasing frequency following a Vogel-Fulcher behaviour (see Fig. 7.6d). We can rule out any relation of the time and frequency-dependence to flux line lattice dynamics, since $EuFe_2P_2$ is far off from any proposed superconducting phase [230, 236].

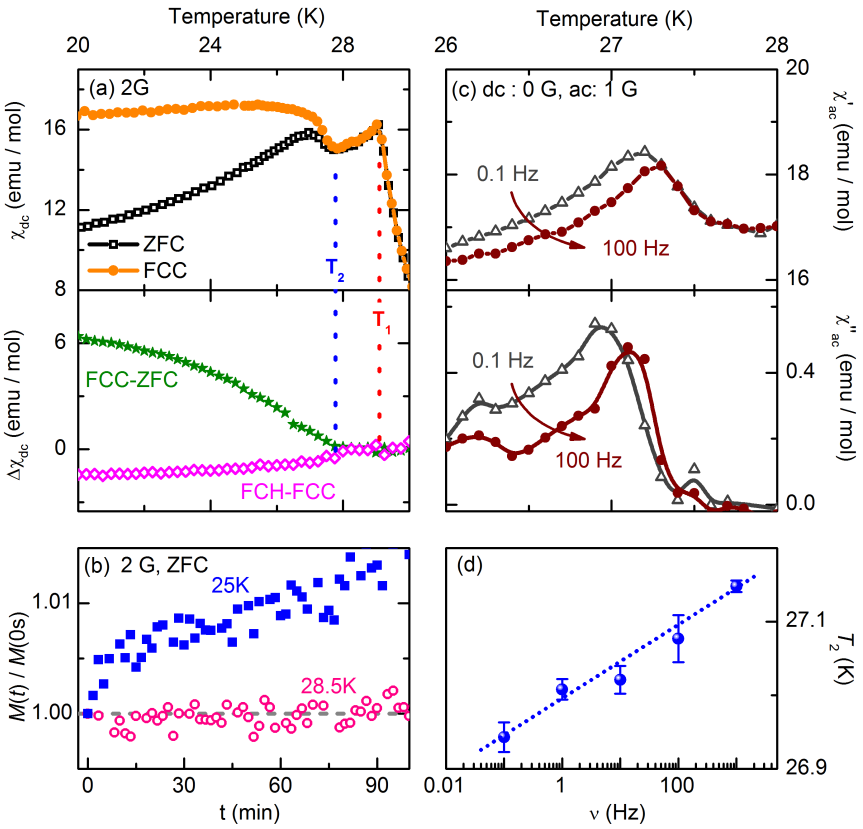


**Figure 7.6:** Magnetization curves of $EuFe_2P_2$ ($H \parallel ab$). (a) Magnetic hysteresis sets in at $T < T_2$, visible in $\chi_{\mathrm{dc,FCC}} - \chi_{\mathrm{dc,ZFC}} > 0$ (green stars) ($\mu_0 H = 2\,\mathrm{G}$); ZFC and FCC curves are depicted in the upper panel for a direct comparison of the characteristic temperatures $T_1$ and $T_2$. Time-dependence for $T < T_2$ is revealed by FC cycling, visible in $\chi_{\mathrm{dc,FCH}} - \chi_{\mathrm{dc,FCC}} < 0$ (pink open diamonds) and (b) time-dependent magnetization after ZFC cooling ($\mu_0 H = 2\,\mathrm{G}$, 25 K: blue closed squares, 28.5 K: pink open circles). (c) A frequency-dependence in the ac susceptibility $\chi'_{\mathrm{ac}}(T)$ and $\chi''_{\mathrm{ac}}(T)$ (no dc field, ac drive amplitude 1 G, 0.1 Hz: dark grey open triangles, 100 Hz: brown closed circles) sets in also below $T_2$. (d) Vogel-Fulcher-Fit of the peak below $T_2$ in $\chi''_{\mathrm{ac}}(T)$.

Until now, magnetic ordering at higher P concentrations in polycrystalline and single crystalline samples of $EuFe_2(As_{1-x}P_x)_2$ was assigned to ferromagnetism [230, 234, 236]. Measurements on polycrystalline samples [234, 236], however, are not able to allow conclusions about a possible antiferromagnetic interlayer coupling, and measurements on single crystals of $EuFe_2(As_{1-x}P_x)_2$ [230] failed to reveal two separate magnetic transitions and their different thermal hysteretic behaviour because of too coarse temperature steps.

In view of the shape of the $M(T)$ anomaly at $T_1$ (see Fig. 7.4c) we suggest that the $Eu^{2+}$ moments in $EuFe_2P_2$ order in a canted $A$-type antiferromagnetic structure with

the spin components being ferromagnetically aligned along the $c$-axis[1]. Additionally, we detect below $T_2$ a second phase transition with glassy character which we associate to the ordering of the in-plane components of the $Eu^{2+}$ moments. The development of a glassy phase below a magnetic phase transition, commonly referred to as re-entrant spin glass [38, 297–299], indicates a competition between antiferromagnetic and ferromagnetic spin exchange interactions in the system.

In the case of $EuFe_2P_2$, the antiferromagnetic RKKY interlayer coupling competes with the ferromagnetic intralayer interactions of the spins. In fact, DFT based calculations revealed a very small energy difference of antiferromagnetic and ferromagnetic ground states for $EuFe_2(As_{1-x}P_x)_2$ [230]. We therefore suggest that in $EuFe_2P_2$, competition between ferro- and antiferromagnetism causes glassy freezing of spin components in the $ab$-plane at $T_2$ and a decoupling of the magnetic Eu layers. Such a freezing of transverse magnetic components following long range magnetic order (which has already set in) is consistent with mean field theoretical calculations for a re-entrant spin glass [39]. Our conclusions are not only supported by the time-dependent magnetization behavior at $T < T_2$, but also by the development of $M(T)$ with external fields: by application of a magnetic field of $\sim 500\,\mathrm{G}$ along the $ab$-plane, the energy barrier between different equilibrium states can be overcome, the glass transition is suppressed and the temperature-dependent magnetization resembles that of $EuFe_2As_2$. This interpretation is consistent with neutron studies by Ryan *et al.* [212], as those are not sensitive to the freezing of the small in-plane spin component, as long as the ferromagnetic spin component along the $c$-axis still exists.

### $\mathbf{EuFe_2(As_{0.835}P_{0.165})_2}$

In order to study the complex interplay of magnetism and superconductivity in mixed As - P samples we have investigated in detail the magnetic and superconducting properties of a single crystal of $EuFe_2(As_{0.835}P_{0.165})_2$. The in-plane electrical resistivity (see Fig. 7.7) proves the onset of superconductivity at $T^*_{\mathrm{c,on}} \sim 22\,\mathrm{K}$ indicated by a steep initial decrease of the resistivity. Zooming into the transition reveals re-entrant behaviour at about 19 K followed by a smooth decrease towards zero resistivity which is achieved only below $T^*_{\mathrm{c},0} \approx 9\,\mathrm{K}$.

Fig. 7.9 displays the corresponding zero-field and field-cooled cooled temperature-dependent magnetization. Both, in- and out-of-plane magnetization are very similar to $EuFe_2P_2$: for $H \parallel ab$, two peaks are visible that are shifted to slightly lower temperatures ($T_1 \sim 19.0\,\mathrm{K}$, $T_2 \sim 16.8\,\mathrm{K}$); for $H \parallel c$, a slight hysteresis below $T_1$ indicates the spin

1 Due to sample shape effects we can not distinguish between $A$-type antiferromagnetism and helimagnetism.

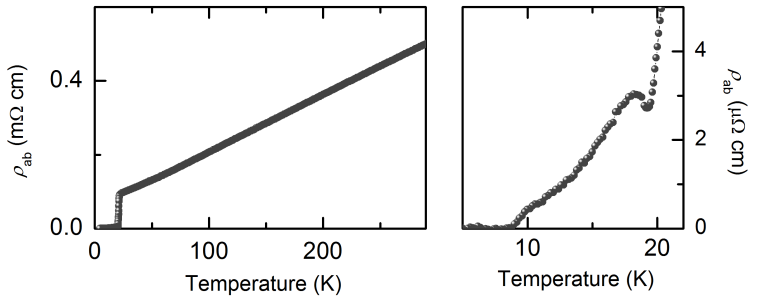


**Figure 7.7:** In-plane resistivity curves of superconducting $EuFe_2(As_{0.835}P_{0.165})_2$ with $T^*_{c,on} \sim 22\,K$. At $T > T^*_{c,on}$, $R(T)$ is linear; below $\sim 19\,K$, a re-entrance of resistivity appears. Zero resistivity is reached only below $T^*_{c,0} \sim 9\,K$

canting along the $c$-axis. Additionally, a pronounced downturn occurs below 15 K for both field directions, which ends up in a diamagnetic signal for $H \parallel c$. While the in-plane low-temperature transition at $T_2$ has already disappeared at 500 G, irreversibilities due to superconductivity remain at least up to 0.5 T.

Further evidence for a spin glass transition can be found in Fig. 7.8, which compares the low-temperature resistivity behaviour to selected ac and dc magnetization data. A difference between ZFC and FCH curves sets in at $T < T_{c,on}$. However, FC cycling reveals two time-dependent glassy transitions, as $\chi_{dc,FCH} - \chi_{dc,FCC} > 0$ at $T < T_{c,on}$ and $\chi_{dc,FCH} - \chi_{dc,FCC} < 0$ at $T < T_2$ (pink open diamonds). We therefore conclude that superconducting $EuFe_2(As_{0.835}P_{0.165})_2$ shows an analogous re-entrant spin glass behaviour as $EuFe_2P_2$. The additional positive peak in the FCH-FCC curve between 17 K and 21 K could be ascribed to vortex dynamics, as it coincides with the steep initial decrease of the resistivity marking the onset of superconductivity.

Having this interpretation in mind, we can also interpret all the other features in the ac susceptibility: the resistivity re-entrance and $T^*_{c,0}$ are both accompanied by a sharp peak in $\chi''_{ac}(T)$. Such a feature, which comes along with a dip in $\chi'_{ac}$ (slightly visible for the 100 G curve) was reported for several high-$T_c$ SC and is known as "peak effect" [300, 301] arising due to a maximum in the critical current density. The broad peak in $\chi''_{ac}(T)$ at $T < T_2$ could be a sign of granular SC or of flux reaching the center of the sample according to Bean's critical state model [302, 303]. However, as $\chi_{dc,FCH} - \chi_{dc,FCC} < 0$ exactly at $T < T_2$, it probably arises due to the spin glass transition. Furthermore, one should note that in-plane ac susceptibility measurements with applied high dc fields $H \parallel ab$ are able to reveal a diamagnetic in-plane shielding signal if the dc field is large enough ($\sim 1\,T$) to saturate the $Eu^{2+}$ magnetism.

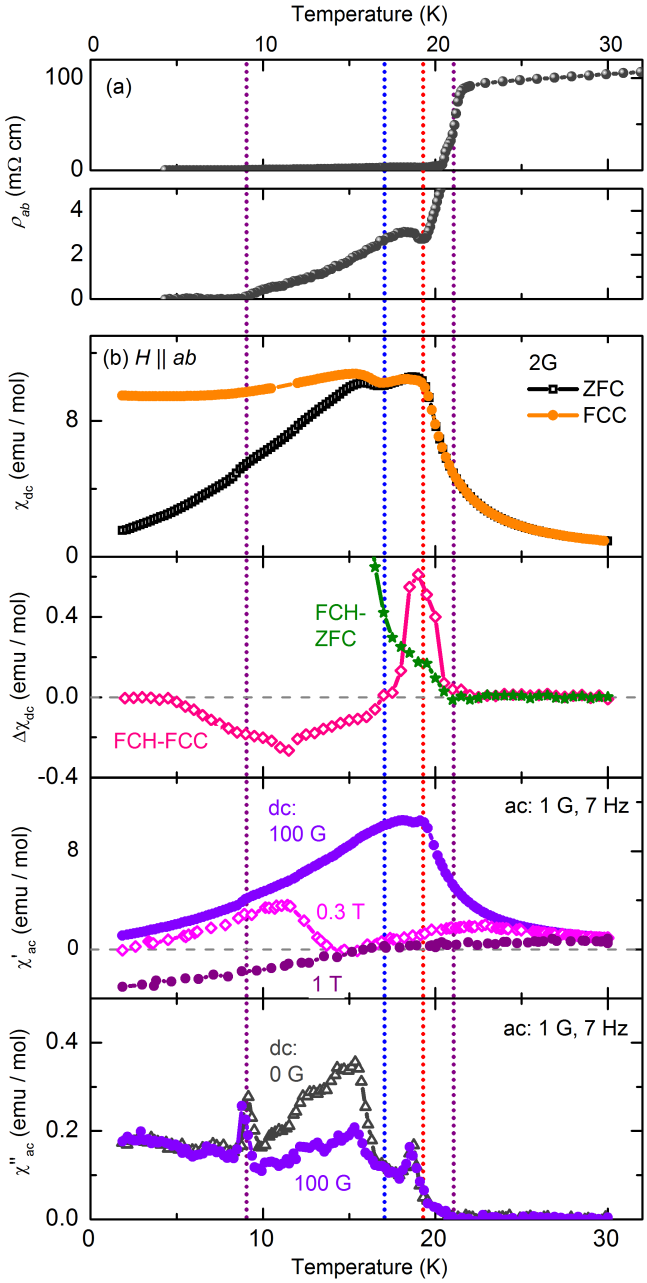


**Figure 7.8:** (a) Details of the resistivity curves as well as (b) in-plane magnetization curves ($H \parallel ab$) of $EuFe_2(As_{0.835}P_{0.165})_2$, in order to determine the transition temperatures. Dashed lines are guides to the eye, highlighting $T^*_{c,50} = T_{c,on} \sim 20.8\,K$ (purple), $T_1 \sim 19.5\,K$ (red), $T_2 \sim 16.8\,K$ (blue) and $T^*_{c,0} \sim 9.0\,K$ (purple). (b) In-plane ZFC (black open squares) and FCC (orange filled circles) magnetization shows at $H = 2\,G$ two magnetic transitions similar to $x = 1.0$ with a steep drop in the ZFC curve below $\sim 15\,K$ (measured with the Quantum Design ultra low field option, see chapter 5.2). A difference between ZFC and FCH curves sets in at $T < T_{c,on}$; FC cycling reveals two time-dependent glassy transitions, as $\chi_{dc,FCH} - \chi_{dc,FCC} > 0$ at $T < T_{c,on}$ and $\chi_{dc,FCH} - \chi_{dc,FCC} < 0$ at $T < T_2$ (pink open diamonds). Combining ac susceptibility measurements (drive 1 G, frequency 7 Hz) with dc fields (0 G: grey open triangles, 100 G: violet closed circles, 0.3 T: pink open diamonds, 1 T: purple closed circles), negative susceptibility $\chi'_{ac} < 0$ is revealed for $H = 1\,T$ below 15 K. $\chi''_{ac}(T)$ shows a non-zero-signal below $T_{c,on}$, a sharp peak at the maximum re-entrant resistivity (that is accompanied by a small dip in $\chi'_{ac}(T)$), a broad hump below $T_2$ and again a sharp peak at $T_{c,0}$. Increasing the dc field from 0 to 100 G only suppresses the broad hump below $T_2$.

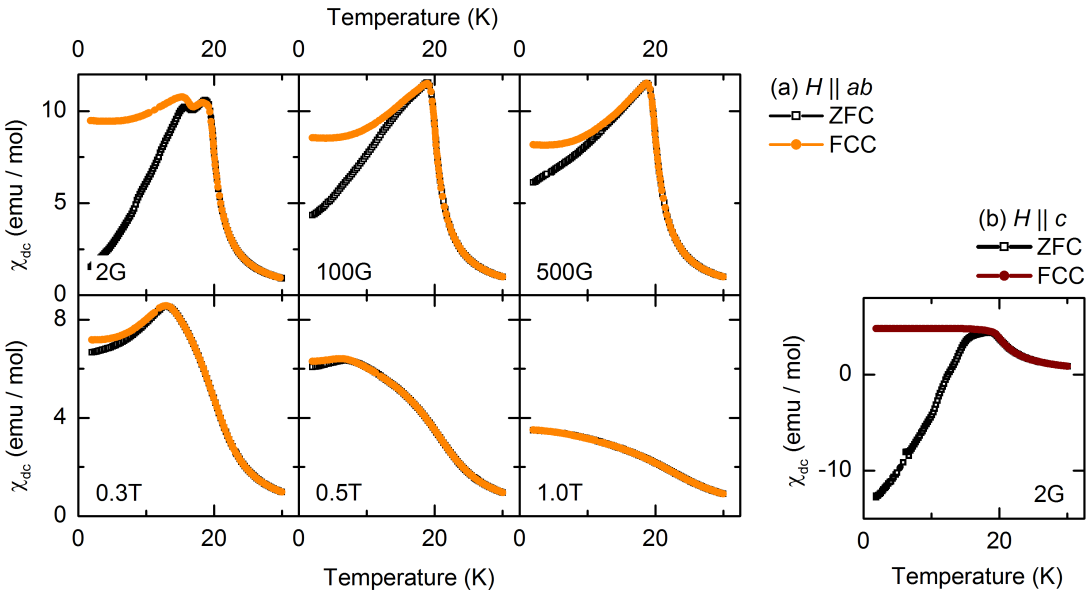


**Figure 7.9:** (a) ZFC (black open squares) and FCC (orange filled circles) in-plane magnetization curves of $EuFe_2(As_{0.835}P_{0.165})_2$ at $H = 2\,G$, $100\,G$, $500\,G$, $0.3\,T$, $0.5\,T$ and $1.0\,T$ ($H \parallel ab$), as well as (b) ZFC (black open squares) and FCC (brown filled circles) out-of-plane magnetization at $H = 2\,G$ (measured with the Quantum Design ultra low field option, see chapter 5.2). The in-plane low-temperature transition at $T_2$ (marked by a shoulder) has disappeared at $500\,G$, however, irreversibilities due to superconductivity remain at least up to $0.5\,T$; out-of-plane, a small hysteresis due to spin canting can be identified, as well as a steep drop in the ZFC curve below $\sim 15\,K$, reaching negative magnetization.

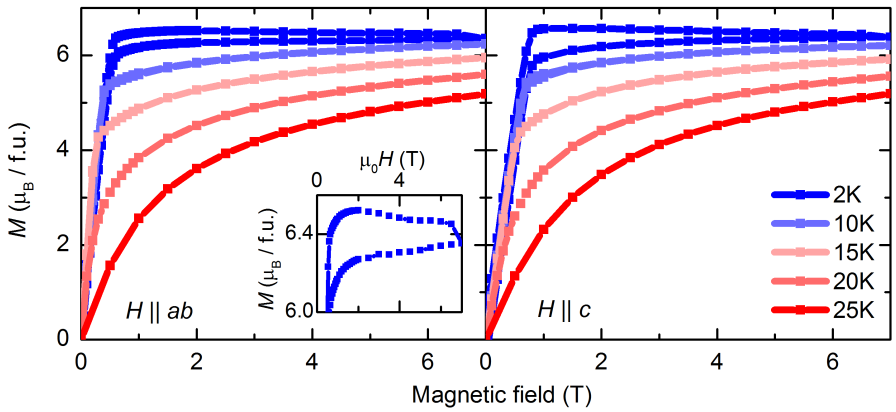


**Figure 7.10:** Field-dependent magnetization curves of $EuFe_2(As_{0.835}P_{0.165})_2$ for $H \parallel ab$ (left) and $H \parallel c$ (right), at several temperatures between $2\,K$ (blue) and $25\,K$ (red). At $2\,K$, a distinct hysteresis that remains up to highest applied fields ($7\,T$) is clearly visible (see also inset), indicating superconductivity.

Finally, we have also measured the in- and out-of-plane field-dependent magnetization curves at various temperatures (see Fig. 7.10). Most remarkably, we find at 2 K a distinct hysteresis that remains up to highest applied fields (7 T), typical for a hard superconductor according to Bean's critical state model (see chapter 3.3.2).

### $EuFe_2(As_{0.65}P_{0.35})_2$

We have also investigated a single crystal of $EuFe_2(As_{0.65}P_{0.35})_2$ in more detail, in order to address the open question about the width of the superconducting dome. Fig. 7.11a displays the corresponding in-plane resistivity, showing a sharp drop around $T_1 \sim 20.7$ K, which fades in a broad shoulder at $T_2 \sim 18.8$ K. Such a resistivity behaviour was interpreted by Cao *et al.* [236] as re-entrant superconductivity.

However, in-plane ZFC magnetization measurements reveal two magnetic transitions similar to $x = 1.0$, indicating the onset of canted antiferromagnetism and re-entrant spin glass behaviour at $T_1$ and $T_2$, respectively (see Fig. 7.11 and Fig. 7.12). Indeed, any out-of-phase susceptibility signal is already suppressed at 100 G, the same field, where the $T_2$ transition gets barely visible in ZFC and FC measurements. Furthermore, no diamagnetic signal is visible in any dc or ac susceptibility measurement. One should note that the double-feature in $M(T)$ curves for superconducting samples was in some cases assigned to result from the Paramagnetic Meissner Effect [234]. However, this effect would only appear in the FC curve [304], whereas we observe features also in ZFC data.

Furthermore, we have also measured the in- and out-of-plane field-dependent magnetization curves at various temperatures (see Fig. 7.13). In contrast to superconducting $EuFe_2(As_{0.835}P_{0.165})_2$ (see Fig. 7.10), we find at 2 K no high-field hysteresis. Therefore, we conclude that $EuFe_2(As_{0.65}P_{0.35})_2$ is not superconducting; it displays similar to $EuFe_2P_2$ canted antiferromagnetism and re-entrant spin glass behaviour.

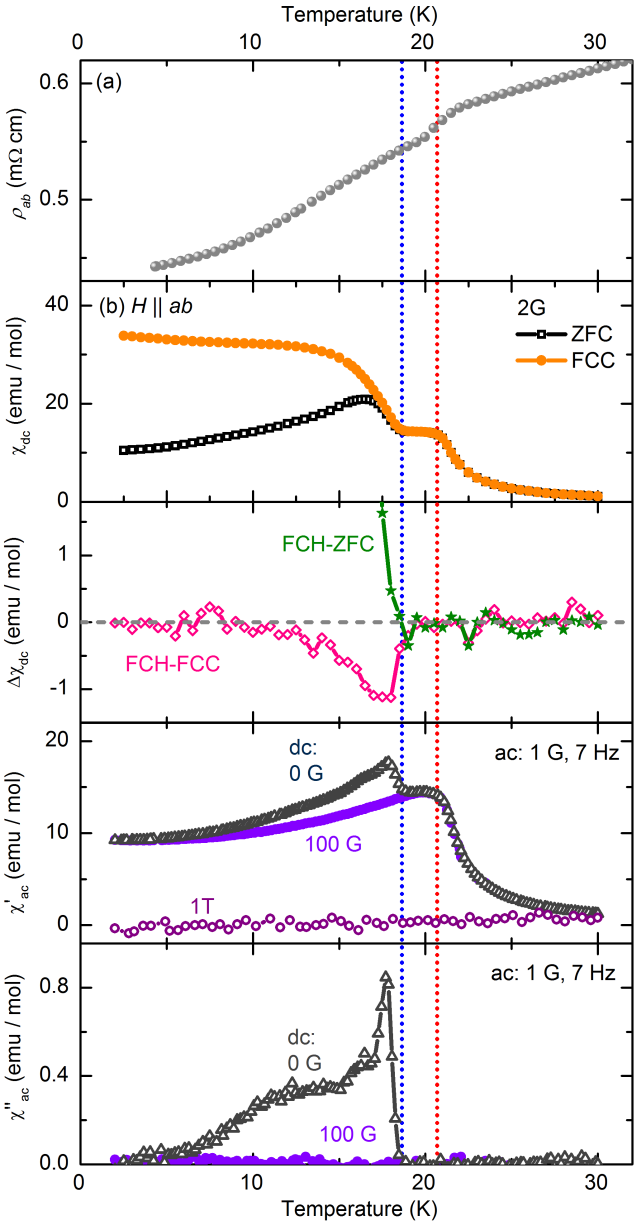


**Figure 7.11:** (a) Details of the resistivity curves as well as (b) in-plane magnetization curves ($H \parallel ab$) of $EuFe_2(As_{0.65}P_{0.35})_2$, in order to determine the transition temperatures. Dashed lines are guides to the eye, highlighting $T_1 \sim 20.7\,\mathrm{K}$ (red) and $T_2 \sim 18.8\,\mathrm{K}$ (blue). (a) The resistivity approaches 22 K rather linear. A sharp drop is visible around $T_1$, which fades in a broad shoulder at $\sim T_2$. (b) The in-plane ZFC (black open squares) and FCC (orange filled circles) magnetization shows at $H = 2\,\mathrm{G}$ two magnetic transitions similar to $x = 1.0$ (measured with the Quantum Design ultra low field option, see chapter 5.2). At $T < T_2$, a difference between ZFC and FCH curves sets in (green filled stars), and FC cycling reveals a glassy transition with $\chi_{\mathrm{dc,FCH}} - \chi_{\mathrm{dc,FCC}} < 0$ (pink open diamonds). Combining ac susceptibility measurements (drive 1 G, frequency 7 Hz) with dc fields (0 G: grey open triangles, 100 G: violet closed circles, 1 T: purple open circles), suppresses in $\chi'_{\mathrm{ac}}(T)$ already at 100 G the $T_2$ transition and at 1 T also the $T_1$ transition; however, there is no signature of negative susceptibility. $\chi''_{\mathrm{ac}}(T)$ shows a non-zero-signal below $T_2$, which is completely suppressed at 100 G.

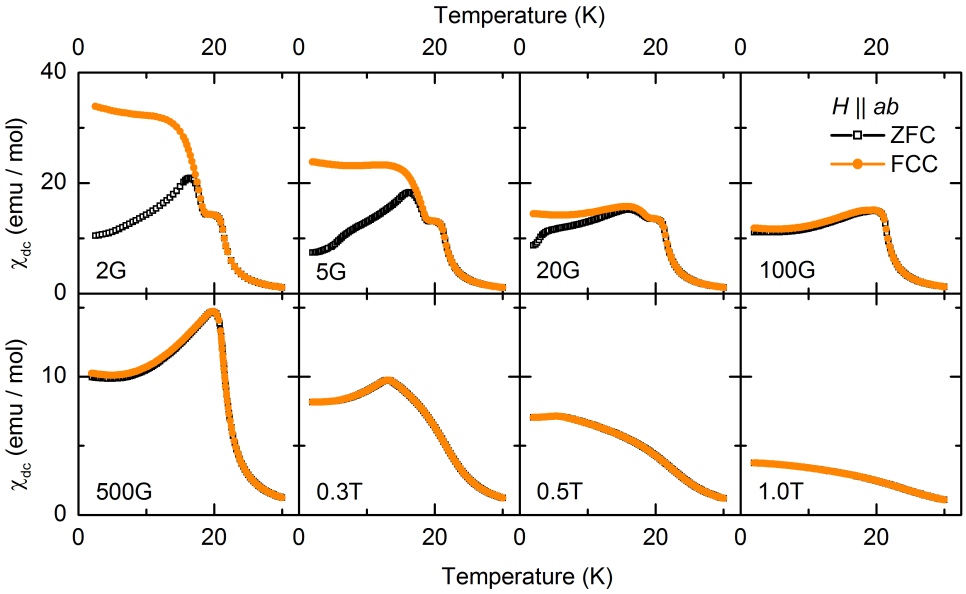


**Figure 7.12:** (a) ZFC (black open squares) and FCC (orange filled circles) in-plane magnetization curves of $EuFe_2(As_{0.65}P_{0.35})_2$ at $H = 2\,\mathrm{G}$, $5\,\mathrm{G}$, $20\,\mathrm{G}$, $100\,\mathrm{G}$, $500\,\mathrm{G}$, $0.3\,\mathrm{T}$, $0.5\,\mathrm{T}$ and $1.0\,\mathrm{T}$ ($H \parallel ab$, $2\,\mathrm{G}$ curves were measured with the Quantum Design ultra low field option, see chapter 5.2). The distinct in-plane low-temperature transition at $T_2$ (marked by a shoulder) has almost vanished at $100\,\mathrm{G}$.

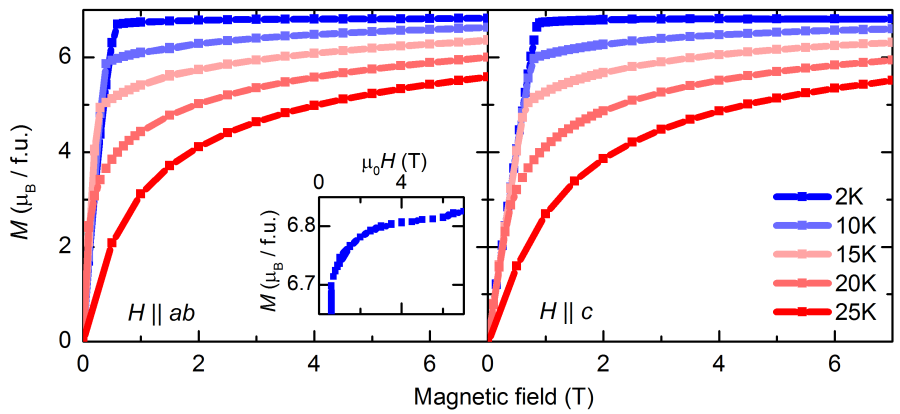


**Figure 7.13:** Field-dependent magnetization curves of $EuFe_2(As_{0.65}P_{0.35})_2$ for $H \parallel ab$ (left) and $H \parallel c$ (right), at several temperatures between $2\,\mathrm{K}$ (blue) and $25\,\mathrm{K}$ (red). No high-field hysteresis can be observed (see also inset).

## 7.3 Phase diagram

In order to follow the compositional dependence of the two magnetic transitions consistently found in $EuFe_2P_2$, $EuFe_2(As_{0.835}P_{0.165})_2$, and $EuFe_2(As_{0.65}P_{0.35})_2$, we have extended our studies to $EuFe_2(As_{1-x}P_x)_2$ single crystals with $x = 0$, 0.055, 0.09, 0.12, 0.16, 0.17, 0.26, 0.35 and 0.39; corresponding in-plane dc magnetization curves measured at 2 G are depicted in Fig. 7.14. In all P substituted specimen we observe two consecutive magnetic transitions, which we ascribe, in analogy to the previous sections, to a canted $A$-type antiferromagnetic transition at $T_1 = T_N$ and to a glassy freezing of the spin components in the $ab$-plane at $T_2 = T_{glass}$, with $T_N > T_{glass}$.

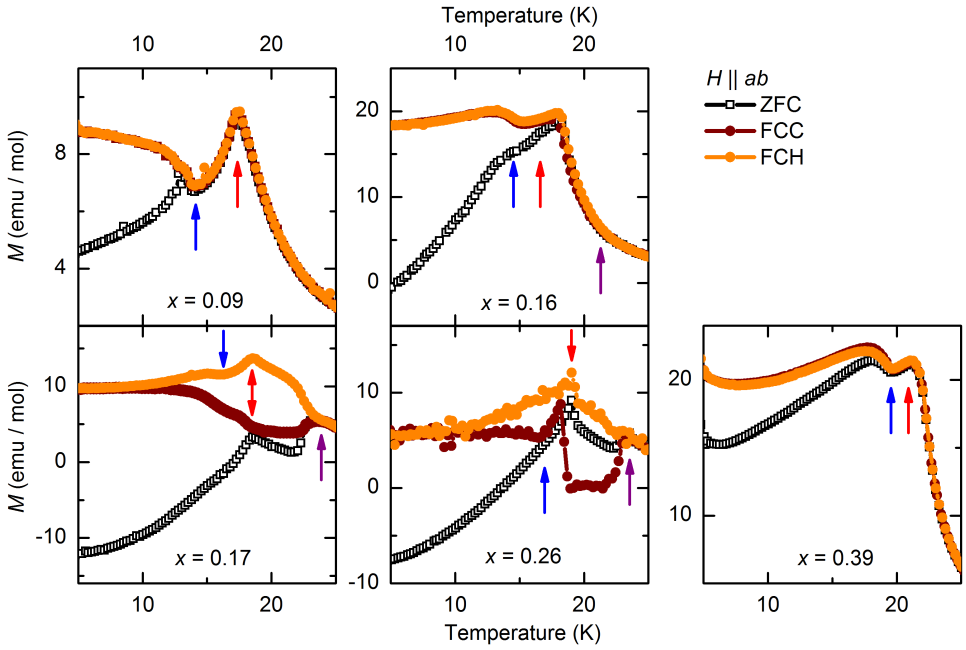


**Figure 7.14:** ZFC (black open squares), FCC (brown filled circles) and FCH (orange filled circles) in-plane magnetization curves of $EuFe_2(As_{1-x}P_x)_2$ with $x = 0.09$, 0.16, 0.17, 0.26 and 0.39 at $H = 2$ G ($H \parallel ab$). Arrows are guides to the eye, highlighting $T_{c,on}$ (purple), $T_1$ (red) and $T_2$ (blue).

In Fig. 7.15 we have compiled the resulting magnetic phase diagram together with the superconducting dome. According to our investigations on single crystals the re-entrant spin glass transition appears for all P substituted specimen. The effect of chemical disorder of the As and P anions on the RKKY-exchange must be ruled out as the origin of the glass transition since it occurs also in well-ordered $EuFe_2P_2$ crystals. We rather ascribe the glass transition to a competition of ferromagnetic interactions within a layer with antiferromagnetic RKKY-interactions between neighbouring layers.

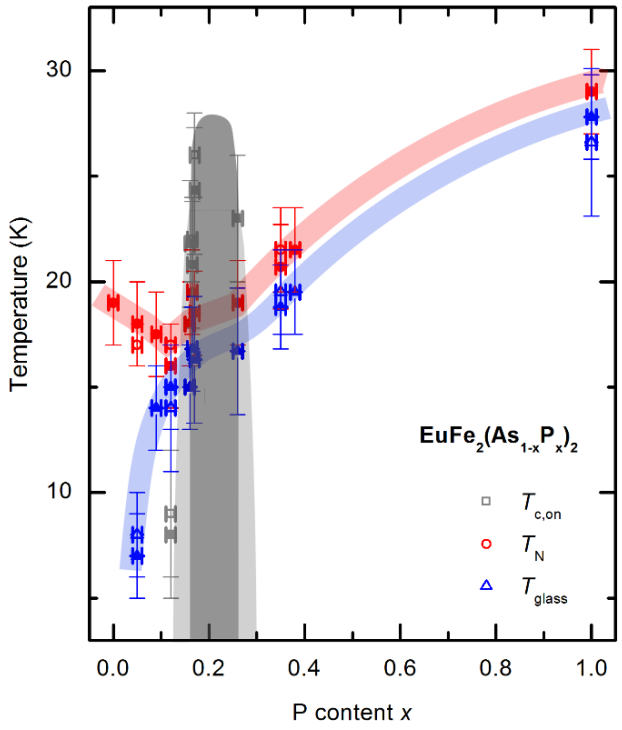


**Figure 7.15:** Phase Diagram of $EuFe_2(As_{1-x}P_x)_2$. $T_N = T_1$ (red dots) indicates a canted $A$-type antiferromagnetic transition, with a ferromagnetic net component of the $Eu^{2+}$ spins along the $c$-direction, $T_{glass} = T_2$ (blue triangles) a spin glass transition due to the freezing of the spins in the $ab$-plane and $T_{c,on}$ the onset of superconductivity (grey squares). Closed symbols indicate transition temperatures deduced from magnetization, open ones from resistivity measurements [305]. Shadowed lines are guides to the eye. The light grey area indicates the onset of superconductivity, while bulk superconductivity is fully developed in the dark grey regime [230, 238].

The transition temperatures exhibit a nonmonotonic behaviour with P substitution. At low P concentration, $0 < x \lesssim 0.12$, the antiferromagnetic $Eu^{2+}$ transition temperature follows the transition temperature of the spin density wave. Coupling of the itinerant Fe magnetism and the $Eu^{2+}$ local spin moments was theoretically predicted and experimentally confirmed by the increasing canting of spins out of the $ab$-plane concomitant with the suppression of the spin density wave (see section 7.1). With increasing canting, the ferromagnetic component of the $Eu^{2+}$ spins along the $c$-direction increases, and the competition with the antiferromagnetic RKKY-interaction between the layers is enhanced which finally leads to the development of the spin glass phase. In the superconducting regime, the transition temperatures vary only slightly with P concentration. When superconduc-

tivity is finally suppressed, both transition temperatures, $T_1$ and $T_2$, increase markedly, probably due to a Lifshitz transition [235, 238, 280] which affects the RKKY-exchange.

Antiferromagnetic interlayer coupling developing up to high P concentrations, as well as a rather narrow superconducting dome, are consistent with experiments on $EuFe_2As_2$ under pressure [222]. Between the concentrations $x \approx 0.12$ and $x \approx 0.26$ the onset of a superconducting transition is found, while fully developed bulk superconductivity occurs in an even narrower regime [230, 238]. As concluded previously, a Lifshitz transition near $x \approx 0.23$ coincides with the upper limit of superconductivity [235, 238, 280]. Investigations of polycrystalline samples, however, resulted in a somewhat broader dome extending to an upper limit of $x \approx 0.4$ [234, 236]. The assignment of the upper limit was based on the assumption that two subsequent resistivity anomalies seen in samples with $x \approx 0.4$ indicate the onset of superconductivity succeeded by a resistivity re-entrance due to $Eu^{2+}$ magnetic ordering. Our experiments on single crystals rather indicate that these two anomalies are purely of magnetic origin as we do not see any signature of superconductivity in our $x$=0.35 crystal.

## 7.4 Outlook

The main results of this chapter were already published in 2011 [9] and 2013 [10]. As the research on Eu based iron pnictides was pretty active since then, this section summarizes the response of the community on our results, as well as general conclusions we can draw for Eu based iron pnictides.

### Eu magnetism

The idea of a ferromagnetic component along the $c$-axis due to the $Eu^{2+}$ spin canting was directly accepted by the community for $EuFe_2(As_{1-x}P_x)_2$ [236], as well as evidenced for Co and Ir doped compounds [33, 253, 254, 257, 263]. We want to note, however, that we would be very careful to interpret the different absolute values of $ab$-plane and $c$-axis magnetization as being connected to this canting [253]: demagnetization effects (see chapter 2.1) play a very important role for the rare earth systems - even in the paramagnetic phase close to the magnetic transition(s) - as can be seen in Fig. 7.16 for the parent compound[1]. When recalculating the susceptibility by considering a demagnetization factor close to that of an infinite flat plate ($N_c \to 1$; the sample thickness is two orders of mag-

1 The volume of the sample was calculated by its mass, molar mass, and the lattice constants published in Ref. [230].

nitude smaller than the in-plane dimensions), one can basically suppress and even reverse the anisotropy.

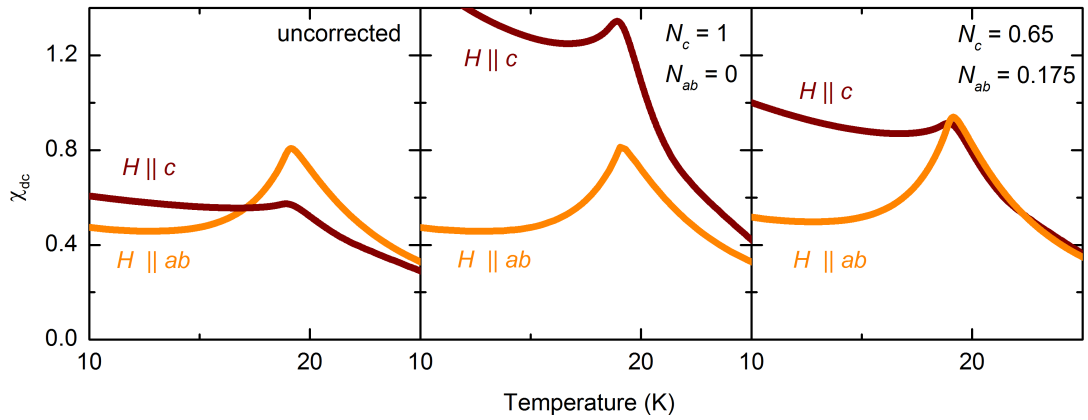


**Figure 7.16:** (a) Temperature-dependent volume ($V$) susceptibility $\chi_{\mathrm{dc}}(T) = M(T)/\mu_0 H/V$ of $EuFe_2As_2$ for $H \parallel ab$ (orange) and $H \parallel c$ (brown) at $H = 20\,\mathrm{G}$: (a) as measured; (b) corrected with the demagnetization factor $N_c = 1$, $N_{ab} = 0$; (c) corrected with $N_c = 0.65$, $N_{ab} = 0.175$. Demagnetization effects are strong enough to reduce or even reverse the anisotropy of $\chi_{\mathrm{dc}}(T)$.

Furthermore, we want to stress that antiferromagnetic interlayer coupling developing up to high P concentrations is consistent with experiments on $EuFe_2As_2$ under pressure [222]. Recent neutron measurements suggest for superconducting Co as well as P substituted compounds that the $Eu^{2+}$ moments are basically aligned along the $c$-axis; a second transition was either not detected [241, 259] or attributed to a minority phase [241]. Importantly, this is not contradictory to our results of the re-entrant spin glass phase: first of all, the neutron measurements can not exclude a small spin component staying in the $ab$-plane; secondly, we do not expect any typical antiferromagnetic signal in the re-entrant spin glass phase. For the future, we suggest neutron studies under an in-plane magnetic field that suppresses the spin glass phase; in this case, possibly antiferromagnetic reflections could be detected.

Finally, we want to note that successive magnetic orderings can be identified also in the case of Ru substitution [31], Co doping [250, 251, 256, 257] and Ir doping [263]. This implies the appearance of a re-entrant spin glass phase in all those compounds.

Therefore, we conclude that our magnetic phase diagram derived for $EuFe_2(As_{1-x}P_x)_2$ (see Fig. 7.15) is characteristic for (non-diluted) Eu based iron pnictides. In order to confirm this, we suggest time-dependent measurements also on other compounds.

### Interplay of superconductivity and magnetism

The question how bulk superconductivity can coexist with $Eu^{2+}$ magnetic ordering is quite fundamental and requires the exact knowledge of the magnetic structure. Consistent with Mössbauer and neutron powder diffraction [212, 234, 241], the results of our experiments imply that in superconducting samples, a large net component of the $Eu^{2+}$ spins is ferromagnetically aligned perpendicular to the layers. In addition, we find that glass-like dynamics and freezing of the in-plane component develops below $T_2$ which destroys coherence between the Eu layers. Superconductivity in the iron pnictides is commonly believed to take place mainly in the FeAs layers. In this scenario, the inner field resulting from the $Eu^{2+}$ ferromagnetic component along the $c$-axis could be screened by the formation of spontaneous vortices perpendicular to the layers [31]. Together with the destroyed coherence between the Eu layers due to the glass dynamics, this scenario might be the key to understand how superconductivity can coexist with the usually strong $Eu^{2+}$ magnetism.

# 8

# OPTICAL PROPERTIES OF $EuFe_2As_2$

In this chapter, the in-plane optical response of $EuFe_2As_2$ is analysed. Particular focus is set on the applicability of different modelling approaches, and the determination of model-independent trends.

## 8.1 Overview

The temperature-dependent in-plane optical reflectivity of $EuFe_2As_2$ was measured in a wide frequency range from 40 to 10000 $cm^{-1}$ (see chapter 5.1), using an infrared Fourier transform spectrometer; the corresponding optical conductivity was calculated via the Kramer's Kronig analysis. For the low-frequency extrapolation, in a first iteration the Hagen Rubens relation was used, which got subsequently replaced in the fitting process; the thus determined temperature-dependence of $\sigma_{dc}$ follows nicely the resistivity curve (as will be shown below). At high frequencies, the optical response was extended up to 30000 $cm^{-1}$ by room temperature measurements with a Woollam spectroscopic ellipsometer[1]; higher frequencies were extrapolated following measurements up to 32 eV carried out for $BaFe_2As_2$ [169].

1 Ellipsometry measurements were performed by J. Braun at the 1. Physical Institute, Stuttgart.

Fig. 8.1a,b displays the thus obtained spectra at 200 K and 290 K, focusing on the high frequency range. There is considerable spectral weight transfer up to very high energies, which probably can be ascribed to Hund's coupling (see chapter 4.4.5); the total spectral weight is not recovered in the infrared frequency range.

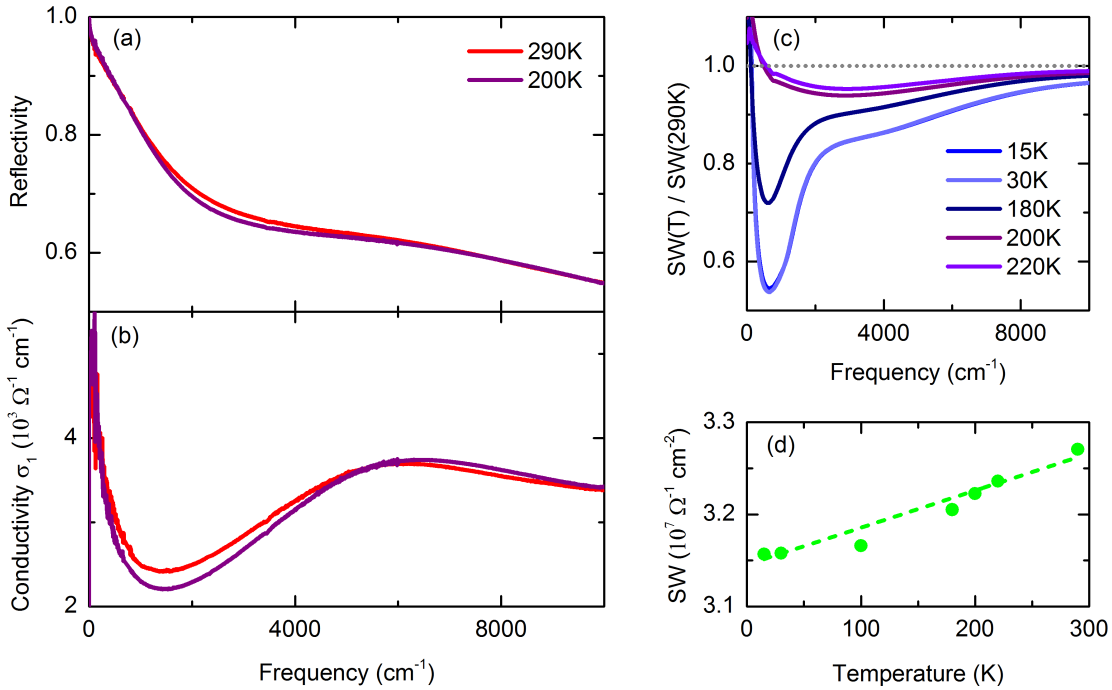


**Figure 8.1:** (a-b) Frequency-dependent in-plane reflectivity and conductivity of $EuFe_2As_2$ at $T$ =200 K (purple) and 290 K (red), as well as (c-d) spectral weight (SW) analysis. While (c) displays the frequency-dependent spectral weight for 15 K (blue), 30 K (light blue), 180 K (dark blue), 200 K (purple) and 220 K (violet) normalized to 290 K, (d) shows the total spectral weight at 10000 $cm^{-1}$; the linear fit (green dashed line) acts as a guide to the eye. With decreasing temperature, spectral weight is shifted to high energies (above $\sim$ 6000 $cm^{-1}$); the total spectral weight is not recovered at 10000 $cm^{-1}$.

At $T < T_{s,SDW} = 190$ K, a gap develops in the optical spectrum, and additional spectral weight transfer appears at low energies (see Fig. 8.1f and Fig. 8.2). We find only one clearly visible gap, leading at 15 K to a peak in the optical conductivity around 1400 $cm^{-1} \approx 10.8\ k_B T_{s,SDW}$. Its asymmetric shape is typical for a spin density wave gap (see chapter 4.3), but could indicate also the existence of two neighbouring features (as theoretically proposed by Yin *et al.* [168]). One should further note the FeAs phonon at around 260 $cm^{-1}$, which gains at $T < T_{s,SDW}$ considerably oscillator strength and shifts to higher frequencies.

Our finding of a single spin density wave gap is consistent with Ref. [184], however, we are also aware that an additional smaller gap around the BCS weak coupling limit was

reported by Moon *et al.* [146]. As we investigated a sample of the same batch as Ref. [184], one can speculate that the occurrence of the low-energy feature might strongly depend on the sample quality[1], but we are not aware of any similar reports for other compounds. Therefore, it is intriguing to relate this untypical behaviour to the influence of the $Eu^{2+}$ magnetism. Unfortunately, while there are predictions for the influence of the spin density wave on the $Eu^{2+}$ magnetism [11], the reverse case is - to our best knowledge - not yet considered theoretically. Furthermore, one should note that the spectra at 15 K and 30 K are basically the same within the experimental error, meaning that $Eu^{2+}$ spin scattering seems to have a negligible influence on the optical properties in the infrared frequency range.

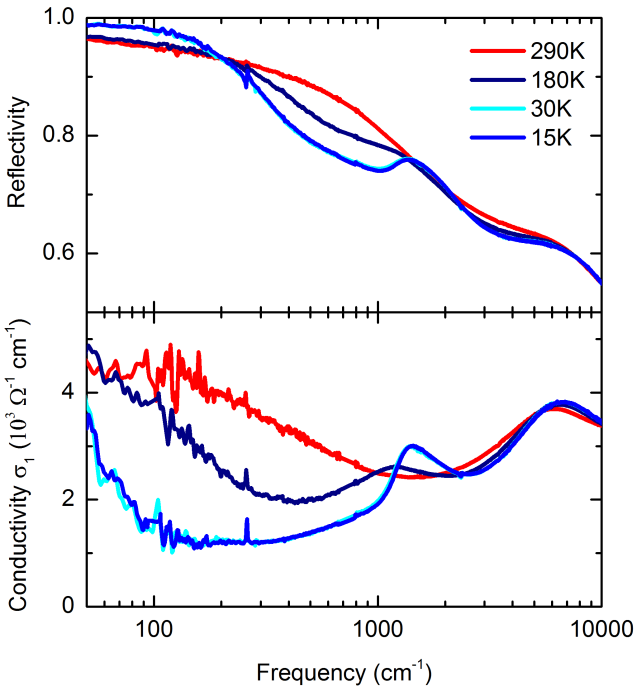


**Figure 8.2:** Frequency-dependent in-plane reflectivity and conductivity of $EuFe_2As_2$ at $T$ =15 K (blue), 30 K (light cyan), 180 K (dark blue) and 290 K (red). At $T < T_{s,SDW}$, a gap develops in the optical spectrum and spectral weight is shifted to $\sim 1150\,cm^{-1}$ and $\sim 1400\,cm^{-1}$ at 180 K and 15 K, respectively; furthermore, the FeAs phonon at around $260\,cm^{-1}$ gains considerably oscillator strength. One should note that the spectra at 15 K and 30 K are the same within the resolution. The noise visible in the conductivity spectrum at low frequencies is typical for a reflectivity close to unity; data are not smoothed.

1 While our sample has a residual resistivity ratio R(300 K)/R(5 K) of $\sim 4.1$, the one of Moon *et al.* has only a ratio of $\sim 2.4$.

## 8.2 Multi-component analysis

As already discussed in chapter 4.4.2, the multiband character of iron pnictides complicates any analysis of optical spectra. Different multi-component models exist, however, it is still not clear which one should be favoured and how much the modelling influences the outcome of the analysis. Therefore, we have analyzed the optical response of twinned $EuFe_2As_2$, using three different modeling approaches and discuss the commonly found features. Importantly, we always show (semi-)logarithmic and linear plots, emphasizing the low- and high-energy range, respectively.

### Broad Drude approach

In 2010, Wu *et al.* proposed that the spectra of iron pnictides contain a temperature-independent background in the mid-infrared energy range that can be fitted by a very broad Drude term [128, 130]. However, a closer inspection reveals that such a temperature-independent approximation is too rough due to the considerable spectral weight transfer up to very high energies (see Fig. 8.1).

In order to investigate, whether such a broad Drude approach with temperature-dependent parameters can be used to nicely describe the infrared response of $EuFe_2As_2$, Fig. 8.3 and Fig. 8.4 display the thus fitted spectra at 290 K and 15 K, respectively. At 290 K, the overall fit quality is good; however, one can note a slight discrepancy in the far-infrared, where the fit first over- and then underestimates the response.

Indeed, this is exactly the energy range, where the model fails at low temperatures: at 15 K, an upturn of the conductivity above $\sim 350\,\mathrm{cm}^{-1}$ implies an additional, broad Lorentzian at frequencies above $1000\,\mathrm{cm}^{-1}$. Fig. 8.4 excludes that a broad Lorentzian around $3.4k_\mathrm{B}T_{\mathrm{s,SDW}}$ (the smaller gap found by Moon *et al.* [146]) can describe this feature. Therefore, we conclude that the broad Drude approach is too oversimplified in order to model nicely the far-infrared response of iron pnictides.

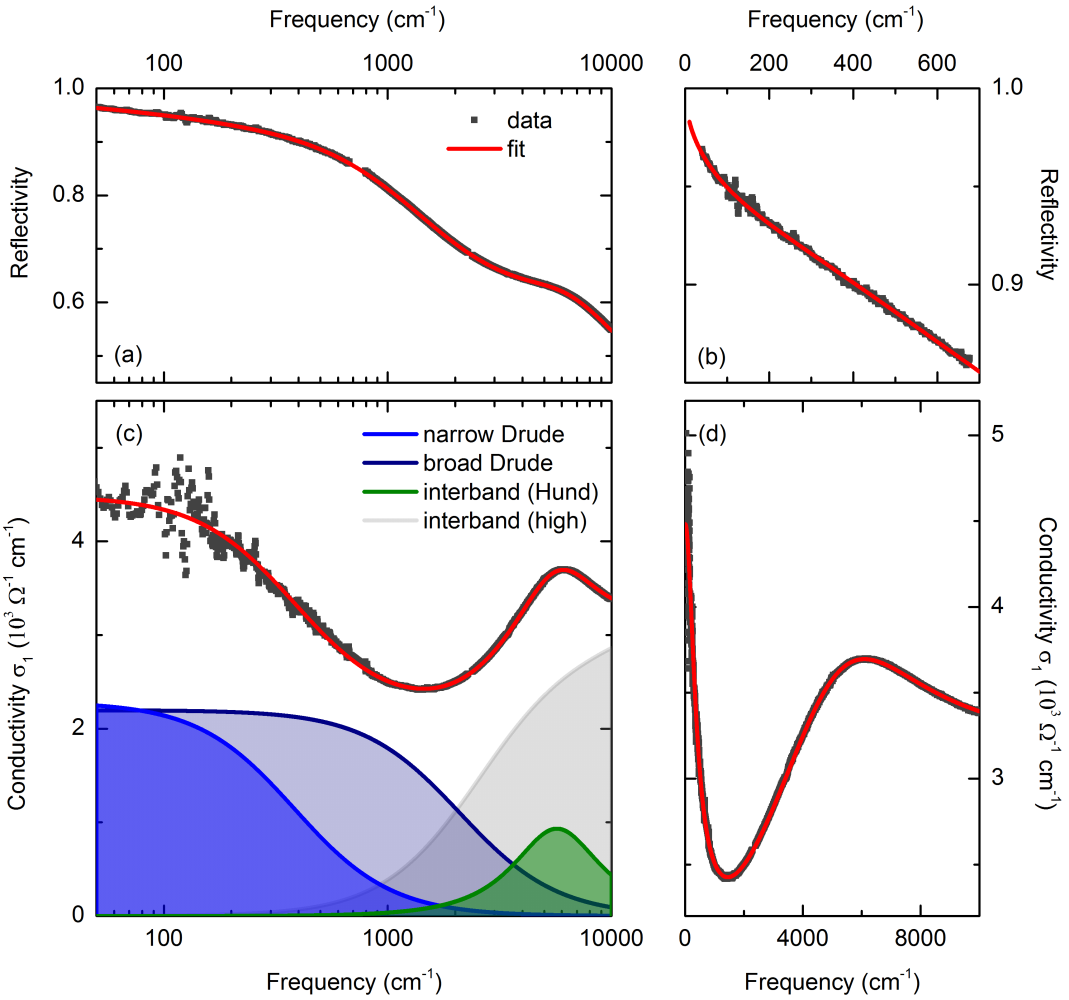


**Figure 8.3:** Frequency-dependent in-plane (a-b) reflectivity and (c-d) conductivity of $EuFe_2As_2$ at $T$ =290 K in different logarithmic and linear plot styles. Grey squares represent data points, red lines the result of a broad Drude fit; the composition of the single components is displayed in (c). The overall fit quality of the broad Drude approach is good; slight discrepancies can be found in the far-infrared.

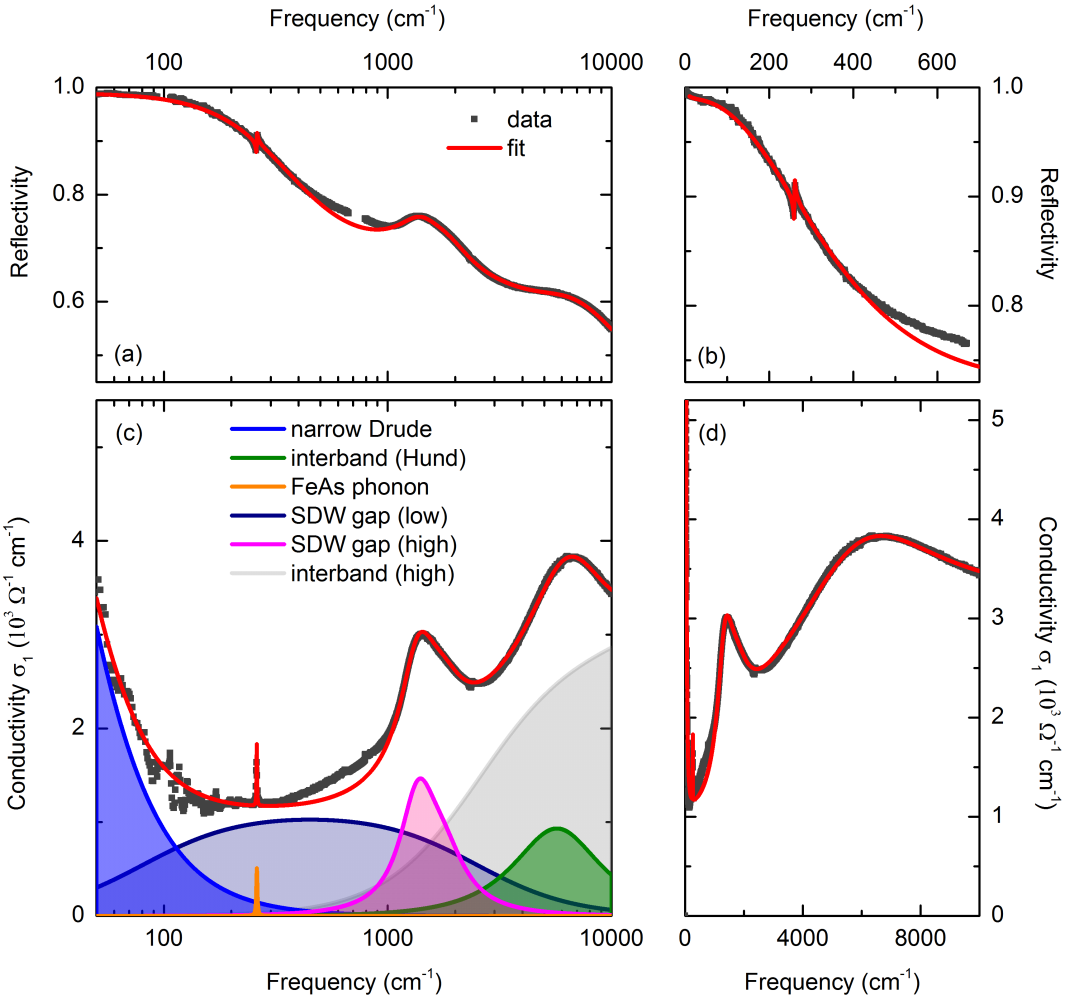


**Figure 8.4:** Frequency-dependent in-plane (a-b) reflectivity and (c-d) conductivity of $EuFe_2As_2$ at $T$ =15 K in different logarithmic and linear plot styles. Grey squares represent data points, red lines the result of a broad Drude fit; the composition of the single components is displayed in (c). A spin density wave gap leads to the piling up of an asymmetric peak at $\sim 1400\,\mathrm{cm}^{-1} \approx 10.8 k_\mathrm{B} T_\mathrm{s,SDW}$. The broad Drude approach fails to fit the spectra between $\sim 350\,\mathrm{cm}^{-1}$ and $1000\,\mathrm{cm}^{-1}$, even if we assume that the broader Drude is gapped with a gap value of $3.4 k_\mathrm{B} T_\mathrm{s,SDW}$.

### MIR band approach

As already noted by Tu *et al.* [142], a multi-component analysis with only one Drude and a series of Lorentzians that model incoherent transport in the mid-infrared is able to describe the carrier dynamics of iron pnictides. Fig. 8.5 and Fig. 8.6 prove that such a fitting approach is able to nicely describe spectra at high and low temperatures, respectively.

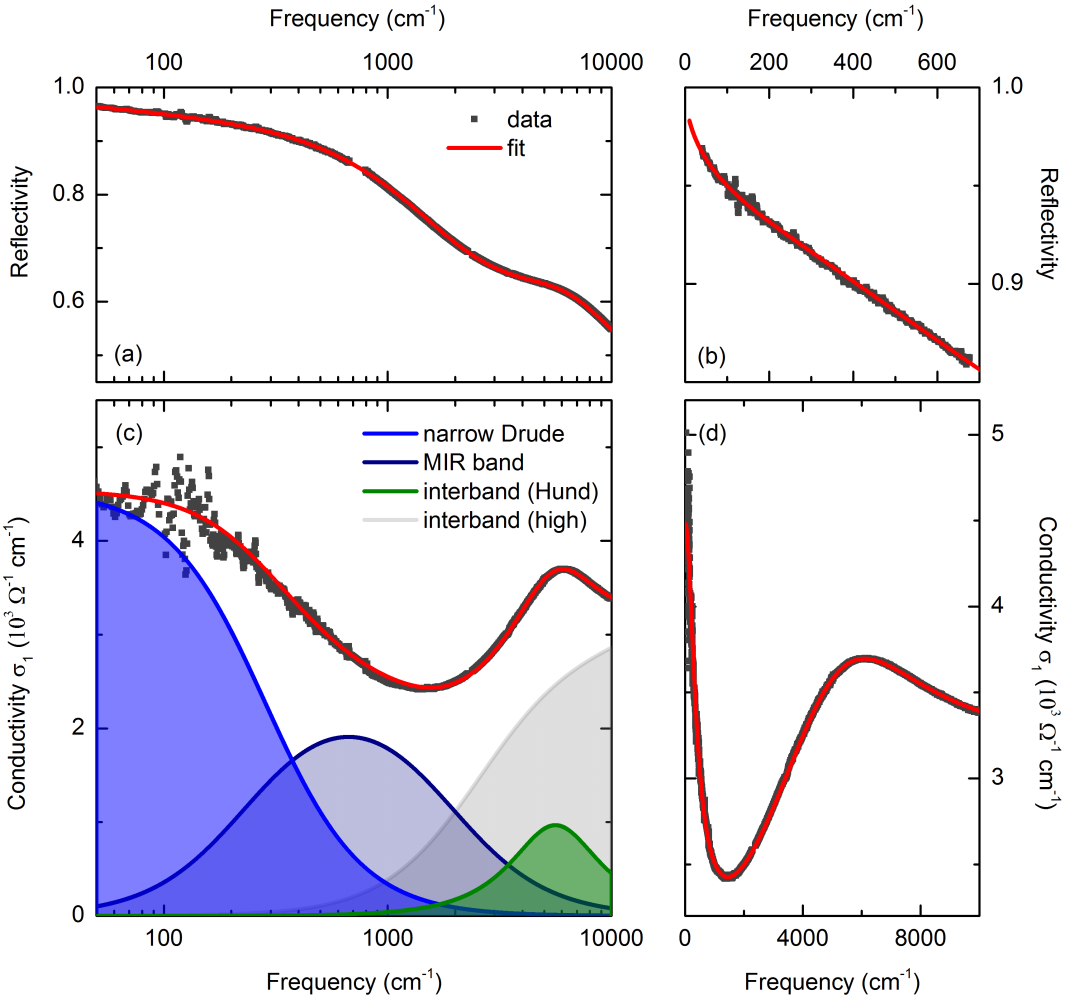


**Figure 8.5:** Frequency-dependent in-plane (a-b) reflectivity and (c-d) conductivity of $EuFe_2As_2$ at $T$ =290 K in different logarithmic and linear plot styles. Grey squares represent data points, red lines the result of a MIR band fit; the composition of the single components is displayed in (c). The MIR band approach nicely describes the spectra above $T_{s,SDW}$.

The corresponding temperature-dependent fit parameters are displayed in Fig. 8.7. Typically for a metal, the Drude component narrows smoothly with decreasing temperature, until the scattering rate rapidly decreases for $T < T_{s,SDW}$ (see Fig. 8.7a). One should note that the obtained $\sigma_{dc}$ values perfectly follow the temperature-dependence of the resistivity.

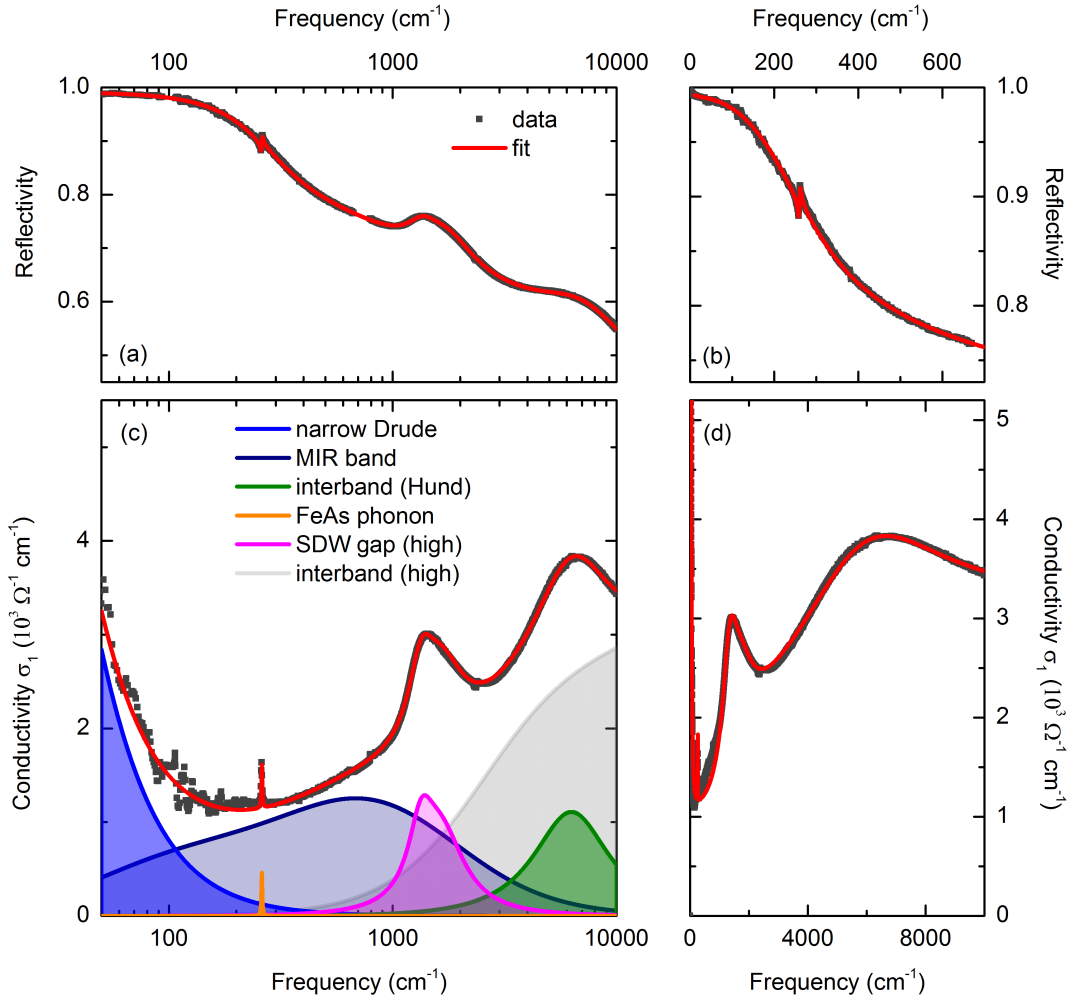


**Figure 8.6:** Frequency-dependent in-plane (a-b) reflectivity and (c-d) conductivity of $EuFe_2As_2$ at $T$ =15 K in different logarithmic and linear plot styles. Grey squares represent data points, red lines the result of a MIR band fit; the composition of the single components is displayed in (c). The MIR band approach nicely describes the spectra below $T_{s,SDW}$.

However, the increase of $\sigma_{dc}$ with lowering temperature does not outweigh the decrease of the scattering rate: Drude spectral weight is already lost above the spin density wave transition. As can be seen in Fig. 8.7c, at $T > T_{s,SDW}$, the spectral weight is transferred to the hump-like structure around 6000 $cm^{-1}$ (and even higher energies), which shows a significant blueshift with decreasing temperature; any spectral weight transfer is stopped below the spin density wave transition. Interestingly, the width of this feature is constant above $T_{s,SDW}$, but decreases rapidly at $T < T_{s,SDW}$ - directly reflecting the behaviour of the Drude component. Those observations indicate a strong relationship to the dynamics

of the itinerant carriers, consistent with the suggestion that the bump originates from Hund's coupling.

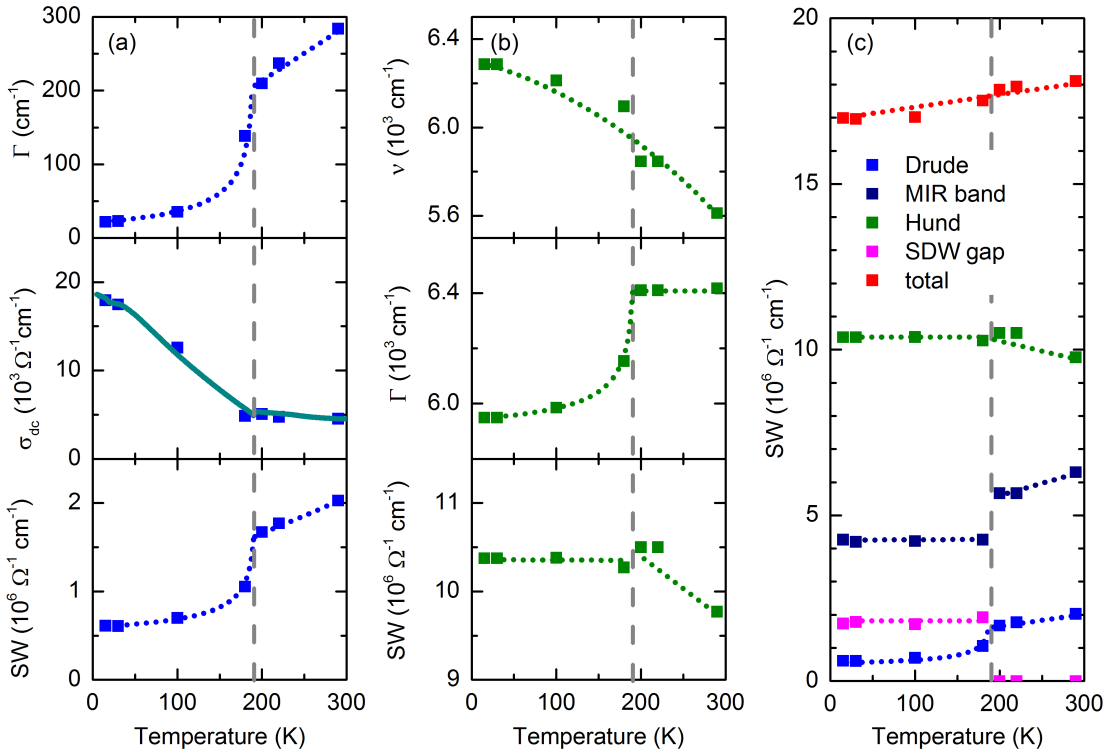


**Figure 8.7:** Temperature-dependent fit parameters for the MIR band approach: (a) Scattering rate $\Gamma$, $\sigma_{\mathrm{dc}}$ compared to results from resistivity measurements (normalized to $\sigma_{\mathrm{dc}}$(300K), cyan curve), and spectral weight (SW) of the Drude component; (b) Center frequency $\nu$, damping $\Gamma$ and spectral weight (SW) of the feature that is attributed to Hund's coupling; (c) spectral weight of the temperature-dependent components. The grey, vertical dashed line denotes $T_{\mathrm{s,SDW}}$; other dashed lines are a guide to the eye.

Fig. 8.7d also displays the spectral weight of the other temperature-dependent fit components. Their total spectral weight decreases with decreasing temperature, as was already discussed in the general spectral weight analysis (see Fig. 8.1). As the MIR band follows the behaviour of the Drude component, it probably contains a strong contribution from itinerant carriers; indeed, the spectral weight gapped in the spin density wave phase mostly corresponds to changes in the mid-infrared frequency range.

### Subtraction approach

As in general, a model that includes two Drude components as well as a mid-infrared band is overdetermined, one needs additional information for a reasonable fitting approach. Here, we focus on the result of recent infrared studies: by subtracting low temperature conductivity spectra from that at room temperature, Marsik *et al.* found for Ba, Sr and Ca compounds a well-defined feature around 1000 $cm^{-1}$ that could be attributed to interband transitions involving Fe hole pockets [12].

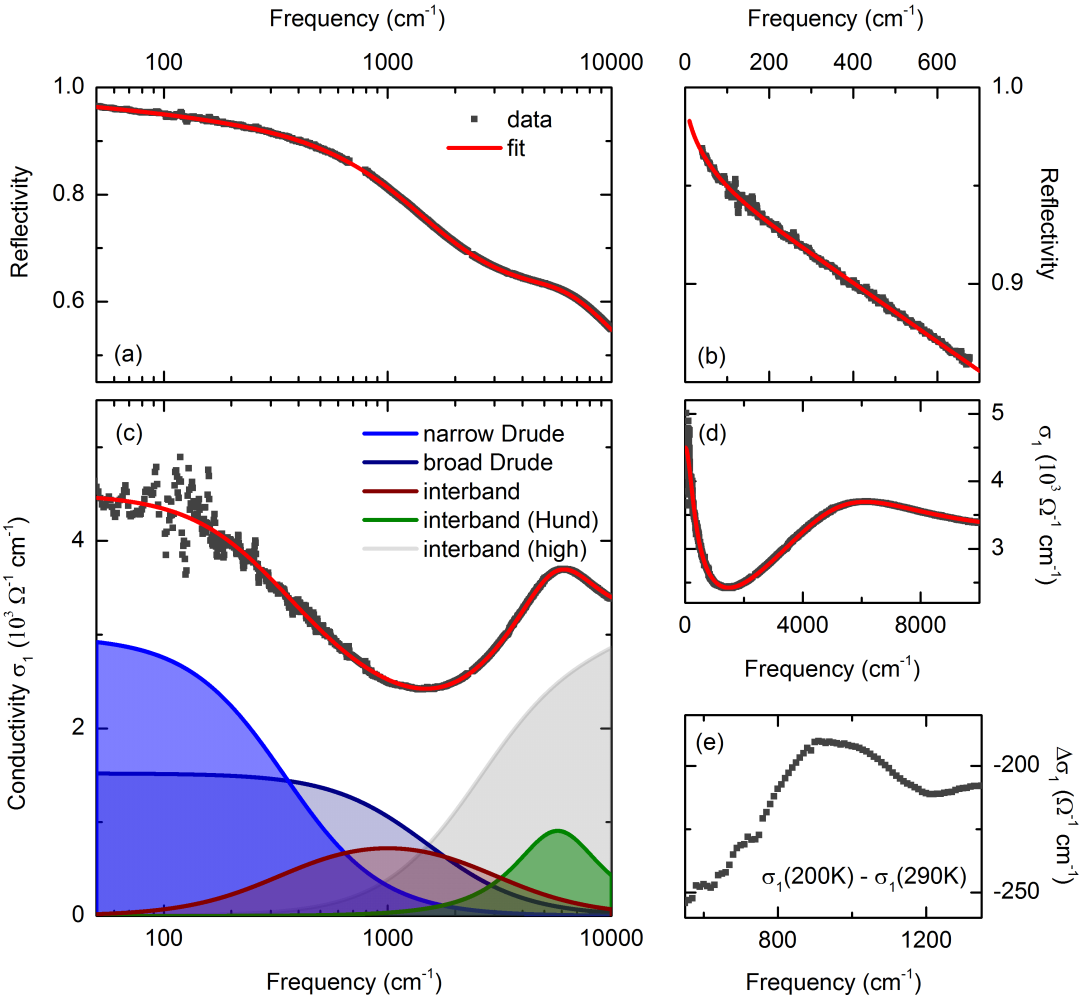


**Figure 8.8:** Frequency-dependent in-plane (a-b) reflectivity and (c-d) conductivity of $EuFe_2As_2$ at $T$ =290 K in different logarithmic and linear plot styles, as well as (e) the conductivity difference $\Delta\sigma_1 = \sigma_1(200\text{K}) - \sigma_1(290\text{K})$. Grey squares represent data points, red lines the result of a fit with two Drude components and a Lorentzian at 1000 $cm^{-1}$ that can be attributed to interband transitions involving Fe hole pockets; the composition of the single components is displayed in (c). The fitting approach nicely describes the spectra above $T_{s,SDW}$.

We believe that such a subtraction feature can be nicely described by a Lorentzian at 1000 $\mathrm{cm}^{-1}$ that broadens with increasing temperature. Indeed, $EuFe_2As_2$ shows the same feature (see Fig. 8.8e). Therefore, we have fitted the spectra with two Drude components and one Lorentzian at 1000 $\mathrm{cm}^{-1}$ that broadens with increasing temperature; the other fit parameters of the Lorentzian are held constant in first approximation. As can be seen in Fig. 8.8 and Fig. 8.9, the spectra can be nicely described by this approach.

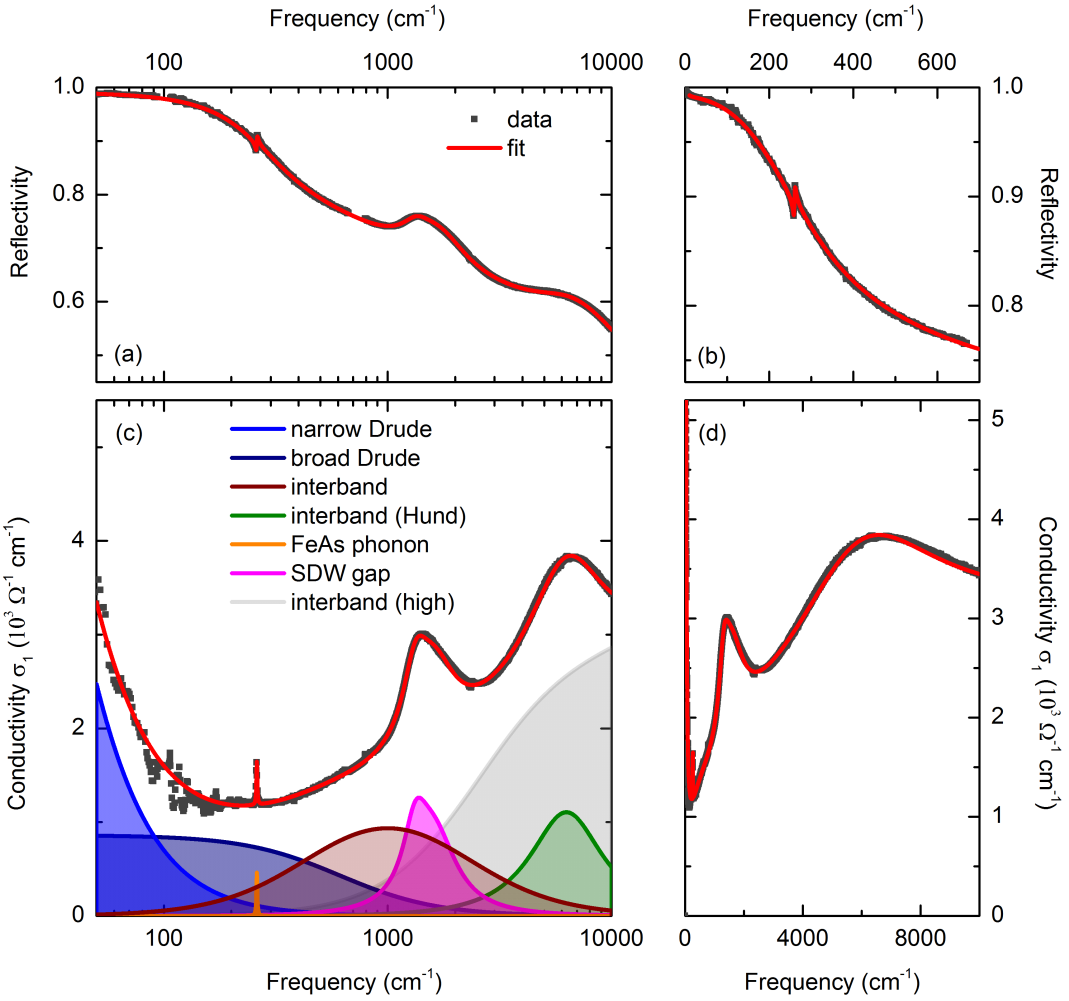


**Figure 8.9:** Frequency-dependent in-plane (a-b) reflectivity and (c-d) conductivity of $EuFe_2As_2$ at $T$ =15 K in different logarithmic and linear plot styles. Grey squares represent data points, red lines the result of a fit with two Drude components and a Lorentzian at 1000 $\mathrm{cm}^{-1}$ that can be attributed to interband transitions involving Fe hole pockets; the composition of the single components is displayed in (c). The fitting approach nicely describes the spectra below $T_{\mathrm{s,SDW}}$.

However, one should note that other fitting variants are possible, too; for instance, we have also fitted the high-temperature spectra under the condition that the broader

Drude should not get too broad (not to violate the Mott-Ioffe-Regel limit), allowing a changing spectral weight of the Lorentzian at 1000 $cm^{-1}$. The corresponding temperature-dependent fit parameters of both fitting approaches are displayed in Fig. 8.10. The results for the narrow Drude and the bump around 6000 $cm^{-1}$ are independent from the fitting approach. However, we can not disentangle the parameters for the broad Drude and the Lorentzian at 1000 $cm^{-1}$; a realistic description probably lies in between or even contains more temperature-dependent Lorentzians (for example another one at 2300 $cm^{-1}$ [12]). However, we want to point out that with this model, we only see gap-like features in the spectral weight of the Drude components, proving that this description is more realistic than a general MIR band approach with only one Drude.

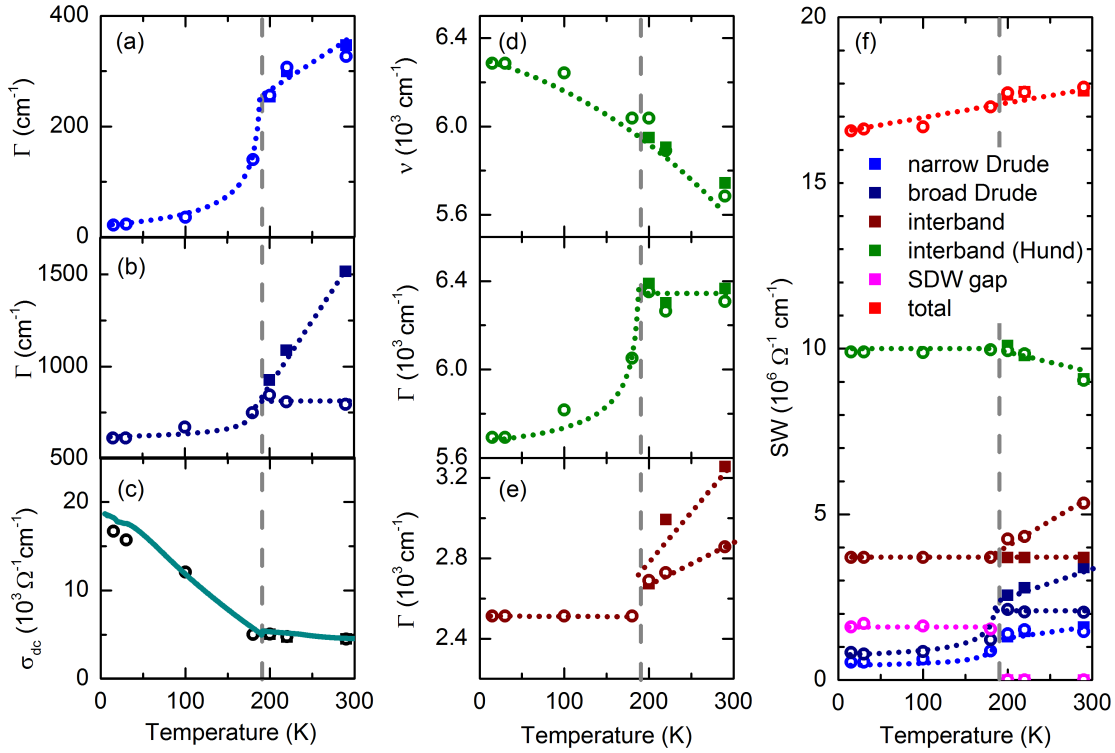


**Figure 8.10:** Temperature-dependent fit parameters for the model with two Drude components and a Lorentzian at 1000 $cm^{-1}$ under two different constraints: in the one case (filled squares), only the damping of the Lorentzian was changed; in the other case (open points), the scattering rate of the broad Drude was forced significantly below 1000 $cm^{-1}$. (a) Scattering rate $\Gamma$ of the narrow Drude; (b) scattering rate $\Gamma$ of the broad Drude; (c) $\sigma_{dc}$ (sum of both Drude components) compared to results from resistivity measurements (normalized to $\sigma_{dc}$(300K), cyan curve); (d) Center frequency $\nu$ and damping $\Gamma$ of the feature that is attributed to Hund's coupling; (e) damping $\Gamma$ of the Lorentzian at 1000 $cm^{-1}$; (f) spectral weight of the temperature-dependent components. The grey, vertical dashed line denotes $T_{s,SDW}$; other dashed lines are a guide to the eye.

### Summary

We have shown exemplarily on $EuFe_2As_2$ that a broad Drude model without any additional interband transitions in the mid-infrared is too oversimplified to describe the temperature-dependent spectra of iron pnictides. In contrast, a more general MIR band approach yields better results. The most realistic results are obtained with a model that contains two Drude components (probably representing electron and hole bands) and a Lorentzian at $1000\,\mathrm{cm}^{-1}$, which can be attributed to interband transitions involving Fe hole pockets [12].

In particular, we find that some fitting results are independent from the model:

- The spin density wave gap affects the spectral weight and the scattering rate of both Drude components.
- For temperatures above $T_{\mathrm{s,SDW}}$, spectral weight is transferred from the narrow Drude, but also from higher frequencies in the mid-infrared (and thus either from the broad Drude or the interband transition at $1000\,\mathrm{cm}^{-1}$), to the bump-like structure around $6000\,\mathrm{cm}^{-1}$ and even higher energies. At $T < T_{\mathrm{s,SDW}}$, this spectral weight transfer stops and the bump considerably narrows - directly reflecting the behaviour of the Drude component(s). Those observations indicate a strong relationship to the dynamics of the itinerant carriers, consistent with the suggestion that the bump originates from Hund's coupling.

# 9

# MAGNETIC DETWINNING OF $EuFe_2As_2$

As it was known that $EuFe_2As_2$ can be completely detwinned by applying relatively small magnetic fields ($\sim 1\,\mathrm{T}$) at temperatures $T < T_{\mathrm{Eu}}$ (see chapter 6.3.1), we performed a series of magneto-optical measurements in order to study the electronic in-plane anisotropy of iron pnictides without the need of complex mechanical detwinning devices. In this chapter, we concentrate on the results from magneto-optical FIR measurements, which revealed a much more complicated magnetic detwinning mechanism than expected from previous neutron studies [7]. Combined with magnetization measurements, the observations can be explained by an indirect magnetoelastic coupling of the $Eu^{2+}$ spins to the lattice. Those findings are further confirmed by resistivity, magneto-resistance, thermal expansion and magnetostriction measurements and are published in Ref. [13]. Finally, preliminary results on infrared measurements over a broad frequency range on persistently detwinned $EuFe_2As_2$ are presented.

For all measurements, a well-defined cooling procedure was obeyed: first, the sample was cooled from $T > T_{\mathrm{s,SDW}}$ to low temperatures in zero magnetic field and the zero-field cooled (ZFC) response was measured. Afterwards, when an in-plane magnetic field

parallel to the $[110]_T$-direction[1] was first applied and then removed, we call this "field treatment" (FT).

## 9.1 Magneto-optical measurements

The far-infrared spectral range is ideal to investigate the detwinning mechanism, as it is governed by the anisotropic spin density wave gap as well as the FeAs phonon, and the zero-field reflectivity is not notably influenced by the $Eu^{2+}$ spin scattering (see chapter 8).

**Detwinning at $T < T_{Eu}$**

Fig. 9.1 displays the FIR reflectivity of $EuFe_2As_2$ at $T = 15\,K$ for $H \parallel [110]_T$ with $H = 0\,T$ (ZFC), $1.0\,T$, and $0\,T$ after field treatment (with $1\,T$). The main observations can be summarized as:

- The zero-field cooled $0\,T$ curves perfectly merge, indicating an initially balanced twin domain ratio[2].
- At a magnetic field of $1\,T$, a notable difference is induced between the two polarizations: while the reflectivity is enhanced for $E \parallel H$, it is suppressed for the perpendicular polarization. At the same time, the FeAs phonon gets strongly reduced for $E \parallel H$ and enhanced for the perpendicular direction. In accordance with optical studies on $BaFe_2As_2$ using mechanical clamps (see chapter 4.4.5), those observations indicate that the crystal is detwinned with the orthorhombic $a$-axis being aligned along the external field: $a \parallel H$. This is consistent with the results from neutron studies [7].
- Surprisingly, we also observe a notable difference between the two polarizations after the magnetic field is switched off, opposite to that at $1\,T$. This indicates a second detwinning process with $b \parallel H$ at even lower magnetic fields, which stays persistent after the field is removed.

In order to investigate this two-step detwinning process in more detail, we have performed a series of magneto-optical FIR measurements with small field steps of $\leq 0.1\,T$. The results for $E \perp H$ are shown in Fig. 9.2 and 9.3; for clarity, the relative reflectivity

1 We adapt the notation of the tetragonal system $[hkl]_T$ which is rotated by $45\,^\circ$ along the $c$-axis with respect to the orthorhombic system $[hkl]_O$, e.g. $[110]_T = [100]_O$

2 The sample was mounted point-like on a copper cone. This avoids not only back-reflections from the sample holder, but also minimizes the glued area and therefore external stress on the sample.

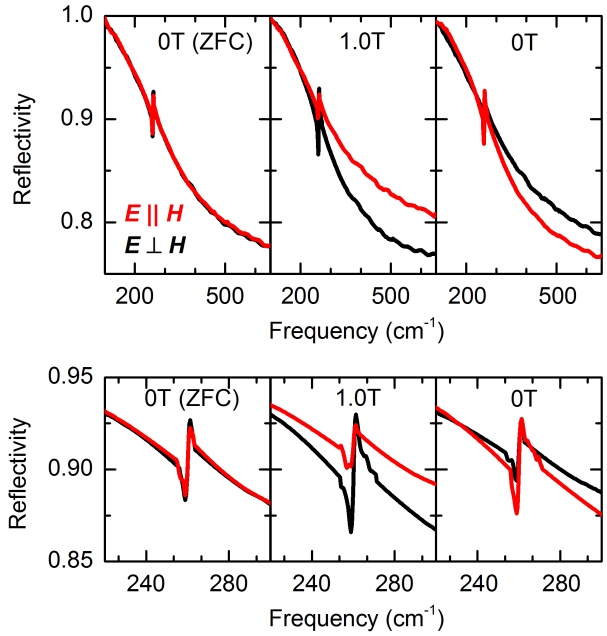


**Figure 9.1:** Frequency-dependent reflectivity of $EuFe_2As_2$ at $T$ =15 K, for $H = 0$ T (ZFC), 1 T and 0 T after FT ($H \parallel [110]_T$); while the upper panel displays the whole FIR range, the lower panel focuses on the FeAs phonon mode at $\sim 260\,\mathrm{cm}^{-1}$. The magnetic field induces anisotropy between $R(E \parallel H)$ (red) and $R(E \perp H)$ (black) as well as changes the FeAs phonon mode, both corresponding to the magnetic detwinning. A distinct anisotropy remains after the magnetic field is switched off; it is opposite to that at 1 T.

is displayed, *i.e.* the reflectivity normalized to its initial zero-field value. While Fig. 9.2 is a false-colour plot of the field and frequency-dependent relative reflectivity, revealing on the first view the main dynamics, Fig. 9.3 resolves the details in a conventional plot. It can be concluded:

- For increasing magnetic fields, the reflectivity rises rapidly at around 0.1 T for frequencies[1] above $\sim 300$ cm$^{-1}$, afterwards staying almost constant. Thus, $H_1 \sim 0.1$ T can be identified as the critical field where twin domains preferentially align with $b \parallel H$. A sharp drop in the reflectivity at $H_2 \sim 0.65$ T marks the second, opposite detwinning process with $a \parallel H$. For higher fields, the reflectivity stays again almost constant.

- For decreasing fields, the latter process is reversible with a slightly lower critical field $\sim 0.60$ T. However, the detwinning at low fields is persistent.

1 The behaviour at lower frequencies is more complex, probably as $Eu^{2+}$ spin scattering plays here a more important role.

- One should note the distinct changes of the FeAs phonon, which is strongly reduced at low and enhanced at high fields (see Fig. 9.3b). Those strong phonon changes (which follow the intensity changes of the reflectivity) support that a structural detwinning causes the electronic anisotropy.

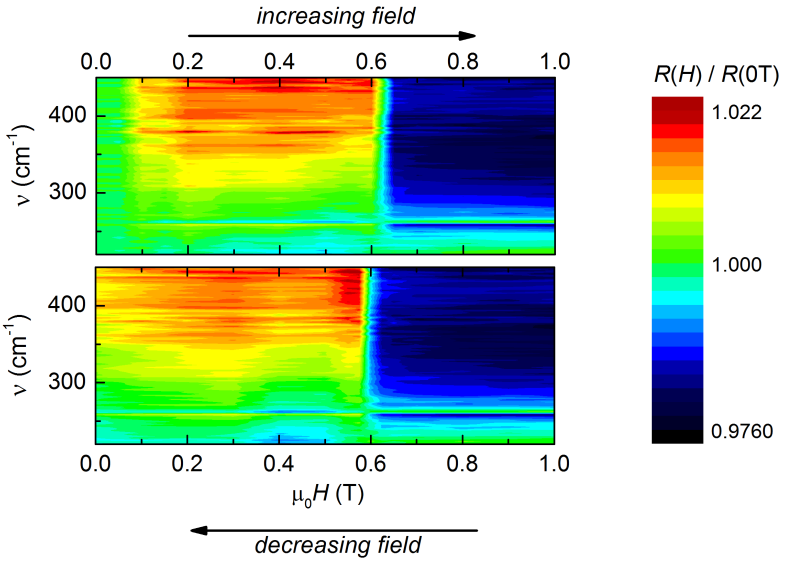


**Figure 9.2:** False colour plot of the frequency- and field-dependent FIR relative reflectivity $R(H)/R(0\,\mathrm{T})$ of $EuFe_2As_2$ at $T = 15\,\mathrm{K}$ ($H \parallel [110]_\mathrm{T}$, $E \perp H$). The detwinning fields (where the reflectivity abruptly de- and increases) can be identified as $H_1 \sim 0.1\,\mathrm{T}$ and $H_2 \sim 0.65\,\mathrm{T}$ for increasing, and $H_2 \sim 0.6\,\mathrm{T}$ for decreasing fields.

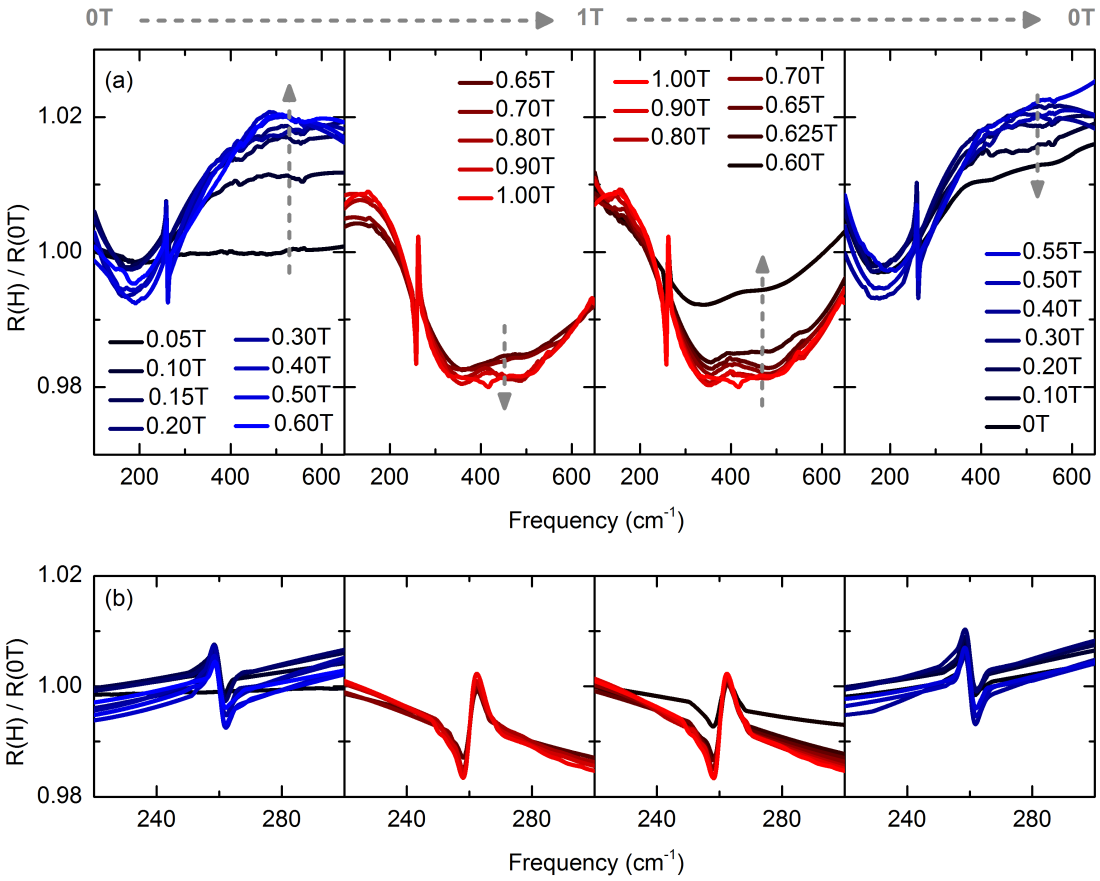


**Figure 9.3:** Frequency-dependent relative reflectivity (normalized to the ZFC reflectivity) of $EuFe_2As_2$ at $T$ =15 K, for $H$ = 0 T (ZFC), 1 T and 0 T after FT ($H \parallel [110]_T$, $E \perp H$); while the upper panel displays the whole FIR range, the lower panel focuses on the FeAs phonon mode at $\sim 260\,cm^{-1}$. For increasing fields (left panels), the reflectivity first decreases and then increases abruptly at $\sim 0.1$ T and $\sim 0.65$ T, respectively. For decreasing fields only the upper process takes place at $\sim$ 0.60 T; the lower process is irreversible. The low-field detwinning is accompanied by a reduction of the FeAs phonon oscillator strength; the high-field process by an enhancement. Grey dashed arrows mark the direction of the spectral changes with sweeping the magnetic field.

### Detwinning at $T > T_{Eu}$

While the neutron studies concentrated on temperatures $T < T_{Eu}$, we have also investigated whether any magnetic detwinning can be observed above $T_{Eu}$.

Fig. 9.4 displays the FIR reflectivity of $EuFe_2As_2$ at $T = 30\,K$ for $H \parallel [110]_T$ with $H = 0\,T$ (ZFC), 1.0 T, and 0 T after field treatment (with 1 T):

- Similar to the measurements at 15 K, the zero-field cooled 0 T curves perfectly merge, proving an initially balanced twin domain ratio as well as the high quality of the measurements.
- At a magnetic field of 1 T, a notable difference is induced between the two polarizations, similar to that at 15 K. This indicates that the crystal gets sufficiently detwinned also at temperatures $T > T_{Eu}$ by small magnetic fields with $a \parallel H$.
- Again, we also observe a notable difference between the two polarizations after the magnetic field is switched off. However, now the direction of the anisotropy is the same as at 1 T, indicating only one (persistent) detwinning process.

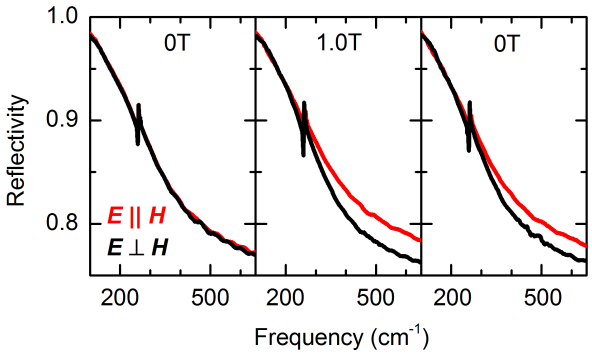


**Figure 9.4:** Frequency-dependent FIR reflectivity of $EuFe_2As_2$ at $T$ =30 K, for $H = 0\,T$ (ZFC), 1 T and 0 T after FT ($H \parallel [110]_T$). The magnetic field induces anisotropy between $R(E \parallel H)$ (red) and $R(E \perp H)$ (black) as well as changes the FeAs phonon mode, both corresponding to the magnetic detwinning. A distinct anisotropy remains after the magnetic field is switched off.

A detailed series of measurements reveals that the detwinning process at 30 K is rather continuous, with the main changes arising between 0.3 T and 0.7 T (see Fig. 9.5). The induced detwinning shows an almost complete persistence.

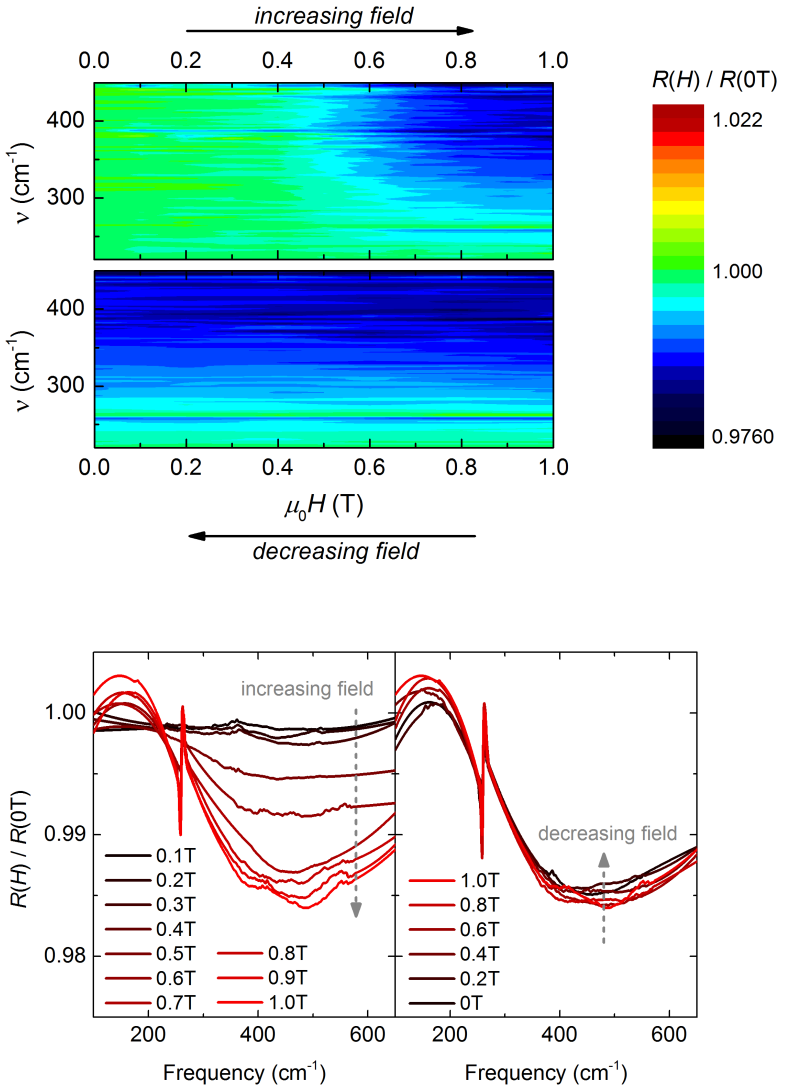


**Figure 9.5:** False colour (upper panel) and conventional plot (lower panel) of the frequency and field-dependent FIR relative reflectivity $R(H)/R(0\,\mathrm{T})$ of $EuFe_2As_2$ at $T$ =30 K ($H \parallel [110]_T$, $E \perp H$). The detwinning is rather continuous, with the main changes arising between 0.3 T and 0.7 T. A distinct anisotropy remains after the magnetic field is switched off.

### Control measurements

In order to verify that the induced anisotropy corresponds to the magnetic detwinning, measurements were repeated on $EuFe_2As_2$ with $H \parallel [100]_T$, *i.e.* with the magnetic field at a 45° angle to the orthorhombic axes and the easy axes of the $Eu^{2+}$ magnetic moments. In this case, no twin is favoured and thus, no detwinning should appear (limited by the accuracy of aligning the crystal perfectly along the $[100]_T$-direction). Additionally, comparison measurements were performed on $BaFe_2As_2$ single crystals with $H \parallel [110]_T$.

As can be seen in Fig. 9.5, in both control experiments no anisotropy is induced within the limit of our resolution. This proves that the observed effects discussed above must be related *(i)* to a redistribution of twins and *(ii)* to the presence of $Eu^{2+}$ moments.

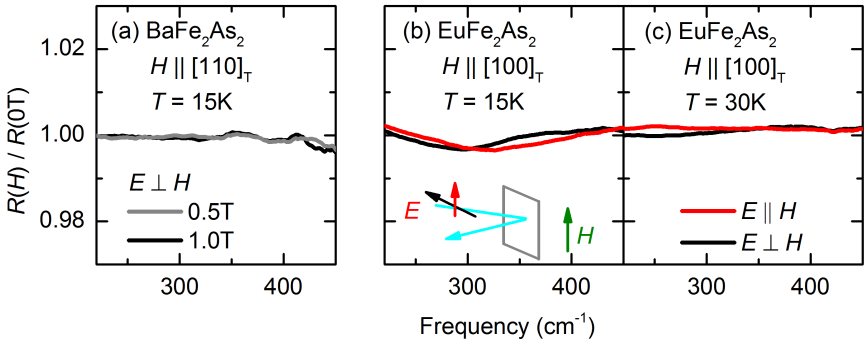


**Figure 9.6:** Frequency-dependent relative reflectivities of $BaFe_2As_2$ ($T$ =15 K) and $EuFe_2As_2$ ($T$ =15 K, 30 K) for different magnetic field directions. Relative reflectivities of (a) $BaFe_2As_2$ with $H \parallel [110]_T = 0.5$ T (grey) and 1 T (black) ($T$ =15 K, $E \perp H$) as well as of (b,c) $EuFe_2As_2$ with $H \parallel [100]_T = 1$ T ((b) $T$ =15 K and (c) 30 K, $E \parallel H$: red, $E \perp H$: black) do not show magnetic field induced anisotropy.

### Heating persistence

As our experiments reveal a persistent detwinning induced by small magnetic fields at low temperatures ($T < T_{s,SDW} = 190$ K), a central question that arises is what happens when a persistently detwinned crystal is heated up. Fig. 9.7 displays a series of reflectivity measurements, where $EuFe_2As_2$ was subject of the following cooling and field treatment procedure:

- Reflectivity spectra were taken after initial zero-field cooling at 30 K and 15 K, revealing an isotropic response (see Fig. 9.7a,b).
- Field treatment at 15 K (with 1 T) induces a distinct anisotropy with $R(E \parallel H) < R(E \perp H)$, corresponding to a persistent detwinning for temperatures $T < T_{Eu}$ with

$b \parallel H$ and a more pronounced spin density wave gap along the $b$-direction (compare Fig. 9.7c with Fig. 8.2).

- This anisotropy persists when heating up to 30 K (see Fig. 9.7d).
- Subsequent field treatment at 30 K (with 1 T) reverses the anisotropy, consistent with a persistent detwinning for temperatures $T > T_{\mathrm{Eu}}$ with $a \parallel H$.

This proves that the persistent detwinning induced at temperatures $T < T_{\mathrm{Eu}}$ is robust against heating up above the $Eu^{2+}$ magnetic ordering temperature. However, subsequent field treatment at $T > T_{\mathrm{Eu}}$ is able to inverse the anisotropy.

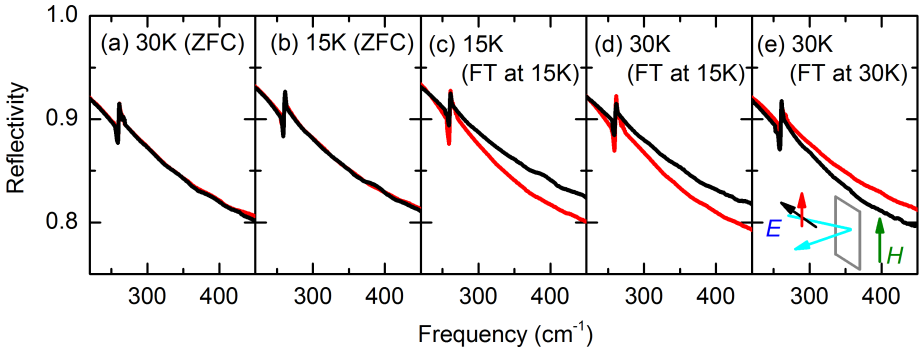


**Figure 9.7:** Frequency-dependent reflectivity of $EuFe_2As_2$ after ZFC at (a) $T = 30$ K and (b) 15 K; the reflectivity is isotropic. (c) Field treatment at 15 K (with 1 T) induces a distinct anisotropy, (d) which persists when heating (in 0 T) to 30 K. (e) Subsequent field treatment at 30 K (with 1 T) reverses the anisotropy.

Indeed, the thus induced anisotropy persists up to the structural and spin density wave transition at $T_{\mathrm{s,SDW}}$, as demonstrated in Fig. 9.8. However, if the crystal was once heated above $T_{\mathrm{s,SDW}}$ and cooled down afterwards in zero field, this anisotropy has completely vanished (see Fig. 9.8d).

## 9.2 Magnetization measurements

Since the magneto-optical measurements indicate that the $Eu^{2+}$ spins drive the detwinning, magnetization measurements[1] should provide further information about the complex detwinning mechanism.

1 For the magnetization measurements, the sample was fixed between two stripes of plastic foil by wrapping Teflon tape around them. This minimize the external stress on the sample.

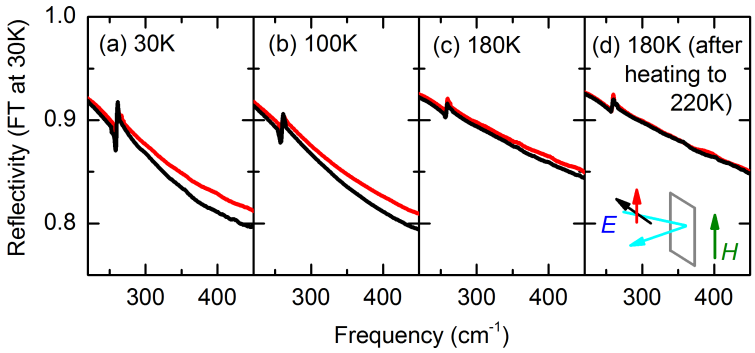


**Figure 9.8:** Frequency-dependent reflectivity of $EuFe_2As_2$ after field treatment at $T = 30\,\mathrm{K}$ with $1\,\mathrm{T}$ ($H \parallel [110]_\mathrm{T}$) for (a) $30\,\mathrm{K}$, (b) $100\,\mathrm{K}$ and (c) $180\,\mathrm{K}$. Although the magnetic field is switched off during the measurement, the reflectivity along the orthorhombic axes is anisotropic. (d) After the crystal was heated to $220\,\mathrm{K}$ (well above $T_{\mathrm{s,SDW}}$) and cooled down again to $180\,\mathrm{K}$, any anisotropy disappeared.

### Detwinning at $T < T_{\mathrm{Eu}}$

Fig. 9.9a displays the field-dependent magnetization at $2\,\mathrm{K}$ for $H \parallel [110]_\mathrm{T}$. In the first field cycling after zero-field cooling, $M(H)$ exhibits two transitions for increasing, but only the upper one for decreasing field. The transition at higher fields can be identified as a spin-flip due to the abrupt increase of the magnetization, which saturates afterwards (see chapter 2.3). In further field sweeps, only the spin-flip is visible. Moreover, the low-field transition is completely invisible for field sweeps with $H \parallel [100]_\mathrm{T}$, suggesting a relationship to the magnetic detwinning with $b \parallel H$ observed in the magneto-optical measurements.

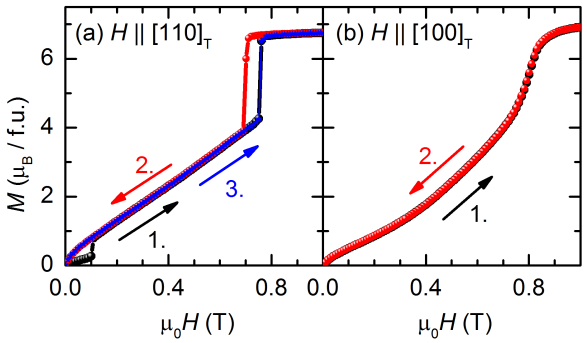


**Figure 9.9:** Field-dependent magnetization of $EuFe_2As_2$ at $T = 2\,\mathrm{K}$ for different magnetic field directions: (a) $H \parallel [110]_\mathrm{T}$ and (b) $H \parallel [100]_\mathrm{T}$. (a) At $\sim 0.7\,\mathrm{T}$, $M(H)$ sharply increases, afterwards reaching saturation. Irreversible behaviour at around $0.1\,\mathrm{T}$ is only observed during the first field cycling and when the field is parallel to the crystal's orthorhombic axes (black points: increasing $H$ after ZFC, red points: decreasing $H$ within the first cycling, blue stars: increasing $H$ in the second cycling).

Temperature-dependent magnetization measurements with $H \parallel [110]_T$ further support this interpretation (see Figure 9.10):

- Zero-field cooled $M(T)$ curves obtained at very low fields show a peak at $T_{Eu}$, however, the magnetization does not drop to zero for lower temperatures (see Fig. 9.10a). Indeed, the curve can be described as a superposition of antiferromagnetic susceptibilities parallel and perpendicular to the easy axes (see chapter 2.3), corresponding to equally distributed twin domains.
- For intermediate fields, $M(T < T_{Eu})$ shows a flat curvature, indicating an antiferromagnetic spin alignment with the easy axes perpendicular to the external field (see Fig. 9.10b). As the easy axes of $EuFe_2As_2$ corresponds to its crystallographic $a$-direction, this is consistent with the low-field magnetic detwinning (that leads to $b \parallel H$).
- A similar flat curvature below $T_{Eu}$ can be observed for very low fields after field treatment (see Fig. 9.10d), indicating that the detwinning with $b \parallel H$ is persistent.
- As expected from the field-dependent magnetization measurements, the transition at $T_{Eu}$ smears out above the spin-flip field, as field enforced ferromagnetism sets in (see Fig. 9.10c).

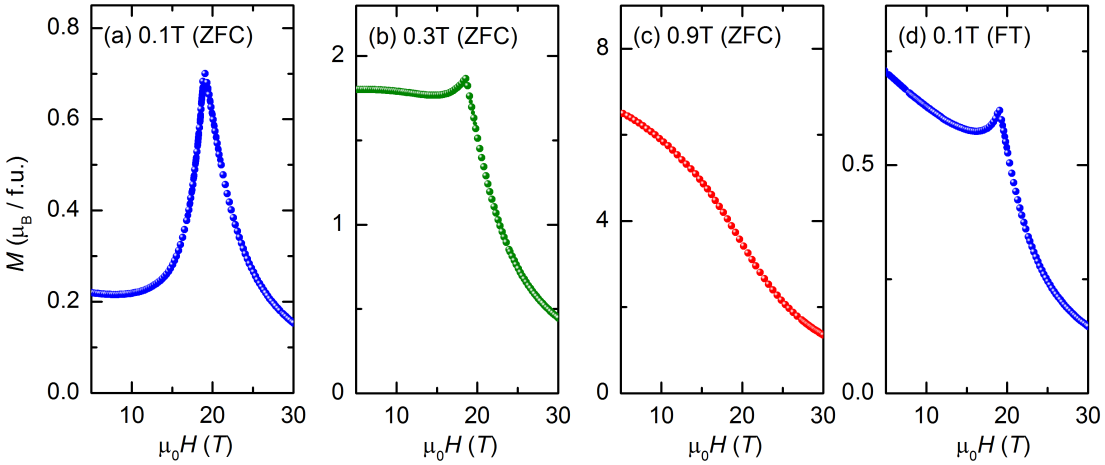


**Figure 9.10:** Temperature-dependent magnetization for $EuFe_2As_2$ at certain magnetic fields $H \parallel [110]_T$ with and without field treatment. (a) 0.1 T (ZFC), (b) 0.3 T (ZFC), (c) 0.9 T (ZFC), and (d) 0.1 T (FT with 1 T). (a) While the ZFC 0.1 T curve displays a cusp at $T_{Eu}$, (d) the corresponding FT curve displays a rather flat magnetization below $T_{Eu}$. (b) The latter curvature is also observed at 0.3 T (after ZFC). (c) $M(T)$ at 0.9 T increases smoothly with decreasing temperature without any distinct anomaly at $T_{Eu}$.

The question remains how exactly the spin-flip is related to the second detwinning process with $a \parallel H$. Therefore, field-dependent magnetization measurements at 15 K are

displayed together with the results from magneto-optical measurements in Fig. 9.11a. The overall magnetization behaviour is very similar to that at 2 K, despite a smooth increase of the magnetization above the spin-flip field due to thermal fluctuations. While the irreversible behaviour in optical and magnetization measurements appears in both cases around $H_1 \sim 0.1$ T, the spin-flip field $H_{SF} \sim 0.5$ T slightly precedes the detwinning process observed in the reflectivity by about 0.1 T.

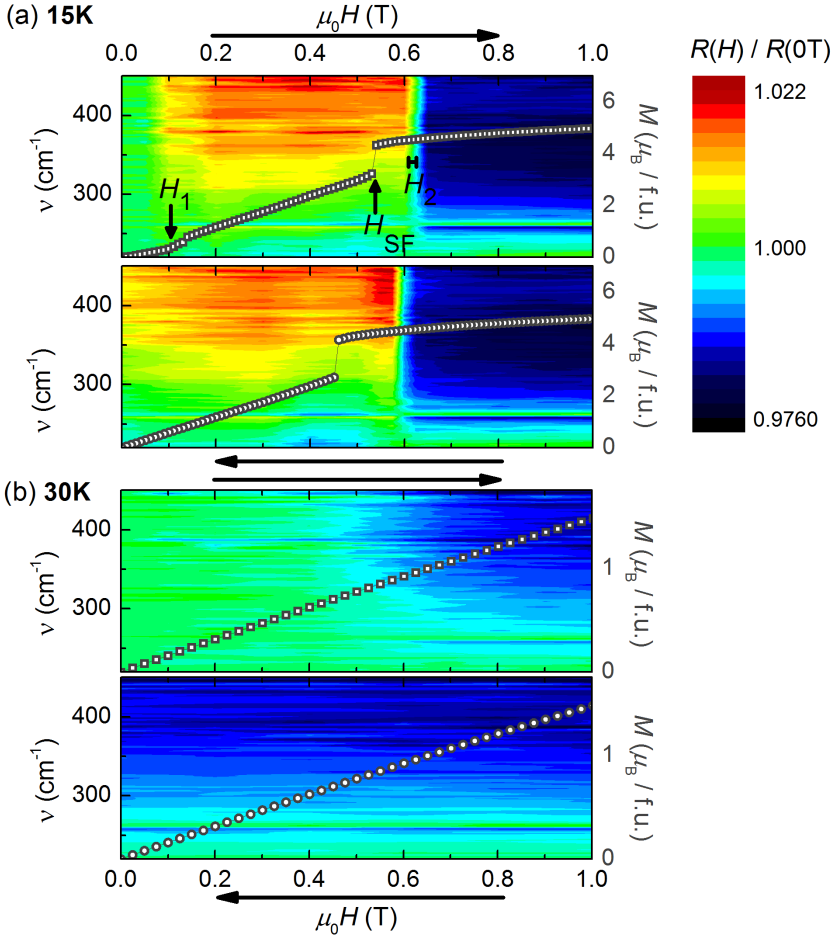


**Figure 9.11:** Field-dependent magnetization $M(H)$ (grey open circles) and false colour plot of the frequency and field-dependent FIR relative reflectivity $R(H)/R(0\,\mathrm{T})$ ($E \perp H$) of $EuFe_2As_2$ at (a) $T$ =15 K and (b) 30 K ($H \parallel [110]_T$). The detwinning fields $H_1$ and $H_2$ as well as the spin-flip field $H_{SF}$ of $Eu^{2+}$ can be identified ($H_1 < H_{SF} < H_2$).

### Detwinning at $T > T_{Eu}$

As can be seen in Fig. 9.11b, no transition is visible in $M(H)$ for $T = 30$ K. It is intriguing to associate the smooth increase of the magnetization with the rather continuous detwinning process at $T > T_{Eu}$.

## 9.3 Detwinning mechanism

In summary, we have to explain how the magnetic detwinning takes place below and above the local $Eu^{2+}$ magnetic ordering. While at $T < T_{Eu}$, the crystal gets detwinned with $b \parallel H$ at very low fields ($\sim 0.1\,T$ at $15\,K$) and with $a \parallel H$ at slightly higher magnetic fields ($\sim 0.6\,T$ at $15\,K$), at $T > T_{Eu}$, only the latter takes place. Most strikingly, a significant imbalance of twin domains remains even when the field is switched off, and the temperature is raised up to $T > T_{s,SDW}$.

### Indirect magneto-elastic coupling

The first question one should address is how the magnetic detwinning fields can be reduced in $EuFe_2As_2$ by more than two orders of magnitude compared to other iron pnictides.

Magneto-elastic coupling usually arises due to spin-orbit interactions. However, the orbital momentum of $Eu^{2+}$ is zero; thus the magnetic anisotropy induced by spin-orbit interactions is negligible. Another possibility to induce magnetic anisotropy is by dipole-dipole interactions. However, the resulting anisotropy is much weaker [306]. Therefore, other unconventional interactions must cause our observations.

From the doped or (chemically) pressurized Eu compounds, it is well known that the $Eu^{2+}$ and $Fe^{2+}$ magnetic orders are strongly intertwined (see chapter 6). Furthermore, the orbital moment of $Fe^{2+}$ is non-zero, leading in $BaFe_2As_2$ to a significant magneto-elastic coupling [24]. Hence, we suggest that the $Eu^{2+}$ spins couple indirectly to the lattice via the $Fe^{2+}$ spins. Such an indirect magneto-elastic coupling was, to the best of our knowledge, not yet observed before.

### Detwinning at $T < T_{Eu}$

In order to explain the two-step detwinning process at temperatures $T < T_{Eu}$, a simple model based on the competition between magneto-crystalline anisotropy $\Delta$, antiferromagnetic exchange coupling $J$ and Zeeman energy is sufficient. Two twin domains have to be considered, one with the easy $a$-axis perpendicular (type $B_{\parallel}$) and one with it parallel (type $A_{\parallel}$) to the external field (see Fig. 9.12a).

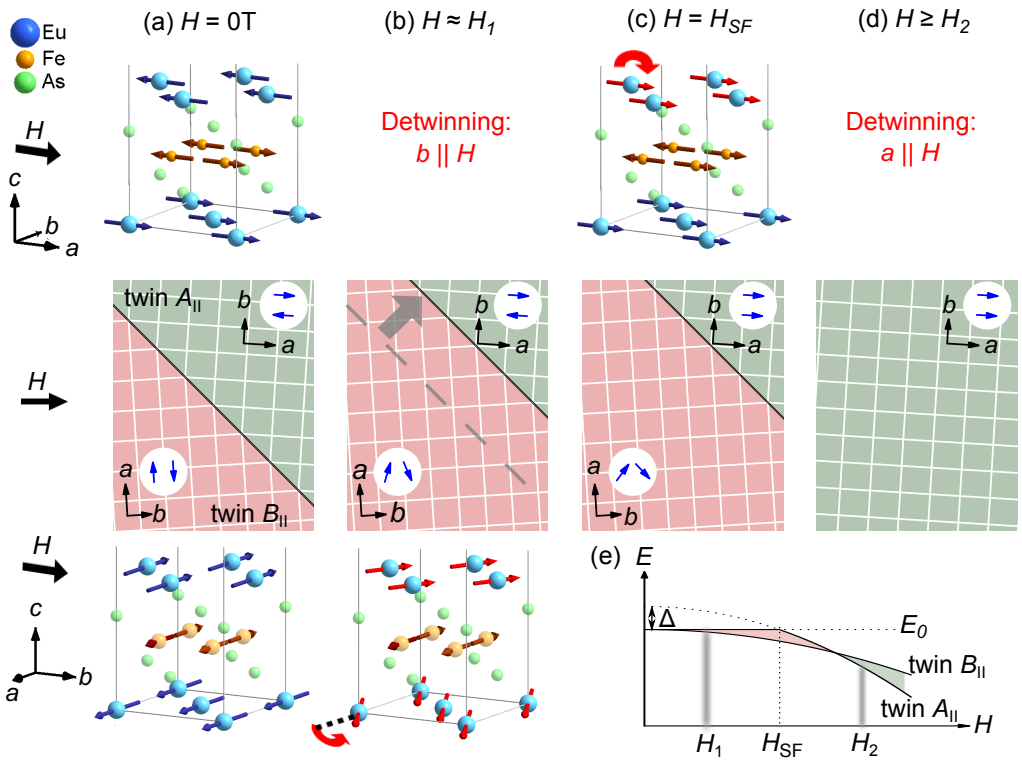


**Figure 9.12:** Sketch of the twin distribution and spin configuration of $EuFe_2As_2$ dependent on an (from left to right increasing) external magnetic field $H \parallel [110]_T$ at $T < T_{Eu}$. Top and bottom rows show a detail of the $EuFe_2As_2$ crystal and magnetic structure (Eu atoms and spins (blue), Fe atoms (yellow) and spins (brown), As atoms (green)) that correspond to the twin distribution sketched in the middle row. (a) For $H = 0\,T$, the ZFC crystal is twinned and the domains are equally distributed. The $Eu^{2+}$ spins are ordered $A$-type antiferromagnetically with the spin direction along the $a$-axis. (b) With external field, twin variant $B_\parallel$ (red, bottom) with $b \parallel H$ gets energetically favoured and therefore grows on the expense of variant $A_\parallel$ (green, top), as soon as the energy difference exceeds the twin boundary pinning energy. (c) With further increasing field, $Eu^{2+}$ spins in the remaining type $A_\parallel$ twins flip along the field direction. Energetically, twin $B_\parallel$ is still more favourable. (d) At slightly higher fields, twin $A_\parallel$ is favoured and the crystal is detwinned with $a \parallel H$. (e) Corresponding energy curves ($E_0$: ground state). While at low fields twin $B_\parallel$ is energetically favourable (red area), twin $A_\parallel$ gets favourable at higher fields (green area). Detwinning takes place at $H_1$ and $H_2$, when the energy gain exceeds the pinning energy of the twin boundary.

After cooling in zero magnetic field, the crystal is twinned with equally distributed variants. The simplest form for the energy is then given by (see chapter 2.3):

$$E = -2M\mu_0 H(\cos\theta + \cos\varphi) + JM^2\cos(\theta+\varphi) \\ -\frac{1}{2}\Delta \begin{cases} \sin^2\theta + \sin^2\varphi & (B_\parallel) \\ \cos^2\theta + \cos^2\varphi & (A_\parallel) \end{cases}, \tag{9.1}$$

where $\theta$ and $\varphi$ are the angles between spins and magnetic field and $E_0 = -JM^2 - \Delta$ is the 0 T ground state energy. Minimizing the energy for $\theta = \varphi$ yields (see Fig. 9.12e):

$$E_{\min}^{B_\parallel} = E_0 - \frac{M^2(\mu_0 H)^2}{2JM^2 + \Delta} \tag{9.2}$$

$$E_{\min}^{A_\parallel} = E_0 + \Delta - \frac{M^2(\mu_0 H)^2}{2JM^2 - \Delta} \tag{9.3}$$

Thus, at low fields, the $Eu^{2+}$ spins of variant $B_\parallel$ gradually rotate towards the direction of the external magnetic field, lowering the system's energy. When $E_{\min}^{B_\parallel} - E_{\min}^{A_\parallel}$ exceeds the twin boundary pinning energy, variant $B_\parallel$ grows irreversibly on the expense of variant $A_\parallel$, and the crystal gets detwinned with $b \parallel H$ (see Fig. 9.12b). Increasing the magnetic field further induces a spin-flip in variant $A_\parallel$ (see Fig. 9.12c), but this twin variant is energetically favourable only at slightly higher fields, when the crystal gets detwinned with $a \parallel H$ (see Fig. 9.12d).

As characteristic for domain dynamics, these processes are strongly irreversible, leading to a significant persistent detwinning.

#### Detwinning at $T > T_{\mathrm{Eu}}$

At $T > T_{\mathrm{Eu}}$, the unordered $Eu^{2+}$ spins gradually align along the direction of the external field, leading to a net magnetic moment along $H$. This favours for $H \parallel [110]_{\mathrm{T}}$ the domain type, where the $Fe^{2+}$ spins are aligned along the field direction. Therefore, a detwinning with $a \parallel H$ can be observed, as soon as the energy gain exceeds the twin boundary pinning energy.

## 9.4 Other techniques

Additional resistivity, magneto-resistance, thermal expansion and magnetostriction measurements were performed in the group of P. Gegenwart (by J. Maiwald, C. Stingl, N. Bach, and I. Pietsch, University of Göttingen / Augsburg). The main results are depicted in Fig. 9.13 and 9.14 and described in detail in Ref. [13].

### Resistivity and magneto-resistance

Resistivity measurements after field treatment impressively demonstrate the persistent detwinning, as a strong anisotropy along the orthorhombic axes remains after the magnetic field was switched off (see Fig. 9.13a,b). Consistent with the magneto-optical measurements, the induced anisotropy is opposite for field treatment below and above $T_{\mathrm{Eu}}$. One should note that its magnitude agrees well with values obtained for mechanically detwinned Eu compounds [197, 240], and remains virtually constant up to $T_{\mathrm{s,SDW}}$.

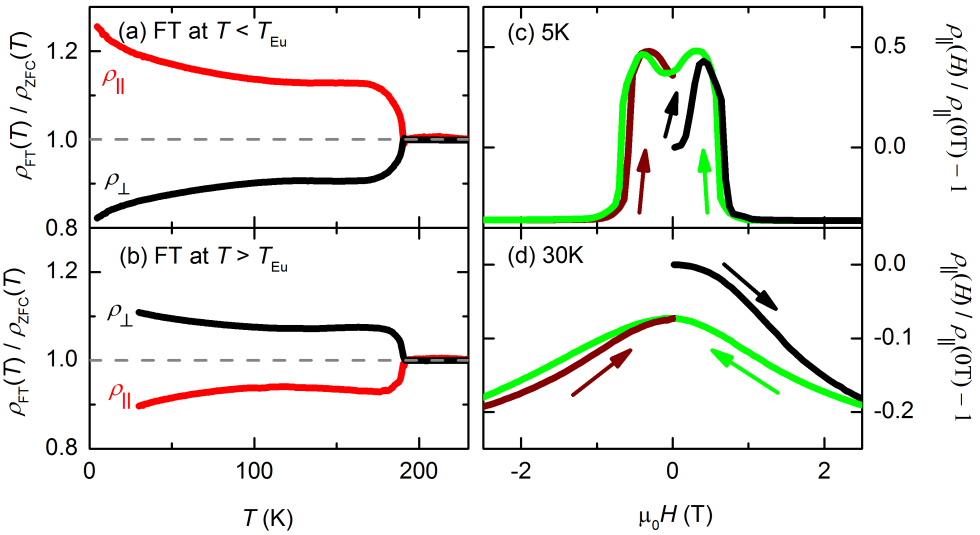


**Figure 9.13:** Resistivity and magneto-resistance of ZFC $EuFe_2As_2$ ($H \parallel [110]_{\mathrm{T}}$, data taken by J. Maiwald, University of Göttingen / Augsburg). (a,b) Temperature-dependent resistivity $\rho_{\mathrm{FT}}(T)$ after field treatment with 4 T for currents parallel (red) and perpendicular (black) to $H$, normalized to the corresponding zero-field cooled value. A strong anisotropy along the orthorhombic axes remains after the magnetic field was switched off. For field treatment at (a) $T = 4$ K and (b) at 30 K the opposite behaviour is observed. (c,d) Magneto-resistance $\rho_{\parallel}(H)/\rho_{\parallel}(0\,\mathrm{T}) - 1$ at (c) 5 K and (d) 30 K. (c) Below $T_{\mathrm{Eu}}$, $\rho_{\parallel}(H)$ first increases and then decreases with increasing $H$; (d) above $T_{\mathrm{Eu}}$, it decreases with increasing $H$. The initial ZFC value is not recovered after field sweeping.

Magneto-resistance measurements further resemble the results obtained by the magneto-optical measurements, however, the critical fields seem to be different (Fig. 9.13c,d). The main reason for this discrepancy is that all electronic contributions add up at zero frequency, meaning that other field-dependent processes such as $Eu^{2+}$ spin scattering also play an important role [198]; this masks the response due to the magnetic detwinning. Moreover, one should note that the electric contacts needed in resistivity measurements

induce significant stress on the sample. Indeed, already this force is often strong enough to partially detwin a sample[1] and might influence transition temperatures and fields.

### Thermal expansion and magnetostriction

Concurrent evidence for a persistent structural detwinning is also found in thermal expansion and magnetostriction measurements (see Fig. 9.14), techniques which directly probe the induced length changes. Relative length changes are of the order of $10^{-3}$, exceeding the typical magnetostriction of Eu based materials by at least two orders of magnitude.

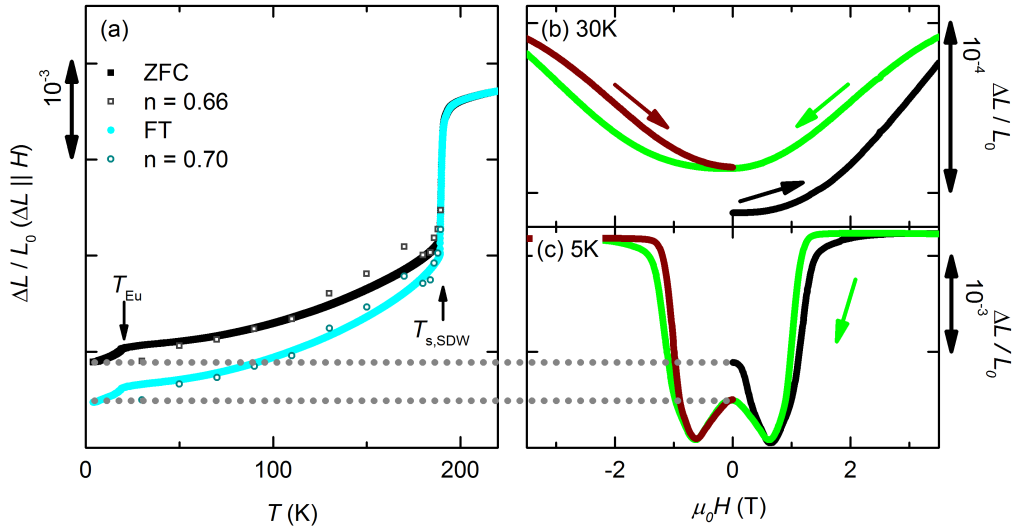


**Figure 9.14:** Thermal expansion and magnetostriction $\Delta L(T)/L_0$ of ZFC $EuFe_2As_2$ ($H \parallel [110]_T$, $\Delta L \parallel H$, data taken by C. Stingl, N. Bach, and I. Pietsch, University of Göttingen). (a) Thermal expansion after zero-field cooling (black) and field treatment with 2 T at 4 K (cyan). Apart from transitions at $T_{Eu}$ and $T_{s,SDW}$, the sample is shorter after field treatment. (b,c) Magnetostriction at (b) 30 K and (c) 5 K for increasing (black, brown) and decreasing (green) $H$. (c) While at $T > T_{Eu}$, the sample expands along $H$, (b) at $T < T_{Eu}$, it first contracts and then expands. The initial ZFC value is not recovered after field sweeping.

By comparing those results with experimentally determined lattice constants [26], one can yield information about the detwinning fraction. Assuming a temperature-independent fraction $n$ of twins with $b \parallel H$, the mean length of a unit cell in field direction follows as

$$\bar{L} = n \cdot b(T) + (1 - n) \cdot a(T). \tag{9.4}$$

1 Therefore, Fig. 9.13 only displays relative values of the resistivity.

The relative length change compared to $a_T$ (the tetragonal lattice constant at 300 K) then reads as:

$$\frac{\Delta L}{L_0} = \frac{\bar{L} - a_T}{a_T} \quad . \tag{9.5}$$

By setting $n = 66\%$, we can reproduce the ZFC curve in Fig. 9.14 reasonably well, indicating that the sample is already partially detwinned due to the uniaxial pressure from the dilatometer, which favours twins with the shorter axis $b \parallel \Delta L$. Nevertheless, the twin configuration can be changed to $n = 70\%$ by field treatment. Importantly, the induced imbalance of twin domains stays constant up to $T_{s,SDW}$

## 9.5 Detwinning fraction

From neutron measurements, we know that the crystal gets completely detwinned at 1 T [7]. However, the question remains whether we can quantize the detwinning fraction after field treatment. Unfortunately, our methods do not provide a key for a quantitative estimate:

- As in $BaFe_2As_2$ the FeAs phonon is only visible along the $b$-direction, it is intriguing to use this phonon in order to determine the detwinning fraction. In our measurements on $EuFe_2As_2$, however, even for 1 T (where the crystal should be completely detwinned according to the neutron studies), the phonon is still visible in $\sigma_a$ (see Fig. 9.15). Its presence could be attributed to the imperfect polarizer and the improper alignment of polarizer and sample with respect to the external magnetic field, however, its suppression along the $a$-direction might be also strongly composition-dependent - similar to the appearance of the smaller spin density wave gap (see also section 9.6). Therefore, we are not able to extract reliable information about the detwinning fraction by our magneto-optical measurements.

- Resistivity measurements show that the anisotropy induced by field treatment agrees well with values obtained for mechanically detwinned Eu compounds [197, 240]. Therefore, the magnetic detwinning provides a good alternative to mechanical devices; however, the absolute value of the detwinning fraction stays unclear.

- Thermal expansion and magnetostriction measurements can not be used to determine the detwinning fraction, as the uniaxial pressure from the dilatometer already detwins the sample partially.

However, we speculate that more information can be extracted from already published neutron diffraction data: in the first manuscript of Xiao *et al.*, where no magnetic fields were used at all, equally distributed twin domains were reported [8]. However, in a later

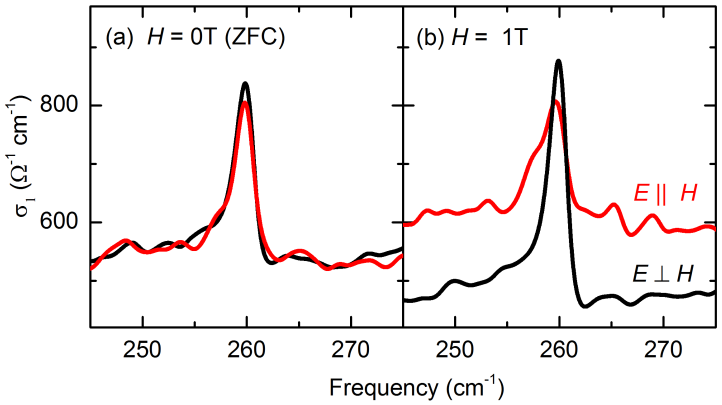


**Figure 9.15:** Polarization-dependent optical conductivity of $EuFe_2As_2$ around the FeAs phonon mode at $\sim 260\,\mathrm{cm}^{-1}$ for 15 K with and without magnetic field; 0 T data were used for an appropriate extrapolation before performing the Kramers-Kronig transformation. (a) 0 T (ZFC), (b) 1 T ($H \parallel [110]_\mathrm{T}$, resolution $1\,\mathrm{cm}^{-1}$). In the magnetic field, the oscillator strength of the phonon is enhanced for $\sigma_\mathrm{b}$ ($E \perp H$, black) and reduced for $\sigma_\mathrm{a}$ ($E \parallel H$, red).

study about the influence of magnetic fields on the structure and $Eu^{2+}$ magnetism, the same authors claimed at 0 T a domain ratio of 1:3 [7]; the low-field detwinning process was not observed at all. We suspect that the authors did not obey a well-defined cooling process, causing at 0 T an imbalanced twin domain ratio due to the persistent detwinning. This would imply that field treatment partially detwins $EuFe_2As_2$ with the domain ratio of 1:3.

One possible explanation why the crystal does not get completely detwinned at $H_1$ and after field treatment is that we have to consider the three-dimensional nature of the $A$-type antiferromagnetism, as presented in Fig. 9.16. Within one layer, $Eu^{2+}$ spins of next-nearest structural domains can be aligned parallel (see Fig. 9.16a,b) or antiparallel (see Fig. 9.16c,d). The reorientation of the intermediate domain will be less favourable for the latter case and might be prohibited. This would lead to a detwinning fraction of 75% (consistent with our reinterpretation of the neutron data): 50% of the domains are initially oriented with $b \parallel H$, additional 25% can be reoriented by the field treatment (see Fig. 9.16a,b).

## 9.6 Further infrared studies

We have also performed first test measurements over a broad energy range on magnetically detwinned samples. However, the detectors available in the FFIR and MIR energy range could not guarantee (in conjunction with the complex magneto-optical setup, see chapter 5.1) a high enough signal-to-noise ratio as well as a sufficient time-stability for a com-

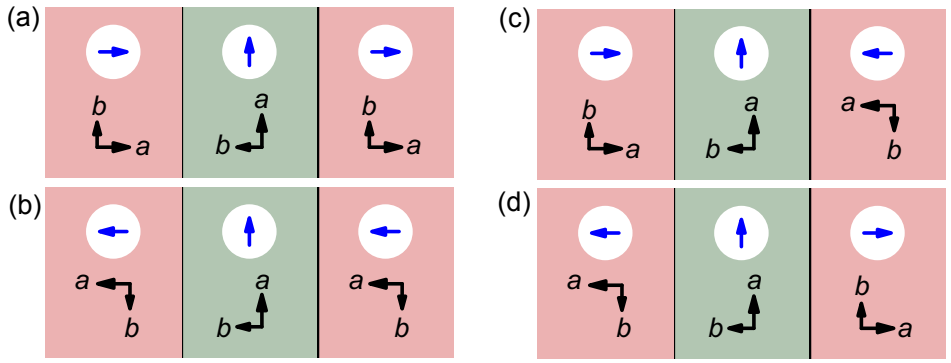


**Figure 9.16:** Considering the three-dimensionality of *A*-type antiferromagnetism could explain, why the crystal gets not completely detwinned at $H_1$. Within one layer, $Eu^{2+}$ spins (blue) of next-nearest structural domains can be aligned (a,b) parallel or (c,d) antiparallel. The reorientation of the intermediate domain will be less favourable for the latter case.

plete gold evaporation run. Therefore, we present here only preliminary results at 30 K[1]. While FIR data are measured completely in the magneto-optical setup, the reflectivity of the other energy ranges were obtained as followed: absolute values achieved in the conventional zero-field cryostat were normalized by the ratio of the reflectivities before and after field treatment, both obtained in the magneto-optical setup. FFIR data are smoothed; due to strong absorptions in the MIR range originating from the non-exchangeable polypropylene windows of the cryostat, the mid-infrared spectrum was strongly smoothed, as well as cutted above 3000 $cm^{-1}$; higher frequencies were extrapolated with the 0 T data, low frequencies according to the $\sigma_{dc}$-values. We note that all spectral ranges perfectly merge (see Fig. 9.17).

Similar to the reports on $BaFe_2As_2$ (see chapter 4.4.5), we observe a strong anisotropy in the mid-infrared frequency range. By fitting with the "subtraction approach" introduced in chapter 8.2, we find $1/\tau_b > 1/\tau_a$ and slightly higher Drude weights for the *a*-direction, similar to Ref. [171]. Furthermore, we confirm that the spin density wave gap around $\approx 10.8 k_B T_{s,SDW}$ consists of two features, with the higher feature stronger visible in the *b*-direction. This is consistent with measurements and theoretical calculations for $BaFe_2As_2$ [168, 169]. However, we do not observe any evidence for a lower spin density wave gap along one of the main crystallographic directions, consistent with our results on the twinned crystal (see section 8.1).

Furthermore, our observations concerning the FeAs phonon differ from the behaviour reported for $BaFe_2As_2$, as already discussed in chapter 9.5. Along the orthorhombic *a*-

1 Further measurements on a newly constructed magneto-optical setup at the 1st Physical Institute, Stuttgart are scheduled.

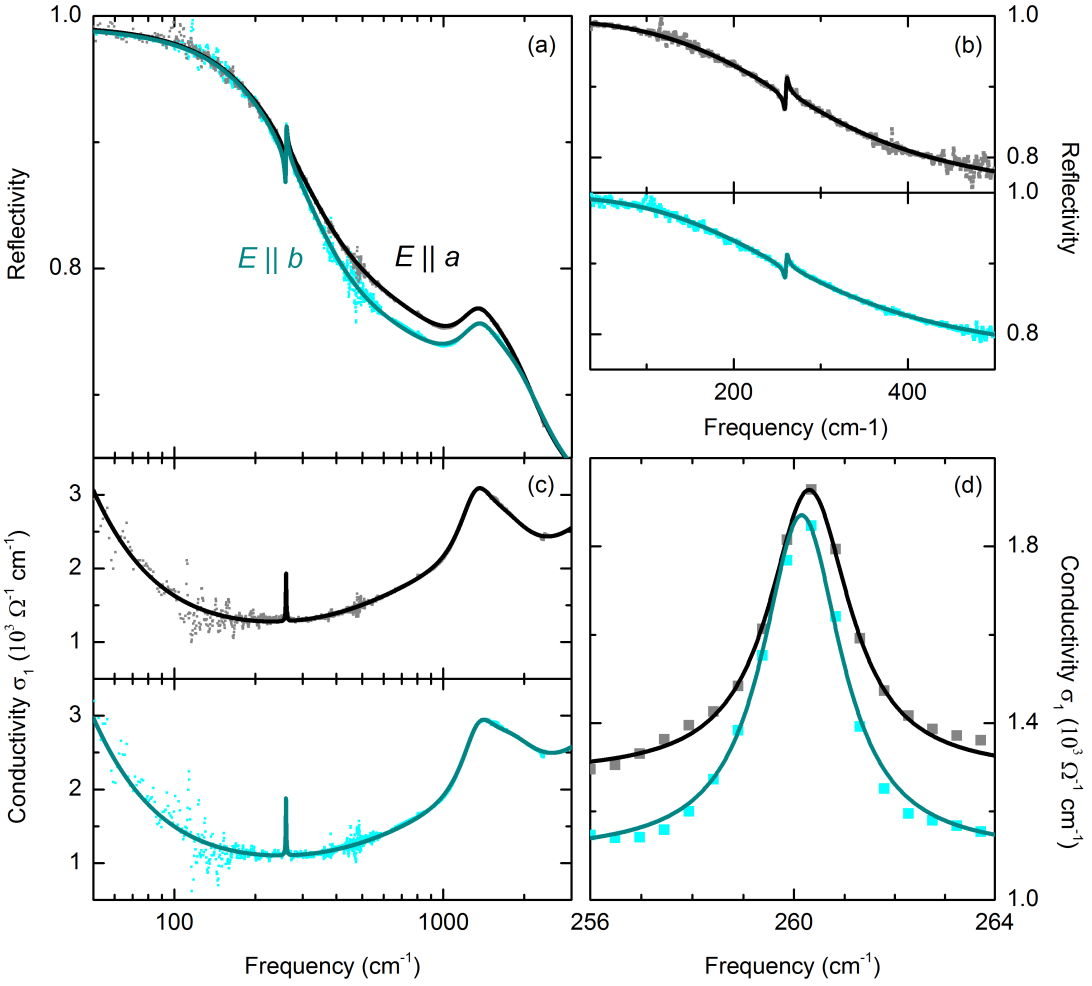


**Figure 9.17:** Frequency-dependent in-plane (a-b) reflectivity and (c-d) conductivity of $EuFe_2As_2$ at $T$ =30 K in different logarithmic and linear plot styles. Grey (light cyan) squares represent data points for $E \parallel a$ ($E \parallel b$), black (dark cyan) lines the corresponding fit with two Drude components and a Lorentzian at 1000 $cm^{-1}$. (d) The phonon is narrower along the $b$-direction and slightly shifted to lower frequencies.

direction, it has a reduced oscillator strength, but does not disappear. Indeed, we are able to identify for $\sigma_a(\omega)$ a slight blueshift of the phonon (see Fig. 9.17d). This blueshift is consistent with a weak higher-energy $a$-axis phonon contribution revealed for $BaFe_2As_2$ by Schafgans *et al.* [174]. We suggest that this contribution is more pronounced in the case of $EuFe_2As_2$. Therefore, high-resolution far-infrared measurements on mechanically detwinned $EuFe_2As_2$ crystals could give important information on the anisotropic phonon dynamics in 122 iron pnictides, which are yet not well understood [171].

## 9.7 Outlook

Our magneto-optical and magnetization measurements reveal a dramatic reduction of magnetic detwinning fields compared to other $AFe_2As_2$ ($A$ = Ba, Sr, Ca) iron pnictides by indirect magneto-elastic coupling of the $Eu^{2+}$ ions. Such an indirect magneto-elastic coupling was, to our best knowledge, not demonstrated before.

We find that only $\sim 0.1\,\mathrm{T}$ are sufficient for persistent detwinning below the local $Eu^{2+}$ ordering, accessible by typical laboratory magnetic fields; a significant imbalance of twin domains remains constant up to the structural and electronic phase transition (190 K). This is surprising from a very fundamental point of view, as the detwinning induced at low temperatures with very small magnetic fields persists up to much higher temperatures and thus energy scales. This may even lead to technical applications.

With respect to the research on high temperature superconductors, the whole effect uncovers a remarkable interdependence between magnetic, electronic and structural effects. It is surprising that the $Eu^{2+}$ magnetic order strongly affects the lattice, although it does not destroy superconductivity in substituted compounds. This opens up unprecedented possibilities for fundamental research concerning the interplay of superconductivity and magnetism. Finally, our findings provide a unique possibility to study macroscopically the intrinsic in-plane anisotropy of iron pnictides without the application of any symmetry-breaking external force.

# 10
# SUMMARY AND OUTLOOK

The investigations carried out in the framework of this thesis reveal that Eu based iron pnictides offer a unique playground to examine the interplay of unconventional electronic properties, superconductivity, itinerant and local magnetism.

Through systematic magnetization studies on a complete set of $EuFe_2(As_{1-x}P_x)_2$ single crystals, we have derived the complex magnetic phase diagram of Eu 122 pnictides (see chapter 7). As a first step, we identified a ferromagnetic out-of-plane component that develops in the underdoped, non superconducting region of the phase diagram, consistent with canted $A$-type antiferromagnetism. In addition, the $Eu^{2+}$ magnetic transition temperature $T_N$ is suppressed similar to the structural and spin density wave transition $T_{s,SDW}$ and rises again as soon as superconductivity sets in. This implies that the $Eu^{2+}$ spin orientation in the parent compound is defined by the spin density wave anisotropy, consistent with theoretical calculations by Akbari *et al.* [11]. Therefore, we conclude significant interactions between the local $Eu^{2+}$ and the (quasi-) itinerant Fe magnetism.

Furthermore, we identified the development of a re-entrant spin glass phase at lower temperatures, characterized by time-dependent processes that appear due to the freezing of the in-plane spin components. The corresponding transition temperature $T_{glass}$ rises quickly in the underdoped region until it is almost as high as $T_N$ for superconducting compounds. For higher P substitution levels, both transition temperatures continuously increase, separated only by $\sim 2\,K$. One should further note the rather narrow supercon-

ducting dome, which might be related to a Lifshitz transition [235] that also affects the RKKY-exchange. However, our studies rule out any change to ferromagnetic interlayer coupling at high P substitutions.

All these findings are probably common features of (non-diluted) Eu based iron pnictides, as discussed on the basis of a review given in chapter 6. It can be speculated that the $Eu^{2+}$ ferromagnetic component along the *c*-axis is screened by the formation of spontaneous vortices perpendicular to the layers [31]. Most importantly, the glass-like dynamics indicate a decoupling of the Eu layers, therefore implying that superconductivity in the intermediate FeAs layers is mostly unaffected by any magnetic interlayer coupling. Thus, our findings elucidate how bulk superconductivity can coexist with the strong $Eu^{2+}$ magnetic ordering.

Despite the interactions of local and itinerant magnetism revealed by our magnetization studies, the electrodynamic response of $EuFe_2As_2$ is surprisingly unaffected by the $Eu^{2+}$ magnetic transition, evidenced by infrared spectra that basically do not change when passing $T_N$ (see chapter 8). However, we are able to confirm earlier results of Wu *et al.* [184], who reported the absence of any spin density wave gap feature around the BCS weak-coupling limit. Although it is intriguing to relate this absence to the local $Eu^{2+}$ magnetism, such a relationship has (yet) no theoretical background.

In order to obtain more information about the general electrodynamic properties of iron pnictides, we have further compared typical fitting approaches. We find that realistic results are obtained with a model that contains two Drude components (probably representing electron and hole bands) and a Lorentzian around $1000\,cm^{-1}$, which can be attributed to interband transitions involving Fe hole pockets [12]. Importantly, we find that regardless of the fitting method, the spin density wave transition affects not only both Drude components, but also the spectral weight transfer to a bump-like structure in the near-infrared and even higher energies. This supports a strong relationship of the latter feature to the dynamics of the itinerant carriers, consistent with correlation effects due to Hund's rule coupling.

Finally, it was demonstrated in chapter 9 that magneto-optical measurements in the far-infrared frequency range are ideal to investigate the magnetic detwinning mechanism in $EuFe_2As_2$. We find that only $\sim 0.1\,T$ are sufficient for a persistent detwinning below the local $Eu^{2+}$ ordering temperature, which is accessible by typical laboratory magnetic fields; above $T_N$, only slightly higher fields (around 1 T) are needed. We ascribe these observations to an indirect magneto-elastic coupling of the $Eu^{2+}$ ions via the $Fe^{2+}$ spins, which was - to our knowledge - not observed before, and give a simple model based on the competition between magneto-crystalline anisotropy, antiferromagnetic exchange coupling and Zeeman

energy. Our findings are further confirmed by magnetization, magneto-striction, thermal expanison and (magneto-)resistance measurements.

Most importantly, the term *persistent* detwinning implies that a significant imbalance of twin domains remains when the magnetic field is switched off and the temperature is raised up to $T_{\mathrm{s,SDW}}$. Such strongly hysteretic behaviour is surprising from a very fundamental point of view, as the detwinning that is induced at low temperatures with very small magnetic fields persists up to much higher temperatures and thus energy scales. In summary, the whole effect uncovers a remarkable interdependence between magnetic, electronic and structural effects in Eu based iron pnictides.

While all studies performed in the framework of this thesis concentrated on $EuFe_2(As_{1-x}P_x)_2$, we suggest that many of our findings have further implications for other materials, especially for rare earth containing high-temperature superconductors such as related Eu 122 pnictides, Ce 1111 pnictides and rutheno-cuprates [82, 307]. In chapter 6 and 7 we have already presented evidence for the canted antiferromagnetic and re-entrant spin glass phase in other Eu 122 pnictides. One should note further that glass-like behaviour was also reported for rutheno-cuprates [308, 309] and CeFePO [310]; this implies that glassy dynamics may be the key to how high-temperature superconductivity can coexist with rare earth magnetism.

Furthermore, we are confident that the low-field persistent detwinning discovered in $EuFe_2As_2$ actually appears also in other rare earth containing materials. Therefore, we are planning further investigations on diluted Eu compounds. Moreover, the persistent magnetic detwinning is also interesting for other experimental techniques such as ARPES [311], where the implementation of additional mechanical devices is challenging, and for theoreticians [312], since it provides the unique possibility to study the macroscopic in-plane anisotropy close to the phase transition without the application of any symmetry-breaking force.

Finally, one should note that the work presented here also opens up very concrete questions concerning the research on Eu based 122 superconductors that we want to address in the near future. In this regard, we suggest that studies on diluted compounds may uncover the source of the anomalies related to the spin density wave (see chapter 8) and the superconducting gap [233]. Likewise, further optical investigations on superconducting $EuFe_2(As_{1-x}P_x)_2$ compounds might reveal more information about the relationship of the Lifshitz transition to the rather narrow superconducting dome. Furthermore, it will be interesting to examine whether the indirect magneto-elastic coupling also influences the nematic fluctuations [313]. Therefore, this thesis can be concluded safe in the knowledge

that it has not only contributed important insights, but also inspired future work in a very interesting field of nowadays solid state research.

# A

# THZ INVESTIGATIONS ON BA 122 THIN FILMS

As already presented in chapter 4.4, many contradictory reports exist about the optical properties of $Ba(Fe_{1-x}Co_x)_2As_2$. In particular, the number of superconducting gaps as well as the origin of the unexpected strong intra-gap absorption is highly debated. In the following, our approaches to contribute to this topic are shortly summarized.

In all cases, a coherent source Terahertz spectrometer (4 - 45 $cm^{-1}$) with a Mach-Zehnder interferometer was used in order to measure the transmission and the corresponding phase shift of $Ba(Fe_{0.9}Co_{0.1})_2As_2$ thin films on dielectric (La,Sr)(Al,Ta)$O_3$ (LSAT) or $CaF_2$ substrates; additional transmission measurements were performed to gain the optical properties of the substrates. Due to multiple reflections at the surfaces, the measured properties oscillate with a periodicity dependent on the optical thickness of the sample (see Fig. A.1).

In the normal state, the optical conductivity of the film can be modeled with a single Drude term, accounting for its metallic nature. In the superconducting state, each maximum is evaluated individually with two Drude terms: one with a very low scattering rate that models the superconducting $\delta$-function, the other one with a high scattering rate accounting for the quasi-particle absorption [148]. The advantage of such an approach is that it is independent of any model, *i.e.* for example of the gap symmetry. A more detailed

description of the measurement technique and the analysis can be found in Ref. [148] and Ref. [314].

## A.1 Fabry-Pérot resonant technique

One of the main problems of such measurements is that the optical intra-gap conductivity of metallic superconductors can be extracted experimentally only with rather large uncertainty, caused by the huge negative value of the dielectric constant that mainly determines the transmission. Therefore, we have performed systematic studies of Fabry-Pérot resonators, which consist of two identical superconducting iron pnictide thin films on LSAT substrates that are positioned face-to-face to each other, separated by a spacer. The corresponding results that are already published in Ref [315] and Ref [316] are summarized in this section.

### Enhancement principle

Fig. A.1a shows exemplarily the calculated transmission of such a Fabry-Pérot arrangement compared to the spectrum of a usual sample (single film on substrate) and the spectrum that would be caused by light passing two identical free standing films. For the Fabry-Pérot arrangement, a complex transmission pattern develops due to multiple reflections at numerous interfaces: the highest peaks arise at frequencies where the transmission of both, the single film on a substrate and the free standing films resonator, is maximized. In the minima of the substrate-film arrangement, the spectrum of the Fabry-Pérot resonator corresponds to the free standing films system. The resonances of the Fabry-Pérot arrangement enhance in amplitude over several orders of magnitude and exceed at some points the transmission of the single film on a substrate. As the maximum sensitivity to $\sigma_1(\omega)$ of the films is achieved when the whole peak structure is experimentally resolved, one is restricted to rather thin films to achieve transmissivity at least of the order $10^{-5}$, which is the resolution limit of the spectrometer.

The enhancement of sensitivity with respect to $\sigma_1(\omega)$ can be demonstrated by nomograms, showing lines of constant transmission coefficient and phase shift plotted in the coordinates of real and imaginary parts of $\sigma(\omega)$ (or other optical constants) of the films. Fig. A.2 compares the nomograms of a single film and a Fabry-Pérot resonator on the basis of 30 nm $Ba(Fe_{0.9}Co_{0.1})_2As_2$ film data that is representative for iron pnictides. The line of constant transmission coefficient is noticeably less steep for the Fabry-Pérot arrangement, meaning that the accuracy to $\sigma_1(\omega)$ is higher, whereas the accuracy to the phase decreases. When fitting the spectra, the accuracy to $\sigma_1(\omega)$ also benefits from "double-structures" in the THz spectra of Fabry-Pérot resonators, which emerge when the resonances between

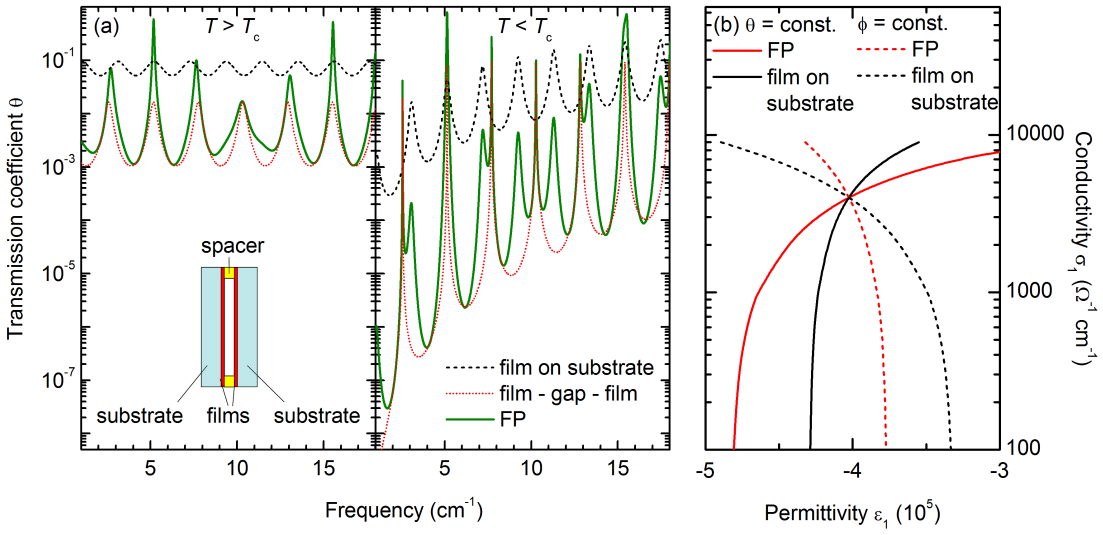


**Figure A.1:** (a) Calculated transmission at temperatures $T > T_c$ (left panel) and $T < T_c$ (right panel) for a single film on substrate (black dashed line), two free standing films (red dashed-dotted line) and the Fabry-Pérot (FP) arrangement (green line). The Fabry-Pérot resonator is shown schematically in the inset of (a). Model parameters are chosen close to measurements ($d_{sub} = 0.495\,mm$, $d_{gap} = 1.934\,mm$, $d_{film} = 30\,nm$, $\sigma_1(T > T_c) = 6000\,\Omega cm^{-1}$, $\sigma_1(T < T_c) = 2000\,\Omega cm^{-1}$, $\omega_p = 3464 cm^{-1}$). (b) Nomogram: calculated constant values of transmission coefficient $\Theta$ (solid lines) and phase shift $\Phi$ (dashed lines) in optical constant coordinates (vertical: $\sigma_1$, horizontal: $\epsilon_1$) with the values typical for a 30 nm $Ba(Fe_{0.9}Co_{0.1})_2As_2$ film in the superconducting state ($T = 5\,K$, $\nu = 5.13\,cm^{-1}$, $\Theta = 0.17$, $\Phi = 3.7\,rad/cm^{-1}$). Black lines show data for a single film on a substrate (LSAT, $d_{sub} = 0.5\,mm$), red lines for the Fabry-Pérot resonator (LSAT, $d_{gap} = 2\,mm$). The line of constant transmission coefficient is noticeably less steep for the Fabry-Pérot arrangement, meaning that the accuracy to $\sigma_1$ is higher, whereas the phase measurement (dashed lines) is more sensitive to $\sigma_1$ in the case of the single film on substrate.

different interfaces coincide. These resonances show different dependence on $\sigma_1(\omega)$ and $\sigma_2(\omega)$ of the films and the shape of the double-structure is thus very characteristic for a distinct ratio of these quantities. Thus, in a narrow frequency range, more information is available than from a spectrum of a single film on a substrate.

### Fitting procedure

In order to account for the complex geometry of the Fabry-Pérot resonator, we expanded our fitting procedure to a five-layer model. Furthermore, we measured the single films for a temperature $T_1 > T_c$ and determine their normal state conductivity $\sigma(T_1)$ (we take $T_1 = 30\,K$ slightly above $T_c \sim 22\,K$). The found value of $\sigma(T_1)$ is then used to precisely determine the geometrical parameters of the Fabry-Pérot system: substrate thickness $d_{sub}$, space between the films $d_{gap}$ ("gap width") and "gap absorption". The latter parameter

accounts for the non-perfect geometry of the resonator (for example due to the non-parallelism of interfaces), which can be modelled in first approximation by a finite (but small) absorption in the gap between the films. Importantly, all spectra are processed with the same set of geometrical parameters.

**Experimental results**

We have determined the optical response of three Fabry-Pérot resonators, consisting of pairs of two identical films ($d_{\mathrm{film}} = 25\,\mathrm{nm}$, 30 nm and 50 nm) that are glued via a spacer (metal or Plexiglas ring, diameter: $\sim 1\,\mathrm{cm}$) face-to-face to each other.

In order to empirically check, whether it is realistic to obtain data of such a Fabry-Pérot arrangement despite experimental challenges, first, a resonator composed of relatively thin films ($d_{\mathrm{film}} = 25\,\mathrm{nm}$, $T_{\mathrm{c}} = 22\,\mathrm{K}$, $d_{\mathrm{film}} \sim 1\,\mathrm{mm}$, $d_{\mathrm{gap}} \sim 1\,\mathrm{mm}$) was examined. We found that the five-layer model describes the spectra nicely, as depicted in Fig A.2a. However, as far as physics is concerned, the film quality was rather poor, as indicated by a very high London penetration depth $\lambda_{\mathrm{L}} \sim 1.46\ \mu\mathrm{m}$ (at 5 K).

As we expected a higher film quality for thicker samples, further measurements were carried out on 50 nm films ($T_{\mathrm{c}} = 21\,\mathrm{K}$, $d_{\mathrm{sub}} \sim 1\,\mathrm{mm}$, $d_{\mathrm{gap}} \sim 1\,\mathrm{mm}$). However, for these thick films the transmission coefficient of the Fabry-Pérot resonator in the superconducting state was too low, *i.e.* beyond the resolution limit of the spectrometer (see Fig A.2b).

30 nm films ($T_{\mathrm{c}} = 23\,\mathrm{K}$, $d_{\mathrm{sub}} \sim 0.5\,\mathrm{mm}$, $d_{\mathrm{gap}} \sim 2\,\mathrm{mm}$) were found to satisfy the requirements given by film quality and resolution limit of the spectrometer (see Fig A.2c). However, we found that an additional factor - the plane-parallelism of the substrates - plays a crucial role for providing the high quality factor of the Fabry-Pérot resonator. In that case, the thickness of the substrates was non-uniform in the range 0.487 mm to 0.505 mm. Thickness measurements of the complete resonator gave values between 2.934 mm and 2.958 mm, meaning that the biggest effect causing a non-parallelism of the whole system came from non-plane-parallel substrates. Since such pronounced non-perfection that leads to the broadening of the Fabry-Pérot resonance peaks in the spectra is not included in the model based on Fresnel optics, we were not able to describe the experimental spectra consistently over a broad frequency and temperature range; the disturbance is too large to be taken into account by the "gap absorption" mentioned above.

In summary, we have shown that our Fabry-Pérot resonators made out of superconducting thin films (on substrates) have theoretically the potential to enhance the sensitivity to the real part of the optical conductivity at very low frequencies. In the experiment, the resolution limit of our setup restrains the film thickness in the case of $Ba(Fe_{0.9}Co_{0.1})_2As_2$ to approximately 30 nm. However, our measurements on 25 nm films proof that the thin film

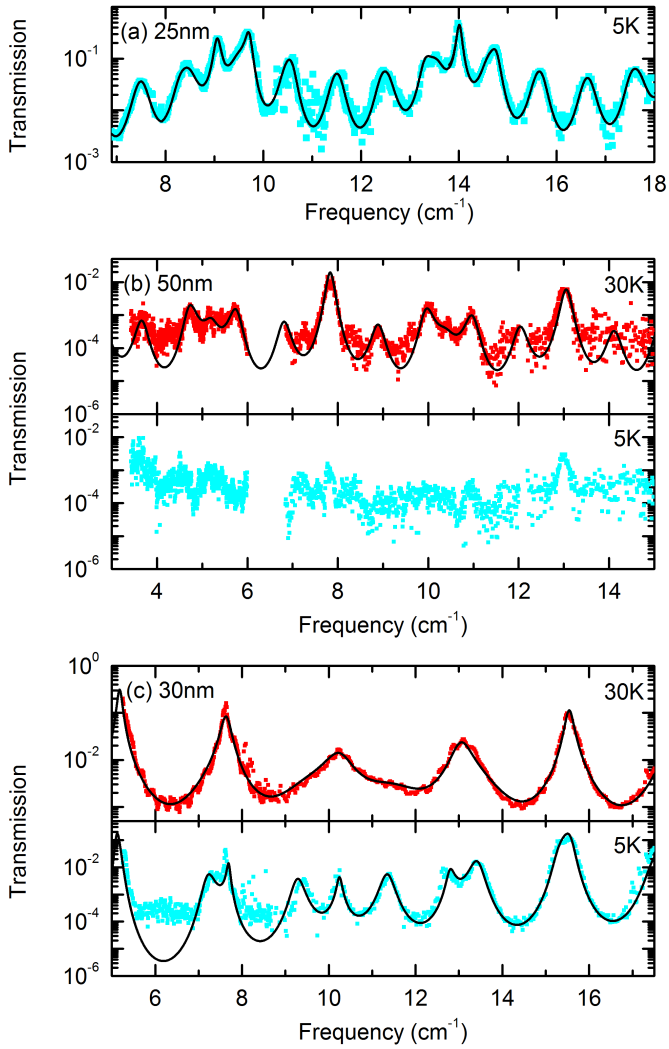


**Figure A.2:** Transmission coefficient spectra (dots) of $Ba(Fe_{0.9}Co_{0.1})_2As_2$ Fabry-Pérot resonators measured at 5 K, fitted (line) with a five-layer-model for the film thicknesses (a) $d_{\mathrm{film}}$ = 25 nm, (b) 30 nm and (c) 50 nm.

quality and homogeneity is still a serious issue for iron pnictides that has to be solved before proceeding with our work. We further note that the success of this approach depends delicately on the uniform thickness of the substrate. One solution would be to deposit two films on both sides of a substrate, which is, however, experimentally challenging.

## A.2 Superfluid density

As already mentioned in the previous section A.1, a common problem of THz investigations on superconductors is the rather huge error of $\sigma_1(\omega)$ at low frequencies. However, the

corresponding imaginary part $\sigma_2(\omega)$ (which determines the penetration depth) can usually be extracted with very high accuracy.

Therefore, our collaborator A. Karakozov has analysed the temperature-dependence of the normalized superfluid density:

$$\rho_s(t) = \lambda_L(0)^2/\lambda_L(t)^2 \tag{A.1}$$

with the relative temperature $t = T/T_c$, using the $\alpha$-model that describes multiband superconductors via BCS-like equations with a reduced critical temperature [317, 318]. This model was then applied to fit the optical properties of one of our $Ba(Fe_{0.9}Co_{0.1})_2As_2$ films on LSAT substrate ($T_c = 22\,K$, $d_{film} = 50\,nm$). Considering the existence of a small energy gap with $2\Delta/k_BT_c \sim 2$ (see Fig. 4.10), the superfluid density can be only described within a model of at least three weakly interacting condensates with $2\Delta/k_BT_c \sim 2$, 3 and 4, as depicted in Fig. A.3. This is an important refinement of the commonly used minimal model which describes the electrodynamic properties of iron pnictides with two effective bands.

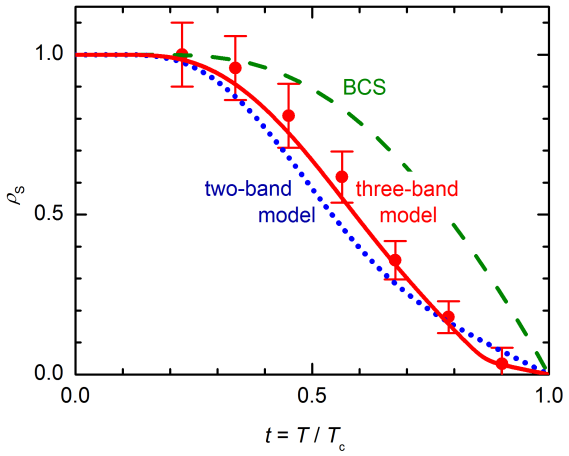


**Figure A.3:** Experimental values for the normalized superfluid density $\rho_s(t) = \lambda_L(0)^2/\lambda_L(t)^2$ (red circles) for a 50 nm $Ba(Fe_{0.9}Co_{0.1})_2As_2$ film with $T_c = 22\,K$. Additionally, calculations for a two-band (blue dotted line) and a three-band fit (red solid line) with a minimum gap $2\Delta/k_BT_c \sim 2$ are compared to a BCS one-band approach (adapted from Ref. [317]). The best description can be obtained by the three-band approach.

## A.3 Irradiation studies

In 2011, Efremov *et al.* predicted that two-band superconductors with $s_\pm$-symmetry might undergo a disorder-induced transition to $s_{++}$-symmetry, with both gaps tending to the same, finite value [319, 320]. As optical spectroscopy is not sensitive to the phase

of the superconducting order parameter, the corresponding zero-crossing of the smaller energy gap would appear as if the gap first closes and then re-emerges. Such a unique behaviour constitutes a smoking gun experiment to proof the $s_{\pm}$-symmetry for iron-based superconductors.

Furthermore, manipulating the scattering rate has also the potential to deliver important information about the origin of the strong intra-gap absorption: while nodes can be lifted by increasing scattering [72], pair-breaking should be rather enhanced (as long as superconductivity is not destroyed too much).

Therefore, we have investigated the effect of proton and $\alpha$-particle irradiation on the optical properties of 50 nm thin $Ba(Fe_{0.9}Co_{0.1})_2As_2$ films on $CaF_2$ substrate. The irradiation was performed on the DanFysik-350 at the P. N. Lebedev Physical Institute of the Russian Academy of Sciences (Moscow) with an energy of 200 keV, which is high enough to guarantee that all particles pass the film. The dose for one irradiation is $2 \cdot 10^{14}\,\mathrm{cm}^{-2}$, corresponding to a decrease of $T_c$ by 2 K per step for protons (see Fig. A.5c), and a decrease of 3.5 K per step for $\alpha$-particles. The latter stronger suppression of $T_c$ is consistent with the creation of magnetic scattering centres [321]; therefore, we concentrate here on the results obtained via proton irradiation. The corresponding investigations were supervised in the framework of this thesis, and can be found in more detail in Ref. [322] and Ref. [323].

### Intra-gap absorption

The unusual strong non-BCS-like intra-gap absorption can be best visualized, when comparing the frequency-dependent conductivity at $T > T_c$ with that at $T \ll T_c$. As displayed in Fig. A.4, even after several irradiation steps that suppress $T_c$ by more than 10 K, the conductivity at lowest frequencies and 5.6 K still exceeds the normal state values. Thus, the intra-gap absorption must originate - at least to some extent - from pair-breaking interband scattering.

### Crossover from $s_{\pm}$- to $s_{++}$-symmetry

In order to observe the crossover from $s_{\pm}$- to $s_{++}$-symmetry of the superconducting order parameter, we track the position of the coherence peak $T_{max}$ for eight irradiation steps[1]; the corresponding $T_c$ value is determined by the abrupt onset of frequency-dependent changes in the measured phase, typical for a superconductor at $T < T_c$. For the $7^{th}$ and

1 If its shape resembles rather a plateau than a peak, we consider the temperature where the plateau sets in as $T_{max}$.

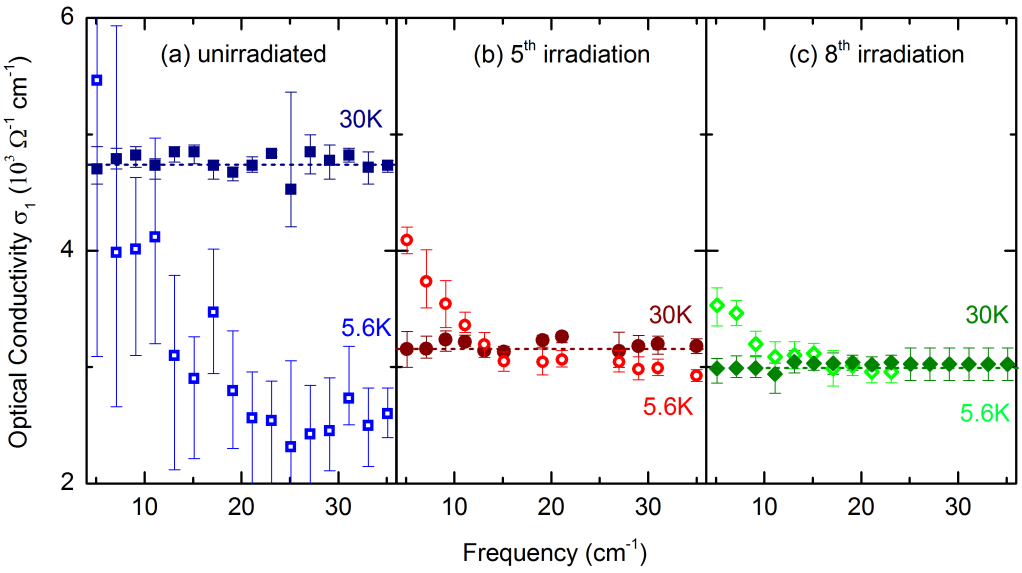


**Figure A.4:** Frequency-dependent optical conductivity $\sigma_1(\omega)$ at 30 K (closed dark symbols) and 5.6 K (open bright symbols) for (a) the unirradiated film ($T_c = 26$ K, blue), (b) the film after five irradiation steps with protons ($T_c = 16$ K, red), as well as (c) the film after eight irradiation steps ($T_c \sim 10$ K, green, adapted from Ref. [322]). In all cases, a strong intra-gap absorption can be observed below $T_c$.

8$^{\text{th}}$ irradiation, however, the transition is already very weak and possibly smeared out too much, in order to determine $T_c$ in this way.

As can be seen in Fig. A.5c, the irradiation suppresses $T_c$ and the residual resistivity ratio ($\sigma$(30K)/$\sigma$(295K)) at least for the first six irradiation steps linearly, meaning that the scattering rate is enhanced proportional to the irradiation dose. In parallel, the coherence peak is quickly suppressed, until it is shifted out of the measured temperature window for the fifth irradiation (see Fig. A.5a and Fig. A.5c). Interestingly, $T_{max}$ is quicker suppressed than $T_c$, meaning that the BCS relation between gap value and critical temperature is violated; this is an important condition to observe the $s_{\pm}$- to $s_{++}$ crossover. Furthermore, the permittivity is reduced significantly with irradiation, while the penetration depth $\lambda_L$ raises almost linearly, consistent with a smooth decrease of the superfluid density.

For the 7$^{\text{th}}$ irradiation, however, the behaviour starts to change. The conductivity in the normal state, as well as the residual resistivity ratio increase slightly. This might indicate that the number of defects got so high that an impurity band has formed, contributing to the overall conductivity. We want to stress, however, that this does not affect our interpretations concerning the coherence peak, as the conductivity in the normal state is still perfectly flat in the THz range (see Fig. A.4c). Our remarkable observation is that at the same time, the coherence peak shifts back to higher frequencies, clearly visible

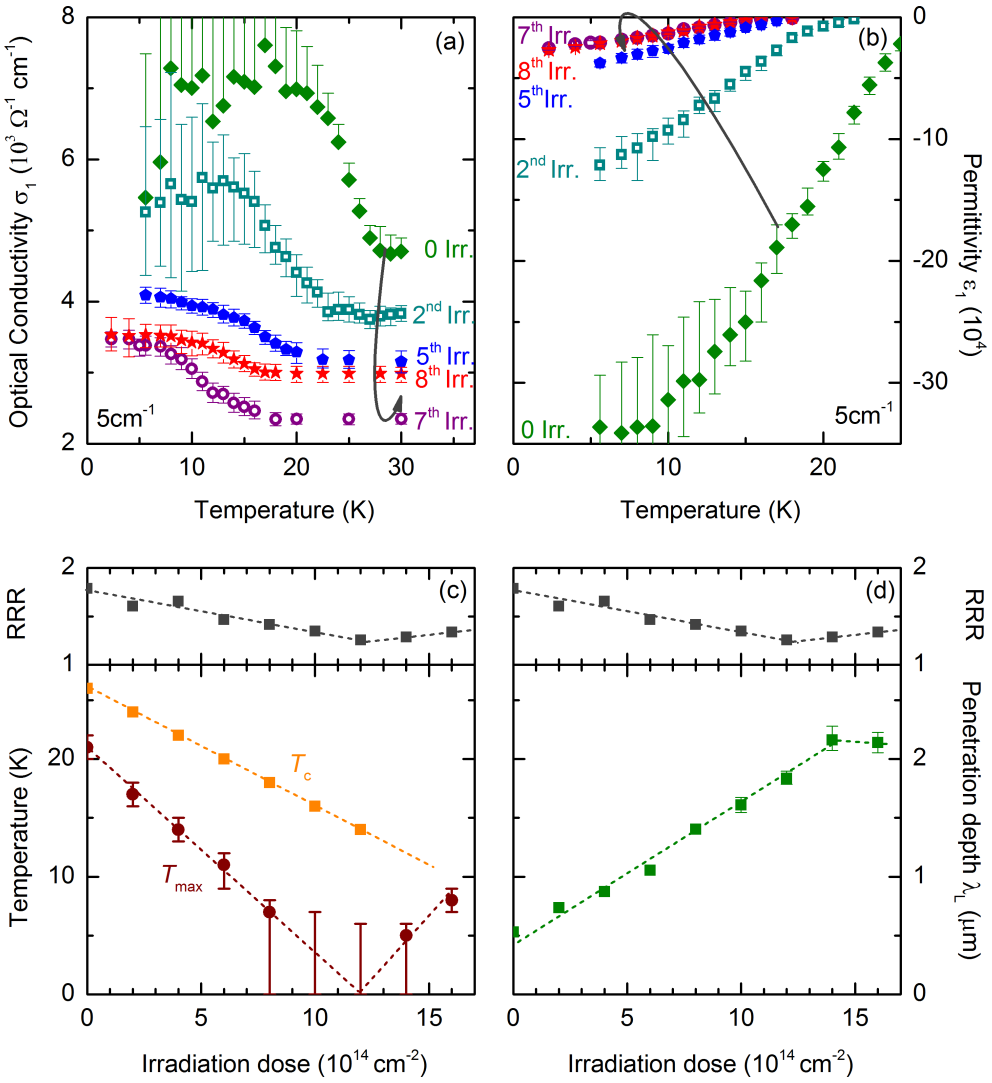


**Figure A.5:** Optical properties of a 50 nm $Ba(Fe_{0.9}Co_{0.1})_2As_2$ film ($T_c$ = 26 K) dependent on the irradiation with protons (dose: $2 \cdot 10^{14}\,cm^{-2}$ per step; adapted from Ref. [322]). (a,b) Temperature-dependent (a) optical conductivity $\sigma_1(T)$ and (b) permittivity $\epsilon_1(T)$ for selected irradiation steps (unirradiated: green closed diamonds, 2nd irradiation: dark cyan open squares, 5th irradiation: blue closed hexagons, 7th irradiation: purple open circles, 8th irradiation: red closed stars). (c,d) Residual resistivity ratio RRR $\sigma(30K)/\sigma(295K)$ (grey squares), compared to (c) the suppression of $T_c$ (orange squares) and the maximum of the coherence peak $T_{max}$, as well as (d) London's penetration depth at $5\,cm^{-1}$ (green squares). Lines and arrows are guides to the eye, stressing that the 8th irradiation clearly deviates from the trend expected from the first irradiation steps.

when comparing in Fig. A.5a $\sigma_1(T)$ of the $7^{\text{th}}$ and $8^{\text{th}}$ irradiation step. Furthermore, the penetration depth saturates, or even tends to decrease. Those observations may indicate a re-appearance of the lower superconducting gap in the measured temperature and frequency window, *i.e.* a crossover from $s_{\pm}$- to $s_{++}$-symmetry of the superconducting order parameter.

# B

# ACKNOWLEDGEMENTS

Writing this thesis sometimes felt like a time travel through the last four years and I got aware once more how lucky I was to have so many people who supported me.

- First of all, I would like to thank my supervisor Prof. Dressel. You always supported and trusted me - probably in some situations more than I did. Most of all, I want to thank you for the warm and familiar atmosphere at your institute.
- I would also thank Prof. Keimer and Prof. Basov for kindly accepting to co-referee this thesis. I always enjoyed discussions with members of your groups.
- Furthermore, I would like to thank Dan Wu. You introduced me with incredible patience in the field of iron pnictides and infrared spectroscopy. We really miss you in our team. Thanks also to Neven Barišić. I learnt a lot from our discussions.
- Work at our institute like we know it would not be possible without the great technical support by Gabi Untereiner, the low temperature and the mechanical workshop, as well as the motherly care of Agni Schmidt.

Furthermore, I want to acknowledge all my collaboration partners, especially:

- The sample growers: H. S. Jeevan in the group of Prof. P. Gegenwart, S. Haindl and K. Iida in the group of Prof. B. Holzapfel, as well as S. Aswartham in the group of S. Wurmehl. Without your support, this thesis would not have been possible.

- Boris Gorshunov and Elena Zhukova, our frequent visitors from Moscow. Boris, I learnt so much more from you than just to "press c". Elena, I always enjoyed the "Hühnerstall" with you.

- R. Kremer, as well as Mrs. Siegle and Mrs. Brücher for the technical support with the specific heat measurements, your confidence concerning the SQUID and the introduction to the ultra low field option. Mr. Kremer, I really learnt a lot while revising the first version of our PRL and I always enjoy(ed) our discussions.

- Prof. D. N. Basov and Kirk Post, as well as all the group members and friends in San Diego: thanks for your great hospitality. Dimitri, I was always inspired, motivated and full of ideas when I came back from your group to Stuttgart. Kirk, you are the most positive person I ever met in my life ("... but look, how stable the temperature is...") and I really appreciate the work with you, especially your russian-american cowboy Helium filling technique as well as the surfing lessons.

- My collaborators in Göttingen (now Augsburg). I learnt a lot from our long discussions.

- Prof. I. Eremin and A. Akbari for the theoretical support and the mutual exchange, as well as Y. Xiao for the discussion of the neutron data; you helped me to survive my first PRB experiences. Thanks also to Prof. J. Fink, Prof. J. Schmalian, Prof. R. Hackl, and Prof. I. Fisher for fruitful discussions.

- D. Efremov and O. Dolgov for a lot of fruitful discussions concerning our thin film measurements.

Furthermore, I have to thank the German Academic Exchange Service, the DFG, as well as the Baden-Württembergische Landesförderung for financial support.

However, the whole thesis would not have been possible without my great colleagues at the 1$^{st}$ Physical Institute:

- First of all, I would like to thank all the Infra-Rats, it was a pleasure to work with all of you. Special thanks for accepting me as "IR Mom" and all the help with the official stuff in the lab.

- Rebecca and Tobi, you were at my side from the first day. Becci, I learnt a lot when passing your “lessons” (which started on my first day at the institute with changing the pump oil). Tobi, no one is a more talented “lab dancer” than you...
- David, Andy and Anja, you enriched our team with new energy and always good mood. David, thanks for the great support in the last two yours, especially while writing the thesis. Andy, I was really grateful when someone finally took my “Küken” burden. Anja, please never ever drink again two energy drinks in a row.
- Uwe, although you chose the other side (without breakfast), thanks for working hardly on re-discovering my optimism.
- Sabrina, Conrad and Eric, thanks for the nice inclusion in your “Team Columbus”. The worst lab day got better with a good mineral water in the evening... Sabrina, we should have thrown this cryostat out of the window.
- Kirk, David, Anja and Conrad, the whole magnetic detwinning project would not have been possible without you and your night shifts.
- My diploma student Felix, my master student Micha, as well as my bachelor students: Kilian, Fabi, Andreas and Alina - I hope that you could learn from me as much as I learnt from you and your questions.
- Tomislav, Eva, Julia and Stefano, thanks a lot for the help in the dc and ellipsometry lab. The work atmosphere was always great.

Special thanks also to my old colleagues from Würzburg, in particular to Prof. Geurts, Prof. Ossau, Prof. Umbach and Prof. Claessen for the reports that supported me in getting my scholarships. Although it was quite some work, I would also like to thank Prof. Honerkamp to suggest me for organizing the SPP summer school.

Finally, I want to thank my family and friends for all the support during the years. I can not find the words to express how much this means to me. Christian, I will never forget when you came to my lab with a freshly baked pizza in an improvised delivery box (and it was still warm). Thanks for all your patience.

# Bibliography


[1] M. R. Norman, Science **332**, 196 (2011).

[2] W. Buckel and R. Kleiner, *Supraleitung*, Wiley, Weihnheim (2013).

[3] D. N. Basov and A. V. Chubukov, Nature Physics **7**, 272 (2011).

[4] Y. Kamihara, T. Watanabe, M. Hirano, and H. Hosono, J. Am. Chem. Soc. **130**, 3296 (2008).

[5] D. C. Johnston, Adv. Phys. **59**, 6 (2010).

[6] I. R. Fisher, L. Degiorgi, and Z. X. Shen, Rep. Prog. Phys. **74**, 124506 (2011).

[7] Y. Xiao, Y. Su, W. Schmidt, K. Schmalzl, C. M. N. Kumar, S. Price, T. Chatterji, R. Mittal, L. J. Chang, S. Nandi, N. Kumar, S. K. Dhar, A. Thamizhavel, and T. Brückel, Phys. Rev. B **81**, 220406(R) (2010).

[8] Y. Xiao, Y. Su, M. Meven, R. Mittal, C.M.N. Kumar, T. Chatterji, S. Price, J. Persson, N. Kumar, S.K. Dhar, A. Thamizhavel, and T. Brückel, Phys. Rev. B **80**, 174424 (2009).

[9] S. Zapf, D. Wu, L. Bogani, H. S. Jeevan, P. Gegenwart, and M. Dressel, Phys. Rev. B **84**, 140503 (2011).

[10] S. Zapf, H. S. Jeevan, T. Ivek, F. Pfister, F. Klingert, S. Jiang, D. Wu, P. Gegenwart, R. K. Kremer, and M. Dressel, Phys. Rev. Lett. **110**, 237002 (2013).

[11] A. Akbari, I. Eremin, and P. Thalmeier, Phys. Rev. B **84**, 134513 (2011).

[12] P. Marsik, C. N. Wang, M. Rössle, M. Yazdi-Rizi, R. Schuster, K. W. Kim, A. Dubroka, D. Munzar, T. Wolf, X. H. Chen, and C. Bernhard, Phys. Rev. B **88**, 180508(R) (2013).

[13] S. Zapf, C. Stingl, K. W. Post, J. Maiwald, N. Bach, I. Pietsch, D. Neubauer, A. Löhle, C. Clauss, S. Jiang, H. S. Jeevan, D. N. Basov, P. Gegenwart, and M. Dressel, Phys. Rev. Lett. **113**, 227001 (2014).

[14] S. Blundell, *Magnetism in Condensed Matter*, Oxford University Press Inc., New York (2001).

[15] J. Bardeen, L. N. Cooper, and J. R. Schrieffer, Phys. Rev. **106**, 162 (1957).

[16] H. Fröhlich, Phys. Rev. **79**, 845 (1950).

[17] J. Bardeen, Phys. Rev. **80**, 567 (1950).

[18] W. L. McMillan, Phys. Rev. **167**, 331 (1968).

[19] L. Gao, Y. Y. Xue, F. Chen, Q. Xiong, R. L. Meng, D. Ramirez, C. W. Chu, J. H. Eggert, and H. K. Mao, Phys. Rev. B **50**, 4260 (1994).

[20] J. G. Bednorz and K. A. Müller, Z. Phys. B **64**, 189 (1986).

[21] E. Fradkin and S. A. Kivelson, Nature Phys. **8**, 864 (2012).

[22] N. Lavrov, Y. Ando, S. Komiya, and I. Tsukada, Phys. Rev. Lett. **87**, 017007 (2001).

[23] A. Lavrov, S. Komiya, and Y. Ando, Nature **418**, 385-386 (2002).

[24] J.-H. Chu, J. G. Analytis, D. Press, T. D. Ladd, Y. Yamamoto, and I. R. Fisher, Phys. Rev. B **81**, 214502 (2010).

[25] J.-H. Chu, H.-K. Kuo, J. G. Analytis, and I. R. Fisher, Science **337**, 710 (2012).

[26] M. Tegel, M. Rotter, V. Wieß, F. M. Schappacher, R. Pöttgen, and D. Johrendt, J. Phys.: Condens. Matter **20**, 452201 (2008).

[27] H. S. Jeevan, Z. Hossain, D. Kasinathan, H. Rosner, C. Geibel, and P. Gegenwart, Phys. Rev. B **78**, 052502 (2008).

[28] Z. Ren, Z. Zhu, S. Jiang, X. Xu, Q. Tao, C. Wang, C. Feng, G. H. Cao, and Z. A. Xu, Phys. Rev. B **78**, 052501 (2008).

[29] C. F. Miclea, M. Nicklas, H. S. Jeevan, D. Kasinathan, Z. Hossain, H. Rosner, P. Gegenwart, C. Geibel, and F. Steglich, Phys. Rev. B **79**, 212509 (2009).

[30] Z. Ren, Q. Tao, S. Jiang, C. Feng, C. Wang, J. Dai, G. Cao, and Z. Xu, Phys. Rev. Lett. **102**, 137002 (2009).

[31] W. H. Jiao, Q. Tao, J. K. Bao, Y. L. Sun, C. M. Feng, Z. A. Xu, I. Nowik, I. Felner, and G. H. Cao, Europhys. Lett. **95**, 67007 (2011).

[32] S. Jiang, H. Xing, G. Xuan, Z. Ren, C. Wang, Z. A. Xu, and G. Cao, Phys. Rev. B **80**, 184514 (2009).

[33] U. B. Paramanik, D. Das, R. Prasad, and Z. Hossain, J. Phys.: Condens. Matter **25**, 265701 (2013).

[34] H. S. Jeevan, Z. Hossain, D. Kasinathan, H. Rosner, C. Geibel, and P. Gegenwart, Phys. Rev. B **78**, 092406 (2008).

[35] M. Reis, *Fundamentals of Magnetism*, Academic Press, Amsterdam (2013).

[36] M. A. Ruderman and C. Kittel, Phys. Rev. **96**, 99 (1954).

[37] M. Getzlaff, *Fundamentals of Magnetism*, Springer, Berlin (2008).

[38] J. A. Mydosh, *Spin Glasses: An Experimental Introduction*, Taylor & Francis, London (1993).

[39] M. Gabay and G. Toulouse, Phys. Rev. Lett. **47**, 201 (1981).

[40] M. Tinkham, *Introduction to Superconductivity*, Dover Publications (2012).

[41] C. A. Reynolds, B. Serin, W. H. Wright, and L. B. Nesbitt, Phys. Rev. **78**, 487 (1950).

[42] E. Mawell, Phys. Rev. **78**, 477 (1950).

[43] R. E. Glover III and M. Tinkham, Phys. Rev. **108**, 243 (1957).

[44] G. M. Eliashberg, Sov. Phys. JETP **11**, 696 (1960).

[45] L. Boeri, O.V. Dolgov, and A. A. Golubov, Phys. Rev. Lett. **101**, 026403 (2008).

[46] M. K. Wu, J. R. Ashburn, C. J. Torng, P. H. Hor, R. L. Meng, L. Gao, Z. J. Huang, Y. Q. Wang, and C. W. Chu, Phys. Rev. Lett. **58**, 908 (1987).

[47] H. Maeda, Y. Tanaka, M. Fukutomi, and T. Asano, Jpn. J. Appl. Phys. **27**, L209 (1988).

[48] M. R. Norman, D. Pines, and C. Kallin, Adv. Phys. **54**, 8 (2005).

[49] N. Doiron-Leyraud, C. Proust, D. LeBoeuf, J. Levallois, J.-B. Bonnemaison, R. Liang, D. A. Bonn, W. N. Hardy, and L. Taillefer, Nature **447**, 565 (2007).

[50] H.-B. Yang, J. D. Rameau, Z.-H. Pan, G. D. Gu, P. D. Johnson, H. Claus, D. G. Hinks, and T. E. Kidd, Phys. Rev. Lett. **107**, 047003 (2011).

[51] N. Harrison and S. E. Sebastian, New J. Phys. **16**, 063025 (2014).

[52] M. C. Boyer, W. D. Wise, K. Chatterjee, M. Yi, T. Kondo, T. Takeuchi, H. Ikuta, and E. W. Hudson, Nature Phys. **3**, 802 (2007).

[53] R.-H. He, M. Hashimoto, H. Karapetyan, J. D. Koralek, J. P. Hinton, J. P. Testaud, V. Nathan, Y. Yoshida, H. Yao, K. Tanaka, W. Meevasana, R. G. Moore, D. H. Lu, S.-K. Mo, M. Ishikado, H. Eisaki, Z. Hussain, T. P. Devereaux, S. A. Kivelson, J. Orenstein, A. Kapitulnik, and Z.-X. Shen, Science **331**, 1579 (2011).

[54] Y. He, Y. Yin, M. Zech, A. Soumyanarayanan, M. M. Yee, T. Williams, M. C. Boyer, K. Chatterjee, W. D. Wise, I. Zeljkovic, T. Kondo, T. Takeuchi, H. Ikuta, P. Mistark, R. S. Markiewicz, A. Bansil, S. Sachdev, E. W. Hudson, and J. E. Hoffman, Science **344**, 608 (2014).

[55] C. V. Parker, P. Aynajian, E. H. da Silva Neto, A. Pushp, S. Ono, Jinsheng Wen, Z. Xu, G. Gu, and A. Yazdani, Nature **468**, 677 (2010).

[56] D. H. Torchinsky, F. Mahmood, A. T. Bollinger, I. Božović, and N. Gedik, Nature Mater. **12**, 387 (2013).

[57] R. Comin, A. Frano, M. M. Yee, Y. Yoshida, H. Eisaki, E. Schierle, E. Weschke, R. Sutarto, F. He, A. Soumyanarayanan, Yang He, M. Le Tacon, I. S. Elfimov, Jennifer E. Hoffman, G. A. Sawatzky, B. Keimer, and A. Damascelli, Science **343**, 390 (2014).

[58] E. H. da Silva Neto, P. Aynajian, Al. Frano, R. Comin, E. Schierle, E. Weschke, A. Gyenis, J. Wen, J. Schneeloch, Z. Xu, S. Ono, G. Gu, M. Le Tacon, and A. Yazdani, Science **343**, 393 (2014).

[59] V. Hinkov, D. Haug, B. Fauqué, P. Bourges, Y. Sidis, A. Ivanov, C. Bernhard, C. T. Lin, and B. Keimer, Science **319**, 597 (2008).

[60] M. J. Lawler, K. Fujita, J. Lee, A. R. Schmidt, Y. Kohsaka, C. K. Kim, H. Eisaki, S. Uchida, J. C. Davis, J. P. Sethna, and E.-A. Kim, Nature **466**, 347 (2010).

[61] J. R. Waldram, *Superconductivity in metals and cuprates*, Institute of Physics Publishing, London (1996).

[62] N. F. Mott, Philos. Mag. **26**, 1015 (1972).

[63] A. F. Yoffe and A. R. Regel, Prog. Semicond. **4**, 237 (1960).

[64] T. Moriya and K. Ueda, Rep. Prog. Phys. **66**, 1299 (2003).

[65] N. L. Wang, H. Hosono, and P. Dai, *Iron-based superconductors*, Pan Stanford, Singapore (2013).

[66] F. Ronning, T. Klimczuk, E. D. Bauer, H. Volz, and J. D. Thompson, J. Phys.: Condens. Matter **20**, 322201 (2008).

[67] Q.-Y. Wang, Z. Li, W.-H. Zhang, Z.-C. Zhang, J.-S. Zhang, W. Li, H. Ding, Y.-B. Ou, P. Deng, K. Chang, J. Wen, C.-L. Song, K. He, J.-F. Jia, S.-H. Ji, Y.-Y. Wang, L.-L. Wang, X. Chen, X.-C. Ma, and Q.-K. Xue, Chin. Phys. Lett. **29**, 037402 (2012).

[68] H. Wadati, I. Elfimov, and G. A. Sawatzky, Phys. Rev. Lett. **105**, 157004 (2010).

[69] I. Mazin, Nature **464**, 183 (2010).

[70] I. I. Mazin, D. J. Singh, M. D. Johannes, and M.-H. Du, Phys. Rev. Lett. **101**, 057003 (2008).

[71] P. J. Hirschfeld, M. M. Korshunov, and I. I. Mazin, Rep. Prog. Phys. **74**, 124508 (2011).

[72] V. Mishra, G. Boyd, S. Graser, T. Maier, P. J. Hirschfeld, and D. J. Scalapino, Phys. Rev. B **79**, 094512 (2009).

[73] E. Wiesenmayer, H. Luetkens, G. Pascua, R. Khasanov, A. Amato, H. Potts, B. Banusch, H.-H. Klauss, and D. Johrendt, Phys. Rev. Lett. **107**, 237001 (2011).

[74] P. Cai, X. Zhou, W. Ruan, A. Wang, X. Chen, D.-H. Lee, and Y. Wang, Nature Commun. **4**, 1596 (2012).

[75] M. A. Tanatar, E. C. Blomberg, A. Kreyssig, M. G. Kim, N. Ni, A. Thaler, S. L. Bud'ko, P. C. Canfield, A. I. Goldman, I. I. Mazin, and R. Prozorov, Phys. Rev. B **81**, 184508 (2010).

[76] M. Yi, D. Luc, J.-H. Chu, J. G. Analytis, A. P. Sorini, A. F. Kemper, B. Moritz, S.-K. Mo, R. G. Moore, M. Hashimoto, W.-S. Lee, Z. Hussain, T. P. Devereaux, I. R. Fisher, and Z.-X. Shen, PNAS 108, 6878 (2011).

[77] S. Kasahara, H. J. Shi, K. Hashimoto, S. Tonegawa, Y. Mizukami, T. Shibauchi, K. Sugimoto, T. Fukuda, T. Terashima, A. H. Nevidomskyy, and Y. Matsuda, Nature Phys. **486**, 382 (2012).

[78] C. Dhital, Z. Yamani, W. Tian, J. Zeretsky, A. S. Sefat, Z. Wang, R. J. Birgeneau, and S. D. Wilson, Phys. Rev. Lett. **108**, 087001 (2012).

[79] E. P. Rosenthal, E. F. Andrade, C. J. Arguello, R. M. Fernandes, L. Y. Xing, X. C. Wang, C. Q. Jin, A. J. Millis, and A. N. Pasupathy, Nature Phys. **10**, 225 (2014).

[80] R. M. Fernandes, A. V. Chubukov, and J. Schmalian, Nature Phys. **10**, 97 (2014).

[81] H. H. Kuo and I. R. Fisher, Phys. Rev. Lett. **112**, 227001 (2014).

[82] G. F. Chen, Z. Li, D. Wu, G. Li, W. Z. Hu, J. Dong, P. Zheng, J. L. Luo, and N. L. Wang, Phys. Rev. Lett. **100**, 247002 (2008).

[83] K. Hashimoto, K. Cho, T. Shibauchi, S. Kasahara, Y. Mizukami, R. Katsumata, Y. Tsuruhara, T. Terashima, H. Ikeda, M. A. Tanatar, H. Kitano, N. Salovich, R. W. Giannetta, P. Walmsley, A. Carrington, R. Prozorov, and Y. Matsuda, Science **22**, 1554 (2012).

[84] T. Shibauchi, A. Carrington, and Y. Matsuda, Annu. Rev. Condens. Matter Phys. **5**, 113 (2014).

[85] D. Manske, *Theory of unconventional superconductors*, Springer, Berlin (2004).

[86] J. P. Carbotte, E. Schachinger, and D. N. Basov, Nature **401**, 354 (1999).

[87] E. G. Maksimov, M. L. Kulić, and O. V. Dolgov, Adv. Cond. Matt. Phys., 423725 (2010).

[88] D. S. Inosov, J. T. Park, P. Bourges, D. L. Sun, Y. Sidis, A. Schneidewind, K. Hradil, D. Haug, C. T. Lin, B. Keimer, and V. Hinko, Nature Phys. **6**, 178 (2010).

[89] A. D. Christianson, E. A. Goremychkin, R. Osborn, S. Rosenkranz, M. D. Lumsden, C. D. Malliakas, I. S. Todorov, H. Claus, D. Y. Chung, M. G. Kanatzidis, R. I. Bewley, and T. Guidi, Nature **456**, 930 (2008).

[90] C. P. Poole Jr, R. Prozorov, H. A. Farach, and R. J. Creswick, *Superconductivity*, Elsevier, Waltham (2014).

[91] M. McElfresh, *Fundamentals of magnetism and magnetic materials*, Quantum Design (1994).

[92] C. P. Bean, Phys. Rev. Lett. **8**, 250 (1962).

[93] Y. Yeshrun, A. P. Malozemoff, and A. Shaulov, Rev. Mod. Phys. **68**, 911 (1996).

[94] S.V. Chong, S. Hashimoto, and K. Kadowaki, Solid State Comm. **150**, 1178 (2010).

[95] Y. B. Kim, C. F. Hempstead, and A. R. Strnad, Phys. Rev. Lett. **129**, 528 (1963).

[96] F. Herlach and N. Miur, *High Magnetic Fields - Science And Technology, Vol. 3*, World Scientific, Singapore (2006).

[97] A. M. Clogston, Phys. Rev. Lett. **9**, 266 (1962).

[98] B. S. Chandrasekhar, Appl. Phys. Lett. **1**, 7 (1962).

[99] N. R. Werthamer, E. Helfand, and P. C. Hohenberg, Phys. Rev. **147**, 295 (1966).

[100] E. Müller-Hartmann and J. Zittartz, Phys. Rev. Lett. **26**, 428 (1971).

[101] K. Winzer, Solid State Comm. **24**, 551 (1977).

[102] K.-H. Müller and V. N. Narozhnyi, Rep. Prog. Phys. **64**, 943 (2001).

[103] P. Fulde and R. A. Ferrell, Phys. Rev. **135**, A550 (1964).

[104] A. I. Larkin and Y. N. Ovchinnikov, Zh. Eksp. Teor. Fiz. **47**, 1136 (1964).

[105] A. I. Larkin and Y. N. Ovchinnikov, Sov. Phys. JETP **20**, (1965).

[106] H. A. Radovan, N. A. Fortune, T. P. Murphy, S. T. Hannahs, E. C. Palm, S. W. Tozer, and D. Hall, Nature **425**, 51 (2003).

[107] P. W. Anderson and H. Suhl, Phys. Rev. **116**, 898 (1959).

[108] M. Tachiki, H. Matsumoto, T. Koyama, and H. Umezawa, Solid State Comm. **34**, 19 (1980).

[109] H. S. Greenside, E. I. Blount, and C. M. Varma, Phys. Rev. Lett. **46**, 49 (1981).

[110] V. Jaccarino and M. Peter, Phys. Rev. Lett. **9**, 290 (1962).

[111] O. Fischer, M. Decroux, S. Roth, R. Chevrel, and M. Sergent, J. Phys. C **8**, L474 (1975).

[112] H. W. Meul, C. Rossel, M. Decroux, O. Fischer, G. Remenyi, and A. Briggs, Phys. Rev. Lett. **53**, 497 (1984).

[113] M. Dressel and G. Grüner, *Electrodynamics of Solids*, Cambridge University Press, Cambridge (2002).

[114] M. Fox, *Optical properties of solids*, Oxford University Press, Oxford (2001).

[115] N. L. Wang, H. Hosono, and P. Dai, *Iron-based Superconductors*, CRC Press, Boca Raton (2013).

[116] D. N. Basov and T. Timusk, Rev. Mod. Phys. **77**, 721 (2005).

[117] M. Tinkham, Phys. Rev. **104**, 845 (1956).

[118] R. A. Ferrell and R. E. Glover, Phys. Rev. **109**, 1398 (1958).

[119] M. Tinkham and R. A. Ferrell, Phys. Rev. Lett. **2**, 331 (1959).

[120] D. C. Mattis and J. Bardeen, Phys. Rev. **111**, 412 (1958).

[121] W. Zimmermann, E. H. Brandt, M. Bauer, E. Seider, and L. Genzel, Physica C **183**, 99 (1991).

[122] U. S. Pracht, E. Heintze, C. Clauss, D. Hafner, R. Bek, D. Werner, S. Gelhorn, M. Scheffler, M. Dressel, D. Sherman, B. Gorshunov, K. S. Il'in, D. Henrich, and M. Siegel, IEEE Trans. THz Sci. Technol. **3**, 269 (2013).

[123] M. M. Qazilbash, J. J. Hamlin, R. E. Baumbach, L. Zhang, D. J. Singh, M. B. Maple, and D. N. Basov, Nature Phys. **5**, 647 (2009).

[124] J. Dong, H. J. Zhang, G. Xu, Z. Li, G. Li, W. Z. Hu, D. Wu, G. F. Chen, X. Dai, J. L. Luo, Z. Fang, and N. L. Wang, Europhys. Lett. **83**, 27006 (2008).

[125] G. F. Chen, Z. Li, G. Li, J. Zhou, D. Wu, J. Dong, W. Z. Hu, P. Zheng, Z. J. Chen, H. Q. Yuan, J. Singleton, J. L. Luo, and N. L. Wang, Phys. Rev. Lett. **101**, 057007 (2008).

[126] A. Dubroka, K. W. Kim, M. Rössle, V. K. Malik, A. J. Drew, R. H. Liu, G. Wu, X. H. Chen, and C. Bernhard, Phys. Rev. Lett. **101**, 097011 (2008).

[127] G. Li, W. Z. Hu, J. Dong, Z. Li, P. Zheng, G. F. Chen, J. L. Luo, and N. L. Wang, Phys. Rev. Lett. **101**, 107004 (2008).

[128] D. Wu, N. Barišić, P. Kallina, A. Faridian, B. Gorshunov, N. Drichko, L. J. Li, X. Lin, G. H. Cao, Z. A. Xu, N. L. Wang, and M. Dressel, Phys. Rev. B **81**, 100512(R) (2010).

[129] M. Nakajima, S. Ishida, K. Kihou, Y. Tomioka, T. Ito, Y. Yoshida, C. H. Lee, H. Kito, A. Iyo, H. Eisaki, K. M. Kojima, and S. Uchida, Phys. Rev. B **81**, 104528 (2010).

[130] N. Barišić, D. Wu, M. Dressel, L. J. Li, G. H. Cao, and Z. A. Xu, Phys. Rev. B **82**, 054518 (2010).

[131] S. J. Moon, A. A. Schafgans, M. A. Tanatar, R. Prozorov, A. Thaler, P. C. Canfield, A. S. Sefat, D. Mandrus, and D. N. Basov, Phys. Rev. Lett. **110**, 097003 (2013).

[132] F. Pfuner, J. G. Analytis, J.-H. Chu, I. R. Fisher, and L. Degiorgi, Eur. Phys. J. B **67**, 513 (2009).

[133] E. van Heumen, Y. Huang, S. de Jong, A. B. Kuzmenko, M. S. Golden, and D. van der Marel, Europhys. Lett. **90**, 37005 (2010).

[134] R. P. S. M. Lobo, Y. M. Dai, U. Nagel, T. Rõõm, J. P. Carbotte, T. Timusk, A. Forget, and D. Colson, Phys. Rev. B **82**, 100506(R) (2010).

[135] A. Charnukha, O. V. Dolgov, A. A. Golubov, Y. Matiks, D. L. Sun, C. T. Lin, B. Keimer, and A. V. Boris, Phys. Rev. B **84**, 174511 (2011).

[136] Y. S. Kwon, J. B. Hong, Y. R. Jang, H. J. Oh, Y. Y. Song, B. H. Min, T. Iizuka, S. Kimura, A. V. Balatsky, and Y. Bang, New J. Phys. **14**, 063009 (2012).

[137] Y. M. Dai, B. Xu, B. Shen, H. H. Wen, J. P. Hu, X. G. Qiu, and R. P. S. M. Lobo, Phys. Rev. B **86**, 100501(R) (2012).

[138] S. J. Moon, A. A. Schafgans, S. Kasahara, T. Shibauchi, T. Terashima, Y. Matsuda, M. A. Tanatar, R. Prozorov, A. Thaler, P. C. Canfield, A. S. Sefat, D. Mandrus, and D. N. Basov, Phys. Rev. Lett. **109**, 027006 (2012).

[139] J. N. Hancock, S. I. Mirzaei, J. Gillett, S. E. Sebastian, J. Teyssier, R. Viennois, E. Giannini, and D. van der Marel, Phys. Rev. B **82**, 014523 (2010).

[140] Y. Imai, F. Nabeshima, D. Nakamura, T. Katase, H. Hiramatsu, H. Hosono, and A. Maeda, J. Phys. Soc. Jpn. **82**, 043709 (2013).

[141] M. Nakajima, S. Ishida, T. Tanaka, K. Kihou, Y. Tomioka, T. Saito, C. H. Lee, H. Fukazawa, Y. Kohori, T. Kakeshita, A. Iyo, T. Ito, H. Eisaki, and S. Uchida, Sci Rep. **4**, 5873 (2014).

[142] J. J. Tu, J. Li, W. Liu, A. Punnoose, Y. Gong, Y. H. Ren, L. J. Li, G. H. Cao, Z. A. Xu, and C. C. Homes, Phys. Rev. B **82**, 174509 (2010).

[143] E. G. Maksimov, A. E. Karakozov, B. P. Gorshunov, A. S. Prokhorov, A. A. Voronkov, E. S. Zhukova, V. S. Nozdrin, S. S. Zhukov, D. Wu, M. Dressel, S. Haindl, K. Iida, and B. Holzapfel, Phys. Rev. B **83**, 140502(R) (2011).

[144] E. G. Maksimov, A. E. Karakozov, A. A. Voronkov, B. P. Gorshunov, S. S. Zhukov, E. S. Zhukova, V. S. Nozdrin, A. S. Prokhorov, S. Haindl, B. Holzapfel, L. Schultz, D. Wu, M. Dressel, K. Iida, P. Kallina, and F. Kurth, JETP **93**, 736 (2011).

[145] A. Akrap, J. J. Tu, L. J. Li, G. H. Cao, Z. A. Xu, and C. C. Homes, Phys. Rev. B **80**, 180502(R) (2009).

[146] S. J. Moon, J. H. Shin, D. Parker, W. S. Choi, I. I. Mazin, Y. S. Lee, J. Y. Kim, N. H. Sung, B. K. Cho, S. H. Khim, J. S. Kim, K. H. Kim, and T. W. Noh, Phys. Rev. B **81**, 205114 (2010).

[147] Z. G. Chen, T. Dong, R. H. Ruan, B. F. Hu, B. Cheng, W. Z. Hu, P. Zheng, Z. Fang, X. Dai, and N. L. Wang, Phys. Rev. Lett. **105**, 097003 (2010).

[148] B. Gorshunov, D. Wu, A. A. Voronkov, P. Kallina, K. Iida, S. Haindl, F. Kurth, L. Schultz, B. Holzapfel, and M. Dressel, Phys. Rev. B **81**, 060509(R) (2010).

[149] A. Perucchi, L. Baldassarre, S. Lupi, J. Y. Jiang, J. D.Weiss, E. E. Hellstrom, S. Lee, C. W. Bark, C. B. Eom, M. Putti, I. Pallecchi, C. Marini, and P. Dore, Eur. Phys. J. B **77**, 25 (2010).

[150] R. V. Aguilar, L. S. Bilbro, S. Lee, C. W. Bark, J. Jiang, J. D. Weiss, E. E. Hellstrom, D. C. Larbalestier, C. B. Eom, and N. P. Armitage, Phys. Rev. B **82**, 180514 (R) (2010).

[151] T. Fischer, A. V. Pronin, J. Wosnitza, K. Iida, F. Kurth, S. Haindl, L. Schultz, B. Holzapfel, and E. Schachinger, Phys. Rev. B **82**, 224507 (2010).

[152] Y. A. Aleshchenko, A. V. Muratov, V. M. Pudalov, E. S. Zhukova, B. P. Gorshunov, F. Kurth, and K. Iida, JETP **94**, 719 (2012).

[153] A. Perucchi, L. Baldassarre, B. Joseph, S. Lupi, S. Lee, C. B. Eom, J. Jiang, J. D. Weiss, E. E. Hellstrom, and P. Dore, Eur. Phys. J. B **86**, 274 (2013).

[154] K. W. Kim, M. Rössle, A. Dubroka, V. K. Malik, T. Wolf, and C. Bernhard, Phys. Rev. B **81**, 214508 (2010).

[155] D. Wu, N. Barišić, M. Dressel, G. H. Cao, Z-A. Xu, J. P. Carbotte, and E. Schachinger, Phys. Rev. B **82**, 184527 (2010).

[156] Y. M. Dai, B. Xu, B. Shen, H. H.Wen, X. G. Qiu, and R. P. S. M. Lobo, Europhys. Lett. **104**, 47006 (2013).

[157] B. B. Jin, T. Dahm, A. I. Gubin, Eun-Mi Choi, Hyun Jung Kim, Sung-IK Lee, W. N. Kang, and N. Klein, Phys. Rev. Lett. **91**, 127006 (2003).

[158] A. Charnukha , P. Popovich , Y. Matiks, D. L. Sun, C. T. Lin, A. N. Yaresko, B. Keimer, and A. V. Boris, Nature Commun. **2**, 219 (2011).

[159] J. Yang, D. Hüvonen, U. Nagel, T. Rõõm, N. Ni, P. C. Canfield, S. L. Bud'ko, J. P. Carbotte, and T. Timusk, Phys. Rev. Lett. **102**, 187003 (2009).

[160] D. Wu, N. Barišić, M. Dressel, G. H. Cao, Z-A. Xu, E. Schachinger, and J. P. Carbotte, Phys. Rev. B **82**, 144519 (2010).

[161] Y. M. Dai, B. Xu, B. Shen, H. Xiao, H. H. Wen, X. G. Qiu, C. C. Homes, and R. P. S. M. Lobo, Phys. Rev. Lett. **111**, 117001 (2013).

[162] A. Lucarelli, A. Dusza, F. Pfuner, P. Lerch, J. G. Analytis, J.-H. Chu, I. R. Fisher, and L. Degiorgi, New J. Phys. **12**, 073036 (2010).

[163] A. A. Schafgans, S. J. Moon, B. C. Pursley, A. D. LaForge, M. M. Qazilbash, A. S. Sefat, D. Mandrus, K. Haule, G. Kotliar, and D. N. Basov, Phys. Rev. Lett. **108**, 147002 (2012).

[164] N. L. Wang, W. Z. Hu, Z. G. Chen, R. H. Yuan, G. Li, G. F. Chen, and T. Xiang, J. Phys.: Condens. Matter **24**, 294202 (2012).

[165] Z. G. Chen, R. H. Yuan, T. Dong, and N. L. Wang, Phys. Rev. B **81**, 100502(R) (2010).

[166] M. Nakajima, T. Tanaka, S. Ishida, K. Kihou, C. H. Lee, A. Iyo, T. Kakeshita, H. Eisaki, and S. Uchida, Phys. Rev. B **88**, 094501 (2013).

[167] A. Dusza, A. Lucarelli, F. Pruner, J.-H. Chu, I.R. Fisher, and L. Degiorgi, Europhys. Lett. **93**, 37002 (2011).

[168] Z. P. Yin, K. Haule, and G. Kotliar, Nature Phys. **7**, 294 (2011).

[169] M. Nakajima, T. Liang, S. Ishida, Y. Tomioka, K. Kihou, C. H. Lee, A. Iyo, H. Eisaki, T. Kakeshita, T. Ito, and S. Uchida, PNAS **108**, 12238 (2011).

[170] A. Dusza, A. Lucarelli, A. Sanna, J.-H. Chu, I.R. Fisher, and L. Degiorgi, New J. of Phys. **14**, 023020 (2012).

[171] M. Nakajima, S. Ishida, Y. Tomioka, K. Kihou, C. H. Lee, A. Iyo, T. Ito, T. Kakeshita, H. Eisaki, and S. Uchida, Phys. Rev. Lett. **109**, 217003 (2012).

[172] A. Dusza, A. Lucarelli, J.-H. Chu, I.R. Fisher, and L. Degiorgi, J. Supercond. Nov. Magn. **26**, 2603 (2013).

[173] C. Mirri, A. Dusza, S. Bastelberger, J.-H. Chu, H.-H. Kuo, I. R. Fisher, and L. Degiorgi, Phys. Rev. B **89**, 060501(R) (2014).

[174] A. A. Schafgans, B. C. Pursley, A. D. LaForge, A. S. Sefat, D. Mandrus, and D. N. Basov, Phys. Rev. B **84**, 052501 (2011).

[175] C. Clauß, *Optical investigations on the charge ordered state of two dimensional conductors*, Diplomarbeit am 1. Physikalischen Institut, Stuttgart (2008).

[176] J. Merz, *Infrarotspektroskopie an Eisenpniktiden*, Bachelorarbeit am 1. Physikalischen Institut, Stuttgart (2014).

[177] A. D. LaForge, A. Frenzel, B. C. Pursley, T. Lin, X. Liu, J. Shi, and D. N. Basov, Phys. Rev. B **81**, 125120 (2010).

[178] W. G. Jenks, I. M. Thomas, and J. P. Wikswo Jr., EAP **19**, 457 (1997).

[179] D. Martien, *Introduction to AC susceptibility*, Quantum Design (2002).

[180] K. Iida, J. Hänisch, R. Hühne, F. Kurth, M. Kidszun, S. Haindl, J. Werner, L. Schultz, and B. Holzapfel, Appl. Phys. Lett. **95**, 192501 (2009).

[181] C. Krellner, N. Caroca-Canales, A. Jesche, H. Rosner, A. Ormeci, and C. Geibel, Phys. Rev. B **78**, 100504(R) (2008).

[182] S. Jiang, Y. Luo, Z. Ren, Z. Zhu, C. Wang, X. Xu, Q. Tao, G. Cao, and Z. A. Xu, New J. Phys. **11** 025007 (2009).

[183] J. Herrero-Martín, V. Scagnoli, C. Mazzoli, Y. Su, R. Mittal, Y. Xiao, T. Brückel, N. Kumar, S.K. Dhar, A. Thamizhavel, and L. Paolasini, Phys. Rev. B. **80**, 134411 (2009).

[184] D. Wu, N. Barišić, N. Drichko, S. Kaiser, A. Faridian, M. Dressel, S. Jiang, Z. Ren, L. J. Li, G. H. Cao, Z. A. Xu, H. S. Jeevan, and P. Gegenwart, Phys. Rev. B **79**, 155103 (2009).

[185] D. Kasinathan, A. Ormeci, K. Koch, U. Burkhardt, W. Schnelle, A. Leithe-Jasper, and H. Rosner, New J. Phys. **11** 025023 (2009).

[186] W. Z. Hu, J. Dong, G. Li, Z. Li, P. Zheng, G. F. Chen, J. L. Luo, and N. L. Wang, Front. Phys. China **4**, 459 (2009).

[187] E. Dengler, J. Deisenhofer, H. A. Krug von Nidda, S. Khim, J. S. Kim, K. H. Kim, F. Casper, C. Felser, and A. Loidl, Phys. Rev. B **81**, 024406 (2010).

[188] T. Terashima, N. Kurita, A. Kikkawa, H. S. Suzuki, T. Matsumoto, K. Murata, and S. Uji, J. Phys. Soc. Jpn. **79**, 103706 (2010).

[189] J. Koo, J. Park, S. K. Cho, K. D. Kim, S.-Y. Park, Y. H. Jeong, Y. J. Park T. Y. Koo, K.-P. Hong, C.-H. Lee, J.-Y. Kim, B.-K. Cho, K. B. Lee, and H.-J. Kim, J. Phys. Soc. Jpn. **79**, 114708 (2010).

[190] M. Tokunaga, I. Katakura, N. Katayama, and K. Ohgushi, J. Low Temp. Phys. **159**, 601) (2010).

[191] S. de Jong, E. van Heumen, S. Thirupathaiah, R. Huisman, F. Massee, J. B. Goedkoop, R. Ovsyannikov, J. Fink, H. A. Dürr, A. Gloskovskii, H. S. Jeevan, P. Gegenwart, A. Erb, L. Patthey, M. Shi, R. Follath, A. Varykhalov, and M. S. Golden, Europhys. Lett. **89**, 27007 (2010).

[192] B. Zhou, Y. Zhang, L. X. Yang, M. Xu, C. He, F. Chen, J. F. Zhao, H. W. Ou, J. Wei, B. P. Xie, T. Wu, G. Wu, M. Arita, K. Shimada, H. Namatame, M. Taniguchi, X. H. Chen, and D. L. Feng, Phys. Rev. B **81**, 155124 (2010).

[193] M. S. Kim, N. H. Sung, Y. Son, M. S. Ko, and B. K. Cho, Appl. Phys. Lett. **98**, 172509 (2011).

[194] H. Kobayashi, S. Ikeda, Y. Yoda, H. Nakamura, and M. Machida, Phys. Rev. B **84**, 184304 (2011).

[195] J. Herrero-Martín, C. Mazzoli, V. Scagnoli, L. Paolasini, H. Walker, Y. Xiao, T. Brückel, R. Mittal, N. Kumar, S. K. Dhar, A. Thamizhavel, and Y. Su, J. Supercond. Nov. Mag. **24**, 705 (2011).

[196] A. Blachowski, K. Ruebenbauer, J. Zukrowski, K. Rogacki, Z. Bukowski, and J. Karpinski, Phys. Rev. B **83**, 134410 (2011).

[197] J. J. Ying, X. F. Wang, T. Wu, Z. J. Xiang, R. H. Liu, Y. J. Yan, A. F. Wang, M. Zhang, G. J. Ye, P. Cheng, J. P. Hu, and X. H. Chen, Phys. Rev. Lett. **107**, 067001 (2011).

[198] Y. Xiao, Y. Su, S. Nandi, S. Price, B. Schmitz, C. M. N. Kumar, R. Mittal, T. Chatterji, N. Kumar, S. K. Dhar, A. Thamizhavel, and T. Brückel, Phys. Rev. B **85**, 094504 (2012).

[199] L. Rettig, R. Cortés, S. Thirupathaiah, P. Gegenwart, H. S. Jeevan, M. Wolf, J. Fink, and U. Bovensiepen, Phys. Rev. Lett. **108**, 097002 (2012).

[200] M. Ikeda, K. Yoshida, and T. Kobayashi, J. Phys. Soc. Jpn.. **81**, 033703 (2012).

[201] S. K. Mohanta, S. N. Mishra, S. M. Davane, S. Layek, and Z. Hossain, Mod. Phys. Lett. B **27**, 1350234 (2013).

[202] M. Ikeda, M. Hagiwara, T. Kobayashi, W. Hirata, S. Miyasaka, and S. Tajima, J. Korean Phys. Soc. **62**, 2007 (2013).

[203] A. Dutta, Anupam, Z. Hossain, and A. K. Gupta, J. Phys.: Condens. Matter **25**, 375602 (2013).

[204] G. Adhikary, N. Sahadev, D. Biswas, R. Bindu, N. Kumar, A. Thamizhavel, S. K. Dhar, and K. Maiti, J. Phys.: Condens. Matter **25**, 225701 (2013).

[205] I. Avigo, R. Cortés, L. Rettig, S. Thirupathaiah, H. S. Jeevan, P. Gegenwart, T. Wolf, M. Ligges, M. Wolf, J. Fink, and U. Bovensiepen, J. Phys.: Condens. Matter **25**, 094003 (2013).

[206] A. V. Tsvyashchenko, V. A. Sidorov, L. N. Fomicheva, K. Gofryk, R. A. Sadykov, and J. D. Thompson, Phys. Status Solidi B **250**, 589 (2013).

[207] F. Drief, S. Kacimi, and A. Zaoui, Comput. Mater. Sci. **84**, 97 (2013).

[208] C. W. Kwang-Hua, Chemical Physics **415**, 186 (2013).

[209] P. F. S. Rosa, B. Zeng, C. Adriano, T. M. Garitezi, T. Grant, Z. Fisk, L. Balicas, R. R. Urbano, and P. G. Pagliuso, arXiv:1402.2412.

[210] H. Raffius, E. Mörsen, B. D. Mosel, and W. Müller-Warmuth, J. Phys. Chem. Solids **49**, 785 (1988).

[211] C. Feng, Z. Ren, S. Xu, S. Jiang, Z. A. Xu, G. Cao, I. Nowik, I. Felner, K. Matsubayashi, and Y. Uwatoko, Phys. Rev. B **82**, 094426 (2010).

[212] D. H. Ryan, J. M. Cardogan, S. Xu, Z. A. Xu, and G. H. Cao, Phys. Rev. B **83**, 132403 (2011).

[213] L. Hua, J. M. Shen, Q. L. Zhu, and L. Chen, Physica B **406**, 47 (2011).

[214] J. Ballinger, L. E. Wenger, Y. K. Vohra, and A. S. Sefat, J. Appl. Phys. **111**, 07E106 (2012).

[215] W. H. Jiao, I. Felner, I. Nowik, and G. H. Cao, J. Supercond. Nov. Magn. **25**, 441 (2012).

[216] H. Raffius, E. Mörsen, B. D. Mosel, W. Müller-Warmuth, W. Jeitschko, L. Terbüchte, and T. Vomhof, J. Phys. Chem. Solids **54**, 135 (1993).

[217] M. Reehuis, W. Jeitschko, M. H. Möller, and P. J. Brown, J. Phys. Chem. Solids **53**, 687 (1992) .

[218] S. Nandi, A. Kreyssig, Y. Lee, Yogesh Singh, J. W. Kim, D. C. Johnston, B. N. Harmon, and A. I. Goldman, Phys. Rev. B **79**, 100407 (2009).

[219] A. Akbari, P. Thalmeier, and I. Eremin New J. Phys. **15** 033034 (2013).

[220] T. Terashima, M. Kimata, H. Satsukawa, A. Harada, K. Hazama, S. Uji, H. S. Suzuki, T. Matsumoto, and K. Murata, J. Phys. Soc. Jpn. **78**, 083701 (2009).

[221] W. Uhoya, G. Tsoi, Y. K. Vohra, M. A. McGuire, A. S. Sefat, B. C. Sales, D. Mandrus, and S. T. Weir, J. Phys.: Condens. Matter **22** 292202 (2010).

[222] K. Matsubayashi, K. Munakata, N. Katayama, M. Isobe, K. Ohgushi, Y. Ueda, N. Kawamura, M. Mizumaki, N. Ishimatsu, M. Hedo, I. Umehara, and Y. Uwatoko, Phys. Rev. B **84**, 024502 (2011).

[223] W. Uhoya, G. Tsoi, Y. K. Vohra, M. A. McGuire, and A. S. Sefat, J. Phys.: Condens. Matter **22** 292202 (2010).

[224] N. Kurita, M. Kimata, K. Kodama, A. Harada, M. Tomita, H. S. Suzuki, T. Matsumoto, K. Murata, S. Uji, and T. Terashima, Phys. Rev. B **83**, 214513 (2011).

[225] N. Kurita, M. Kimata, K. Kodama, A. Harada, M. Tomita, H. S. Suzuki, T. Matsumoto, K. Murata, S. Uji, and T. Terashima, Phys. Rev. B **83**, 100501(R) (2011).

[226] H. B. Banks, W. Bi, L. Sun, G. F. Chen, X. H. Chen, and J. S. Schilling, Physica C **471**, 476 (2011).

[227] N. Kurita, M. Kimata, K. Kodama, A. Harada, M. Tomita, H. S. Suzuki, T. Matsumoto, K. Murata, S. Uji, and T. Terashima, J. Phys.: Conf. Ser. **273**, 012098 (2011).

[228] N. Kurita, M. Kimata, K. Kodama, A. Harada, M. Tomita, H. S. Suzuki, T. Matsumoto, K. Murata, S. Uji, and T. Terashima, J. Phys.: Conf. Ser. **391**, 012132 (2012).

[229] N. Kurita, M. Kimata, K. Kodama, A. Harada, M. Tomita, H. S. Suzuki, T. Matsumoto, K. Murata, S. Uji, and T. Terashima, Phys. Rev. B **88**, 224510 (2013).

[230] H. S. Jeevan, D. Kasinathan, H. Rosner, and P. Gegenwart, Phys. Rev. B **83**, 054511 (2011).

[231] A. Ahmed, M. Itou, S. Xu, Z. Xu, G. Cao, Y. Sakurai, J. Penner-Hahn, and A. Deb, Phys. Rev. Lett. **105**, 207003 (2010).

[232] L. Sun, J. Guo, G. Chen, X. Chen, X. Dong, W. Lu, C. Zhang, Z. Jiang, Y. Zou, S. Zhang, Y. Huang, Q. Wu, X. Dai, Y. Li, J. Liu, and Z. Zhao, Phys. Rev. B **82**, 134509 (2010).

[233] D. Wu, G. Chanda, H. S. Jeevan, P. Gegenwart, and M. Dressel, Phys. Rev. B **83**, 100503(R) (2011).

[234] I. Nowik, I. Felner, Z. Ren, G. H. Cao, and Z. A. Xu, J. Phys.: Condens. Matter **23**, 065701 (2011).

[235] S. Thirupathaiah, E. D. L. Rienks, H. S. Jeevan, R. Ovsyannikov, E. Slooten, J. Kaas, E. van Heumen, S. de Jong, H. A. Duerr, K. Siemensmeyer, R. Follath, P. Gegenwart, M. S. Golden, and J. Fink, Phys. Rev. B **84**, 014531 (2011).

[236] G. Cao, S. Xu, Z. Ren, S. Jiang, C. Feng, and Z. A. Xu, J. Phys.: Condens. Matter **23**, 464204 (2011)

[237] Z. Guguchia, A. Shengelaya, A. Maisuradze, L. Howald, Z. Bukowski, M. Chikovani, H. Luetkens, S. Katrych, J. Karpinski, and H. Keller, J. Supercon. Nov. Magn. **26**, 285 (2012).

[238] Y. Tokiwa, S.-H. Hübner, O. Beck, H. S. Jeevan, and P. Gegenwart, Phys. Rev. B **86**, 220505(R) (2012).

[239] W. Li, J. X. Zhu, Y. Chen, and C. S. Ting, Phys. Rev. B **86**, 155119 (2012).

[240] S. Jiang, H. S. Jeevan, J. Dong, and P. Gegenwart, Phys. Rev. Lett. **110**, 067001 (2013).

[241] S. Nandi, W. T. Jin, Y. Xiao, Y. Su, S. Price, D. K. Shukla, J. Strempfer, H. S. Jeevan, P. Gegenwart, and T. Brückel, Phys. Rev. B **89**, 014512 (2014).

[242] S. Nandi, W. T. Jin, Y. Xiao, Y. Su, S. Price, W. Schmidt, K. Schmalzl, T. Chatterji, H. S. Jeevan, P. Gegenwart, and T. Brückel, Phys. Rev. B **90**, 094407 (2014).

[243] J. Munevar, H. Micklitz, M. Alzamora, C. Argüello, T. Goko, F. L. Ning, T. Munsie, T. J. Williams, A. A. Aczel, G. M. Luke, G.F. Chen, and W. Yu, Solid State Commun. **187**, 18 (2014).

[244] X. Xu, W. H. Jiao, N. Zhou, Y. K. Li, B. Chen, C. Cao, J. Dai, A. F. Bangura, and G. Cao, Phys. Rev. B. **89**, 104517 (2014).

[245] W. H. Jiao, J. K. Bao, Q. Tao, H. Jiang, C. M. Feng, Z. A. Xu, and G. H. Cao, J. Phys.: Conf. Ser. **400**, 022038 (2012).

[246] S. Sharma, A. Bharathi, K. Vinod, C. S. Sundar, V. Srihari, S. Sen, H. Ghosh, A. K. Sinha, and S. K. Deb, arXiv:1312.7055

[247] S. Nandi, M. G. Kim, A. Kreyssig, R. M. Fernandes, D. K. Pratt, A. Thaler, N. Ni, S. L. Bud'ko, P. C. Canfield, J. Schmalian, R. J. McQueeney, and A. I. Goldman, Phys. Rev. Lett. **104**, 057006 (2010).

[248] J. J. Ying, T. Wu, Q. J. Zheng, Y. He, G. Wu, Q. J. Li, Y. J. Yan, Y. L. Xie, R. H. Liu, X. F. Wang, and X. H. Chen, Phys. Rev. B **81**, 052503 (2010).

[249] X. B. Chen, Z. A. Ren, H. S. Ding, and L. H. Liu, Sci. China **53**, 1212 (2010).

[250] M. Nicklas, M. Kumar, E. Lengyel, W. Schnelle, and A. Leithe-Jasper, J. Phys.: Conf. Ser. **273**, 012101 (2011).

[251] I. Nowik, I. Felner, Z. Ren, G. H. Cao, and Z. A. Xu, New J. Phys. **13**, 023033 (2011).

[252] Z. Guguchia, J. Roos, A. Shengelaya, S. Katrych, Z. Bukowski, S. Weyeneth, F. Murányi, S. Strässle, A. Maisuradze, J. Karpinski, and H. Keller, Phys. Rev. B **83**, 144516 (2011).

[253] Z. Guguchia, S. Bosma, S. Weyeneth, A. Shengelaya, R. Puzniak, Z. Bukowski, J. Karpinski, and H. Keller, Phys. Rev. B **84**, 144506 (2011).

[254] A. Blachowski, K. Ruebenbauer, J. Zukrowski, Z. Bukowski, K. Rogacki, P. J. W. Moll, and J. Karpinski, Phys. Rev. B **84**, 174503 (2011).

[255] M. Matusiak, Z. Bukowski, and J. Karpinski, Phys. Rev. B **83**, 224505 (2011).

[256] V. H. Tran, T. A. Zaleski, Z. Bukowski, L. M. Tran, and A. J. Zaleski, Phys. Rev. B **85**, 052502 (2012).

[257] V. H. Tran, Z. Bukowski, L. M. Tran, and A. J. Zaleski, New J. Phys. **14**, 073052 (2012).

[258] F. A. Garcia, A. Leithe-Jasper, W. Schnelle, M. Nicklas, H. Rosner, and J. Sichelschmidt, New J. Phys. **14**, 063005 (2012).

[259] W. T. Jin, S. Nandi, Y. Xiao, Y. Su, O. Zaharko, Z. Guguchia, Z. Bukowski, S. Price, W. H. Jiao, G. H. Cao, and T. Brückel, Phys. Rev. B **88**, 214516 (2013).

[260] C. Rumble, M. Itou, S. Jiang, Z. A. Xu, G. Cao, Y. Sakurai, J. Penner-Hahn, and A. Deb, J. Appl. Phys. **113**, 013907 (2013).

[261] Z. Ren, X. Lin, Q. Tao, S. Jiang, Z. Zhu, C. Wang, G. Cao, and Z. Xu, Phys. Rev. B **79**, 094426 (2009).

[262] I. Nowik, I. Felner, Z. Ren, Z. A. Xu, and G. H. Cao, J. Phys.: Conf. Ser. **217**, 012121 (2010).

[263] W. H. Jiao, H. F. Zhai, J. K. Bao, Y. K. Luo, Q. Tao, C. M. Feng, Z. A. Xu, and G. H. Cao, New J. Phys. **15**, 113002 (2013).

[264] U. B. Paramanik, P. L. Paulose, S. Ramakrishnan, A. K. Nigam, C. Geibel, and Z. Hossain, Supercond. Sci. Technol. **27**, 075012 (2014).

[265] L. J. Li, Y. K. Luo, Q. B. Wang, H. Chen, Z. Ren, Q. Tao, Y. K. Li, X. Lin, M. He, Z. W. Zhu, G. H. Cao, and Z. A. Xu, New J. Phys. **11**, 025008 (2008).

[266] W. Z. Hu, J. Dong, G. Li, Z. Li, P. Zheng, G. F. Chen, J. L. Luo, and N. L. Wang, Phys. Rev. Lett. **101**, 257005 (2008).

[267] A. Mitsuda, T. Matoba, F. Ishikawa, Y. Yamada, and H. Wada, J. Phys. Soc. Jpn. **79**, 073704 (2010).

[268] A. Mitsuda, S. Seike, T. Matoba, H. Wada, F. Ishikawa, and Y. Yamada, J. Phys.: Conf. Ser. **273**, 012100 (2011).

[269] P. F. S. Rosa, C. Adriano, W. Iwamoto, T. M. Garitezi, T. Grant, Z. Fisk, and P. G. Pagliuso, Phys. Rev. B **86**, 165131 (2012)

[270] Y. He, T. Wu, G. Wu, Q. J. Zheng, Y. Z. Liu, H. Chen, J. J. Ying, R. H. Liu, X. F. Wang, Y. L. Xie, Y. J. Yan, J. K. Dong, S. Y. Li, and X. H. Chen, J. Phys.: Condens. Matter **22**, 235701 (2010).

[271] R. Hu, S. L. Bud'ko, W. E. Straszheim, and P. C. Canfield, Phys. Rev. B **83**, 094520 (2011).

[272] H. A. Krug von Nidda, S. Kraus, S. Schaile, E. Dengler, N. Pascher, M. Hemmida, M. J. Eom, J. S. Kim, H. S. Jeevan, P. Gegenwart, J. Deisenhofer, and A. Loidl, Phys. Rev. B **86**, 094411 (2012).

[273] R. Sarkar, R. Nath, P. Khuntia, H. S. Jeevan, P. Gegenwart, and M. Baenitz, J. Phys.: Condens. Matter **24**, 045702 (2012).

[274] R. Hu, E. D. Mun, M. M. Altarawneh, C. H. Mielke, V. S. Zapf, S. L. Bud'ko, and P. C. Canfield, Phys. Rev. B **85**, 064511 (2012).

[275] Anupam, P. L. Paulose, H. S. Jeevan, C. Geibel, and Z. Hossain, J. Phys.: Condens. Matter **21**, 265701 (2009).

[276] V. A. Gasparov, H. S. Jeevan, and P. Gegenwart, JETP Letters **89**, 294 (2009).

[277] N. Pascher, J. Deisenhofer, H.-A. Krug von Nidda, M. Hemmida, H. S. Jeevan, P. Gegenwart, and A. Loidl, Phys. Rev. B **82**, 054525 (2010).

[278] H. S. Jeevan and P. Gegenwart, J. Phys.: Conf. Ser. **200**, 012060 (2010).

[279] Anupam, P. L. Paulose, S. Ramakrishnan, and Z. Hossain, J. Phys.: Condens. Matter **23**, 455702 (2011).

[280] J. Maiwald, H. S. Jeevan, and P. Gegenwart, Phys. Rev. B **85**, 024511 (2012).

[281] T. Dey, P. Khuntia, A. V. Mahajan, Anupam, and Z. Hossain, Europ. Phys. J. B **86**, 458 (2013).

[282] V. A. Gasparov, A. Audouard, L. Drigo, A. I. Rodigin, C. T. Lin, W. P. Liu, M. Zhang, A. F. Wang, X. H. Chen, H. S. Jeevan, J. Maiwald, and P. Gegenwart, Phys. Rev. B **87**, 094508 (2013).

[283] K. Sasmal, B. Lv, B. Lorenz, A. M. Guloy, F. Chen, Y.-Y. Xue, and C.-W. Chu, Phys. Rev. Lett. **101**, 107007 (2008).

[284] Y. Qi, Z. Gao, L. Wang, D. Wang, X. Zhang, and Y. Ma, New J. Phys. **10** 123003 (2008).

[285] Y. Qi, L. Wang, Z. Gao, X. Zhang, D. Wang, C. Yao, C. Wang, C. Wang, and Y. Ma, New J. Phys. **14**, 033011 (2012).

[286] Anupam, V. K. Anand, P. L. Paulose, S. Ramakrishnan, C. Geibel, and Z. Hossain, Phys. Rev. B **85**, 144513 (2012).

[287] Y. R. Jang, J. B. Hong, B. H. Min, M. A. Jung, Y. Y. Song, H. J. Oh, K. J. Lee, M. H. Jung, S. Kanematsu, K. Imura, K. Deguchi, N. K. Sato, and Y. S. Kwon, Supercond. Sci. Technol. **24**, 085017 (2011).

[288] T. Wu, G. Wu, H. Chen, Y. L. Xie, R. H. Liu, X. F. Wang, and X. H. Chen, J. Magn. Magn. Mater **321**, 3870 (2009).

[289] F. A. Garcia, E. M. Bittar, C. Adriano, T. M. Garitezi, C. Rettori, and P. G. Pagliuso, J. Phys.: Conf. Ser. **273**, 012093 (2011).

[290] B. Zhou, L. X. Yang, F. Chen, M. Xu, T. Wu, G. Wu, X. H. Chen, and D. L. Feng, J. Phys. Chem. Solids **72**, 474 (2011).

[291] M. Zhang, J. J. Ying, Y. J. Yan, A. F. Wang, X. F. Wang, Z. J. Xiang, G. J. Ye, P. Cheng, X. G. Luo, J. Hu, and X. H. Chen, Phys. Rev. B **85**, 092503 (2012).

[292] T. Moriya and K. Ueda, Adv. in Phys. **49**, 555 (2000).

[293] P. Richard, C. Capan, J. Ma, P. Zhang, N. Xu, T. Qian, J. D. Denlinger, G.-F. Chen, A. S. Sefat, Z. Fisk, and H. Ding, J. Phys.: Condens. Matter **26**, 035702 (2014).

[294] M. Xia, W. H. Jiao, Z. R. Ye, Q. Q. Ge, Y. Zhang, J. Jiang, R. Peng, X. P. Shen, Q. Fan, G. H. Cao, T. Zhang, B. P. Xie, and D. L. Feng, J. Phys.: Condens. Matter **26**, 265701 (2014).

[295] X. Xu, W. H. Jiao, N. Zhou, Y. K. Li, B. Chen, C. Cao, J. Dai, A. F. Bangura, and G. Cao, Phys. Rev. B **89**, 104517 (2014).

[296] F. Klingert, *Magnetic Investigations on $EuFe_2As_2$ - Superconductors*, Diplomarbeit am 1. Physikalischen Institut, Stuttgart (2012).

[297] B. Maji, K. G. Suresh and A. K. Nigam, J. Phys.: Condens. Matter **23**, 506002 (2011).

[298] A. C. D. van Enter and J. L. van Hemmen, Phys. Rev. B **31**, 603 (1985).

[299] K. Jonason, J. Mattsson, and P. Nordblad, Phys. Rev. B **53**, 6507 (1996).

[300] A. M. Campbell and J. E. Evetts, Adv. i. Phys. **21**, 199 (1972).

[301] J. Giapintzakis, R. L. Neiman, D. M. Ginsberg, and M. A. Kirk, Phys. Rev. B **50**, 16001 (1994).

[302] M. C. Frischherzt, F. M. Sauerzopft, H. W. Webert, M. Murakamit, and G. A. Emel'chenko, Supercond. Sci. Technd. **8**, 485 (1995).

[303] G. Prando, P. Carretta, R. De Renzi, S. Sanna, A. Palenzona, M. Putti, and M. Tropeano, Phys. Rev. B **83**, 174514 (2011).

[304] W. Braunisch, N. Knauf, V. Kataev, S. Neuhausen, A. Grütz, A. Kock, B. Roden, D. Khomskii, and D. Wohlleben, Phys. Rev. Lett. **68**, 1908 (1992).

[305] F. Pfister, *Anisotroper Transport in eisenbasierten Supraleitern*, Bachelorarbeit am 1. Physikalischen Institut, Stuttgart (2013).

[306] M. Colarieti-Tosti, S. I. Simak, R. Ahuja, L. Nordström, O. Eriksson, D. Åberg, S. Edvardsson, and M. S. S. Brooks, Phys. Rev. Lett. **91**, 157201 (2003).

[307] L. Bauernfeind, W. Widder, and H. F. Braun, Physica C **254**, 151 (1995).

[308] C. A. Cardoso, F. M. Araujo-Moreira, V. P. S. Awana, E. Takayama-Muromachi, O. F. de Lima, H. Yamauchi, and M. Karppinen, Phys. Rev. B **67**, 020407(R) (2003).

[309] S. Garcia, L. Ghivelder, and I. Felner, Phys. Rev. B **79**, 054506 (2009).

[310] S. Lausberg, J. Spehling, A. Steppke, A. Jesche, H. Luetkens, A. Amato, C. Baines, C. Krellner, M. Brando, C. Geibel, H.-H. Klauss, and F. Steglich, Phys. Rev. Lett. **109**, 216402 (2012).

[311] Private communication with Prof. J. Fink, IFW Dresden.

[312] Private communication with Prof. J. Schmalian, KIT.

[313] Private communication with Prof. I. Fisher, Stanford.

[314] U. Pracht, *THz Spectroscopy on Quantum Phase Transition in Ultra-Thin Films of Titanium Nitride*, Masterarbeit am 1. Physikalischen Institut, Stuttgart (2012).

[315] S. Zapf, B. Gorshunov, D. Wu, E. Zhukova, V. S. Nozdrin, S. Haindl, K. Iida, and M. Dressel, J. Supercond. Nov. Magn. **21**, 1557 (2013).

[316] A. S. Prokhorov, E. S. Zhukova, A. A. Boris, I. E. Spektor, B. P. Gorshunov, V. S. Nozdrin, E. A. Motovilova, L. S. Kadyrov, S. Zapf, S. Haindl, K. Iida, M. Dressel, K. V. Chizh, M. S. Storozhevykh, L. V. Arapkina, V. A. Chapnin, O. V. Uvarov, V. P. Kalinushkin, and V. A. Yuryev, Radiophys. Quant. Electr. **56**, 620 (2014).

[317] A. E. Karakozov, S. Zapf, B. Gorshunov, Y. G. Ponomarev, M. V. Magnitskaya, E. Zhukova, A. S. Prokhorov, V. B. Anzin, and S. Haindl, Phys. Rev. B **90**, 014506 (2014).

[318] A. E. Karakozov, B. P. Gorshunov, Y. G. Ponomarev, A. S. Prokhorov, M. V. Magnitskaya, E. Zhukova, K. Iida, M. Dressel, S. Zapf, and S. Haindl, JETP Letters **100**, to be translated (2014).

[319] D. V. Efremov, M. M. Korshunov, O. V. Dolgov, A. A. Golubov, and P. J. Hirschfeld, Phys. Rev. B **84**, 180512(R) (2011).

[320] D. V. Efremov, A. A. Golubov, and O. V. Dolgov, New J. Phys. **15**, 013002 (2013).

[321] C. Tarantini, M. Putti, A. Gurevich, Y. Shen, R. K. Singh, J. M. Rowell, N. Newman, D. C. Larbalestier, P. Cheng, Y. Jia, and H.-H. Wen, Phys. Rev. Lett. **104**, 087002 (2010).

[322] M. Schilling, *THz investigation on iron-based superconductors*, Masterarbeit am 1. Physikalischen Institut, Stuttgart (2014).

[323] A. Baumgartner, *THz Untersuchungen an eisenbasierten Supraleiter*n, Bachelorarbeit am 1. Physikalischen Institut, Stuttgart (2013).

# CURRICULUM VITAE

## Education

| | |
|---|---|
| 1996–2005 | Friedrich-Dessauer-Gymnasium Aschaffenburg |
| 2005–2010 | Julius-Maximilians-Universität Würzburg, elite program "FOKUS Physik" |
| since 06/2010 | PhD project, Prof. Dressel, University of Stuttgart |

## Experience

| | |
|---|---|
| 09/2007–10/2007 | MPI FKF Stuttgart, Department Kern, Dr. Vogelgesang, Bachelor thesis: Wavelength Dependent Optoelectronic Characterization of Carbon Nanotube Based Field Effect Transistors |
| 08/2008–09/2008 | University of Würzburg, EP3 Molenkamp, Prof. Geurts, internship: Infrared-Spectroscopy on $GdMnO_3$ |
| 01/2009–04/2009 | UC Berkeley, Department of Chemistry, Prof. Pines, co-worker on the project: Imaging a Temperature Gradient via NMR |
| 04/2009-04/2010 | University of Würzburg, EP3 Molenkamp, Prof. Geurts, Master thesis: Spinflip-Raman-Spectroscopy on CdMnTe / CdMgZnTe - Quantum Well Structures |
| since 06/2010 | University of Stuttgart, $1^{st}$ Physical Institute, Prof. Dressel: infrared and THz spectroscopy, SQUID magnetometry, dc resistivity, teaching (laboratory courses), supervision of four Bachelor and two Master students |
| 04/2013-09/2013 | Several visits at the UC San Diego, Department of Physics, Prof. Basov: magneto-optical investigations on $EuFe_2As_2$ |

## Selected scholarships and Awards

| | |
|---|---|
| 09/2010–04/2012 | Scholarship of the Postgraduate Research Grants Program of Baden-Württemberg |
| 03/2012 | Best Poster Award at the International Conference on Magnetism and Superconductivity, Istanbul |
| 03/2014 | Düker Award for the best scientific presentation of a research project for school students |

# DECLARATION OF ORIGINALITY

I hereby declare that this thesis and the work reported herein was composed by and originated entirely from me. Information derived from the published and unpublished work of others has been acknowledged in the text and references.